

**EFFECT OF OPERATING CONDITIONS AND
PARTICLE PROPERTIES ON ELECTROSTATICS AND
ENTRAINMENT IN GAS-SOLID FLUIDIZED BEDS**

by

Turki A. Al-Smari

B.Sc., King Saud University, Al-Riyadh, Saudi Arabia, 2002
M.A.Sc., King Saud University, Al-Riyadh, Saudi Arabia, 2006

A THESIS SUBMITTED IN PARTIAL FULFILLMENT OF THE
REQUIREMENTS FOR THE DEGREE OF

DOCTOR OF PHILOSOPHY

in

THE FACULTY OF GRADUATE AND POSTDOCTORAL STUDIES
(Chemical and Biological Engineering)

THE UNIVERSITY OF BRITISH COLUMBIA
(Vancouver)

June, 2014

© Turki A. Al-Smari, 2014

Abstract

The effects of superficial gas velocity, pressure, and temperature on entrainment and electrostatic charge with glass beads and polyethylene as bed particles were investigated in a fluidization column of 0.15 m inner diameter and 2.0 m height. Four collision probes at different levels, a freeboard sampler, and a current detection pipe measured the electrostatics in the bed, freeboard, and column exit. The entrainment and electrostatic charge inside the bed and freeboard region increased as the superficial gas velocity or pressure increased. Temperature had negligible effect on the entrainment over the limited range studied. However, electrostatic charges decreased and the charge polarity reversed as the bed temperature increased from 20 to 75 °C.

The calculated electrostatic forces resulting from fine-fine and fine-coarse particle interactions are comparable to the gravitational force on fine particles in the fluidized bed. Entrainment empirical correlations developed in this work showed much better performance after the effect of electrostatic forces was taken into account, with the entrainment flux decreasing as electrostatic forces increase. The Choi et al. (1999) entrainment correlation shows better prediction of the entrainment flux in our system after the effect of the electrostatic force is considered.

The electrostatic charges in the bed decreased with increasing air relative humidity. The charge density of fines decreased and entrainment increased as the air relative humidity increased. The relative humidity had no effect on the charge density or entrainment of polyethylene particles, which can also probably be attributed to the hydrophobic nature of polyethylene.

The magnitude of electrostatic charges generated inside the fluidized bed increased slightly as the size of the coarse particles decreased. The entrainment decreased as the coarse particle size decreased. The electrostatic charges increased and entrainment decreased as the coarse particle density increased.

The magnitude of electrostatic charges generated inside the fluidized bed increased and entrainment decreased as the fine particle density increased. The electrostatic charges and entrainment also increased as the fine concentration increased. The fines concentration had little or no effect on fines charge densities. Bipolar charging was observed in all experiments with fine particles charged positively, whereas large particles were charged negatively.

Preface

All the work presented in this thesis was completed by the author under the supervision of Professors John Grace and Xiaotao Bi at the University of British Columbia. The author developed the experimental design, conducted the experimental work, operated the fluidization pilot plant, compiled the results and wrote this dissertation.

Some of the results from Chapter 3 were presented at the 62nd Canadian Chemical Engineering Conference, October 14-17, 2012 in Vancouver, BC. Also some of the results from Chapter 4 were presented at AIChE 2013 Conference, November 3-8, 2013 in San Francisco, CA.

The main chapters of this thesis will be revised for submission to journals for publication.

Table of Contents

Abstract.....	ii
Preface.....	iv
Table of Contents.....	v
List of Tables.....	ix
List of Figures	x
Nomenclature	xxiv
Acknowledgements	xxvi
Dedication.....	xxvii
Chapter 1: Introduction.....	1
1.1 Particle Entrainment	3
1.2 Parameters Affecting Particle Entrainment.....	4
1.2.1 Effect of Temperature	4
1.2.2 Effect of Pressure	5
1.2.3 Effect of Superficial Gas Velocity	5
1.2.4 Effect of Freeboard and Expand Bed Height	5
1.2.5 Effect of Particle Properties	6
1.2.6 Effect of Electrostatics	7
1.3 Electrostatic Phenomena	9
1.4 Electrostatic Charge Generation Mechanism	9
1.4.1 Triboelectrification	9
1.4.2 Frictional Charging	10
1.4.3 Thermionic Emission Charging	11
1.5 Electrostatics Measurement Techniques	11
1.5.1 Electrostatic Probes.....	11
1.5.1.1 Induction Probes.....	11
1.5.1.2 Capacitance Probes	12
1.5.1.3 Collision Probes	13
1.5.2 Faraday Cup	14

1.5.3 Current Detecting Pipe.....	15
1.6 Parameters Affecting Electrostatics in Bubbling Fluidized Beds	16
1.6.1 Influence of Gas Velocity	16
1.6.2 Influence of Operating Pressure and Temperature	17
1.6.3 Influence of Gas Properties – Relative Humidity	18
1.6.4 Influence of Particles Properties.....	19
1.7 Solid Particles Classification.....	19
1.8 Fluidization Flow Regime	20
1.9 Thesis Objectives.....	21
1.10 Thesis Outline.....	22
Chapter 2: Experimental Equipment and Procedure.....	23
2.1 High-Pressure System – Air Compressor.....	23
2.2 Elevated-Pressure Fluidization Column.....	24
2.3 Instrumentation and Measurements.....	26
2.3.1 Fluidization Column Operating Variables and Measurements.....	27
2.3.2 Electrostatic Charge Measurement Techniques.....	27
2.3.2.1 Collision Ball Probes.....	27
2.3.2.2 Freeboard Sampler	29
2.3.2.3 Current Detecting Pipe	30
2.4 Bed Materials	31
2.4.1 Coarse Particles.....	31
2.4.2 Added Fine Particles	33
2.4.3 Binary Mixtures	36
2.5 Experimental Methodology.....	37
Chapter 3: Results and Discussion: Effect of Operating Parameters.....	40
3.1 Collision Ball Probes Location and Sensitivity.....	40
3.2 Effect of Operating Parameters	42
3.2.1 Effect of Superficial Gas Velocity	43
3.2.1.1 Glass Beads	43
3.2.1.2 Polyethylene.....	51
3.2.2 Effect of Operating Pressure.....	56
3.2.2.1 Glass Beads	56

3.2.2.2 Polyethylene	62
3.2.3 Effect of Operating Temperature	67
3.2.3.1 Glass Beads	67
3.2.3.2 Polyethylene	74
3.3 Summary	78
Chapter 4: Results and Discussion: Effect of Gas Properties	79
4.1 Humidification.....	79
4.2 Effect of Gas Relative Humidity	80
4.2.1 Fines Material: Glass Beads.....	80
4.2.2 Fines Material: Alumina (Al ₂ O ₃)	89
4.2.3 Fines Material: Polyethylene	93
4.3 Summary	100
Chapter 5: Results and Discussion: Effect of Particle Properties.....	101
5.1 Effect of Coarse Particle Properties	101
5.1.1 Effect of Average Particle Size.....	101
5.1.2 Effect of Particle Density and Type.....	107
5.1.3 Summary	117
5.2 Effect of Fine Particle Properties	118
5.2.1 Effect of Fines Density and Type	118
5.2.2 Effect of Fines Concentration	124
5.2.3 Bipolar Charging.....	135
5.2.4 Summary	136
Chapter 6: Relationship between Electrostatics and Entrainment.....	137
6.1 Comparison of Forces on Particles.....	137
6.2 Relationship between Entrainment and Electrostatic	139
6.2.1 Derivation of Correlation	139
6.2.2 Comparison of Correlation	142
6.3 Summary	147
Chapter 7: Conclusions and Recommendations	149
7.1 Conclusions	150
7.2 Recommendations for Future Work.....	152
References.....	153

Appendix A:Equipment Photographs	163
A.1 Experimental Apparatus	163
A.2 Fluidization Straight Section	164
A.3 Fluidization Expanded Section.....	165
A.4 Fluidization Unit Engineering Drawing	166
A.5 Electrostatics Measurement Techniques	167
Appendix B:Paticle Size Distribution Graphs.....	170
Appendix C:Particle Properties	180
C.1 Calculation of Minimum Fluidization Velocity of M3 Binary Mixture	180
C.2 Calculation of Total Surface Area of GBF	181
C.3 Calculation of Electrostatic and Gravity Forces	181

List of Tables

Table 2.1: Relevant properties of coarse particles.....	32
Table 2.2: Properties of fine particles employed in this study.	34
Table 2.3: Properties of binary particle mixtures.	36
Table 4.1: Charge density, q_m ($\mu\text{C}/\text{kg}$), charge/surface ratio, q_s ($\mu\text{C}/\text{m}^2$) and entrainment flux, W_s ($\text{kg}/\text{m}^2\cdot\text{s}$) for different fines and different air relative humidities with large glass beads particles (GBL) as the major bed component. $P = 414$ kPa, $T = 20 \pm 2^\circ\text{C}$ and $U_g = 0.3$ m/s.	99
Table 6.1: Comparison of interparticle forces in a fluidized bed for different binary mixtures ($P= 414$ kPa, $T = 20 \pm 2^\circ\text{C}$ and $U_g = 0.3$ m/s)	138
Table 6.2: Summary of experimental findings for mixture M3. For particles properties, see Tables 2.1 and 2.2	139
Table 6.3: Range of variables for the data on which the Choi et al. (1999) correlation is based.....	143
Table 6.4: Summary of empirical correlations investigated in this chapter	147

List of Figures

Figure 1.1 Correlations used to predict the entrainment rate (from George and Grace, 1981), rectangular column 0.254 m x 0.432 m, Silica sand particles, $d_p = 102 \mu\text{m}$	2
Figure 1.2 Fluidized bed zones (from Wouter, 2008)	3
Figure 1.3 Particle ejection mechanisms (from Yang, 2003)	4
Figure 1.4 Relative humidity effect zones (adapted from Kato and Li, 2001). RHe and RHc denote electrostatic and capillary relative humidity of gas, whereas K is the elutriation rate constant.....	8
Figure 1.5 Triboelectrification charging mechanism (adapted from Jones, 1997)	10
Figure 1.6 Induction probe (from Boland and Geldart, 1971).....	12
Figure 1.7 Capacitance probe (from Guardiola et al., 1992).....	13
Figure 1.8 Collision ball probe (adapted from Park et al., 2002b).....	14
Figure 1.9 Faraday cup (adapted from Cross, 1987)	15
Figure 1.10 Current detecting pipe (adapted from Matsusaka and Masuda, 2006).....	16
Figure 1.11 Geldart solids classification (adapted from Geldart, 1973)	20
Figure 1.12 Gas-solid flow regimes (from Grace, 1986)	21
Figure 2.1 Schematic of overall layout of fluidization unit. PR: pressure regulator, PVC: pressure control valve.	24
Figure 2.2 Schematic of fluidization column..	26
Figure 2.3 Collision ball probe (from Moughrabiah et al., 2009).	28
Figure 2.4 Locations of collision ball probes.	29
Figure 2.5 Schematic of freeboard sampler.....	30
Figure 2.6 Schematic of current detecting pipe.....	31
Figure 2.7 SEM images of coarse particles used in this study.....	33
Figure 2.8 SEM images of fine particles investigated during this study.....	35

Figure 3.1 Net cumulative charges measured by probe D in freeboard as a function of time for binary mixture M3. $P = 207$ kPa, $T = 20 \pm 2^\circ\text{C}$, $U_g = 0.6$ m/s, $RH = 12 \pm 2\%$. For physical properties of particles, see Tables 2.1, 2.2 and 2.3. Numbers on curves denote probe D distance above distributor plate (in m). 41

Figure 3.2 Cumulative charge as a function of time for air flow through empty column. $P = 207$ kPa, $T = 20 \pm 2^\circ\text{C}$, $U_g = 0.3$ m/s, $RH = 12 \pm 2\%$. For position of probes, see Figure 2.4. 42

Figure 3.3 Effect of superficial gas velocity on net cumulative charges as a function of time at different axial positions in a bed of binary mixture M3. $P = 207$ kPa, $T = 20 \pm 2^\circ\text{C}$, $RH = 12 \pm 2\%$. For physical properties of particles, see Tables 2.1, 2.2 and 2.3. Numbers on curves denote superficial gas velocity (in m/s). For probe positions, see Figure 2.4. 44

Figure 3.4 Net cumulative charges measured by probe A as a function of time in a bed of binary mixture M3. $P = 207$ kPa, $T = 20 \pm 2^\circ\text{C}$, $U_g = 0.6$ m/s, $RH = 12 \pm 2\%$. For physical properties of particles, see Tables 2.1, 2.2 and 2.3. For probe position, see Figure 2.4. 45

Figure 3.5 Effect of superficial gas velocity on net cumulative charges in freeboard as a function of time for binary mixture M3. $P = 207$ kPa, $T = 20 \pm 2^\circ\text{C}$, $RH = 12 \pm 2\%$. For physical properties of particles, see Tables 2.1, 2.2 and 2.3. Numbers on curves denote superficial gas velocity (in m/s). For position of probe D, see Figure 2.4. 45

Figure 3.6 Standard deviation of charge fluctuations in freeboard as a function of superficial gas velocity for binary mixture M3. $P = 207$ kPa, $T = 20 \pm 2^\circ\text{C}$, $RH = 12 \pm 2\%$. For physical properties of particles, see Tables 2.1, 2.2 and 2.2. For position of probe D, see Figure 2.4. 46

Figure 3.7 Charge density of glass bead fines measured by freeboard sampler as a function of superficial gas velocity for binary mixture M3. $P = 207$ kPa, $T = 20 \pm 2^\circ\text{C}$, $RH = 12 \pm 2\%$. For physical properties of particles, see Tables 2.1, 2.2 and 2.3. For freeboard sampler details, see Figure 2.5. Error bars correspond to $\pm 90\%$ confidence intervals 46

Figure 3.8 Current flow through current detection pipe at column exit for binary mixture M3 as a function of superficial gas velocity. $P = 207$ kPa, $T = 20 \pm 2^\circ\text{C}$, $RH = 12 \pm 2\%$. For physical properties of particles, see Tables 2.1, 2.2 and 2.3. For current-detecting pipe details, see Figure 2.6. 47

Figure 3.9 Entrainment flux measured for binary mixture M3 as function of superficial gas velocity. P = 207 kPa, T = 20±2°C, RH = 12±2%. For physical properties of particles, see Tables 2.1, 2.2 and 2.3. Error bar corresponds to ± 90% confidence interval. 47

Figure 3.10 Comparison of measured entrainment flux for binary mixture M3 with predictions from empirical correlations as a function of superficial gas velocity. P = 207 kPa, T = 20±2°C, RH = 12±2%. For physical properties of particles, see Tables 2.1, 2.2 and 2.3..... 51

Figure 3.11 Effect of superficial gas velocity on net cumulative charges as a function of time at different axial positions in bed of binary mixture M10. P = 207 kPa, T = 20±2°C, RH = 12±2%. For physical properties of particles, see Tables 2.1, 2.2 and 2.3. Numbers on curves denote superficial gas velocity (in m/s). For probe positions, see Figure 2.4..... 53

Figure 3.12 Standard deviation of charge fluctuations in freeboard as a function of superficial gas velocity for binary mixture M10. P = 207 kPa, T = 20±2°C, RH = 12±2%. For physical properties of particles, see Tables 2.1, 2.2 and 2.2. For position of probe D, see Figure 2.4 54

Figure 3.13 Charge density of fine glass bead measured by freeboard sampler as a function of superficial gas velocity for binary mixture M10. P = 207 kPa, T = 20±2°C, RH = 12±2%. For physical properties of particles, see Tables 2.1, 2.2 and 2.3. For freeboard sampler details, see Figure 2.5. Error bar corresponds to ± 90% confidence interval 54

Figure 3.14 Current flow through current detection pipe at column exit for binary mixture M10 as a function of superficial gas velocity. P = 207 kPa, T = 20±2°C, RH = 12±2%. For physical properties of particles, see Tables 2.1, 2.2 and 2.3. For current detecting pipe details, see Figure 2.6.. 55

Figure 3.15 Entrainment flux measured for binary mixture M10 as a function of superficial gas velocity. P = 207 kPa, T = 20±2°C, RH = 12±2%. For physical properties of particles, see Tables 2.1, 2.2 and 2.3. Error bars correspond to ± 90% confidence intervals..... 55

Figure 3.16 Effect of pressure on net cumulative charges as a function of time at different axial positions in bed containing mixture M3. U_g = 0.3 m/s, T = 20±2°C, RH = 12±2%. For physical properties of particles, see Tables 2.1, 2.2 and 2.3. Numbers on curves denote absolute pressure (in kPa). For probe positions, see Figure 2.4 58

Figure 3.17 Standard deviation of charge fluctuations in freeboard as function of pressure for binary mixture M3. $U_g = 0.3$ m/s, $T = 20\pm 2^\circ\text{C}$, $\text{RH} = 12\pm 2\%$. For physical properties of particles, see Tables 2.1, 2.2 and 2.2. For position of probe D, see Figure 2.4.....	59
Figure 3.18 Effect of pressure on charge density of fines measured by freeboard sampler in binary mixture M3. $U_g = 0.3$ m/s, $T = 20\pm 2^\circ\text{C}$, $\text{RH} = 12\pm 2\%$. For physical properties of particles, see Tables 2.1, 2.2 and 2.3. For freeboard sampler details, see Figure 2.5. Error bars correspond to $\pm 90\%$ confidence intervals.....	59
Figure 3.19 Current flow through current detection pipe at column exit in binary mixture M3 as function of pressure. $U_g = 0.3$ m/s, $T = 20\pm 2^\circ\text{C}$, $\text{RH} = 12\pm 2\%$. For physical properties of particles, see Tables 2.1, 2.2 and 2.3. For current detecting pipe details, see Figure 2.6..	60
Figure 3.20 Entrainment flux measured for binary mixture M3 as function of pressure. $U_g = 0.3$ m/s, $T = 20\pm 2^\circ\text{C}$, $\text{RH} = 12\pm 2\%$. For physical properties of particles, see Tables 2.1, 2.2 and 2.3. Error bars correspond to $\pm 90\%$ confidence intervals.....	60
Figure 3.21 Effect of pressure on net cumulative charges as function of time at different axial positions in a bed of binary mixture M10. $U_g = 0.3$ m/s, $T = 20\pm 2^\circ\text{C}$, $\text{RH} = 12\pm 2\%$. For physical properties of particles, see Tables 2.1, 2.2 and 2.3. Numbers on curves denote absolute pressure (in kPa). For probe positions, see Figure 2.4.	64
Figure 3.22 Standard deviation of charge fluctuations in freeboard as function of pressure for binary mixture M10. $U_g = 0.3$ m/s, $T = 20\pm 2^\circ\text{C}$, $\text{RH} = 12\pm 2\%$. For physical properties of particles, see Tables 2.1, 2.2 and 2.2. For position of probe D, see Figure 2.4.....	65
Figure 3.23 Effect of pressure on charge density of fines measured by freeboard sampler in binary mixture M10. $U_g = 0.3$ m/s, $T = 20\pm 2^\circ\text{C}$, $\text{RH} = 12\pm 2\%$. For physical properties of particles, see Tables 2.1, 2.2 and 2.3. For freeboard sampler details, see Figure 2.5. Error bars correspond to $\pm 90\%$ confidence intervals.....	65
Figure 3.24 Current flow through current detection pipe at column exit in binary mixture M10 as function of pressure. $U_g = 0.3$ m/s, $T = 20\pm 2^\circ\text{C}$, $\text{RH} = 12\pm 2\%$. For physical properties of particles, see Tables 2.1, 2.2 and 2.3. For current detecting pipe details, see Figure 2.6.....	66

Figure 3.25 Entrainment flux measured for binary mixture M10 as function of pressure. $U_g = 0.3$ m/s, $T = 20 \pm 2^\circ\text{C}$, $\text{RH} = 12 \pm 2\%$. For physical properties of particles, see Tables 2.1, 2.2 and 2.3. Error bars correspond to $\pm 90\%$ confidence intervals.....	66
Figure 3.26 Effect of temperature on net cumulative charges as function of time at different axial positions in bed of binary mixture M3. $U_g = 0.3$ m/s, $P = 414$ kPa, $\text{RH} = 12 \pm 6\%$. For physical properties of particles, see Tables 2.1, 2.2 and 2.3. Numbers on curves denote bed temperature (in $^\circ\text{C}$). For probe positions, see Figure 2.4.....	69
Figure 3.27 Standard deviation of charge fluctuations in freeboard as function of bed temperature for binary mixture M3. $U_g = 0.3$ m/s, $P = 414$ kPa, $\text{RH} = 12 \pm 6\%$. For physical properties of particles, see Tables 2.1, 2.2 and 2.2. For position of probe D, see Figure 2.4.....	70
Figure 3.28 Effect of bed temperature on charge density of fines measured by freeboard sampler in binary mixture M3. $U_g = 0.3$ m/s, $P = 414$ kPa, $\text{RH} = 12 \pm 6\%$. For physical properties of particles, see Tables 2.1, 2.2 and 2.3. For freeboard sampler details, see Figure 2.5. Error bars correspond to $\pm 90\%$ confidence intervals.....	70
Figure 3.29 Current flow through current detection pipe at column exit in binary mixture M3 as function of bed temperature. $U_g = 0.3$ m/s, $P = 414$ kPa, $\text{RH} = 12 \pm 6\%$. For physical properties of particles, see Tables 2.1, 2.2 and 2.3. For current-detecting pipe details, see Figure 2.6.....	71
Figure 3.30 Entrainment flux for binary mixture M3 as function of bed temperature. $U_g = 0.3$ m/s, $P = 414$ kPa, $\text{RH} = 12 \pm 6\%$. For physical properties of particles, see Tables 2.1, 2.2 and 2.3. Error bars correspond to $\pm 90\%$ confidence intervals.....	71
Figure 3.31 Effect of bed temperature on net cumulative charges as function of time at different axial positions in binary mixture M10. $U_g = 0.3$ m/s, $P = 414$ kPa, $\text{RH} = 12 \pm 6\%$. For physical properties of particles, see Tables 2.1, 2.2 and 2.3. Numbers on curves denote bed temperature (in $^\circ\text{C}$). For probe positions, see Figure 2.4.....	75
Figure 3.32 Standard deviation of charge fluctuations in freeboard as function of bed temperature for binary mixture M10. $U_g = 0.3$ m/s, $P = 414$ kPa, $\text{RH} = 12 \pm 6\%$. For physical properties of particles, see Tables 2.1, 2.2 and 2.2. For position of probe D, see Figure 2.4.....	76

Figure 3.33 Effect of bed temperature on charge density of fines measured by freeboard sampler in binary mixture M10. $U_g = 0.3$ m/s, $P = 414$ kPa, $RH = 12 \pm 6\%$. For physical properties of particles, see Tables 2.1, 2.2 and 2.3. For freeboard sampler details, see Figure 2.5. Error bars correspond to $\pm 90\%$ confidence intervals.....	76
Figure 3.34 Current flow through current detection pipe at column exit in binary mixture M10 as function of bed temperature. $U_g = 0.3$ m/s, $P = 414$ kPa, $RH = 12 \pm 6\%$. For physical properties of particles, see Tables 2.1, 2.2 and 2.3. For current-detection pipe details, see Figure 2.6.....	77
Figure 3.35 Entrainment flux for binary mixture M10 as function of bed temperature. $U_g = 0.3$ m/s, $P = 414$ kPa, $RH = 12 \pm 6\%$. For physical properties of particles, see Tables 2.1, 2.2 and 2.3. Error bars correspond to $\pm 90\%$ confidence intervals.....	77
Figure 4.1 Effect of relative humidity of fluidizing air on net cumulative charges as a function of time at different axial positions in a bed of binary mixture M3. For physical properties of particles, see Tables 2.1, 2.2 and 2.3. $P = 414$ kPa, $T = 20 \pm 2^\circ\text{C}$, and $U_g = 0.3$ m/s. Numbers on curves denote % RH. For probe positions, see Figure 2.4.....	81
Figure 4.2 Standard deviation of charge fluctuations in the freeboard as a function of air relative humidity for a binary mixture M3. For physical properties of particles, see Tables 2.1, 2.2 and 2.3. $P = 414$ kPa, $T = 20 \pm 2^\circ\text{C}$ and $U_g = 0.3$ m/s. For position of probe D, see Figure 2.4.....	82
Figure 4.3 Charge density of glass bead fines measured by the freeboard sampler as a function of air relative humidity for a binary mixture M3. $P = 414$ kPa, $T = 20 \pm 2^\circ\text{C}$ and $U_g = 0.3$ m/s. For physical properties of particles, see Tables 2.1, 2.2 and 2.3. For freeboard sampler details, see Figure 2.5. Error bars correspond to $\pm 90\%$ confidence intervals.....	82
Figure 4.4 Current flow through current detection pipe at column exit for a binary mixture M3 as a function of air relative humidity. $P = 414$ kPa, $T = 20 \pm 2^\circ\text{C}$ and $U_g = 0.3$ m/s. For physical properties of particles, see Tables 2.1, 2.2 and 2.3. For current-detecting pipe details, see Figure 2.6.....	83

Figure 4.5 Entrainment flux measured from a binary mixture M3 as a function of air relative humidity. P = 414 kPa, T = 20±2°C and U _g = 0.3 m/s. For physical properties of particles, see Tables 2.1, 2.2 and 2.3. Error bars correspond to ± 90% confidence intervals.....	83
Figure 4.6 Current flow through collision ball probes in a bed of binary mixture M3 as a function of air relative humidity. P = 210 kPa, T = 20±2°C and U _g = 0.6 m/s. For physical properties of particles, see Tables 2.1, 2.2 and 2.3. For probe positions, see Figure 2.4.....	87
Figure 4.7 Charge density of fine glass beads measured by freeboard sampler as a function of air relative humidity in a binary mixture M3. P = 210 kPa, T = 20±2°C and U _g = 0.6 m/s. For physical properties of particles, see Tables 2.1, 2.2 and 2.3. For freeboard sampler details, see Figure 2.5. Error bars correspond to ± 90% confidence intervals.....	87
Figure 4.8 Entrainment flux measured from a binary mixture M3 as a function of air relative humidity. P = 210 kPa, T = 20±2°C and U _g = 0.6 m/s. For physical properties of particles, see Tables 2.1, 2.2 and 2.3. Error bars correspond to ± 90% confidence intervals.....	88
Figure 4.9 Effect of relative humidity of fluidizing air on net cumulative charges as a function of time at different axial positions in a bed of binary mixture M6. For physical properties of particles, see Tables 2.1, 2.2 and 2.3. P = 414 kPa, T = 20±2°C, and U _g = 0.3 m/s. Numbers on curves denote % RH. For probe positions, see Figure 2.4.....	90
Figure 4.10 Standard deviation of charge fluctuations in the freeboard as a function of air relative humidity for a binary mixture M6. For physical properties of particles, see Tables 2.1, 2.2 and 2.2. P = 414 kPa, T = 20±2°C and U _g = 0.3 m/s. For position of probe D, see Figure 2.4.....	91
Figure 4.11 Charge density of Al ₂ O ₃ fines measured by freeboard sampler as a function of air relative humidity in a binary mixture M6. P = 414 kPa, T = 20±2°C and U _g = 0.3 m/s. For physical properties of particles, see Tables 2.1, 2.2 and 2.3. For freeboard sampler	

details, see Figure 2.5. Error bars correspond to $\pm 90\%$ confidence intervals.....	91
Figure 4.12 Entrainment flux from binary mixture M6 as a function of air relative humidity. $P = 414$ kPa, $T = 20\pm 2^\circ\text{C}$ and $U_g = 0.3$ m/s. For physical properties of particles, see Tables 2.1, 2.2 and 2.3. Error bars correspond to $\pm 90\%$ confidence intervals.....	92
Figure 4.13 Current flow through current detection pipe at column exit in binary mixture M6 as a function of air relative humidity. $P = 414$ kPa, $T = 20\pm 2^\circ\text{C}$ and $U_g = 0.3$ m/s. For physical properties of particles, see Tables 2.1, 2.2 and 2.3. For current-detecting pipe details, see Figure 2.6.....	92
Figure 4.14 Effect of relative humidity of fluidizing air on net cumulative charges as a function of time at different axial positions in bed of binary mixture M9. For physical properties of particles, see Tables 2.1, 2.2 and 2.3. $P = 414$ kPa, $T = 20\pm 2^\circ\text{C}$, and $U_g = 0.3$ m/s. Numbers on curves denote % RH. For probe positions, see Figure 2.4.....	95
Figure 4.15 Standard deviation of charge fluctuations in the freeboard as a function of air relative humidity for a binary mixture M9. For physical properties of particles, see Tables 2.1, 2.2 and 2.3. $P = 414$ kPa, $T = 20\pm 2^\circ\text{C}$ and $U_g = 0.3$ m/s. For position of probe D, see Figure 2.4.....	96
Figure 4.16 Charge density of polyethylene fines measured by freeboard sampler as a function of air relative humidity for binary mixture M9. $P = 414$ kPa, $T = 20\pm 2^\circ\text{C}$ and $U_g = 0.3$ m/s. For physical properties of particles, see Tables 2.1, 2.2 and 2.3. Error bars correspond to $\pm 90\%$ confidence intervals. For freeboard sampler details, see Figure 2.5.....	96
Figure 4.17 Entrainment flux measured from a binary mixture M9 as a function of air relative humidity. $P = 414$ kPa, $T = 20\pm 2^\circ\text{C}$ and $U_g = 0.3$ m/s. For physical properties of particles, see Tables 2.1, 2.2 and 2.3. Error bars correspond to $\pm 90\%$ confidence intervals.....	97
Figure 4.18 Current flow through current detection pipe at column exit for binary mixture M9 as a function of air relative humidity. $P = 414$ kPa, $T = 20\pm 2^\circ\text{C}$ and $U_g = 0.3$ m/s. For	

physical properties of particles, see Tables 2.1, 2.2 and 2.3. For current detecting pipe details, see Figure 2.6.....	97
Figure 5.1 Effect of coarse particle size on net cumulative charges as a function of time at different axial positions in beds of binary mixtures M1, M2 and M3. For physical properties of particles, see Tables 2.1, 2.2 and 2.3. $P = 414$ kPa, $T = 20 \pm 2^\circ\text{C}$, and $U_g = 0.3$ m/s. Letters on curves denote mixture types. For probe positions, see Figure 2.4.....	102
Figure 5.2 Standard deviation of charge fluctuations in the freeboard as a function of coarse particle average size in beds of binary mixtures M1, M2 and M3. For physical properties of particles, see Tables 2.1, 2.2 and 2.3. $P = 414$ kPa, $T = 20 \pm 2^\circ\text{C}$ and $U_g = 0.3$ m/s. For position for probe D, see Figure 2.4.....	103
Figure 5.3 Charge density measured by freeboard sampler as a function of coarse particle average size in beds of binary mixtures M1, M2 and M3. For physical properties of particles, see Tables 2.1, 2.2 and 2.3. $P = 414$ kPa, $T = 20 \pm 2^\circ\text{C}$ and $U_g = 0.3$ m/s. Error bar corresponds to $\pm 90\%$ confidence interval. For freeboard sampler details, see Figure 2.5.....	103
Figure 5.4 Current flow through current detection pipe at column exit as a function of coarse particle average size in beds of binary mixtures M1, M2 and M3. For physical properties of particles, see Tables 2.1, 2.2 and 2.3. $P = 414$ kPa, $T = 20 \pm 2^\circ\text{C}$ and $U_g = 0.3$ m/s. For current detecting pipe details, see Figure 2.6.....	104
Figure 5.5 Entrainment flux measured from beds of binary mixtures M1, M2 and M3 as a function of coarse particle average size, $P = 414$ kPa, $T = 20 \pm 2^\circ\text{C}$ and $U_g = 0.3$ m/s. For physical properties of particles, see Tables 2.1, 2.2 and 2.3. Error bar corresponds to $\pm 90\%$ confidence interval.....	104
Figure 5.6 Effect of coarse particle type on net cumulative charges as a function of time at different axial positions in beds of binary mixtures M3 and M10. For physical properties of particles, see Tables 2.1, 2.2 and 2.3. $P = 414$ kPa, $T = 20 \pm 2^\circ\text{C}$, and $U_g = 0.3$ m/s. Letters on curves denote mixture types. For probe positions, see Figure 2.4.....	108

Figure 5.7 Standard deviation of charge fluctuations in the freeboard as a function superficial gas velocity in beds of binary mixtures M3 and M10. For physical properties of particles, see Tables 2.1, 2.2 and 2.3. $P = 414 \text{ kPa}$, $T = 20 \pm 2^\circ\text{C}$. For position of probe D, see Figure 2.4.....109

Figure 5.8 Charge density measured by freeboard sampler as a function of superficial gas velocity in beds of binary mixtures M3 and M10. For physical properties of particles, see Tables 2.1, 2.2 and 2.3. $P = 414 \text{ kPa}$, $T = 20 \pm 2^\circ\text{C}$. Error bars correspond to $\pm 90\%$ confidence intervals. For freeboard sampler details, see Figure 2.5.....109

Figure 5.9 Current flow through current detection pipe at column exit as a function of superficial gas velocity in beds of binary mixtures M3 and M10. For physical properties of particles, see Tables 2.1, 2.2 and 2.3. $P = 414 \text{ kPa}$, $T = 20 \pm 2^\circ\text{C}$. For current detecting pipe details, see Figure 2.6.....110

Figure 5.10 Entrainment flux measured from beds of binary mixtures M3 and M10 as a function of superficial gas velocity. $P = 414 \text{ kPa}$, $T = 20 \pm 2^\circ\text{C}$. For physical properties of particles, see Tables 2.1, 2.2 and 2.3. Error bars correspond to $\pm 90\%$ confidence intervals.....110

Figure 5.11 Effect of coarse particle type on net cumulative charges as a function of time at different axial positions in beds of binary mixtures M10 and M11. For physical properties of particles, see Tables 2.1, 2.2 and 2.3. $P = 414 \text{ kPa}$, $T = 20 \pm 2^\circ\text{C}$, and $U_g = 0.3 \text{ m/s}$. Letters on curves denote mixture types. For probe positions, see Figure 2.4.....114

Figure 5.12 Standard deviation of charge fluctuations in the freeboard as a function of superficial gas velocity in beds of binary mixtures M10 and M11. For physical properties of particles, see Tables 2.1, 2.2 and 2.3. $P = 414 \text{ kPa}$, $T = 20 \pm 2^\circ\text{C}$. For position of probe D, see Figure 2.4.....115

Figure 5.13 Charge density measured by freeboard sampler as a function of superficial gas velocity in beds of binary mixtures M10 and M11. For physical properties of particles, see Tables 2.1, 2.2 and 2.3. $P = 414 \text{ kPa}$, $T = 20 \pm 2^\circ\text{C}$. Error bars correspond to $\pm 90\%$ confidence intervals. For freeboard sampler details, see Figure 2.5.....115

Figure 5.14 Current flow through current detection pipe at column exit as a function of superficial gas velocity in beds of binary mixtures M10 and M11. For physical properties of particles, see Tables 2.1, 2.2 and 2.3. P = 414 kPa, T = 20±2°C. For current detecting pipe details, see Figure 2.6.....	116
Figure 5.15 Entrainment flux measured from beds of binary mixtures M10 and M11 as a function of superficial gas velocity. P = 414 kPa, T = 20±2°C. For physical properties of particles, see Tables 2.1, 2.2 and 2.3. Error bars correspond to ± 90% confidence intervals.....	116
Figure 5.16 Effect of fine types on net cumulative charges as a function of time at different axial positions in beds of binary mixtures M3, M6 and M9. For physical properties of particles, see Tables 2.1, 2.2 and 2.3. P = 414 kPa, T = 20±2°C, and U _g = 0.3 m/s. Letters on curves denote mixture types. For probe positions, see Figure 2.4.....	119
Figure 5.17 Standard deviation of charge fluctuations in the freeboard as a function of superficial gas velocity in beds of binary mixtures M3, M6 and M9. For physical properties of particles, see Tables 2.1, 2.2 and 2.3. P = 414 kPa, T = 20±2°C. For position of probe D, see Figure 2.4.....	120
Figure 5.18 Charge density measured by freeboard sampler as a function of superficial gas velocity in beds of binary mixtures M3, M6 and M9. For physical properties of particles, see Tables 2.1, 2.2 and 2.3. P = 414 kPa, T = 20±2°C. Error bars correspond to ± 90% confidence intervals. For freeboard sampler details, see Figure 2.5.....	120
Figure 5.19 Current flow through current detection pipe at column exit as a function of superficial gas velocity in beds of binary mixtures M3, M6 and M9. For physical properties of particles, see Tables 2.1, 2.2 and 2.3. P = 414 kPa, T = 20±2°C. For current detecting pipe details, see Figure 2.6.....	121
Figure 5.20 Entrainment flux from beds of binary mixtures M3, M6 and M9 as a function of superficial gas velocity. P = 414 kPa, T = 20±2°C. For physical properties of particles, see Tables 2.1, 2.2 and 2.3. Error bars correspond to ± 90% confidence intervals.....	121
Figure 5.21 Effect of fines concentration on net cumulative charges as a function of time at different axial positions in beds of binary mixtures M3, M4, M5 and mono-size GBL.	

For physical properties of particles, see Tables 2.1, 2.2 and 2.3. $P = 414 \text{ kPa}$, $T = 20 \pm 2^\circ\text{C}$, and $U_g = 0.3 \text{ m/s}$. Letters on curves denote mixture types. For probe positions, see Figure 2.4.....125

Figure 5.22 Standard deviation of charge fluctuations in the freeboard as a function of fines concentration in beds of binary mixtures M3, M4, M5 and mono-size GBL. For physical properties of particles, see Tables 2.1, 2.2 and 2.3. $P = 414 \text{ kPa}$, $T = 20 \pm 2^\circ\text{C}$ and $U_g = 0.3 \text{ m/s}$. For position of probe D, see Figure 2.4.....126

Figure 5.23 Charge density measured by freeboard sampler as a function of fines concentration in beds of binary mixtures M3, M4, M5 and mono-size GBL. For physical properties of particles, see Tables 2.1, 2.2 and 2.3. $P = 414 \text{ kPa}$, $T = 20 \pm 2^\circ\text{C}$ and $U_g = 0.3 \text{ m/s}$. Error bar corresponds to $\pm 90\%$ confidence interval. For freeboard sampler details, see Figure 2.5.....126

Figure 5.24 Current flow through current detection pipe at column exit as a function of fines concentration in beds of binary mixtures M3, M4, M5 and mono-size GBL. For physical properties of particles, see Tables 2.1, 2.2 and 2.3. $P = 414 \text{ kPa}$, $T = 20 \pm 2^\circ\text{C}$ and $U_g = 0.3 \text{ m/s}$. For details of current-detecting pipe, see Figure 2.6.....127

Figure 5.25 Entrainment flux from beds of binary mixtures M3, M4, M5 and mono-size GBL as a function of fines concentration. $P = 414 \text{ kPa}$, $T = 20 \pm 2^\circ\text{C}$ and $U_g = 0.3 \text{ m/s}$. For physical properties of particles, see Tables 2.1, 2.2 and 2.3. Error bar corresponds to $\pm 90\%$ confidence interval.....127

Figure 5.26 Effect of fines concentration on net cumulative charges as a function of time at different axial positions in beds of binary mixtures M6, M7, M8 and mono-size GBL. For physical properties of particles, see Tables 2.1, 2.2 and 2.3. $P = 414 \text{ kPa}$, $T = 20 \pm 2^\circ\text{C}$, and $U_g = 0.3 \text{ m/s}$. Letters on curves denote mixture types. For probe positions, see Figure 2.4.....131

Figure 5.27 Standard deviation of charge fluctuations in the freeboard as a function of fines concentration in beds of binary mixtures M6, M7, M8 and mono-size GBL. For physical properties of particles, see Tables 2.1, 2.2 and 2.3. $P = 414 \text{ kPa}$, $T = 20 \pm 2^\circ\text{C}$ and $U_g = 0.3 \text{ m/s}$. For position of probe D, see Figure 2.4.....132

Figure 5.28 Charge density measured by the freeboard sampler as a function of fines concentration in beds of binary mixtures M6, M7, M8 and mono-size GBL. For physical properties of particles, see Tables 2.1, 2.2 and 2.3. $P = 414$ kPa, $T = 20 \pm 2^\circ\text{C}$ and $U_g = 0.3$ m/s. Error bar corresponds to $\pm 90\%$ confidence interval. For freeboard sampler details, see Figure 2.5.....	132
Figure 5.29 Current flow through current detection pipe at column exit as a function of fines concentration in beds of binary mixtures M6, M7, M8 and mono-size GBL. For physical properties of particles, see Tables 2.1, 2.2 and 2.3. $P = 414$ kPa, $T = 20 \pm 2^\circ\text{C}$ and $U_g = 0.3$ m/s. For current detecting pipe details, see Figure 2.6.....	133
Figure 5.30 Entrainment flux measured from beds of binary mixtures M6, M7, M8 and mono-size GBL as a function of fines concentration. $P = 414$ kPa, $T = 20 \pm 2^\circ\text{C}$ and $U_g = 0.3$ m/s. For physical properties of particles, see Tables 2.1, 2.2 and 2.3. Error bar corresponds to $\pm 90\%$ confidence interval.....	131
Figure 6.1 Comparison of entrainment flux predicted by empirical correlation (equation 6.1) with experimentally measured values for mixture M3. For physical properties of particles, see Tables 2.1, 2.2 and 2.3.....	142
Figure 6.2 Comparison of entrainment flux predicted by Choi et al. (1999) correlation (equation 6.2) with experimentally measured values for mixture M3 in this project. For physical properties of particles, see Tables 2.1, 2.2 and 2.3.....	144
Figure 6.3 Comparison of entrainment fluxes predicted by refitted Choi et al. (1999) correlation (equation 6.6) with experimentally measured values for mixture M3. For physical properties of particles, see Tables 2.1, 2.2 and 2.3.....	145
Figure 6.4 Comparison of entrainment flux predicted by modified Choi et al. (1999) correlation (equation 6.7) with experimentally measured values for mixture M3. For physical properties of particles, see Tables 2.1, 2.2 and 2.3.....	146
Figure A.1 Photograph of experimental apparatus.....	163
Figure A.2 Photograph of fluidization section.....	164
Figure A.3 Photograph of fluidization expanded section.....	165
Figure A.4 Fluidization unit engineering drawing.....	166

Figure A.5 Photograph of collision ball probe.....	167
Figure A.6 Photograph of freeboard sampler.....	168
Figure A.7 Photograph of current detection pipe.....	169
Figure B.1 Particle size distribution of GBF particles.....	170
Figure B.2 Particle size distribution of PEF particles.....	170
Figure B.3 Particle size distribution of Al ₂ O ₃ particles.....	171
Figure B.4 Particle size distribution of GBS particles.....	171
Figure B.5 Particle size distribution of GBM particles.....	172
Figure B.6 Particle size distribution of GBL particles.....	172
Figure B.7 Particle size distribution of HDPE particles.....	173
Figure B.8 Particle size distribution of LDPE particles.....	173
Figure B.9 Particle size distribution of M1 particles.....	174
Figure B.10 Particle size distribution of M2 particles.....	174
Figure B.11 Particle size distribution of M3 particles.....	175
Figure B.12 Particle size distribution of M4 particles.....	175
Figure B.13 Particle size distribution of M5 particles.....	176
Figure B.14 Particle size distribution of M6 particles.....	176
Figure B.15 Particle size distribution of M7 particles.....	177
Figure B.16 Particle size distribution of M8 particles.....	177
Figure B.17 Particle size distribution of M9 particles.....	178
Figure B.18 Particle size distribution of M10 particles.....	178
Figure B.19 Particle size distribution of M11 particles.....	179

Nomenclature

Ar	Archimedes number
A_S	Total particles surface area (m^2)
d_C	Mean particle diameter of coarse particles (μm)
d_M	Mean particle diameter of mixture (μm)
d_P	Mean particle diameter (μm)
d_F	Mean particle diameter of fine particles (μm)
F_d	Drag force per projection area (N/m^2)
F_e	Electrostatic force (N)
F_G	Gravitational force per projection area (N/m^2)
F_g	Gravitational force (N)
g	Gravitational acceleration ($9.81 m/s^2$)
k	Dielectric constant (-)
I	Current flow through pipe (pA)
m_F	Mass (kg)
MU	Mechanical unit (can be unit of force, acceleration or pressure)
n	Number of particles (-)
P	Absolute pressure in freeboard (kPa)
q_C	Charges on coarse particles (C)
q_F	Charges on fine particles (C)
q_m	Charge-to-mass ratio ($\mu C/kg$)
Q_s	Charge-to-surface area ratio ($\mu C/m^2$)
RH	Relative humidity (%)
T	Bed temperature ($^{\circ}C$)
U_g	Superficial gas velocity (m/s)

U_{mf}	Minimum fluidization velocity (m/s)
U_{mb}	Minimum bubbling velocity (m/s)
U_t	Terminal velocity (m/s)
W_s	Entrainment flux (kg/m ² .s)
X_F	Mass fraction of fine particles (-)

Greek Symbols

ρ_C	Particle density of coarse particles (kg/m ³)
ρ_F	Particle density of fine particles (kg/m ³)
ρ_g	Fluidizing gas density (kg/m ³)
ρ_M	Particle density of mixture (kg/m ³)
ρ_p	Particle density (kg/m ³)
φ	Particle sphericity (-)
μ	Fluidizing gas viscosity (kg/m .s)
ϵ_0	Electric constant (C ² /N .m ²)

Acknowledgements

I would like to express my sincere gratitude to my supervisors, Prof. John Grace and Prof. Xiaotao Bi, for their continuous support and excellent guidance throughout this challenging research project. Special thanks to you for believing in me and giving me the opportunity to be part of the Fluidization Research Group. I am fortunate and honoured to have such role models in my life. Throughout my research, I learned from your humility and dedication as well as your inspiring knowledge in this research field.

I also want to thank my committee members Prof. Jim Lim and Prof. Hongshen Ma for their valuable suggestions, encouragement, and support through the course of my PhD project.

I am grateful to my employer, SABIC, for sponsoring me and for giving me the opportunity to complete my graduate studies.

Special thanks go to my dear friend Dr. Wajeeh Moughrabiah for his ongoing support, helpful discussions, and encouragement throughout my studies. I also want to thank Dr. Ted Knowlton from PSRI and Dr. Shuji Matsusaka from Kyoto University for their valuable advices and helpful discussions throughout my research project.

I would like to acknowledge the staff of the Chemical Engineering Department for their friendship and help. Special thanks to Doug Yuen and Gordon Cheng for their expertise, valuable advice, and help in modifying experimental setup.

It is my pleasure to have an opportunity to thank my dear friends at Acadia Park who encouraged me to accomplish this work and made my life at UBC such an enjoyable experience.

I am grateful to fellow professors, graduate students, and group members for their love and valuable suggestions. Special thanks go to Prof. Naoko Ellis, Dr. Lifeng Zhang, Dr. Farzaneh Jalalinejad, Chuan He and Sina Tabianian for their ongoing support, useful discussions, and encouragement throughout my studies.

I am also grateful to the Natural Sciences and Engineering Research Council of Canada for their financial support.

Dedication

This thesis is dedicated to my beloved parents, Abdulrhman Alsmari and Latifa Alrays. I could not have achieved my goals throughout my life without their love and support. It is also dedicated with love to my wife, Albandari Aldakhil, whose support and endless love helped me complete this work, and to my children, Reemas and Linda, who have filled my life with happiness and love. I also wish to dedicate this work to my beloved sisters, Moneerh, Badoor, and Nouf, and my beloved brothers Thamer, Mohammed, Mansour, and Khild, who have been a source of love, encouragement and support to me throughout my life.

Chapter 1: Introduction

In gas-solid fluidized beds, fluidization occurs when solid particles are transformed into a fluid-like state by being suspended in a gas (Kunii & Levenspiel, 1991). The fluid flows upwards through the solids at such a velocity that the gravitational force on the particles is counteracted, and the solids are supported by the upward-flowing fluid. Fluidized beds have many advantages, such as excellent gas-solid contacting and heat transfer. Due to these advantages, gas-solid fluidized beds have numerous industrial applications, such as catalytic cracking, drying, polymerization of olefins, heat exchange, acrylonitrile manufacture and coating.

One of the disadvantages of fluidized bed reactors is particle entrainment. The high gas velocities present in fluidized beds often result in fine particles becoming entrained in the fluid. Pollution control regulations and high solids costs in some cases (e.g. for catalytic reactors) make it necessary to recover the solid particles entrained from the fluidized bed (Briens et al., 1992). Proper design of solids recovery equipment, such as cyclones, requires accurate predictions of both the solid flux and the size distribution of the entrained solids.

Entrainment phenomena are still not well understood since many parameters affect the entrainment rate. Numerous empirical correlations have been proposed for predicting the flux of entrained solids. Figure 1.1 summarizes predictions of the commonly used correlations to predict the entrainment rate in fluidized beds for a particular set of experimental conditions. As indicated in this figures, predictions derived from these correlations may differ by several orders of magnitude, even when the particles, column and operating conditions are well within the normal range of fluidized bed operations. Theoretical approaches based purely on hydrodynamic principles have also tended to fail badly. None of the correlations shown in Figure 1.1 makes any allowance for electrostatic effects. One possibility is that the failure of these approaches to consider electrostatic forces is responsible, in part or to a large extent, for the wide range of results and for the discrepancies in predicting entrainment.

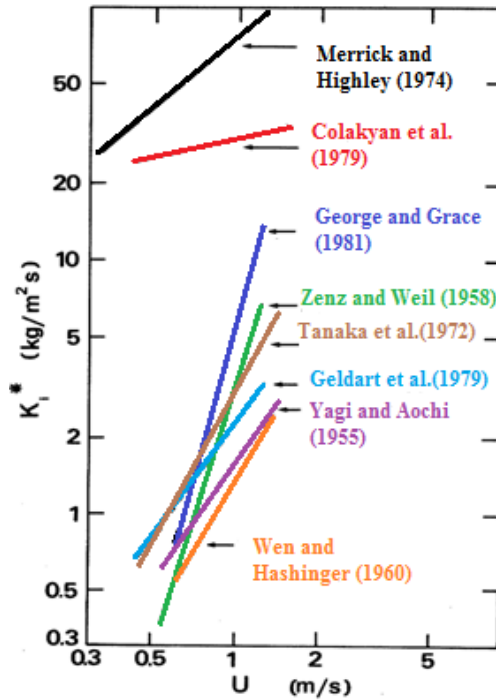


Figure 1.1 Correlations used to predict the entrainment rate (from George and Grace, 1981), rectangular column 0.254 m x 0.432 m, Silica sand particles, $d_p = 102 \mu\text{m}$.

The nature of gas-solid fluidization processes produces continuous motion and rubbing among bed particles such that the generation of electrostatic charges is inevitable. The electrostatic charges in fluidized systems can interfere with the normal hydrodynamics of the bed, resulting in particle-wall adhesion, inter-particle cohesion, electrostatic discharges, wall sheeting and even explosions, all of which can affect plant safety and economics (Cross, 1987). Electrostatic phenomena in gas-solid fluidization have been reported for many years (Lewis et al., 1949, Miller and Logwinuk, 1951, Osberg and Charlesworth, 1951) and need to be better understood.

The aim of this study is to investigate the influence of particle properties, gas relative humidity (RH) and operating variables, such as pressure, temperature, fluidizing air velocity, simultaneously on both particle entrainment and electrostatic charges to gain a better understanding of how operating conditions and electrostatic influence particle entrainment in gas-solid fluidized beds.

1.1 Particle Entrainment

Entrainment refers to the removal of solid particles from a fluidized bed by transport of these solids through the freeboard and out of the vessel (Yang, 2003). Solids entrainment becomes approximately constant at a certain height above the bed; this height is denoted as the transport disengaging height (TDH) (e.g. Baron et al., 1988). Figure 1.2 illustrates the most important zones in a fluidized bed.

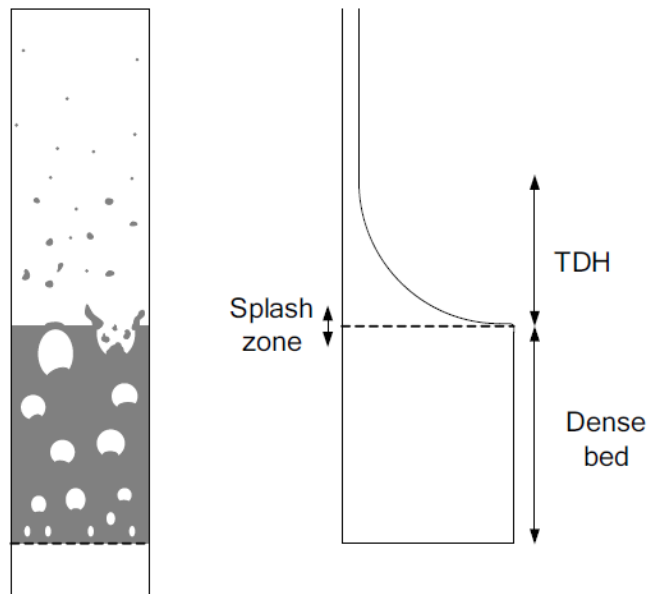


Figure 1.2 Fluidized bed zones (from Wouter, 2008)

In order for the solids to be entrained, particles must be ejected into the freeboard and then carried through it. Ejection of solid particles from the fluidized bed into the freeboard can occur by different mechanisms (Levy et al., 1983) as shown in Figure 1.3. There are two main mechanisms. The first occurs when the solids at the bed surface become part of the bubble roof and are thrown upward into the freeboard as the bubble breaks the bed surface (Nose model). The second mechanism occurs when some solids in the wake of rising bubbles are thrown upward into the freeboard as bubbles burst at the surface (Wake model). The main difference between bubble nose particles and bubble wake particles is that the particles ejected into the freeboard from the nose are highly dispersed, whereas those from the wake remain in denser clumps (Yang, 2003).

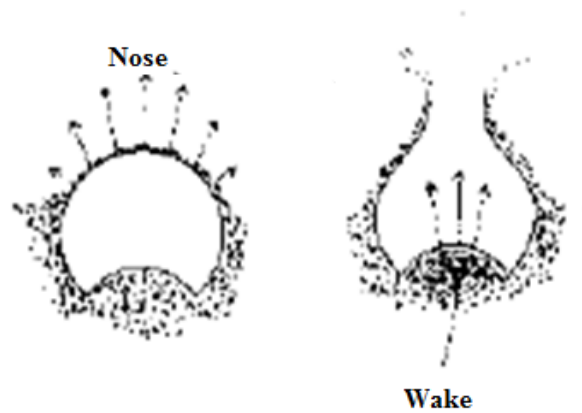


Figure 1.3 Particle ejection mechanisms (from Yang, 2003)

For environmental and financial reasons, it is necessary to recover the solid particles entrained from fluidized beds, requiring additional equipment and operational costs (Zenz & Weil, 1958). Accurate prediction of solid particles entrainment rates and size distribution in the freeboard are important for the proper design of cyclones and other gas-solid separation equipment (Alan & Hamdullahpur, 1993).

1.2 Parameters Affecting Particle Entrainment

1.2.1 Effect of Temperature

Temperature has a large effect on the fluid properties, as well as the properties of some solids, depending on the composition. George and Grace (1981) studied the effect of temperature on solids entrainment fluxes in a pilot scale fluidized bed over a temperature range of 300 to 445 K. They found that the temperature had little effect on entrainment rate over this limited range. Choi et al. (1989) reported that the particle entrainment rate decreased with increasing temperature. Other researchers (Merrick and Highley, 1974; Lee et al., 1990, 1992; Park et al., 1991) obtained similar results in fluidized bed combustors. In contrast, Romanova et al. (1980) and Milne et al. (1993) reported that the particle entrainment rate increased as temperature increased. Knowlton et al. (1990) investigated the effect of temperature on entrainment in a pressurized fluidized bed. They found that particle entrainment rate increased with both gas viscosity and gas density. Choi et al. (1998) measured the effect of temperature on the entrainment rate from a gas-solid fluidized bed

with variations of gas velocity, bed temperature and particle properties. They found that entrainment rate increased after an initial decrease with increasing bed temperature. They concluded that the influence of temperature on entrainment rate decreased as the particle density or gas velocity increased.

1.2.2 Effect of Pressure

Increasing pressure increases the gas density, increasing the tendency of a gas to carry solid particles. May and Russel (1954) and Chan and Knowlton (1984) reported that the entrainment rate increased as pressure increased.

1.2.3 Effect of Superficial Gas Velocity

High superficial gas velocity in the fluidized bed reactors results in more carry-over of particles. If the superficial gas velocity is increased, bed expansion increases and larger bubbles rise more quickly. Therefore the ejection velocity of bubbles erupting at the bed surface also increases. In addition, upwards drag on the particles in the freeboard is increased, resulting in increased carry-over of solid particles from the fluidized bed (Kato and Ito, 1972).

Many researchers (e.g. Baron et al., 1990; Nakagawa et al., 1994; Ma and Kato, 1998; Choi et al., 2001) have reported that the entrainment rate increased strongly as superficial gas velocity increased, typically with entrainment proportional to U to the power of 3 to 4.

1.2.4 Effect of Freeboard and Expanded Bed Height

As stated above, the entrainment flux becomes approximately constant at a certain height above the bed surface, the TDH. The freeboard zone of fluidization columns provides space for disengagement of particles. Baron et al. (1988) found that the entrainment rate decreased exponentially with freeboard height. Anderson and Leckner (1989) and Tannous et al. (2008) obtained similar results and, in addition, concluded that the mean particle size decreased exponentially with height in the freeboard. Baron et al. (1990) investigated the effect of dense bed height on the rate of solid particle entrainment. They reported that the entrainment rate increased as the bed height increased. This could be due to larger bubbles and reduced freeboard heights for a given overall equipment height.

1.2.5 Effect of Particle Properties

Solid particles in fluidized bed industrial applications cover a very wide range of properties. Entrainment and elutriation rates are affected by these properties. It is well known that the terminal velocity for a single particle decreases as the particle diameter decreases. Therefore, for smaller particles, a lower terminal velocity is expected, resulting in greater entrainment from the fluidized bed at a given gas velocity.

Kato and Ito (1972) and Tasirin and Geldart (1999) reported that elutriation increased as the particle size decreased in a gas-solid fluidized bed. Different results were reported by Baeyens et al. (1992), Ma and Kato (1998) and Nakazato et al. (2004) who investigated the effect of adding very fine particles on the elutriation rate constant. They concluded that the elutriation rate constant increased with decreasing particle size; however, below a critical particle size the elutriation rate constant no longer increased. They attributed this to interparticle adhesion forces. Baeyens et al. (1992) proposed a method for calculating the particle critical size at which adhesion forces become negligible compared with other forces. Choi et al. (2001) investigated the effect of fine particles on the entrainment of coarse particles. They found that the rate of carryover of coarse particles increased with the increasing proportion of fine particles in the bed. They also reported that the effect of fine particles on the elutriation rate of coarse particles decreased as the gas velocity increased, whereas the bed particle size distribution had only a minor effect on the elutriation rate of fine particles.

The effect of coarse particle density on the entrainment from a gas-solid fluidized bed was evaluated by Nakazato et al. (2004). They found that the entrainment of fine and coarse particles decreased as the coarse particle density increased. Kato and Li (2001) studied the effect of bed coarse particle diameter on the entrainment rate. They reported that the elutriation rate constant for Geldart group C particles in a fluidized bed of fine-coarse particle mixtures decreased with increasing mean diameter of the coarse particles in the bed for a constant superficial gas velocity.

1.2.6 Effect of Electrostatics

In a fluidized bed, interparticle interactions occur due to different forces, such as van der Waals, electrostatics, capillary and collision forces. Interparticle forces have been reported to have a significant effect on the entrainment rate of fine particles from a fluidized bed (Kato and Li, 2001).

Extensive studies (Geldart and Wong, 1987; Baron et al., 1992; Baeyens et al., 1992; Ma and Kato, 1998) have been conducted on the effect of van der Waals forces on the entrainment of fine particles. These forces are only appreciable when the particles come sufficiently close together, and they then produce significant attractive atomic interactions. These forces are strongly influenced by the size of the entrained particles. Adhesion forces become important when the entrained particles are smaller than a critical size (Geldart and Wong, 1987).

The effect of electrostatics on entrainment has received little attention. The generation of static charges is quite complex. Electrons or ions can transfer between two bodies in contact, forming electrical double layers of charges of opposite sign. If the bodies are suddenly pulled apart, the original electronic equilibrium cannot be re-established, and one of the surfaces gains more electrons or ions than before the contact, while the other has a deficit (Cross, 1987).

Geldart and Wong (1985) studied the effect of gas relative humidity (RH) on particle entrainment from a fluidized bed. They found that the entrainment rate decreased when the gas RH increased to above 60%. They believed that powder cohesivity was responsible for this phenomenon, and that electrostatic forces, which are influenced by gas humidity, had a negligible effect in their system. On the other hand, Baron et al. (1987) concluded that the entrainment rate decreased by 45% when the gas RH was reduced from 30 to 10% in a bubbling fluidized bed. They attributed this to an increase in pressure drop in the freeboard (~ 50% of the total pressure drop) due to electrostatic interactions between the particles and column wall. Briens et al. (1992) investigated the effect of electrostatics in a bubbling fluidized bed. They concluded that electrostatic forces had no effect on the size distribution of the entrained particles; consequently, these forces were not responsible for particle agglomeration. However, they found that electrostatic forces greatly affected particle entrainment. On the other hand, Mehrani and Giffin (2013) reported that RH had little or no

effect on particle entrainment rate. They attributed this result to the hydrophobic nature of the polyethylene particles tested in their study.

The effect of electrostatic forces on the elutriation of fine particles from a gas-solids fluidized bed was also studied by Kato and Li (2001). They proposed three zones to explain the variation of interparticle forces with gas RH, as shown in Figure 1.4. At low RH ($RHe:RH \leq 32\%$), electrostatic forces were determined to be dominant forces, and the elutriation rate constant increased as the RH of the gas increased due to the decrease in the electrostatic potential of bed particles. At high RH ($RHc:RH \geq 66\%$), the elutriation rate constant was found to decrease with increasing gas RH due to the effect of the capillary and van der Waals forces, whereas electrostatic forces were believed to have a minor affect.

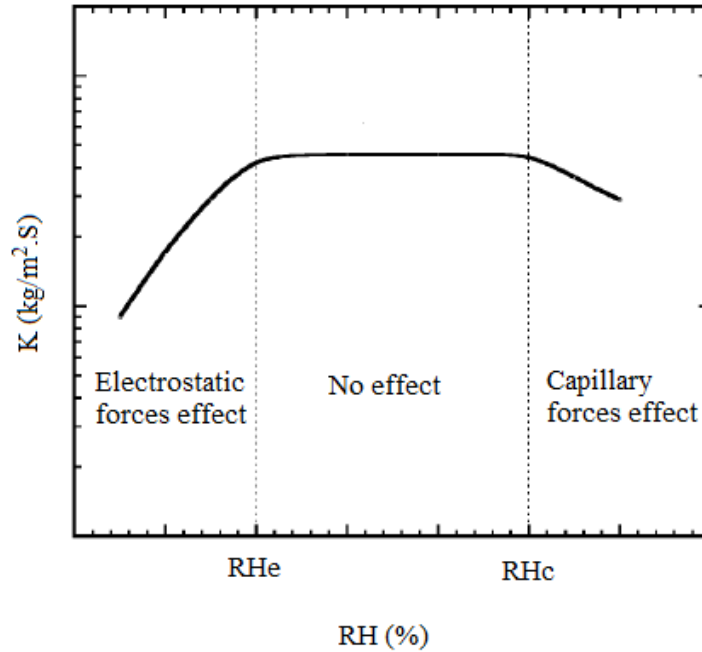


Figure 1.4 Relative humidity effect zones (adapted from Kato and Li, 2001). RHe and RHc denote electrostatic and capillary relative humidity of gas, whereas K is the entrainment rate constant

Mehrani (2005) and Mehrani et al. (2012) measured electrostatic charge generation in a bubbling fluidized bed based on a Faraday cup. They observed that entrained fine particles carried charges, leaving a net charge behind. Also, they found that the charge density of entrained fines is higher than the charge density of large particles in the bed. They concluded that the entrainment of fine particles may contribute significantly to net charge build-up in a

fluidized bed. In an elevated-pressure unit, Moughrabiah et al. (2009) reported that the charge polarity in the freeboard region was opposite to that at all three measurement levels inside the dense bed, indicating that the fine particles entrained from the fluidized bed carried charges, leaving behind a net charge of opposite polarity inside the bed. Rokkam et al. (2010a) developed a CFD model to study the effect of electrostatics on entrainment of fine polymer particles in fluidized bed reactor. In their simulation, lower entrainment rate was observed when fine particles were charged. In another study (Rokkam et al, 2010b) the rate of entrainment was predicted to be lower for charged catalyst particles than for uncharged particles.

1.3 Electrostatic Phenomena

Since the 1940s, a number of researchers (e.g. Lewis et al., 1949; Miller and Logwinuk, 1951; Osberg and Charlesworth, 1951) have encountered electrostatic effects in fluidized beds by observing the adhesion of particles to reactor walls and their influence on fluidization behaviour (Jones, 1997). Problems associated with fluidized bed electrification include particle-wall adhesion, inter-particle cohesion and electrostatic discharges. Particles of dielectric materials, such as glass and polyolefin, tend to generate significant electrostatic charges in fluidized beds. The charged particles can coat vessel walls, requiring frequent cleaning. Frequent shutdowns and mechanical cleaning can negatively affect plant economics and safety. The charged particles can also interfere with sensors and bed internals, and they can significantly alter bed hydrodynamics.

1.4 Electrostatic Charge Generation Mechanism

Fluidization by its nature is associated with continuous contact and separation, as well as with friction of particles against each other and against the vessel wall, leading to electrostatic charge generation. The charge generation mechanism is not well understood due to its complexity. In gas-solid fluidized beds, particles can be charged due to triboelectrification, frictional charging and thermionic emissions in high-temperature processes.

1.4.1 Triboelectrification

Triboelectrification involves the generation of electrical charges due to rubbing of materials.

As shown in Figure 1.5, when two solid bodies come into contact with each other, charges can move from one to the other based on the energy of electrons and ions at the surfaces until charge equilibrium is reached (Fan and Zhu, 1998).

Triboelectrification, also known as contact electrification, occurs due to the difference in the initial Fermi energy levels of the materials at the contact surface until the energy levels are equalized. The Fermi energy level is the highest occupied energy level at an absolute temperature of 0 K (Cross, 1987). The energy required to move an electron from the top of the energy distribution, out of the metal to infinity, is called the work function (Cross, 1987). Upon separation, particles that lose electrons become positively charged, whereas those that gain electrons become negatively charged. The charge polarity of a material is affected by different factors, such as material purity, surface finish, particle shape and moisture content (Cross, 1987).

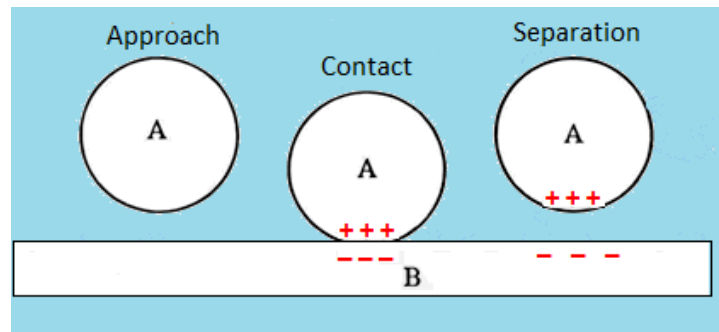


Figure 1.5 Triboelectrification charging mechanism (adapted from Jones, 1997)

1.4.2 Frictional Charging

Frictional charging occurs when the surfaces of solid particles rub against each other and/or against the reactor walls. In industrial gas-solid fluidized beds, frictional charging is often identified as the main charging mechanism. In cases where the reactor diameter is sufficiently large to neglect wall effects, particle rubbing becomes the dominant source of charge generation inside the reactor. According to Cross (1987), charge generation between similar materials due to frictional charging can be as great as for dissimilar materials. Boland and Geldart (1971) attributed the charges generated in a gas-solid fluidized bed to the motion of solid particles in the wakes of gas bubbles. Montgomery (1959) reported that charge generation increased with rubbing velocity and as the force at contact increased. Cross

(1987) concluded that the charge transfer is influenced by friction energy more than by the nature of the material. In large industrial gas-solid fluidized beds, frictional charging is the main source of charge generation since wall effects can be neglected (Park et al., 2002a).

1.4.3 Thermionic Emission Charging

Thermal electrification can occur when solid particles are exposed to very high temperatures (>1,000 K). The electrons inside solid particles can gain energy from a high temperature field to overcome the energy barriers and be freed. Therefore, the bed becomes thermally electrified (Fan and Zhu, 1998).

1.5 Electrostatic Measurement Techniques

Different experimental measurement techniques have been employed by previous researchers to measure electrostatic charges in gas-solid fluidized beds. The two main techniques are Faraday cups and electrostatic probes. Electrostatic probes measure the cumulative charges generated inside the bed, whereas Faraday cups determine the charges on particle surfaces. A third method, discussed in this section, is a current detecting pipe technique that has been used by previous researchers in gas-solid pipe flow to measure the charges transferred from the particles to the pipe wall. In this study, all three techniques were employed in a gas-solid fluidized bed to measure the electrostatic charges generated in the fluidized bed.

1.5.1 Electrostatic Probes

Electrostatic charges that build up inside a gas-solid fluidized bed and on its walls have been measured by previous researchers using three types of electrostatic probes:

1.5.1.1 Induction Probes

Induction probes have been used by many researchers, e.g. Boland and Geldart (1971/1972) and Chen et al. (2006). Figure 1.6 shows the induction probe utilized by Boland and Geldart (1971). The principle behind these probes is that a real charge induces an image of itself on conducting surfaces. This type of probe is generally mounted on the wall of the column, with part of the wall between the tip of the probe and the inner surface of the column. These non-contacting probes have the advantage of not disturbing the flow because they are not in direct

contact with the fluidized bed. However, a disadvantage is that they primarily measure the charge build-up on the column walls rather than the charges inside the bed.

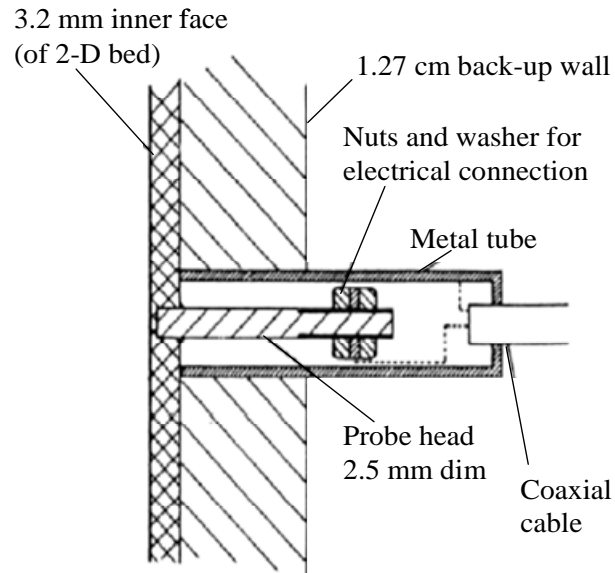


Figure 1.6 Induction probe (from Boland and Geldart, 1971)

1.5.1.2 Capacitance Probes

Capacitance probes have been used by a number of researchers, e.g. Wolny and Kazmierczak (1989) and Guardiola et al. (1992). Figure 1.7 shows the capacitance probe developed by Guardiola et al. (1992) to measure the degree of electrification by determining the potential difference between a metallic probe in contact with the bed and a metallic distributor. The probe placed along the axis of the column was 0.052 m in diameter and constructed from a Perspex tube; the capacitance probe was 5 mm in diameter and made from a copper tube. The distributor plate was made from stainless steel and was grounded. The disadvantages of this method include disturbing the flow and averaging the effect of electrostatic charges over the entire fluidized bed, rather than obtaining localized measurements.

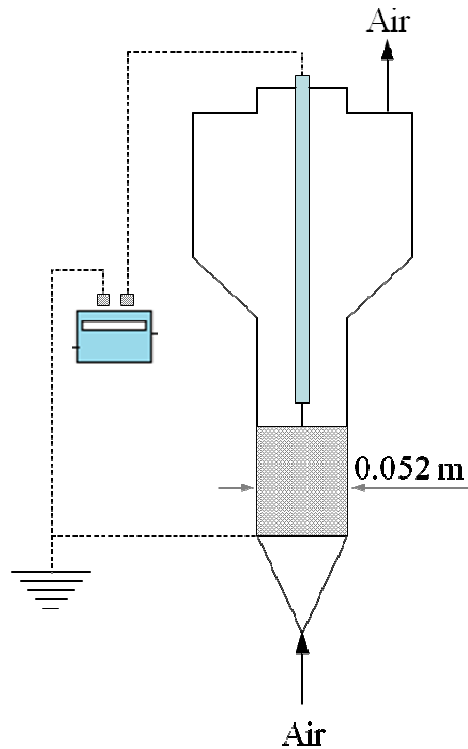


Figure 1.7 Capacitance probe (from Guardiola et al., 1992)

1.5.1.3 Collision Probes

Collision probes have been employed in a number of studies (e.g. Ciborowski and Wlodarski, 1962; Fujino et al., 1985; Park et al., 2002b; Chen et al., 2003a; Moughrabiah et al., 2009). The contacting probes are made of highly conductive materials. These were either suspended or mounted in the column, and electrically connected to electrometers to measure the potential or current generated inside the fluidized bed. Low accuracy due to particles adhesion to the tip of the probe and disturbing the flow are major drawbacks of collision probes. The most common type of collision probes is a ball probe. Figure 1.8 shows the collision ball probe used by Park et al., (2002b) to measure charge inducement and transfer due to bubble movement in a two-dimensional fluidized bed.

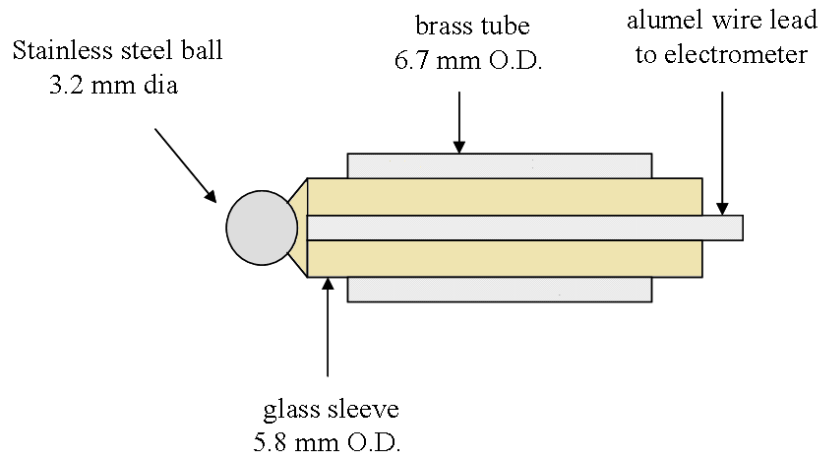


Figure 1.8 Collision ball probe (adapted from Park et al., 2002b)

1.5.2 Faraday Cup

Faraday cups have been used by previous researchers (e.g. Tardos and Pfeffer, 1980; Wolny and Opalinski, 1983; Ali et al., 1998; Zhao et al., 2000; Wang et al., 2004; Mehrani, 2005; Mehrani and Giffin, 2013) to measure net charge build-up on particle surfaces directly. A Faraday cup is a double-walled vessel of any suitable shape, as illustrated in Figure 1.9. The outer cup is grounded and functions as a screen, preventing external fields from affecting the measurements. The inner cup is connected to an electrometer to measure charges by detecting the voltage across a known capacitor. When a charged object enters the inner cup, an equal and opposite charge is induced on the wall of the inner cup. This charge is stored on the capacitor in the electrometer and measured (Cross, 1987). The Faraday cup method has some disadvantages, such as the possibility additional charging during handling of solid particles before entering the inner cup and the ability to measure only overall charges of withdrawn samples.

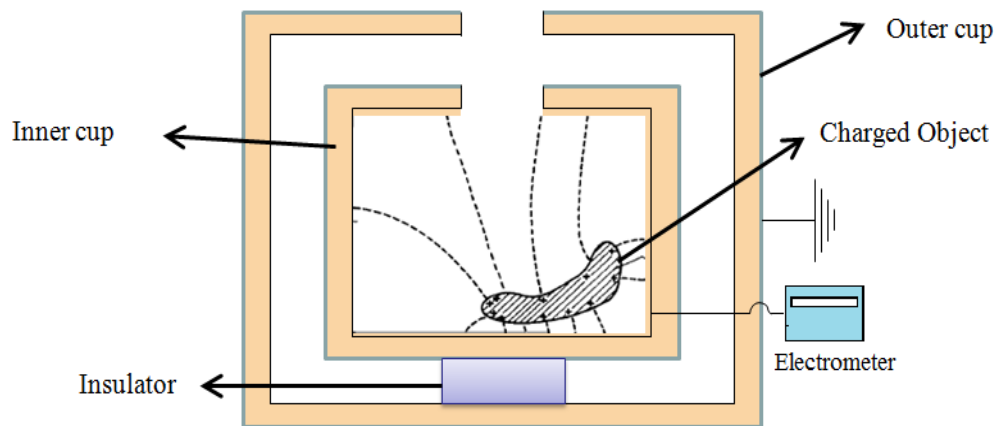


Figure 1.9 Faraday cup (adapted from Cross, 1987)

1.5.3 Current Detecting Pipe

A current detecting pipe has been used by several previous researchers (e.g. Masuda et al. 1976, 1994; Cartwright et al., 1985; Nieh and Nguyen, 1988; Gajewski, 1989; Wang et al., 2004, Matsusaka and Masuda, 2006) to measure the electric current generated from a metal pipe in a gas-solids pipe flow system directly. In gas-solids pipe flow, particles are charged as a result of repeated collisions with the pipe inner wall. The amount of charges transferred from solid particles to the wall per unit time is nearly equal to the electric current flowing from the wall to earth. This generated current is measured by an electrometer connected to the detecting pipe surface. These detecting pipes can be used in dilute phase gas-solids pipe flow when particles can freely collide with the pipe inner wall, and the effect of particle-particle interactions is neglected; however, for dense phase gas-solids pipe flow, these detecting pipes give lower efficiency because the surrounding particles prevent free particle-pipe interactions (Matsusaka et al., 2010). Such detecting pipes could be made of different materials, such as copper, stainless steel and conductive PTFE, with electrical isolation and an electric shielding around the detecting pipe to prevent electrical noise, as shown in Figure 1.10.

An advantage of current detecting pipes is that they do not disturb the flow because they are not in direct contact with the gas-solids flow. However, a disadvantage is low accuracy due to particle adhesion to the pipe inner wall at low gas velocities.

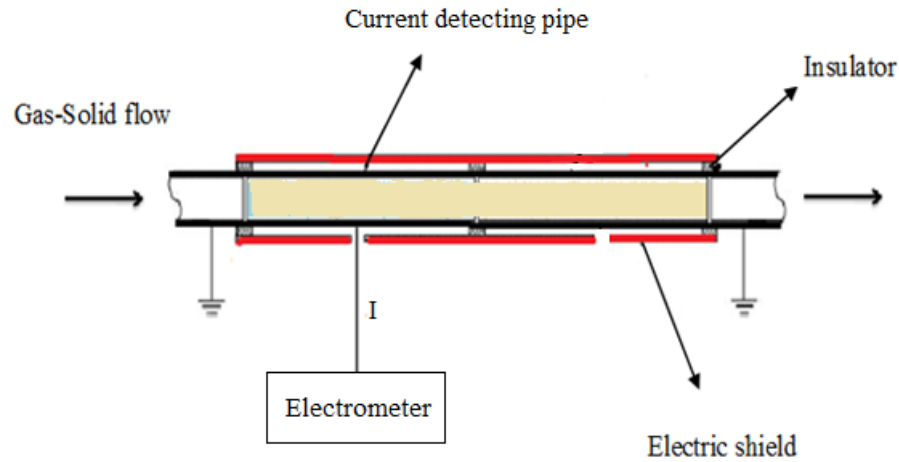


Figure 1.10 Current detecting pipe (adapted from Matsusaka and Masuda, 2006)

1.6 Parameters Affecting Electrostatics in Bubbling Fluidized Beds

Most industrial gas-solids fluidized bed reactors operate at high pressures, high temperatures and over a wide ranges of gas velocities. The gasification of coal and polyolefin generation are good examples of industrial processes that operate at elevated temperature and pressure. It is therefore very useful to understand how fluidized bed reactors perform at elevated temperature and pressure and with different gas and particles properties. Some researchers have investigated the influence of these parameters on bubble behaviour and electrostatic charge generation in bubbling fluidized beds.

1.6.1 Influence of Gas Velocity

It has been reported that collisions between particles surrounding bubbles results in charge generation in bubbling fluidized beds. Boland and Geldart (1971) noted that electrostatic charges in gas-solid fluidized beds are generated by the motion of particles around the bubbles. Darton et al. (1977) found that the bubble size increases as gas velocity increases.

Several researchers (e.g. Ciborowski and Wlodarski, 1962; Guardiola et al., 1996; Yao et al., 2002, Chen et al., 2003) reported increases in electrostatic charge generation due to increases in fluidizing gas velocity. They explained the increase in electrostatic charge generation as a result of an increase in bubble size and rise velocity. All the above studies were conducted at atmospheric pressure. Moughrabiah et al. (2009) studied the influence of superficial gas velocity on electrostatic charge generation in an elevated-pressure bubbling fluidized bed. They performed their experiments with polyethylene particles and glass beads in a three-dimensional fluidized bed. They concluded that the bed electrification increases as the superficial gas velocity increases. They explained their results by the formation of bigger bubbles and higher bubble rise velocities that enhanced particle motion in the bed.

1.6.2 Influence of Operating Pressure and Temperature

Limited work has been devoted to study the effect of pressure and temperature on electrostatic charge generation in gas-solid fluidized beds. Most previous experiments were conducted at ambient temperature and atmospheric pressure.

Several researchers (e.g. Botterill and Desai, 1972; Barreto et al., 1983; Chitester et al., 1984; Li and Kuipers, 2002) have studied the influence of pressure on bubble behaviour in gas-solid fluidized beds and reported that higher pressure resulted in smoother fluidization and smaller bubbles. Kawabata et al. (1981) studied the effect of pressure (up to 800 kPa) in a two-dimensional fluidized bed containing sand particles. They found that bubble size was not influenced by elevated pressure. Olowson and Almstedt (1990) conducted free bubbling experiments at elevated pressures (up to 1600 kPa) in a fluidization column containing silica sand. They observed that the rise velocity and mean bubble frequency increased, whereas bubble size decreased with increasing pressure. Newton et al. (2001) showed that the mean bubble diameter decreased and bubble velocity increased as the pressure increased. Boland and Geldart (1971) reported that the degree of charging in a fluidization column containing glass beads particles increased as the bubble size increased. Yao et al. (2002) studied the influence of bubble behaviour on electrostatic charges in a Plexiglas fluidization column of 0.089 m inner diameter containing polyethylene particles. They used a collision ball probe to measure the local electrostatic charges. Their results showed that electrostatic charges in a gas-solid fluidized bed are affected by the bubble behaviour.

Moughrabiah et al. (2009) investigated the effect of operating pressure (up to 724 kPa) on the degree of bed electrification in a three-dimensional fluidized bed containing glass beads. Their experiments showed that, as the pressure increased, the degree of electrification increased. They attributed these results to the increase in bubble rise velocity, frequency and volume fraction.

The effect of temperature is still not well understood. Some researchers (Mii et al., 1973; Yoshida et al., 1974) studied the effect of temperature on fluidization behaviour. They concluded that both the frequency of bubble formation and the quality of fluidization increased as temperature increased. On the other hand, Newton et al. (2001) investigated the effect of temperature on bubble behaviour in a gas-solid fluidized bed, finding that the bubble frequency decreased and bubbles became larger as temperature increased. Moughrabiah et al. (2009) investigated the influence of temperature (up to 90°C) on the degree of electrification inside a gas-solid fluidized bed by conducting freely bubbling experiments with glass beads and low-density polyethylene particles. They found that as the bed temperature increased, the degree of bed electrification decreased. They attributed these results to the smaller and slower bubbles as temperature increased.

1.6.3 Influence of Gas Properties – Relative Humidity

Controlling gas humidity is a common technique to prevent or reduce electrostatic charges in gas-solid fluidized beds. The influence of gas RH on electrostatic charges inside fluidized beds has been investigated by several researchers. Ciborowski and Wlodarski (1962) concluded that increasing the fluidizing gas RH results in a decrease in bed potential. They attributed these results to increases in the rate of charge dissipation. Other researchers (Boland and Geldart, 1972; Tardos and Pfeffer, 1980; Wolny and Kazmierczak, 1989; Guardiola et al., 1996; Park et al., 2002; Mehrani, 2005; Moughrabiah et al., 2009; Mehrani and Giffin, 2013) reported that increasing the gas RH reduces electrostatic effects in a gas-solid fluidized bed. They attributed their results to the increase in the solids surface conductivity and higher charge dissipation rate. Mehrani et al. (2007) investigated the influence of fluidizing gas RH on the charge density (charge-to mass ratio) of fine glass beads particles. They found that as the gas RH increased, the charge density decreased.

This technique has several issues. First, high gas humidity (> 75%) tends to result in excessive capillary forces that cause defluidization (Guardiola et al., 1996). Second,

humidification is not feasible for some gas-solids industrial fluidized bed reactors where humidity poisons the catalyst. Finally, this technique has been found to be ineffective in high-temperature processes (Ciborowski and Wlodarski, 1962).

1.6.4 Influence of Particles Properties

In triboelectrification charging, the generation of electrostatic charges is due to rubbing between materials. The charge polarity of the materials can be influenced by several factors, such as purity, particle shape, moisture content and surface finish (Cross, 1987).

Guardiola et al. (1996) investigated the effect of particle size on bed electrification and found that as the particle size increases, electrification in the fluidized bed increases. On the other hand, Mehrani et al. (2007) conducted experiments in a Faraday cup fluidized bed with a binary mixture of particles consisting of large and fine glass beads. It was found that the fine particles carried higher charges per unit mass than the larger particles.

Several researchers (Ali et al., 1998; Zhao et al., 2000; Mehrani, 2005; Inculet et al., 2006; Mehrani et al., 2007; Moughrabiah et al., 2009) have reported bipolar charging. Bipolar charging has been described as contact charging between solid particles of the same material but different sizes. Ali et al. (1998) found that for one type of particles, small particles charged negatively and large ones charged positively. Similar results were reported by Zhao et al. (2000). Mehrani (2005) performed experiments in a fluidized bed with binary mixtures of large and fine glass beads particles. They found that the entrained fines (30 μm mean diameter) were positively charged, whereas larger particles (566 μm mean diameter) were negatively charged. Mehrani et al. (2007) concluded that the charges carried by the fine particles were more likely due to charge separation. Moughrabiah et al. (2009) measured the electrostatic charges of entrained fine glass beads particles using a collision ball probe mounted in the freeboard zone of a fluidized bed. It was found that the polarity in the freeboard was opposite to that of the dense bed of large glass beads below.

1.7 Solid Particles Classification

In fluidized beds, different types of solid particles fluidize differently depending on such factors as drag, particle interactions and physical properties. Based on particle diameter and density, Geldart (1973) classified different types of solids in air at atmospheric temperature and pressure into four groups, namely A, B, C and D particles. Figure 1.11 illustrates the

Geldart classification of particles for air at ambient conditions. For extension to other gases, temperatures and pressures, see Grace (1986). In this study, groups A (fine) and B (coarse) particles are used.

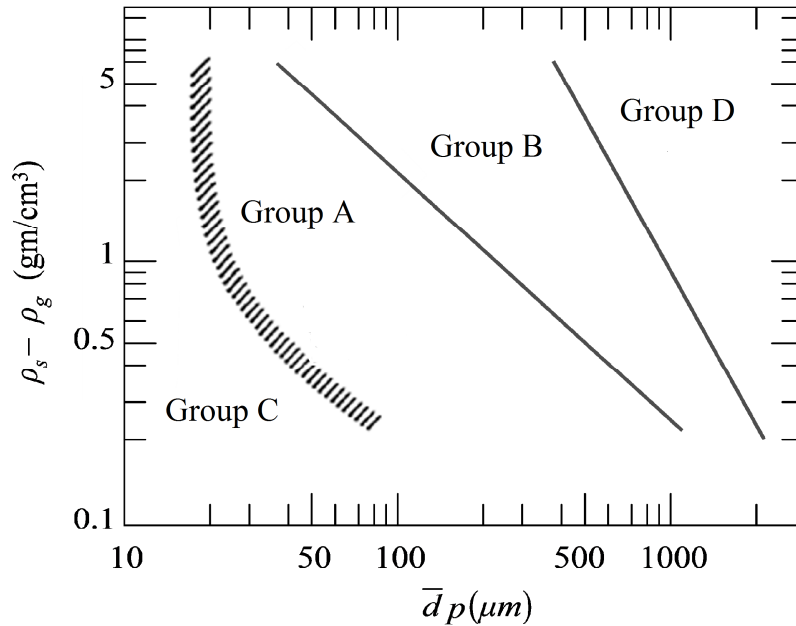


Figure 1.11 Geldart solids classification (adapted from Geldart, 1973)

1.8 Fluidization Flow Regimes

In gas-solid fluidized beds, as the gas velocity increases, different flow regimes are encountered, as illustrated in Figure 1.12. For Geldart group B and D particles in gas-solid fluidized beds, the bed is transformed from a fixed bed into a bubbling fluidized bed when the superficial gas velocity (U_g) exceeds the minimum fluidization velocity (U_{mf}). For Geldart group A particles, the bubbles appear when the gas velocity exceeds the minimum bubbling velocity ($U_{mb} > U_{mf}$) (Yang, 2003). In this study, only the bubbling flow regime is investigated.

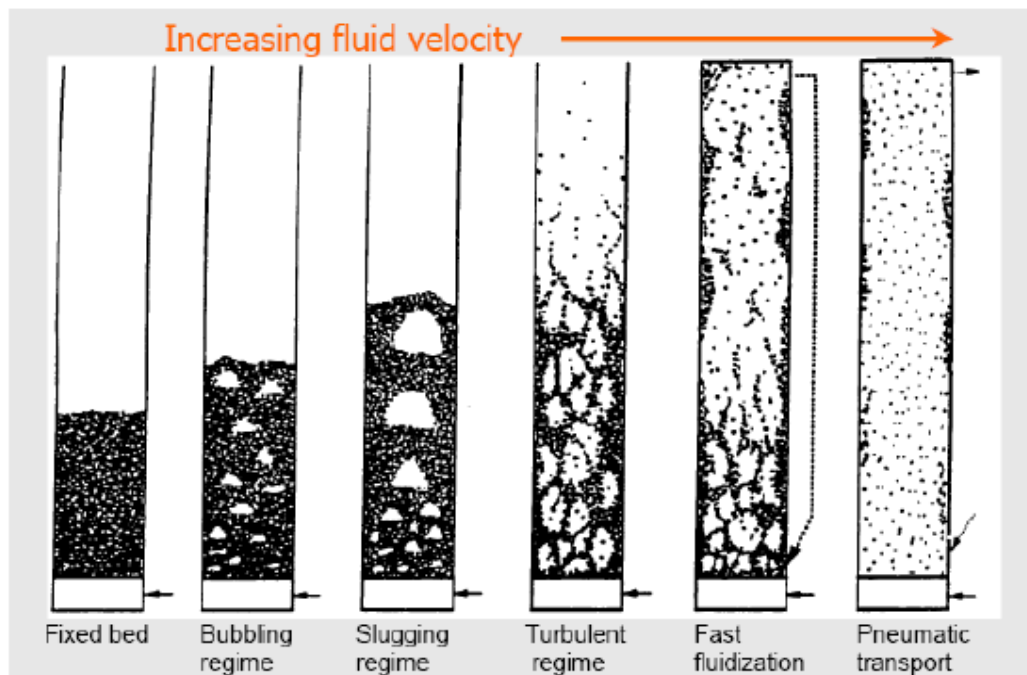


Figure 1.12 Gas-solid flow regimes (from Grace, 1986)

1.9 Thesis Objectives

The main goal of this research project is to gain a better understanding of the particle entrainment and how it is influenced by operating conditions, electrostatic and particle properties in gas-solid fluidized beds. This was investigated by simultaneously measuring the particle entrainment flux, electrostatic charges inside a fluidized bed and the charge on entrained particles as a function of operating conditions and bed properties.

Specific objectives contributing to this goal are:

- To develop adequate measurement techniques to determine the particle entrainment flux from the fluidized bed and the electrostatic charge on the entrained particles.
- To determine the effect of different operating variables, such as pressure, temperature and gas velocity on particle entrainment and electrostatics.
- To identify the effect of fluidizing gas relative humidity on particle entrainment and electrostatic charges.
- To investigate the influence of particle properties (such as size, type and density) on particle entrainment and electrostatic charges in fluidized beds.

- To study the relationship between entrainment and electrostatics and investigate whether it is important to include the effect of electrostatic when modeling or correlating solids entrainment from fluidized beds.

1.10 Thesis Outline

Chapter 2 describes the experimental equipment and methodology. The first section describes the fluidization column air system, including the air compressor, refrigeration unit, dryers and buffer tank. The second section provides details of the fluidization column. The third provides details of the instrumentation and measurement techniques, such as pressure and temperature sensors, pressure control valve, pressure transducers, collision ball probes, freeboard sampling pipe and current detection pipe. The fourth section provides details of the properties of the particles studied. The final section describes the experimental procedure.

Chapter 3 presents the experimental results for the effect of operating variables on the particle entrainment flux and electrostatic charge inside a fluidized bed. Results and analysis of experiments performed at different gas velocity, temperature and pressure are given.

Chapter 4 focuses on the influence of gas relative humidity (RH) on particle entrainment flux and electrostatic charge in a fluidized bed. Results of experiments carried out at different gas RH for different fine particle types are presented and analyzed.

Chapter 5 provides details of the experimental results on the influence of coarse and fine particle properties on the entrainment flux and electrostatic charge in fluidized beds. Results and analysis of experiments performed with different coarse and fine particles, sizes, concentrations and densities are presented.

Chapter 6 is devoted to the influence of electrostatic on particle entrainment flux at different operating conditions in a fluidized bed. Results and analysis are presented.

Chapter 7 presents the overall conclusions and recommendations for future work.

Additional experimental results, detailed engineering drawings and photographs of the equipment are given in the appendices.

Chapter 2: Experimental Equipment and Procedure

Chapter 2 describes the experimental equipment, including the high-pressure air system, elevated-pressure fluidization column, instrumentation for measuring pressure, flow and temperature, control systems, collision ball probes, freeboard-sampling pipe (based on Faraday cup principle) and current-detecting pipe. It also presents the properties of the solid particles used in the experiments and describes the experimental procedures.

2.1 High-Pressure System – Air Compressor

High-pressure air was supplied by a rotary screw compressor (KAESER Model SK19) to pressurize the column to the required operating pressure. The compressor is equipped with a Sigma Control System to provide the option of automatic control of the discharged air pressure. It includes safety pressure relief valves and an emergency stop button. The high-pressure air was dried by passing through a refrigeration unit (KAESER Model TA11) and vapour-removal filters, located downstream of the compressor. The refrigeration unit and filters can be totally or partially bypassed, which helps to control the relative humidity (RH) of the fluidizing air.

To deliver the high-pressure air to the column at constant pressure, a high-pressure buffer tank (120 gallon) was installed upstream of the column inlet. A silica gel dryer was also installed between the buffer tank and the column inlet. This dryer can be totally or partially bypassed to maintain the RH of the fluidizing air in the required range.

The overall layout of the elevated-pressure fluidization unit is shown in Figure 2.1.

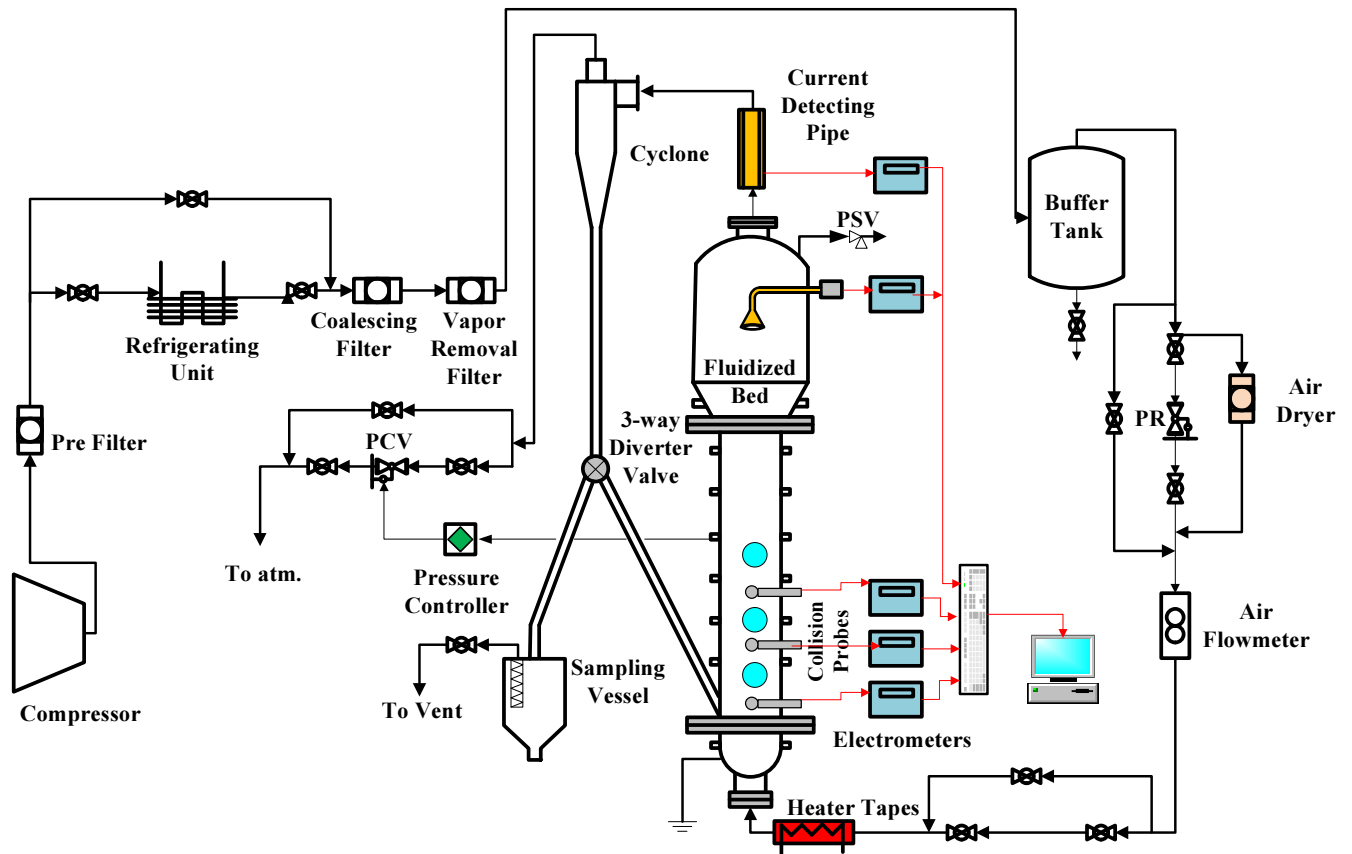


Figure 2.1 Schematic of overall layout of fluidization unit. PR: pressure regulator, PVC: pressure control valve.

2.2 Elevated-Pressure Fluidization Column

The fluidization experiments were performed in a modified three-dimensional elevated-pressure (up to 1000 kPa) fluidization column constructed of stainless steel, with an inner diameter of 0.15 m and a height of 2.0 m. The modified fluidization column originally built for Moughrabiah (2009), is equipped with a distributor consisting of two stainless steel perforated plates, each containing 50 aligned holes. The holes in the upper and lower plates are 4 and 5.5 mm in diameter, respectively. A steel screen with 15 μm openings is installed between the two plates to prevent fine particles from dropping into the windbox. The distributor plates are designed to have an open area ratio of 3.8%.

The particles entrained from the vessel by gas at the top of the column pass through an external cyclone. For a wider range of superficial gas velocities, two alternative cyclones (inside diameter 75 and 51 mm) constructed from stainless steel were employed to capture and return entrained particles via a dip-leg through a port whose centre was 150 mm above the distributor plate. A 1-inch (25 mm) high-pressure rated three-way diverting valve with 60 degree outlets ports, specially manufactured by Quality Controls, Inc. was installed on the dip-leg, downstream of the cyclone. In normal operation, the solid particles recovered by the cyclone are directed via the three-way valve into the fluidization column. For entrainment rate measurements, they are diverted into a cone-shaped sampling vessel, 100 mm inner diameter and 254 mm height. A sintered metal filter (provided by Mott Corporation) with 90% collection efficiency of 10 μm openings was installed in the sampling vessel at the exit line to prevent losses of fines during sampling.

The fluidization column is equipped with three sight glasses, each 25.4 mm in diameter, to allow visual observation inside the column. Figure 2.2 shows a schematic diagram of the fluidization column.

Detailed engineering drawings and photographs of the fluidization unit are provided in the Appendix A.

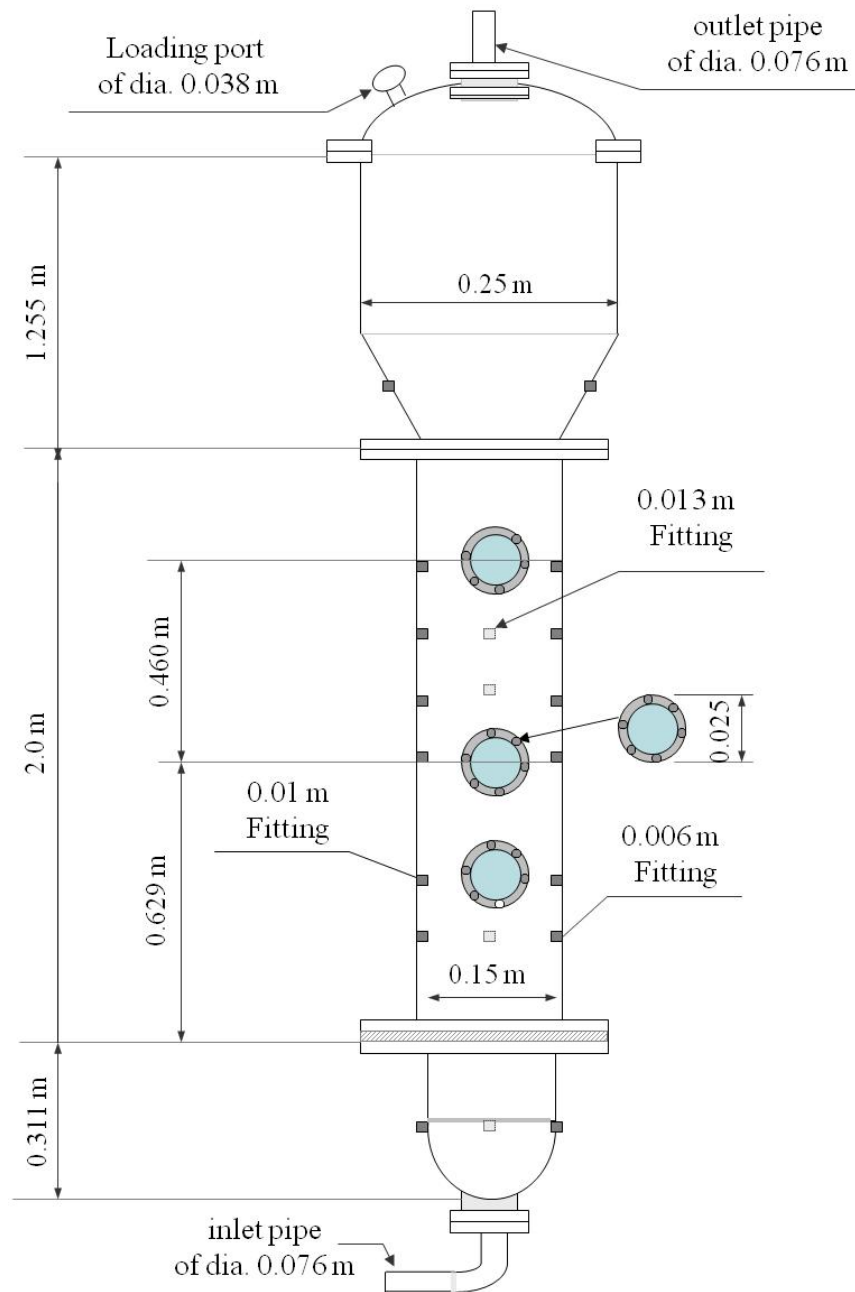


Figure 2.2 Schematic of fluidization column.

2.3 Instrumentation and Measurements

The fluidization column was equipped with several instruments and control systems, such as pressure transducers, pressure control valve, pressure safety valve, pressure and temperature sensors, flowmeters, hygrometers, electrical heating tapes, electrostatic collision ball probes, freeboard sampling pipe, and current detecting pipe.

2.3.1 Fluidization Column Operating Variables and Measurements

The bed temperature was measured at different levels by two bi-metal dial thermometers immersed inside the column. The bed temperature was controlled by electrical heating tapes (Omega HTWC) wrapped around the fluidization column and the inlet pipe. The air flowrate was measured by a mass flowmeter located on the column inlet pipe, equipped with a valve to adjust the flowrate to the desired value. The RH of the incoming air was monitored by a hygrometer (Vaisala Model HMP238) immersed in the bed. This hygrometer can measure RH from 0 to 100% and with $\pm 1\%$ accuracy. The RH of the exit stream was also monitored using a portable digital hygrometer (Omega Model RH71, $\pm 2\%$ accuracy).

The pressure inside the fluidization column was measured by pressure transducers (Omega Model PX4200, $\pm 0.25\%$ accuracy). These were frequently back-flushed by high-pressure air to prevent blockage by fine particles. The pressure of the column was controlled by a pressure control valve (Fisher-Rosemount 24000C-series) located on the cyclone gas outlet line. To protect the fluidization column from excessive pressure build-up, a pressure relief valve was installed downstream of the column. Differential pressure transducers (Omega Model PX750, $\pm 0.25\%$ accuracy) were used to measure the pressure drops.

2.3.2 Electrostatic Charge Measurement Techniques

2.3.2.1 Collision Ball Probes

The degree of electrification in the bed was measured by four collision ball probes, identical to those described and employed by Moughrabiah et al. (2009). Each probe consisted of a stainless steel ball, 5.3 mm in diameter, connected to a stainless steel wire. Ceramic and polyethylene tubes 5.5 and 8.75 mm in diameter, respectively, were used to protect the probe and maintained high resistance to the ground. In addition, a brass tube 12.7 mm in diameter was used to eliminate any disturbances due to build-up of charges on the fluidization column walls.

A schematic of the electrostatic collision ball probe is provided in Figure 2.3.

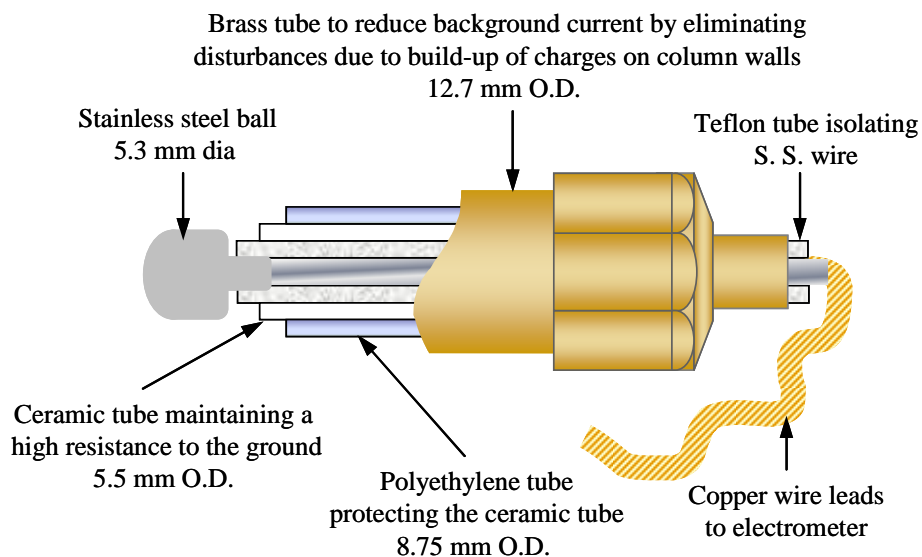


Figure 2.3 Collision ball probe (from Moughrabiah et al., 2009)

The degree of electrification in the bed was characterized by measuring the cumulative charges induced and transferred through the collision ball probes. Four collision probes were mounted so that they were centred on the axis of the column and at different levels, 0.15, 0.31, 0.55 and 0.97 m above the distributor plate, as shown in Figure 2.4. Each probe was connected directly to an electrometer (Kistler model 5010B), able to measure charges from ± 10.0 pC to ± 1.0 μ C. The electrometer was connected to a computer through a DAS08 data acquisition card to record the measured signals.

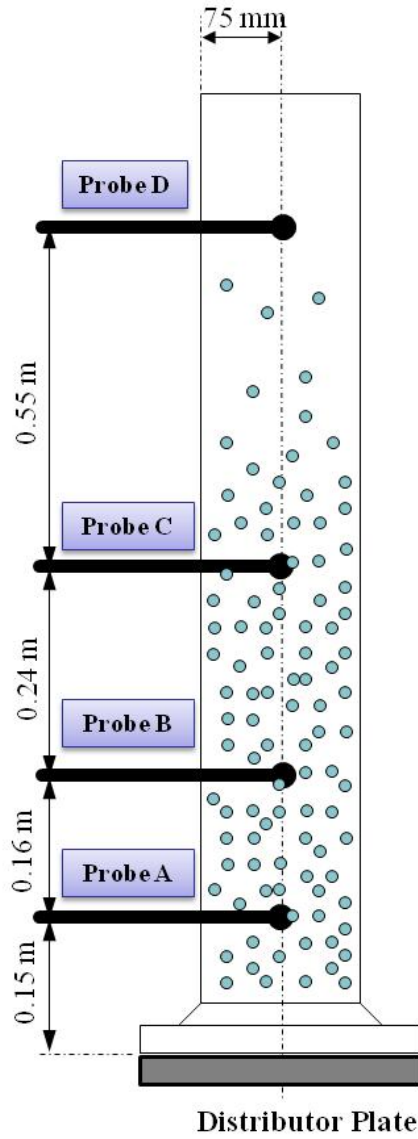


Figure 2.4 Locations of collision ball probes.

2.3.2.2 Freeboard Sampler

To measure the charge density of entrained particles in the freeboard, a sampling pipe inspired by the Faraday cup concept was developed. The sampling pipe was mounted in the freeboard at the centre of the fluidization column. It consists of two copper pipes insulated from each other by Black Epoxy (832B), as shown in Figure 2.5. The sampling pipe intake was designed with a cone shape and a maximum inner diameter of 51 mm to enhance the solid particle collection efficiency from the dilute phase stream. The inner pipe was 19 mm in inner diameter and 127 mm in length, whereas the outer pipe was 25.4 mm in inner

diameter. The entrained particles were collected in a filter (provided by IMP CO Ltd.) with 0.0063 m² surface area and 89% collection efficiency of 10 μm particulates placed at the end of sampling pipe. The mass of fine particles collected was determined by weighing the filter before and after each run by an analytical balance with an accuracy of ±0.0002 g. A high-pressure air tube was connected to the sampler to facilitate flushing of the sampling pipe and to provide small positive flow to prevent blockage by fine particles.

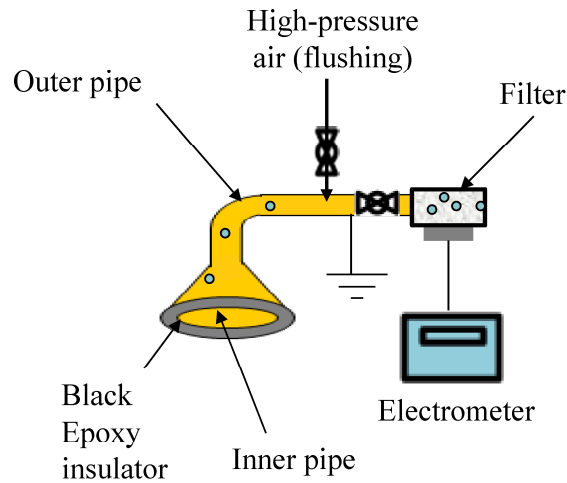


Figure 2.5 Schematic of freeboard sampler.

2.3.2.3 Current Detecting Pipe

To measure the degree of electrification of entrained particles in the fluidization column exit line, a current detecting pipe similar to those used by Matsusaka and Masuda (2006) was developed. This is a 17-4 PH stainless steel pipe, 25.4 mm in diameter, 4 mm in thickness and 400 mm long, installed at the column exit line, as shown in Figure 2.6. It is coated internally with Ni (work function=5.35 eV). The principle underlying this technique is that, in a gas-solid pipe flow, particles are charged by collisions with the interior pipe walls. The charge transferred from the solid particles to the wall per unit time is essentially equal to the electric current flowing from the wall to the earth.

The degree of entrained particles electrification was characterized by measuring the electrical current transferred from entrained fine particles to the metal pipe by collisions. To prevent electrical noise, an electric shield (grounded) made from copper was installed around the detecting pipe and insulated by a small piece of Teflon. The current detecting pipe was connected directly to an electrometer (Kistler model 5010B) by a triaxial cable to protect signals against external interference. The electrometer was also connected to a computer through a DAS08 data acquisition card to record the measured signals. Photographs of the collision ball probe, freeboard sampling pipe, current detecting pipe and electrometer are provided in the Appendix A.

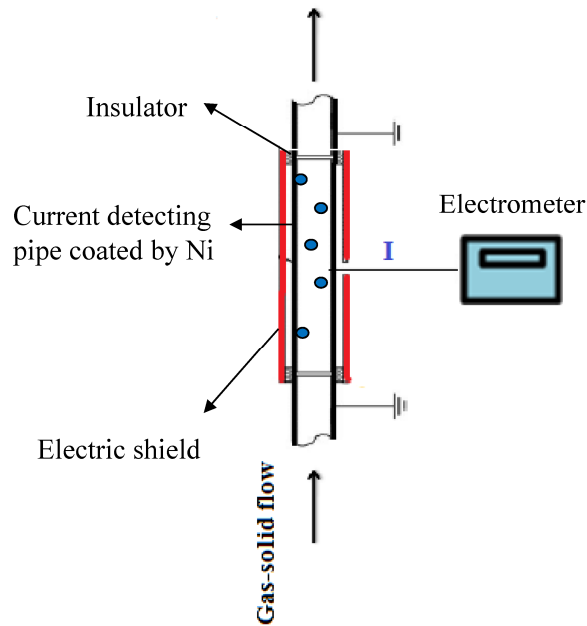


Figure 2.6 Schematic of current detecting pipe

2.4 Bed Materials

2.4.1 Coarse Particles

The particles described in this section will for convenience be referred to as “coarse”. The coarse particles tested in this study included glass beads (GB) of different sizes, high-density polyethylene (HDPE) and low-density polyethylene (LDPE) of different properties. The glass beads were supplied by Potters Industries Inc. The polyethylene particles provided by NOVA Chemicals Inc. and Saudi Basic Industries Corporation (SABIC), sieved to the

desired size ranges, are non-smooth and non-spherical. They represent typical industrial conditions, whereas the glass beads with smooth and spherical surface represent ideal particles.

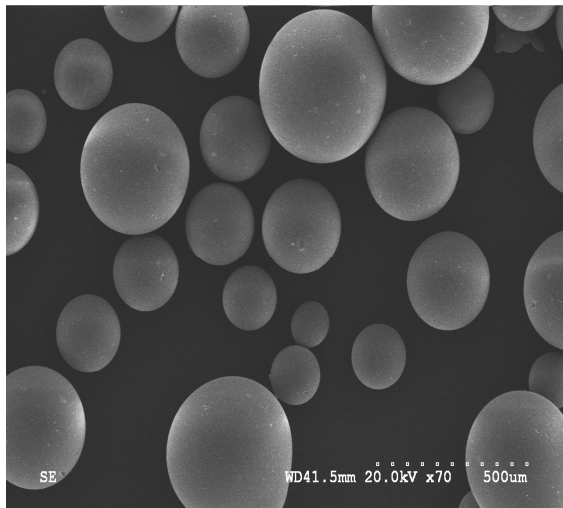
The key physical properties of the coarse particles used in this study are shown in Table 2.1.

Table 2.1 Relevant properties of the coarse particles.

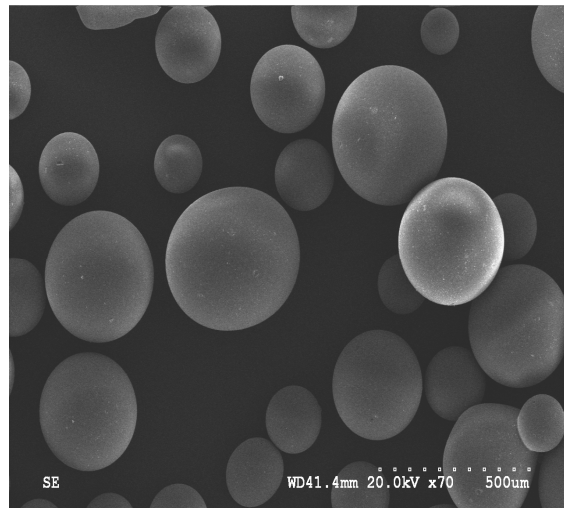
	GBS	GBM	GBL	HDPE	LDPE
Particle density, ρ_p (kg/m ³)	2500	2500	2500	965	797
Size range (μm)	106-212	212-425	425-600	500-600	500-600
Volume-weighted mean dia (μm)	155	357	560	553	573
Sphericity (-)	~1	~1	~1	~0.75	~0.77
Dielectric constant (-)	5-10	5-10	5-10	2.3	2.3

The coarse particle densities were provided by the suppliers. The size distributions and the volume weighted mean diameter were measured by a Malvern Mastersizer 2000 (see Appendix B for size distribution graphs). The sphericity of the coarse particles was provided by the suppliers. The dielectric constants were obtained from Reitz et al. (1993) and Jiang et al. (1994).

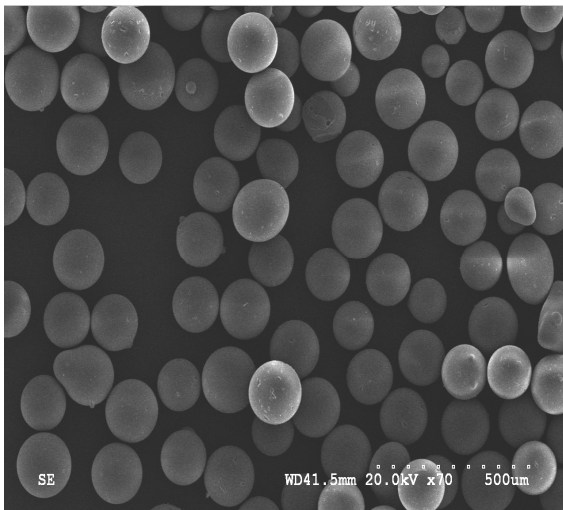
The physical surface structure, such as sphericity and roughness of all coarse particles, was analyzed by Scanning Electron Microscopy (SEM). Figures 2.7a, 2.7b and 2.7c show that the glass beads are closely spherical whereas Figure 2.7d establishes that the polyethylene particles are non-spherical and have uneven surfaces.



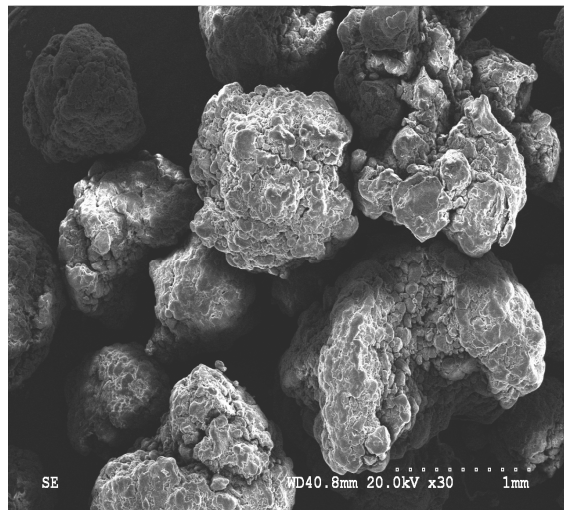
(a) GBL



(b) GBM



(c) GBS



(d) LDPE

Figure 2.7 SEM images of coarse particles used in this study.

2.4.2 Added Fine Particles

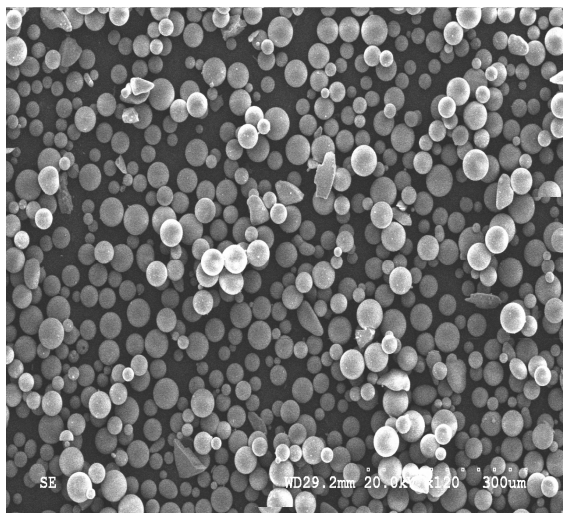
The fines particles employed in this study were fine glass beads (GBF), fine polyethylene (PEF) and fine Aluminium oxide (Al_2O_3). Their key physical properties are provided in Table 2.2.

Table 2.2 Properties of fine particles employed in this study.

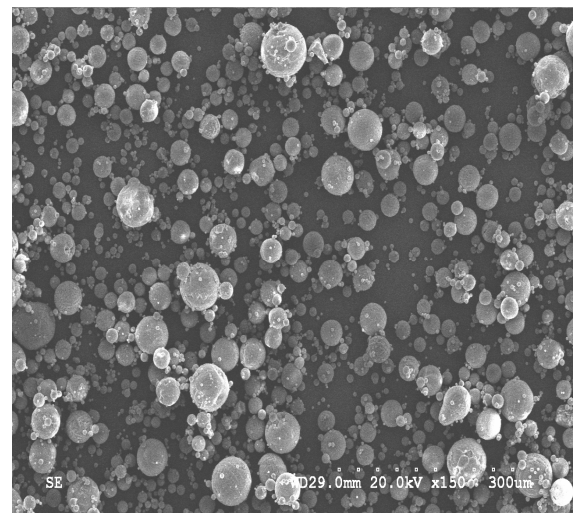
	GBF	Al₂O₃	PEF
Particle density, ρ_p (kg/m ³)	2700	3200	940
Size range (μm)	25-50	18-73	23-72
Volume-weighted mean diameter (μm)	38	42	45
Particle sphericity	~1	~0.9	~0.78
Dielectric constant	5-10	4-11	~2.3

The fines densities and sphericities were provided by the suppliers. The size range and volume-weighted mean diameters were measured by using a Malvern Mastersizer 2000 (see the Appendix B for size distribution graphs). The fine glass beads were supplied by Potters Industries Inc in the desired size range. The polyethylene powder was provided by Sigma-Aldrich Co. The spherical alumina (Al₂O₃) was provided by Industrial Powder Inc. Typical applications of Al₂O₃ include acting as a filler for molding materials, base powder for baking ceramic and blasting materials, and spacers.

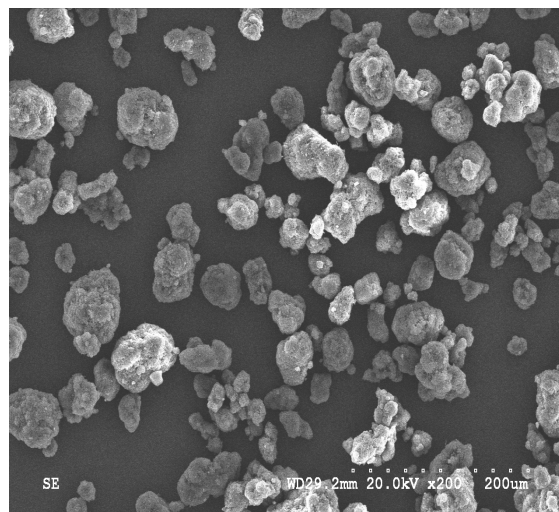
The shape and physical surface structure, such as sphericity and roughness of all fine particles, were analyzed by SEM. Figures 2.8a and 2.8b show that GBF and Al₂O₃ are closely spherical, whereas Figure 2.8c provides evidence that the PEF particles are non-spherical and have uneven surfaces.



(a) GBF



(b) Al₂O₃



(c) PEF

Figure 2.8 SEM images of fine particles tested during this study

According to the Geldart (1973) classification of powders, the coarse particles (GBS, GBM, GBL, HDPE and LDPE) were all group B particles, whereas the fine particles (PEF, Al₂O₃ and GBF) were all group A particles.

2.4.3 Binary Mixtures

Different binary mixtures were tested to investigate the influence of operating conditions, electrostatics and particle properties on entrainment in fluidized bed. The coarse particles, such as glass beads and polyethylene, were used as the mono-sized particles, and different fine particles, as showed in Table 2.2, were added to provide binary mixtures. The key physical properties of the mixtures are provided in Table 2.3.

Table 2.3 Properties of binary particle mixtures.

	Mixture		Vol.- weighted mean dia. (μm)	Loosely packed voidage	Specific surface area (m^2/g)	U_{mf} at 20 °C and 414 kPa (m/s)
	Coarse	Fines (wt %)				
M1	GBS	GBF (5%)	136	0.368	0.0182	0.0154
M2	GBM	GBF (5%)	257	0.372	0.0096	0.0528
M3	GBL	GBF (5%)	342	0.375	0.0075	0.0883
M4	GBL	GBF (10%)	246	0.373	0.0104	0.0484
M5	GBL	GBF (15%)	191	0.371	0.0134	0.0299
M6	GBL	Al_2O_3 (5%)	377	0.376	0.0083	0.1211
M7	GBL	Al_2O_3 (10%)	282	0.374	0.0121	0.0724
M8	GBL	Al_2O_3 (15%)	225	0.370	0.0159	0.0470
M9	GBL	PEF (5%)	233	0.377	0.0072	0.0170
M10	HDPE	GBF (5%)	442	0.622	0.0176	0.1311
M11	LDPE	GBF (5%)	472	0.466	0.0208	0.1440

The size distributions, volume-weighted mean diameters and specific surface areas were measured by a Malvern Mastersizer 2000 (see Appendix B for size distribution graphs). Loose- packed voidages were determined by adding a known-weight of the particles to a known-volume container. Then, water (or ethanol for polyethylene particles) was added into the container to fill the total volume. The total mass (container + water + particles) was measured, and by knowing the density of water, the volume of added water and loose packed bed was then calculated.

The minimum fluidization velocities, U_{mf} , of binary mixtures were estimated using the correlation given by Goossens et al. (1971). Several trials were made to measure U_{mf} experimentally as recommended by Kunii and Levenspiel (1991); however, due to frequent

blockages in differential pressure taps, it was difficult to obtain conventional fluidization curves (pressure drop vs. gas velocity) for the binary mixtures. Chiba et al. (1979) found that the experimental procedure used to measure the U_{mf} for mono-size particles is not applicable to binary mixtures, and U_{mf} could not be determined accurately. Goossens et al. (1971) modified the correlation of Wen and Yu (1966) to account for mixture particle density and mixture particle mean diameter, and found that the new correlation could be employed for binary mixtures. For detailed calculations of U_{mf} for the binary mixtures in this study, see the Appendix C.

2.5 Experimental Methodology

The following methods were used to study the effect of operating conditions, gas and particle properties on solids entrainment flux, electrostatic charges inside the fluidized bed and charges on entrained particles.

- Gas Velocity Variation Experiments

To investigate the influence of gas velocity on the electrostatic charges generated inside the fluidized bed, entrainment flux and charge density of fine particles, free-bubbling experiments were performed with binary mixtures M3 and M10. The superficial gas velocity, U_g was varied from 0.2 to 0.6 m/s.

To isolate the effect of other operating parameters, these experiments were conducted at 207 kPa and ambient temperature. The RH of the air was maintained at $12\pm 2\%$. The collision ball probe locations and static bed height (~ 0.54 m) were the same for all experiments. The bed was fluidized for around 1.0 h to achieve steady state before data were collected. The degree of electrification in the bed was then characterized by the four collision ball probes. The online freeboard sampler (Faraday cup), located in the freeboard was utilized to measure the fines charge density by withdrawing samples from particles within the freeboard. The entrainment flux of solid particles recovered by the cyclone was measured directly by diverting the solid particles via a three-way diverter valve into a stainless steel sampling container. Then, the collected solids were weighed and the entrainment flux was calculated. The volume of collected samples was small enough, that the withdrawal of each sample did not influence the fines concentration in the bed appreciably. The entrainment flux and fines charge density were measured at

least four times for different experimental conditions. After each run, the collected solid particles were returned to the fluidization column. Also, the detection stainless pipe coated with Ni (see section 2.3.2.3) was used to measure the current generated by entrained fine particles passing through the reactor outlet line.

- Temperature Variation Experiments

To study the effect of temperature on the electrostatic charges generated inside the fluidized bed, entrainment flux and charge density of fine particles in the freeboard, free bubbling experiments were performed with binary mixtures M3, and M10 at a freeboard pressure of 414 kPa and at superficial gas velocity $U_g = 0.3$ m/s. The experimental procedures were the same as those described previously. The temperature of the bed was varied from 25 to 75 °C.

- Pressure Variation Experiments

Free bubbling fluidization was performed at room temperature with superficial gas velocity, $U_g = 0.3$ m/s and the RH of the gas maintained at $12 \pm 2\%$. In these experiments, the same procedures described previously were repeated. The air pressure was varied from 207 to 517 kPa to determine the influence of pressure on electrostatic charges generation inside a fluidized bed, flux and charge density of entrained particles. Binary mixtures M3 and M10 were tested in these experiments.

- Relative Humidity Variation Experiments

To investigate the effect of fluidizing gas RH, free bubbling experiments were conducted at room temperature with a freeboard pressure of 414 kPa and bed fluidization at a superficial gas velocity, $U_g = 0.3$ m/s. The previous runs were repeated at a freeboard pressure of 210 kPa, and higher superficial gas velocity, $U_g = 0.6$ m/s. Binary mixtures M3, M6 and M9 were used in these experiments. In this set of experiments, the RH of the fluidizing air was varied from 3 to 38% by passing the air through a compressor refrigerator dryer or a silica gel dryer.

- Coarse Particles Properties Experiments

To investigate the effect of coarse particle size on electrostatic charge generation, entrainment flux and charge density of fine particles in the freeboard, free-bubbling experiments were conducted with the M1, M2 and M3 binary mixtures of different sizes of coarse glass beads (see Table 2.3). These experiments were performed at room temperature with a freeboard pressure of 414 kPa and a superficial gas velocity, U_g of 0.3 m/s. The RH of the gas was maintained at $12\pm 2\%$.

To study the effect of coarse particle type, binary mixtures M3 and M10 having glass beads and polyethylene particles, respectively, but fine glass beads of the fines were used. In addition, binary mixtures M10 and M11 of polyethylene with different densities (LLDPE and HDPE) were tested to investigate the effect of coarse particle density.

- Fine Particle Properties Experiments

To determine the effect of fines wt%, binary mixtures M3, M4, M5, M6, M7 and M8 were studied, with the fines (glass beads in M3 to M5 or alumina in M6 to M8) varied from 5 to 15 wt%. Free bubbling experiments were conducted at room temperature with a freeboard pressure of 414 kPa. The bed was fluidized at a superficial gas velocity, U_g of 0.3 m/s. The RH of the gas was maintained at $12\pm 2\%$. In addition, binary mixtures M3, M6 and M9 with different fines types and densities were tested to investigate the effect of the fines particle density and type.

Chapter 3: Results and Discussion: Effect of Operating Parameters

The elevated-pressure fluidization column portrayed in the previous chapter was used to measure the entrainment flux and electrostatic charges generated inside the bed at different levels and in the freeboard region. The effect of operating parameters, such as superficial gas velocity, operating pressure and bed temperature, were investigated for binary particle mixtures of glass beads and polyethylene (whose particle properties are provided in Tables 2.2 and 2.3). This chapter presents and discusses the experimental results.

3.1 Collision Ball Probes Location and Sensitivity

To characterize the electrostatic charges at different locations in a fluidized bed, three collision ball probes (A, B and C) were immersed at different axial locations in the bed (see Figure 2.4). In addition, a fourth probe (D) was normally mounted in the freeboard, 1.1 m above the distributor plate, also shown in Figure 2.4. However, in preliminary experiments, probe D was mounted at a lower level, 0.89 m above the distributor plate, and it was observed that, at high superficial gas velocities, negative charges were measured by probe D, as shown in Figure 3.1. This is probably because, at high superficial gas velocities and as bubbles erupted at the bed surface, more negatively charged coarse particles were ejected into the freeboard region and collided with probe D. As a result, negative charges were transferred to the probe. Since the function of probe D was to measure the electrostatic charges carried by fine particles in the freeboard, probe D was relocated to the higher level, and positive charges were then measured for the fine particles in the freeboard region.

The induced electrical field in the bed could influence the signals measured from each of the collision ball probes; therefore, the sensitivity of the probe was set to 1 pC/Mechanical Unit (MU) to localize the measurements for each probe (Moughrabiah, 2009).

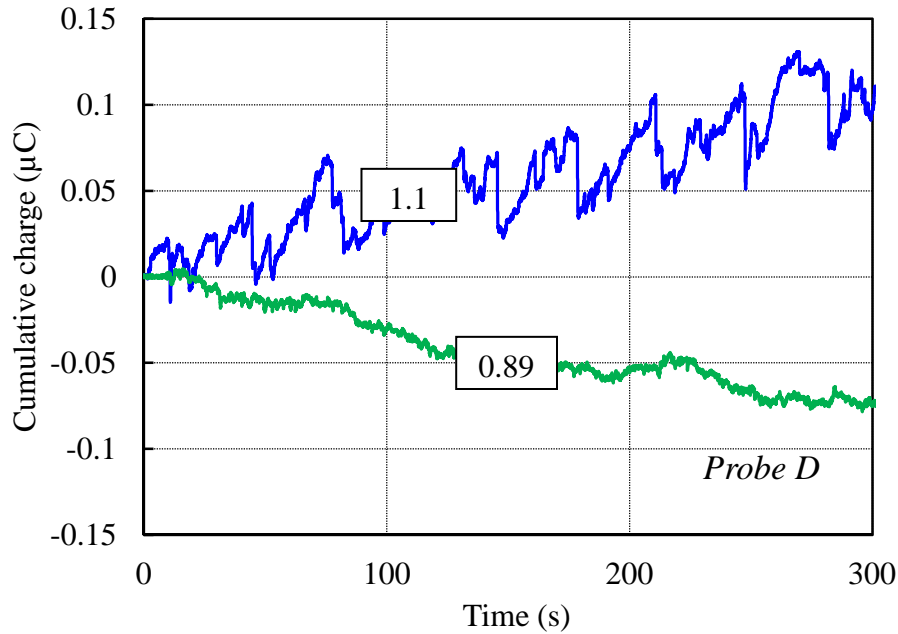


Figure 3.1 Net cumulative charges measured by probe D in freeboard as a function of time for binary mixture M3. $P = 207 \text{ kPa}$, $T = 20 \pm 2^\circ\text{C}$, $U_g = 0.6 \text{ m/s}$, $\text{RH} = 12 \pm 2\%$. For physical properties of particles, see Tables 2.1, 2.2 and 2.3. Numbers on curves denote probe D distance above distributor plate (in m).

The collision ball probes and current detection pipe (see section 2.3.2) were connected directly to an electrometer (Kistler model 5010B). This electrometer is able to measure charges from $\pm 10.0 \text{ pC}$ to $\pm 1.0 \text{ }\mu\text{C}$. To verify that the fluidizing air alone does not carry electrostatic charges that could influence the binary mixture results, air alone was passed through the empty fluidization column while the charges were measured, by the probes in the bed and freeboard regions, and by the current detection pipe at the column exit. The column absolute pressure was maintained constant at 207 kPa , while the temperature and relative humidity of the air were nearly constant ($T = 20 \pm 2^\circ\text{C}$ and $\text{RH} = 12 \pm 2\%$). The fluidizing air was introduced to the column at a superficial gas velocity of 0.3 m/s for $\sim 300 \text{ s}$. The electrostatic charges measured by the ball probes and current detection pipe are plotted versus time in Figure 3.2. It can be seen that the fluidizing air alone carries negligible charges.

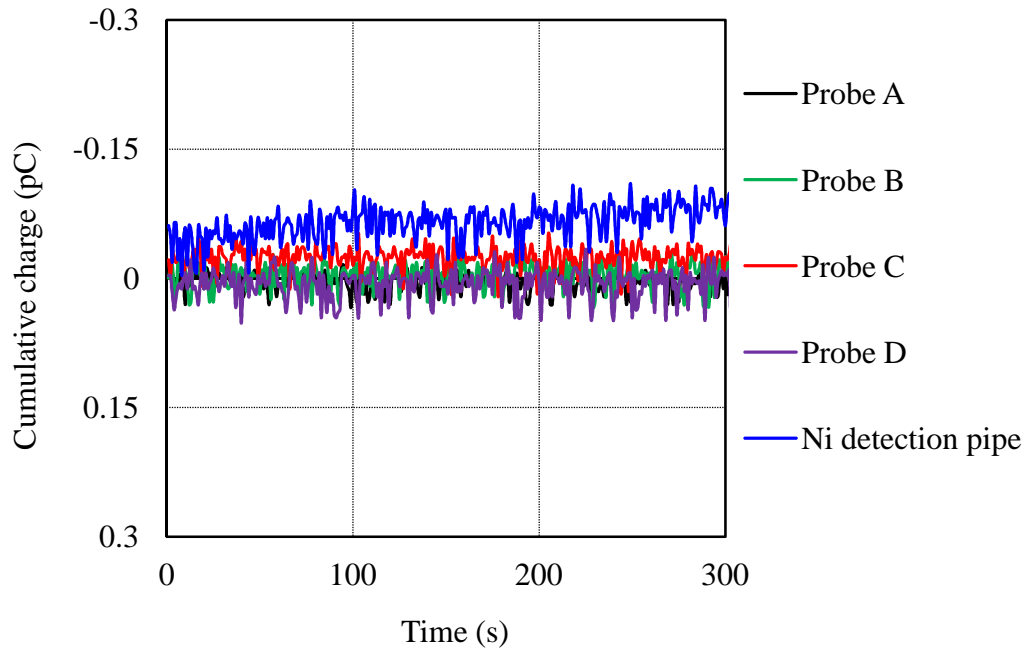


Figure 3.2 Cumulative charge as a function of time for air flow through empty column. $P = 207 \text{ kPa}$, $T = 20 \pm 2^\circ\text{C}$, $U_g = 0.3 \text{ m/s}$, $\text{RH} = 12 \pm 2\%$. For position of probes, see Figure 2.4.

3.2 Effect of Operating Parameters

Electrostatics and particle entrainment in gas-solid fluidized beds have been studied separately by a number of researchers, as reviewed in Chapter 1. It has been found that the electrostatics and particle entrainment in gas-solid fluidized beds are influenced by many factors. Most previous studies were performed at ambient operating conditions. To gain a better understanding of the influence of operating conditions on particle entrainment and electrostatics in gas-solid fluidized beds, our investigation was conducted by simultaneously measuring the particle entrainment flux, electrostatic charges inside a fluidized bed and the charge on entrained particles, while varying key operating parameters such as superficial gas velocity, pressure and temperature.

3.2.1 Effect of Superficial Gas Velocity

3.2.1.1. Glass Beads

Free-bubbling experiments were conducted in the three-dimensional fluidization column described in Chapter 2, with collision ball probes at four levels, as shown in Figure 2.4, in the presence of the freeboard sampler shown in Figure 2.5, and the current detecting pipe shown in Figure 2.6, to investigate the effect of superficial gas velocity on electrostatic charges generated inside the fluidized bed, entrainment flux (W_s) and charge density (q_m) of entrained fine particles. These experiments were conducted utilizing relatively large glass beads (GBL) as the mono-sized particles, with GBF as added fines for the binary mixture (M3 in Table 2.3). For the particle physical properties, see Tables 2.1 and 2.2. The height of the static bed was ~ 0.54 m in all cases. The temperature, pressure and air relative humidity were maintained nearly constant at $20 \pm 2^\circ\text{C}$, 207 kPa and $12 \pm 2\%$ respectively to isolate the effect of superficial gas velocity, which was varied from 0.2 to 0.6 m/s.

In each experiment, the bed was fluidized for approximately an hour to achieve steady state before data were collected. The net cumulative charge generated inside the bed was then measured by the three collision ball probes during fluidization and plotted versus time, as shown in Figure 3.3. Figure 3.4 shows the net cumulative charge measured by collision ball probe A, plotted versus time. Figures 3.5 and 3.6 show the cumulative charge and the standard deviation of charge fluctuations registered by probe D in the freeboard region as a function of superficial gas velocity, after filtering the net cumulative charge curves using a high-pass filter with a cut-off frequency of 0.03 Hz. The charge density of the sampled fine glass beads is plotted versus superficial gas velocity in Figure 3.7. Figure 3.8 shows the effect of superficial gas velocity on the current flow through the detection pipe due to direct charge transfer. The influence of superficial gas velocity on the solids entrainment flux is displayed in Figure 3.9.

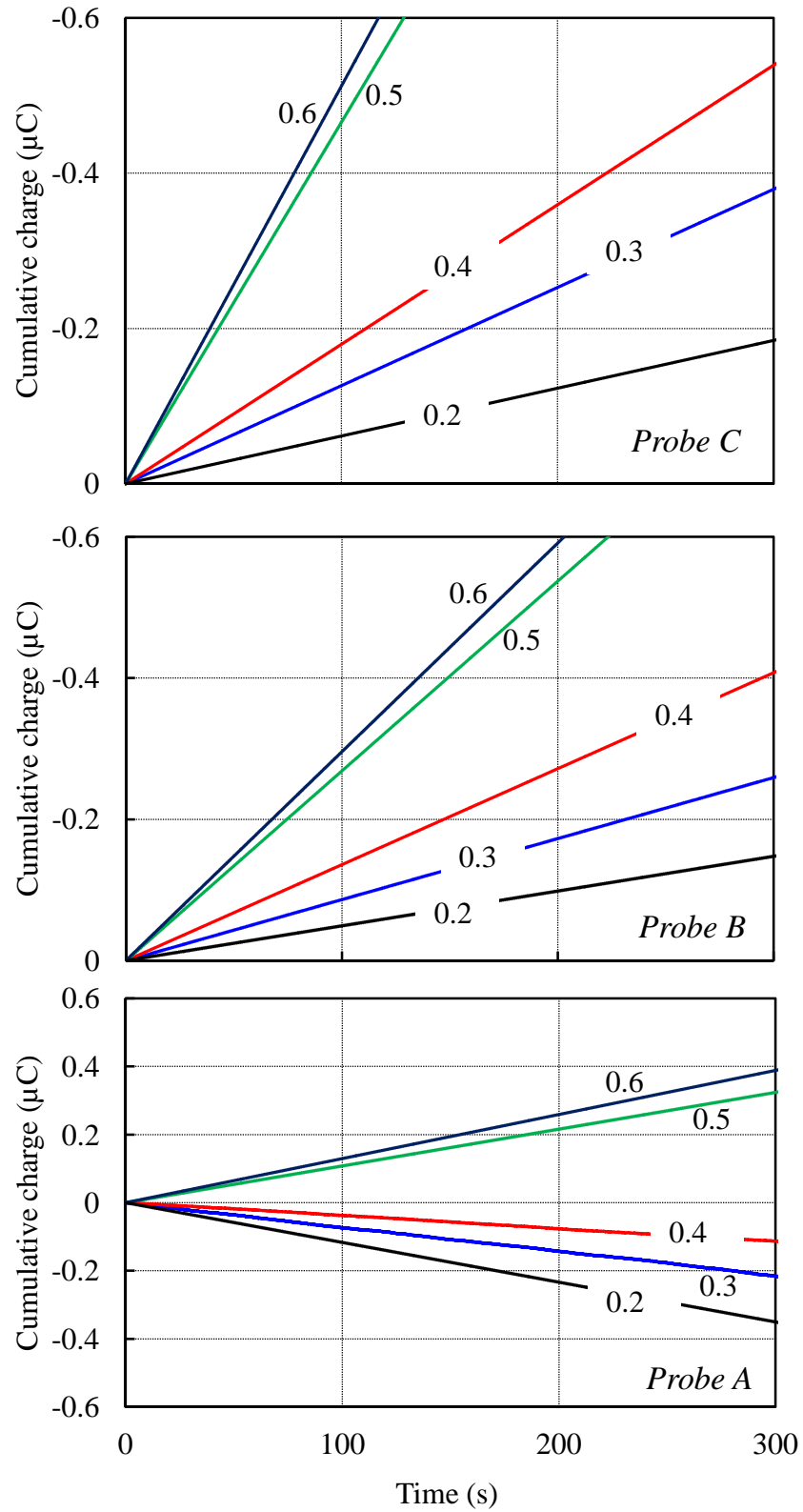


Figure 3.3 Effect of superficial gas velocity on net cumulative charges as a function of time at different axial positions in a bed of binary mixture M3. $P = 207 \text{ kPa}$, $T = 20 \pm 2^\circ\text{C}$, $RH = 12 \pm 2\%$. For physical properties of particles, see Tables 2.1, 2.2 and 2.3. Numbers on curves denote superficial gas velocity (in m/s). For probe positions, see Figure 2.4.

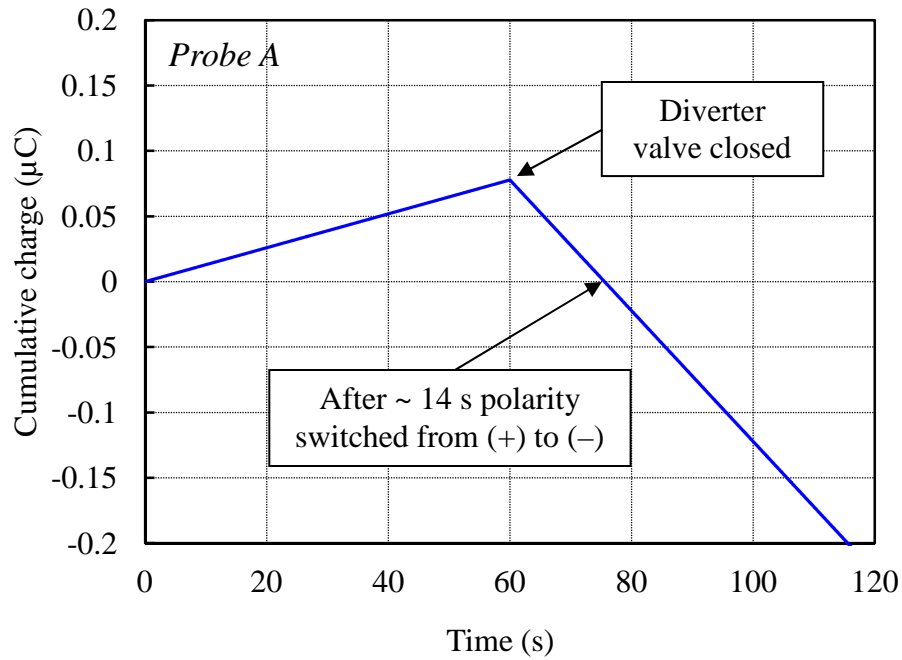


Figure 3.4 Net cumulative charges measured by probe A as a function of time in a bed of binary mixture M3. $P = 207$ kPa, $T = 20 \pm 2^\circ\text{C}$, $U_g = 0.6$ m/s, $RH = 12 \pm 2\%$. For physical properties of particles, see Tables 2.1, 2.2 and 2.3. For probe position, see Figure 2.4.

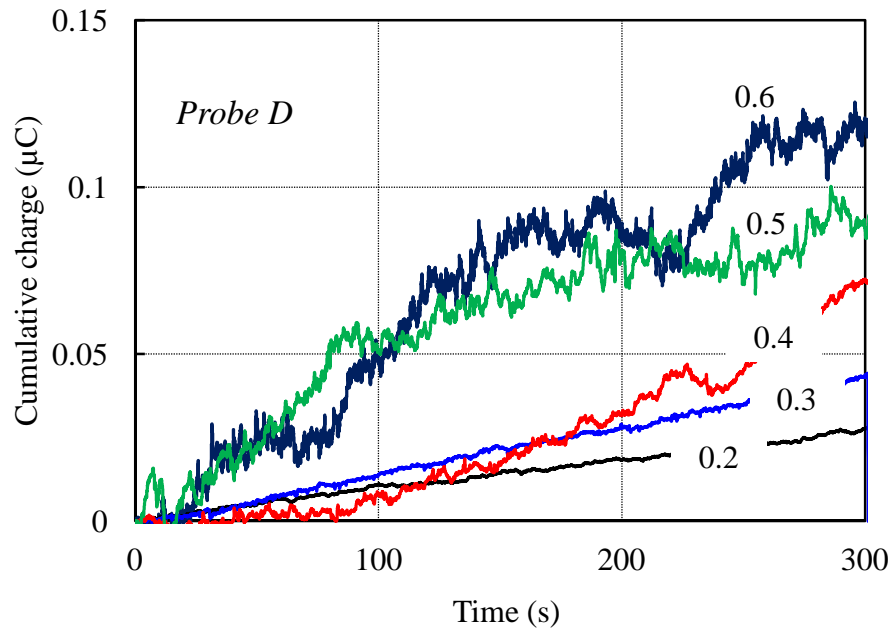


Figure 3.5 Effect of superficial gas velocity on net cumulative charges in freeboard as a function of time for binary mixture M3. $P = 207$ kPa, $T = 20 \pm 2^\circ\text{C}$, $RH = 12 \pm 2\%$. For physical properties of particles, see Tables 2.1, 2.2 and 2.3. Numbers on curves denote superficial gas velocity (in m/s). For position of probe D, see Figure 2.4.

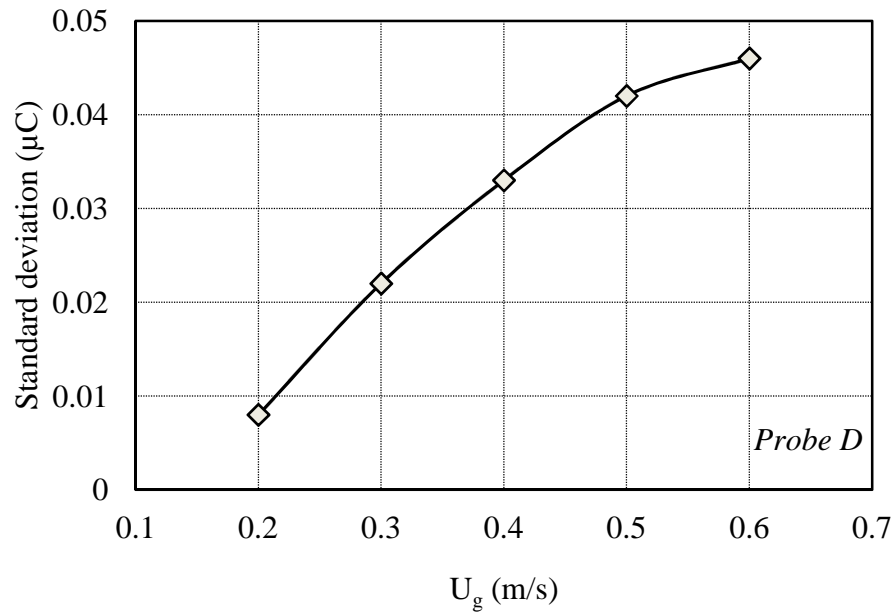


Figure 3.6 Standard deviation of charge fluctuations in freeboard as a function of superficial gas velocity for binary mixture M3. $P = 207$ kPa, $T = 20 \pm 2^\circ\text{C}$, $\text{RH} = 12 \pm 2\%$. For physical properties of particles, see Tables 2.1, 2.2 and 2.2. For position of probe D, see Figure 2.4.

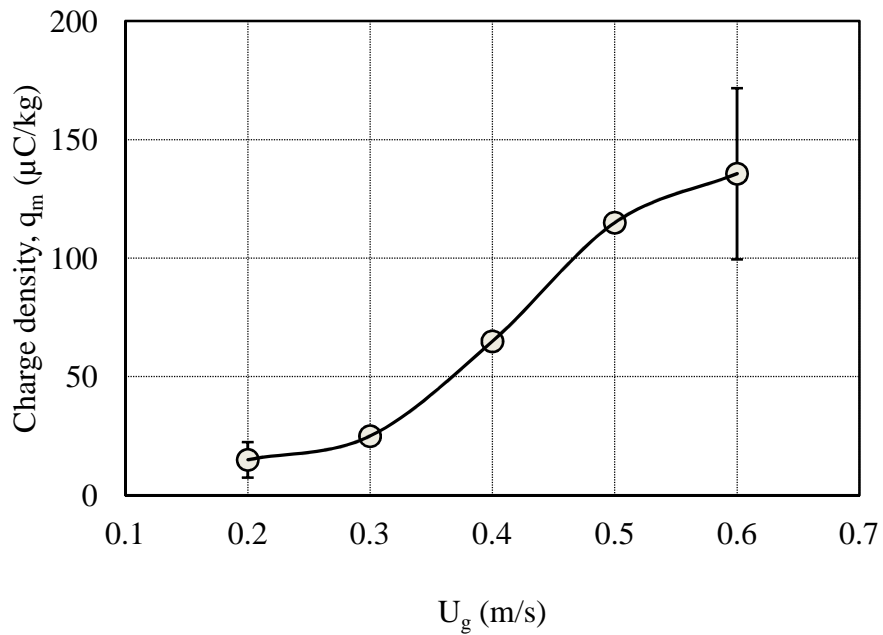


Figure 3.7 Charge density of glass bead fines measured by freeboard sampler as a function of superficial gas velocity for binary mixture M3. $P = 207$ kPa, $T = 20 \pm 2^\circ\text{C}$, $\text{RH} = 12 \pm 2\%$. For physical properties of particles, see Tables 2.1, 2.2 and 2.3. For freeboard sampler details, see Figure 2.5. Error bars correspond to $\pm 90\%$ confidence intervals.

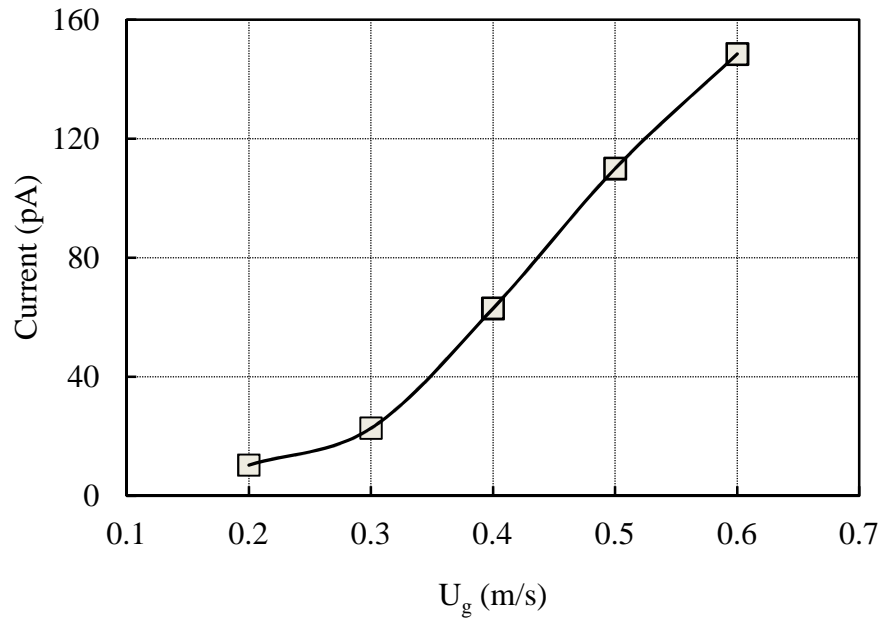


Figure 3.8 Current flow through current detection pipe at column exit for binary mixture M3 as a function of superficial gas velocity. $P = 207$ kPa, $T = 20 \pm 2^\circ\text{C}$, $\text{RH} = 12 \pm 2\%$. For physical properties of particles, see Tables 2.1, 2.2 and 2.3. For current-detecting pipe details, see Figure 2.6.

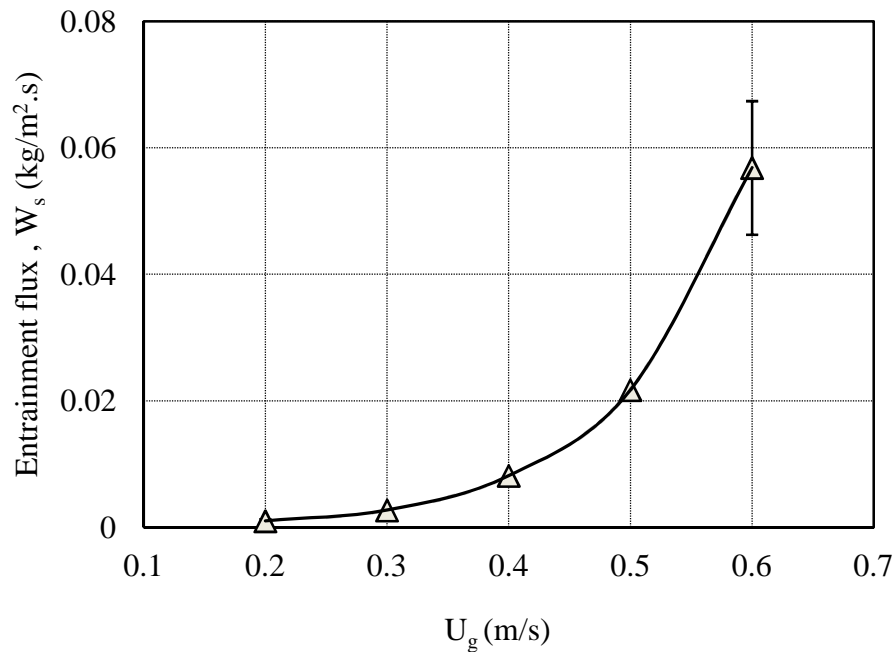


Figure 3.9 Entrainment flux measured for binary mixture M3 as function of superficial gas velocity. $P = 207$ kPa, $T = 20 \pm 2^\circ\text{C}$, $\text{RH} = 12 \pm 2\%$. For physical properties of particles, see Tables 2.1, 2.2 and 2.3. Error bar corresponds to $\pm 90\%$ confidence interval.

The experimental results shown in Figure 3.3 reveal that the magnitude of electrostatic charges measured in the bed at different heights by probes A, B and C for binary mixture M3 increased linearly as the superficial gas velocity increased. In addition, it can be seen that, with two exceptions, the bed particles were charged negatively at all three levels inside the dense bed (probe A, B and C). At superficial gas velocities > 0.4 m/s, the polarity measured by probe A switched to positive, probably due to the high concentration of fines at that location. The high gas velocity resulted in more fines being entrained from the column and the returning point of these fines to the column was located at the same level as probe A, resulting in more collisions between probe A and returning fines. This explanation was confirmed by closing the diverter valve in the return line. It was observed that after ~ 14 s the polarity measured by probe A switched from positive to negative, resulting from the decreased concentration of fines, as shown in Figure 3.4.

The experimental results in Figures 3.5 and 3.7 indicate that the charges on the fines in the freeboard measured by probe D and the freeboard sampler increased as the superficial gas velocity increased. It can be seen that the polarity of fines in the freeboard region was opposite to that inside the dense bed, indicating that the fines entrained from the bed carried opposite charges, leaving a net charge of opposite polarity inside the bed. Figures 3.6 and 3.8 show that the charge fluctuations in the freeboard region measured by probe D and the current flow through the current detection pipe at the column exit for binary mixture M3 increased as the superficial gas velocity increased, reflecting the increase in the concentration of fine particles in the freeboard and at the column exit.

These increases in electrostatic charges could be due to the formation of larger bubbles and greater bubble rise velocity that enhanced particle motion and particle-particle collisions in the bed. Many previous researchers (e.g. Davidson and Harrison, 1963; Geldart, 1972; Mori and Wen, 1975; Darton, 1977) have reported that the average bubble diameter increases with increasing superficial gas velocity. Boland and Geldart (1971) concluded that electrostatic charges in gas-solid fluidized beds are generated by the motion of particles around bubbles. Another contributor to the increase in electrostatics charges observed in our experiments is likely to be the increase in particle velocity at the time of particle-probe contact, since the velocity at the time of contact influences the amount of charge transferred during any

rubbing process between similar or dissimilar materials (Cross, 1987). These findings are consistent with those reported by earlier researchers (Ciborowski and Wlodarski, 1962; Guardiola et al., 1996; Yao et al., 2002, Chen et al., 2003, Moughrabiah et al., 2009) who found that electrostatic charge generation increased as the fluidizing gas velocity increased. Moughrabiah et al. (2009) investigated the effect of superficial gas velocity on electrostatic charge generation in the same elevated-pressure column as in this work, performing their experiments with mono-sized glass bead particles (group B) in a three-dimensional bubbling fluidized bed. They found that bed electrification increased as the excess gas velocity, ($U - U_{mf}$), increased from 0.03 to 0.12 m/s.

As indicated by the results for probes B and C in Figure 3.11, it was also observed that as the superficial gas velocity increased beyond 0.4 m/s, the charge transfer became less sensitive to the superficial gas velocity. This could be due to the reduction in the contact time between the bed solid particles and the collision ball probes. Similar results were reported by Yao et al. (2002), who found that the net charge transfer measured by a collision ball probe in a three-dimensional fluidized bed did not change significantly when the superficial gas velocity was varied. They attributed these results to the reduction in collision frequency between particles and the probe as the superficial gas velocity increased.

The influence of superficial gas velocity on the solid entrainment flux was also investigated, as shown in Figure 3.9. Procedures similar to those described in Section 2.5 were followed to measure the entrainment flux. As expected, as the air superficial velocity increased, the entrainment flux increased. From Figure 3.7, it can be seen that greater charge density was measured at higher superficial gas velocity, which could promote particle-particle and particle-wall adhesion, reducing the entrainment flux. However, these experimental results show that, when the superficial gas velocity increased, entrainment flux increased, even though the charge density increased. This increase in entrainment flux was probably due to the greater effect of the increase in superficial gas velocity, which led to higher entrainment flux. This increase in entrainment flux could be explained by the increase in bubble velocity, frequency and upward drag forces exerted on the particles in the freeboard as the superficial gas velocity increased, possibly overcoming adhesion forces between particles resulting from their higher electrostatic charges.

Several researchers (e.g. Chan and Knowlton, 1984; Baron et al., 1990; Nakagawa et al., 1994; Ma and Kato, 1998; Choi et al., 2001; Kato and Li, 2001; Nakazato et al., 2004) have investigated the effect of superficial gas velocity on entrainment, finding that the entrainment rate increased strongly as superficial gas velocity increased. Ma and Kato (1998) studied the effect of superficial gas velocity on the elutriation rate constant of fines in a fluidization column (inner diameter 0.071 m; height 0.1 m) containing binary mixtures of silica sand (Geldart group B) and limestone fines (groups A and C). Their results showed that the fines elutriation rate constant increased as the superficial gas velocity increased from 0.3 to 0.9 m/s. Tasirin and Geldart (1998) investigated the effect of superficial gas velocity on the entrainment of FCC powder (group A) in a fluidization column of inner diameter 0.152 m and height 2.4 m. They found that the entrainment flux increased as the superficial gas velocity increased from 0.2 to 0.8 m/s and attributed these findings to increases in bubble velocity and frequency.

In our experiments, the measured entrainment flux of the M3 binary mixture was compared to the entrainment flux predicted using different several empirical correlations from the literature. The comparison is shown in Figure 3.10 where entrainment flux is plotted versus superficial gas velocity. It can be seen that all of the selected correlations over-predict the entrainment flux measured experimentally in our work and that there is wide divergence between correlations predictions. These discrepancies in entrainment correlation predications are probably related to the fact that each author developed these correlations using different numbers of variables, such as operating conditions (pressure, temperature and superficial gas velocity) and fluidization column geometry, each of which influenced the entrainment flux from the fluidized bed. In addition, as discussed in Chapter 1, electrostatics not included in any of the empirical correlations, could be responsible for much of the discrepancy in the predictions. The goal of our work is to gain a better understanding of the effect of operating conditions and particle properties on entrainment and electrostatics in gas-solid fluidized beds. This study may help to explain why the empirical correlations (which do not consider electrostatics) fail to give reliable predications.

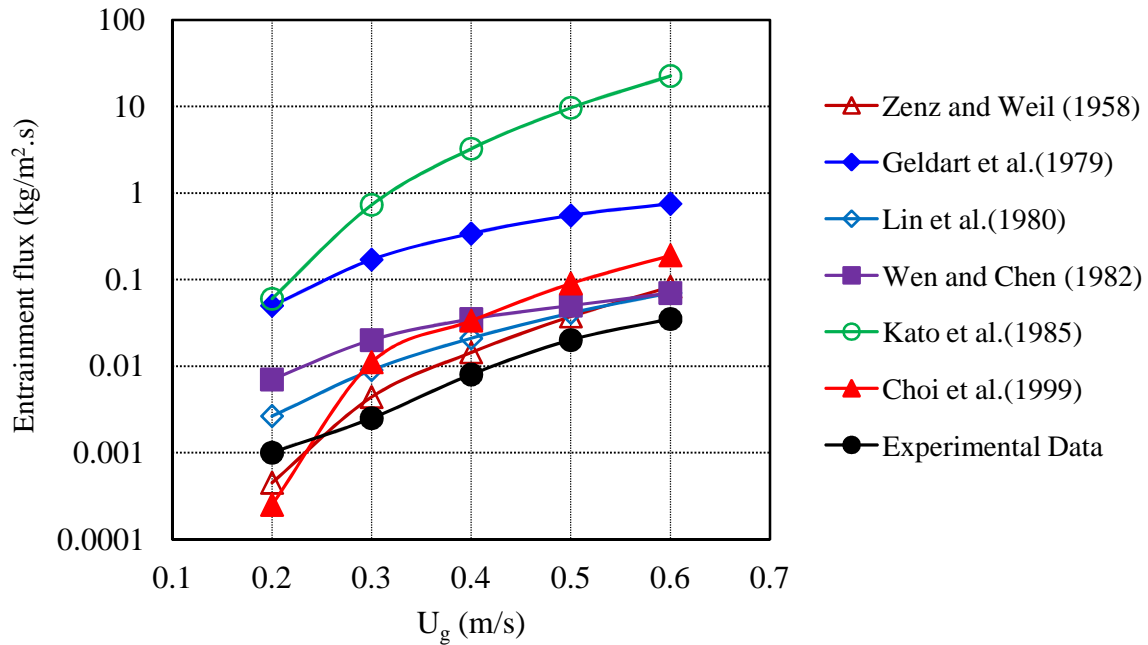


Figure 3.10 Comparison of measured entrainment flux for binary mixture M3 with predictions from empirical correlations as a function of superficial gas velocity. P = 207 kPa, T = 20±2°C, RH = 12±2%. For physical properties of particles, see Tables 2.1, 2.2 and 2.3.

3.2.1.2. Polyethylene

Free-bubbling experiments, similar to those described in section 3.2.1.1 were conducted in the same three-dimensional fluidized bed column with collision ball probes at four levels, a freeboard sampler, and a current detecting pipe, as shown in Figures 2.4, 2.5 and 2.6, respectively. As before, the experiments investigated the effect of fluidizing gas superficial velocity on electrostatic charges generated inside the fluidized bed, entrainment flux and charge density of entrained fine particles. This set of experiments utilized relatively large polyethylene (HDPE) particles as the mono-sized particles, with fine glass beads (GBF) as added fines for the binary mixture (M10, in Table 2.3). For particle physical properties, see Tables 2.1 and 2.2. The height of the static bed was ~0.54 m in all cases. To isolate the effect of superficial gas velocity, temperature, pressure and air relative humidity were all maintained nearly constant at 20±2°C, 207 kPa and 12±2%, respectively. Superficial gas velocity was varied from 0.2 to 0.6 m/s. In each experiment, the bed was fluidized for approximately an hour to achieve steady state before data were recorded. The net cumulative charge generated inside the bed then measured by the three collision ball probes during

fluidization is plotted versus time in Figure 3.11. Figure 3.12 also shows the standard deviation of charge fluctuations registered by probe D in the freeboard region as a function of superficial gas velocity after filtering the net cumulative charge curves using a high-pass filter (cut-off frequency, 0.03 Hz). Figure 3.13 plots the charge density of the fine glass bead particles sampled versus superficial gas velocity. Figure 3.14 shows the effect of superficial gas velocity on the current flow through the detection pipe due to direct charge transfer. The influence of superficial gas velocity on the solid entrainment flux can be seen from Figure 3.15.

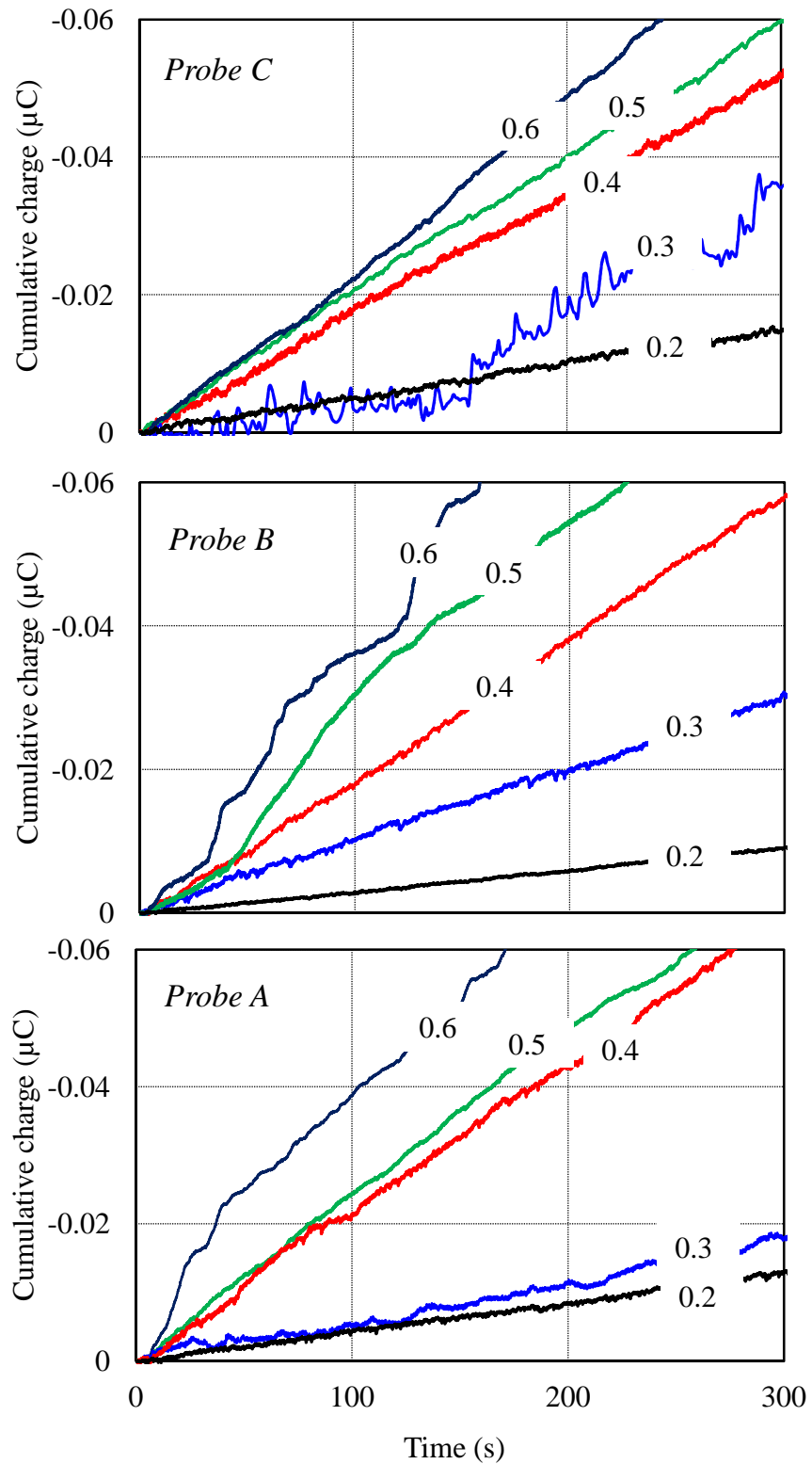


Figure 3.11 Effect of superficial gas velocity on net cumulative charges as a function of time at different axial positions in bed of binary mixture M10. $P = 207 \text{ kPa}$, $T = 20 \pm 2^\circ\text{C}$, $\text{RH} = 12 \pm 2\%$. For physical properties of particles, see Tables 2.1, 2.2 and 2.3. Numbers on curves denote superficial gas velocity (in m/s). For probe positions, see Figure 2.4.

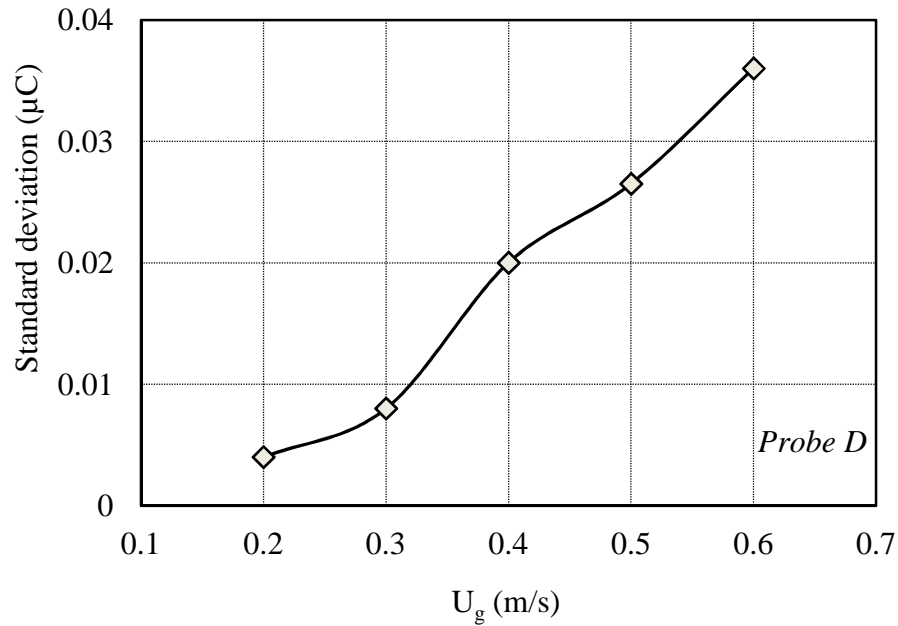


Figure 3.12 Standard deviation of charge fluctuations in freeboard as a function of superficial gas velocity for binary mixture M10. $P = 207 \text{ kPa}$, $T = 20 \pm 2^\circ\text{C}$, $\text{RH} = 12 \pm 2\%$. For physical properties of particles, see Tables 2.1, 2.2 and 2.2. For position of probe D, see Figure 2.4.

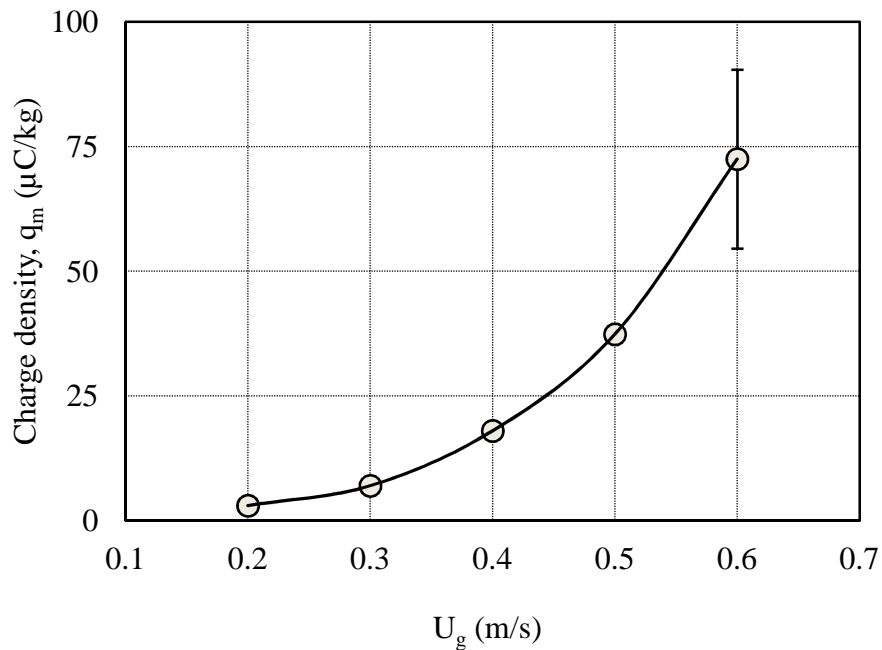


Figure 3.13 Charge density of fine glass bead measured by freeboard sampler as a function of superficial gas velocity for binary mixture M10. $P = 207 \text{ kPa}$, $T = 20 \pm 2^\circ\text{C}$, $\text{RH} = 12 \pm 2\%$. For physical properties of particles, see Tables 2.1, 2.2 and 2.3. For freeboard sampler details, see Figure 2.5. Error bar corresponds to $\pm 90\%$ confidence interval.

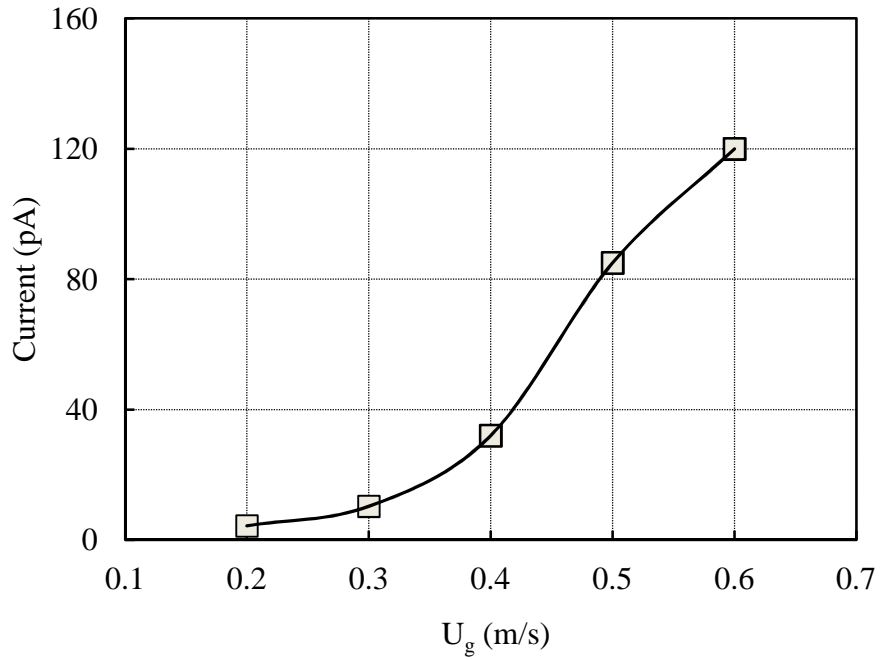


Figure 3.14 Current flow through current detection pipe at column exit for binary mixture M10 as a function of superficial gas velocity. $P = 207$ kPa, $T = 20 \pm 2^\circ\text{C}$, $RH = 12 \pm 2\%$. For physical properties of particles, see Tables 2.1, 2.2 and 2.3. For current detecting pipe details, see Figure 2.6.

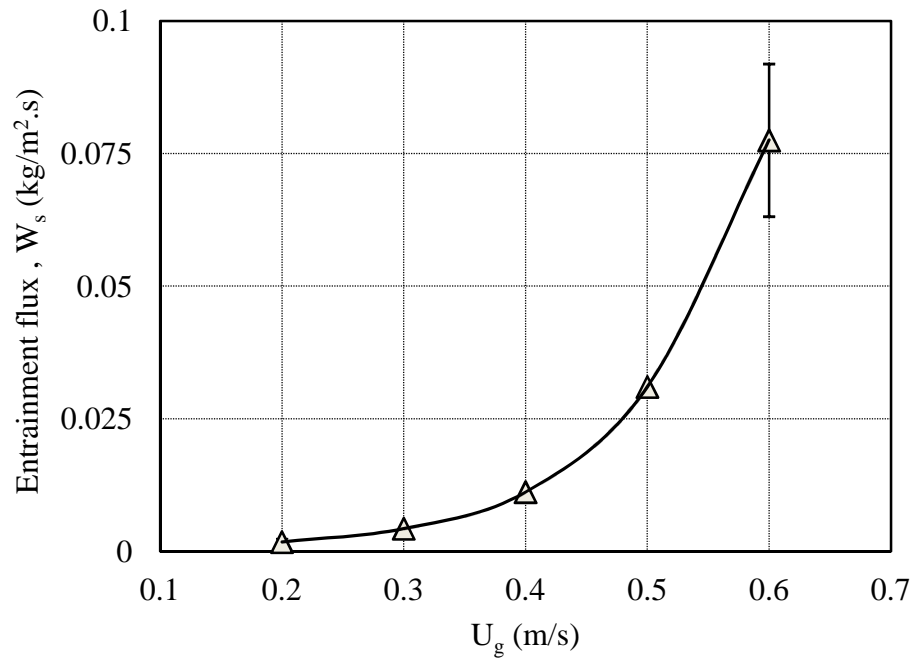


Figure 3.15 Entrainment flux measured for binary mixture M10 as a function of superficial gas velocity. $P = 207$ kPa, $T = 20 \pm 2^\circ\text{C}$, $RH = 12 \pm 2\%$. For physical properties of particles, see Tables 2.1, 2.2 and 2.3. Error bars correspond to $\pm 90\%$ confidence intervals.

Figures 3.11–3.15 for binary mixture (M10) indicate that the magnitude of electrostatic charges in the bed as well as freeboard region, and the entrainment flux all increased as the superficial gas velocity increased. As explained above, this is probably due to the significant impact of superficial gas velocity on bubbles, affecting both electrostatics and entrainment flux. The increase in superficial gas velocity enhances the motion and interactions between solid particles in the gas-solid fluidized bed due to increases in bubble size and velocity, leading to increased electrostatic charge generation. At the same time, increasing superficial gas velocity resulted in higher bubble velocity and greater ejection velocities at the bed surface, resulting in greater upwards drag on particles in the freeboard, which in turn increased the entrainment flux. It was also observed in these experimental results that the polarity of the bed particles (as determined by probes A, B and C) was negative, whereas the polarity of the fines in the freeboard region (probe D) was positive. Bipolar charging is discussed in Chapter 5.

These experimental results are consistent with those reported by Yao et al. (2002) who investigated the effect of superficial gas velocity on electrostatic charge generation in a 0.089 m inner diameter and 1.2 m height three-dimensional Plexiglas fluidization column with mono-sized polyethylene resin particles of mean diameter 378 and 318 μm , using a collision ball probe. They found that the charge density of particles surrounding the bubble increased as the superficial gas velocity increased from 0.12 to 0.53 m/s.

3.2.2 Effect of Operating Pressure

3.2.2.1 Glass Beads

To investigate the effect of operating pressure on the electrostatic charge generated inside the fluidized bed, the entrainment flux and the charge density of entrained fine particles were determined in free-bubbling experiments with GBL as the mono-sized particles and GBF as the added fines (binary mixture M3, in Table 2.3). For physical properties of the particles, see Tables 2.1 and 2.2. These experiments were conducted in the same three-dimensional fluidization column with collision ball probes at four levels, a freeboard sampler, and a current detecting pipe (illustrated in Figures 2.4 to 2.6, respectively). The static bed height was again ~ 0.54 m in all cases. Temperature, superficial air velocity and air relative humidity

were maintained nearly constant (at $20 \pm 2^\circ\text{C}$, 0.3 m/s and $12 \pm 2\%$ respectively) to isolate the effect of operating pressure. The absolute pressure in the freeboard was varied from 207 to 517 kPa. To achieve steady state, the bed was fluidized for approximately one hour before data were collected,

The net cumulative charge generated in the bed, measured by the collision ball probes, is plotted versus time in Figure 3.16. The standard deviation of charge fluctuations measured by probe D in the freeboard region is presented in Figure 3.17 as a function of pressure after filtering the net cumulative charge curves using a high-pass filter with a cut-off frequency of 0.03 Hz. The charge density of the fine particles and current flow through the current detection pipe at the column exit due to direct charge transfer are plotted versus pressure in Figures 3.18 and 3.19, respectively. The entrainment flux is plotted versus operating freeboard pressure in Figure 3.20.

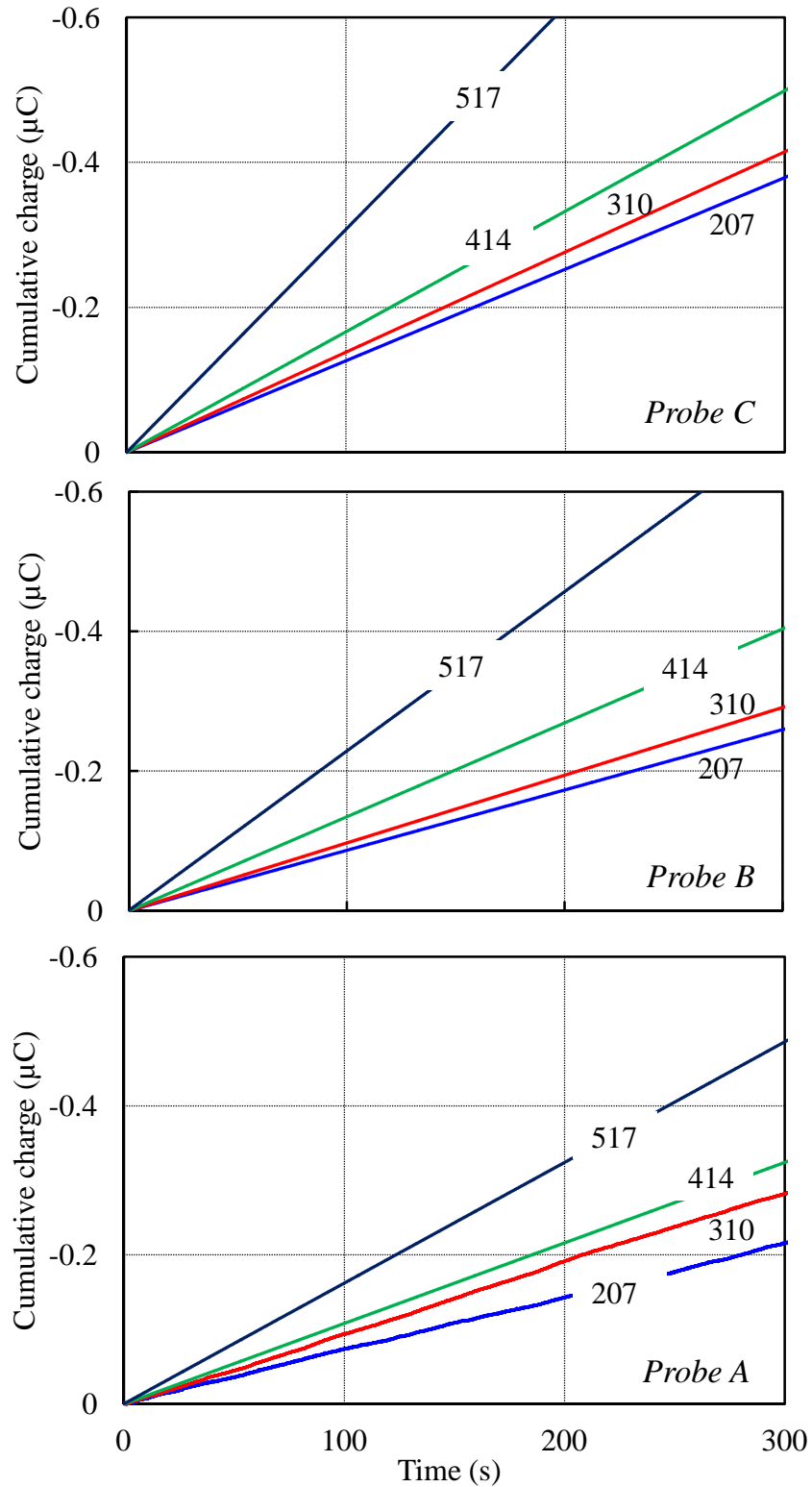


Figure 3.16 Effect of pressure on net cumulative charges as a function of time at different axial positions in bed containing mixture M3. $U_g = 0.3$ m/s, $T = 20 \pm 2^\circ\text{C}$, $RH = 12 \pm 2\%$. For physical properties of particles, see Tables 2.1, 2.2 and 2.3. Numbers on curves denote absolute pressure (in kPa). For probe positions, see Figure 2.4.

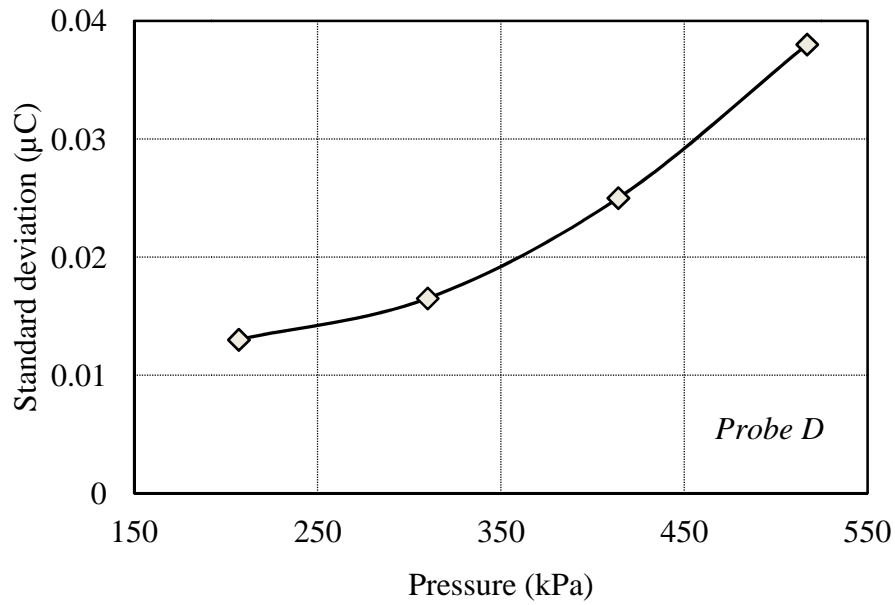


Figure 3.17 Standard deviation of charge fluctuations in freeboard as function of pressure for binary mixture M3. $U_g = 0.3$ m/s, $T = 20 \pm 2^\circ\text{C}$, $\text{RH} = 12 \pm 2\%$. For physical properties of particles, see Tables 2.1, 2.2 and 2.2. For position of probe D, see Figure 2.4.

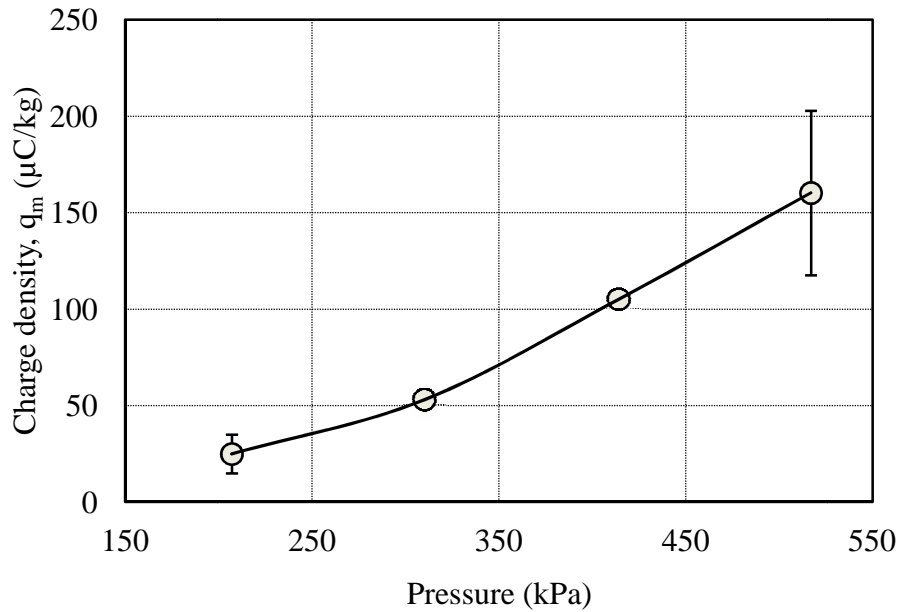


Figure 3.18 Effect of pressure on charge density of fines measured by freeboard sampler in binary mixture M3. $U_g = 0.3$ m/s, $T = 20 \pm 2^\circ\text{C}$, $\text{RH} = 12 \pm 2\%$. For physical properties of particles, see Tables 2.1, 2.2 and 2.3. For freeboard sampler details, see Figure 2.5. Error bars correspond to $\pm 90\%$ confidence intervals.

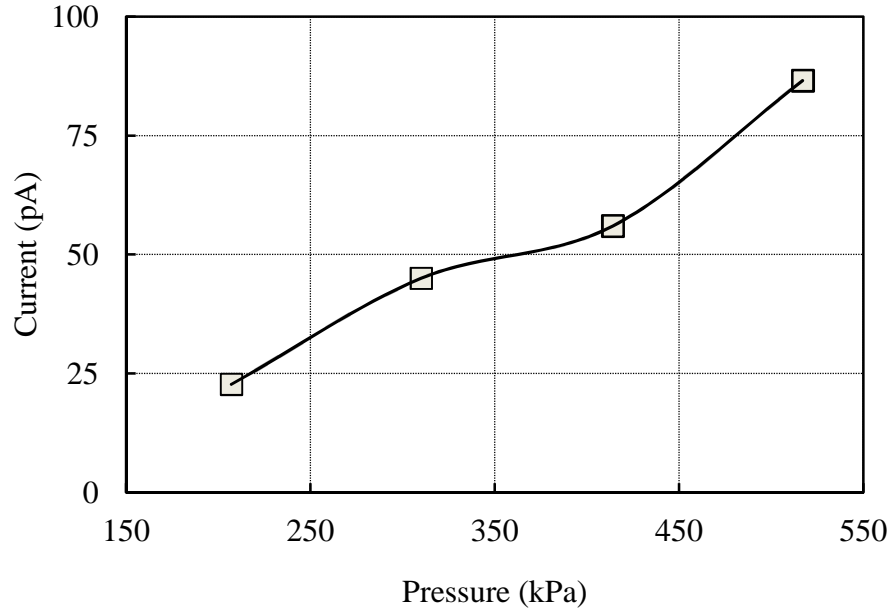


Figure 3.19 Current flow through current detection pipe at column exit in binary mixture M3 as function of pressure. $U_g = 0.3$ m/s, $T = 20 \pm 2^\circ\text{C}$, $\text{RH} = 12 \pm 2\%$. For physical properties of particles, see Tables 2.1, 2.2 and 2.3. For current detecting pipe details, see Figure 2.6.

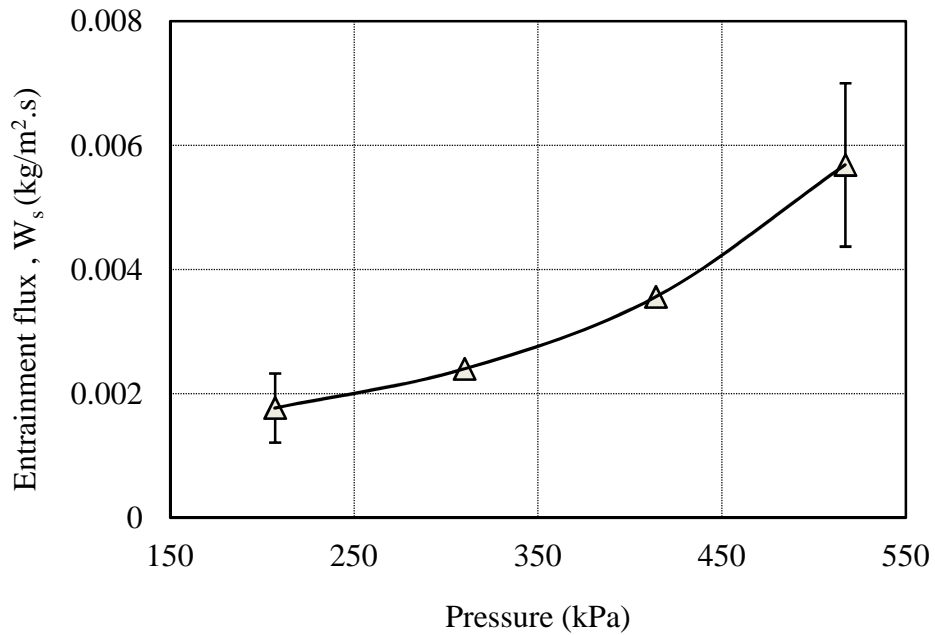


Figure 3.20 Entrainment flux measured for binary mixture M3 as function of pressure. $U_g = 0.3$ m/s, $T = 20 \pm 2^\circ\text{C}$, $\text{RH} = 12 \pm 2\%$. For physical properties of particles, see Tables 2.1, 2.2 and 2.3. Error bars correspond to $\pm 90\%$ confidence intervals.

The experimental results in Figure 3.16, show that the magnitude of the electrostatic charges measured in the bed at different heights by probes A, B and C for binary mixture M3 increased as the operating pressure increased. In the freeboard region, as shown in Figures 3.17 and 3.18, the experimental results indicate that the electrostatic charges on GBF fines in the freeboard measured by probe D and the freeboard sampler increased as the pressure increased. Figure 3.19 also shows that as the pressure increased, the current transfer through the current detection pipe at the column exit due to interaction between the GBF particles and the inner pipe surface increased.

Olowson and Almstedt (1990) and Olssen et al. (1995) investigated the effect of elevated pressure (up to 1600 kPa) on bubble behaviour. Their fluidization column, which contained silica sand (group B) particles, had a rectangular cross-sectional area of 0.2 m \times 0.3 m and a height of 2.2 m. They found that the rise velocity and mean bubble frequency increased as the operating pressure increased. Yao et al. (2002) studied the influence of bubble behaviour on electrostatic charges in a Plexiglas fluidization column of 0.089 m inner diameter containing polyethylene particles. They reported that the bubble behaviour influenced the electrostatic charge generation in a gas-solid fluidized bed. Based on these previously published results, the increase in electrostatic charges observed in our experiments as the pressure increased is probably related to increases in bubble frequency and rise velocity, which enhanced both the motion of particles surrounding bubbles and particle-particle collisions.

Our results are consistent with those of Moughrabiah et al. (2009) who investigated the effect of operating pressure (up to 724 kPa) on the degree of bed electrification in the same three-dimensional fluidization column containing glass beads (group B particles). Those experiments also showed that as the pressure increased, the degree of electrification in the bed increased. The authors attributed these results to increases in bubble rise velocity, bubble frequency and bubble volume fraction.

The effect of pressure on the solid entrainment flux is shown in Figure 3.20. The results indicate that the entrainment flux increased as the operating pressure increased. As noted previously with respect to the superficial gas velocity experiments, pressure affects both electrostatics and entrainment. In these experiments, the increase in entrainment flux was

probably due to increased bubble velocity and frequency as the pressure increased, which in turn led to a larger number of particles being ejected into the freeboard when bubbles erupted at the bed surface. In addition, upward drag forces exerted by the gas on the particles increase as pressure increases due to the greater gas density, which could also help to overcome adhesion forces between particles, and reduce agglomerates.

Our results in Figure 3.20 are consistent with those reported by Chan and Knowlton (1984) who studied the effect of pressure on the entrainment flux in a three-dimensional fluidization column (0.3 m inner diameter) containing sand particles (group A). They found that the entrainment rate increased as the pressure increased from 446 to 3202 kPa, and they attributed these results to the increase in gas density, and hence in upwards drag, as the pressure increased.

3.2.2.2. Polyethylene

Similar free-bubbling experiments were conducted utilizing coarse polyethylene (HDPE) and glass beads fines (GBF) as the mono-sized particles and added fines, respectively. The resulting binary mixture, M10, is detailed in Table 2.3, and individual particle properties are provided in Tables 2.1 and 2.2. The previously described three-dimensional fluidization column bed with collision ball probes (Figure 2.4), freeboard sampler (Figure 2.5), and current-detecting pipe (Figure 2.6) were again used to investigate the effects of pressure on the electrostatic charges generated inside the fluidized bed, and on the entrainment flux and charge density of entrained fine particles. Experimental conditions were also the same as in the previously described experiments, with the static bed height ~ 0.54 m in all experiments, and the temperature, superficial air velocity and air relative humidity maintained nearly constant at $20 \pm 2^\circ\text{C}$, $U_g = 0.3$ m/s and $12 \pm 2\%$, respectively, to isolate the effect of pressure which was varied from 207 to 517 kPa. As in the previous experiments, the bed was first fluidized for approximately an hour to achieve steady state before data were collected.

The net cumulative charge was then measured by the collision ball probes and plotted versus time, as shown in Figure 3.21. Figure 3.22 shows the standard deviation of charge fluctuations measured by probe D in the freeboard region versus pressure, after filtering the

net cumulative charge curves using a high-pass filter with a cut-off frequency of 0.03 Hz. The fine particle charge density and current flow through the current-detecting pipe at the column exit due to direct charge transfer are plotted in Figures 3.23 and 3.24, respectively, as a function of pressure. Entrainment flux is plotted against operating pressure in Figure 3.25.

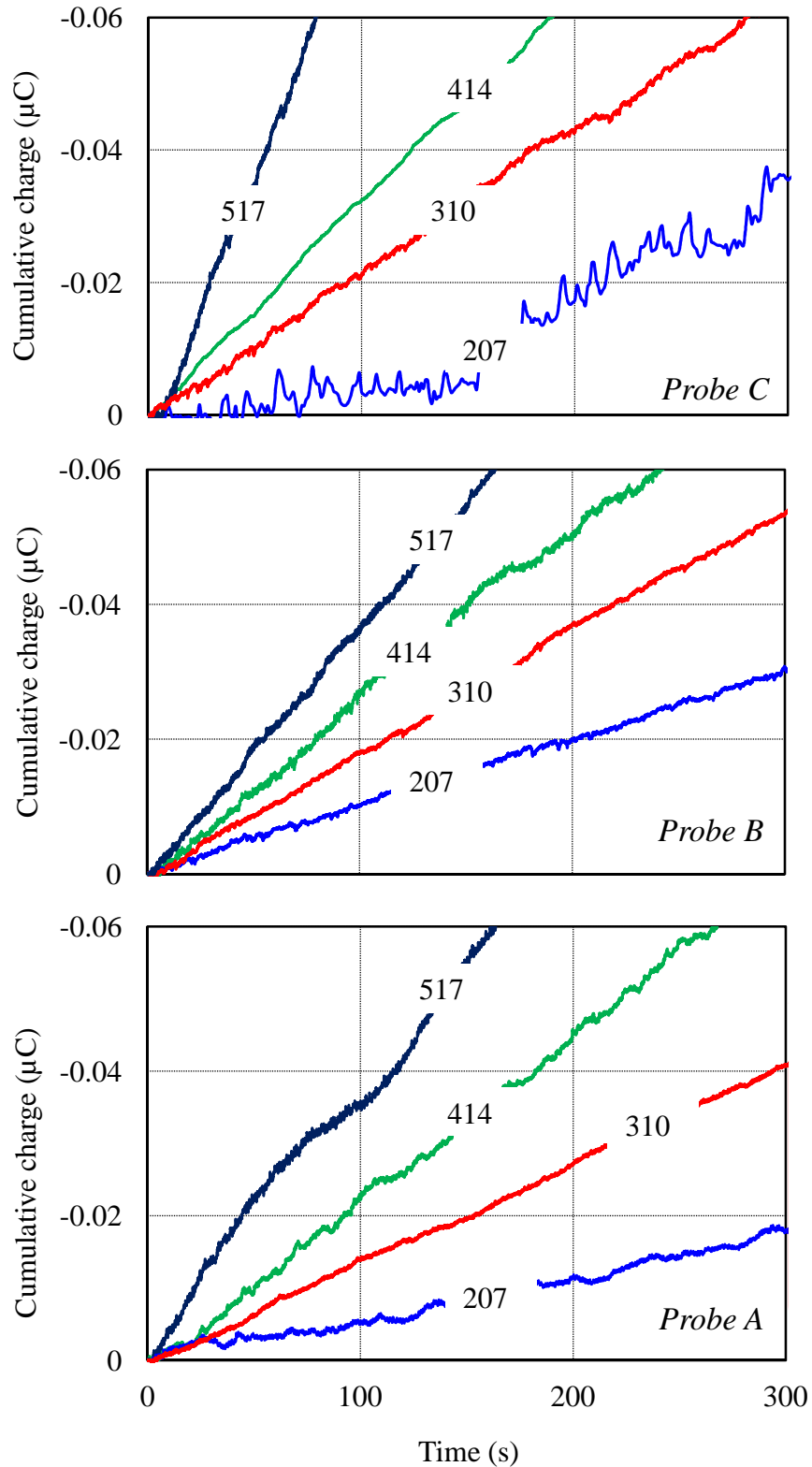


Figure 3.21 Effect of pressure on net cumulative charges as function of time at different axial positions in a bed of binary mixture M10. $U_g = 0.3$ m/s, $T = 20 \pm 2^\circ\text{C}$, $\text{RH} = 12 \pm 2\%$. For physical properties of particles, see Tables 2.1, 2.2 and 2.3. Numbers on curves denote absolute pressure (in kPa). For probe positions, see Figure 2.4.

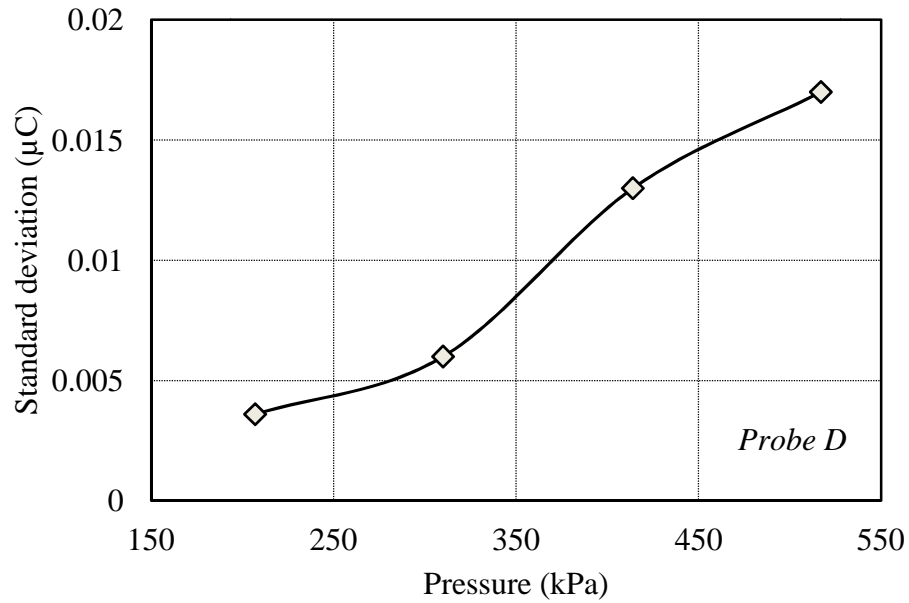


Figure 3.22 Standard deviation of charge fluctuations in freeboard as function of pressure for binary mixture M10. $U_g = 0.3 \text{ m/s}$, $T = 20 \pm 2^\circ\text{C}$, $\text{RH} = 12 \pm 2\%$. For physical properties of particles, see Tables 2.1, 2.2 and 2.2. For position of probe D, see Figure 2.4.

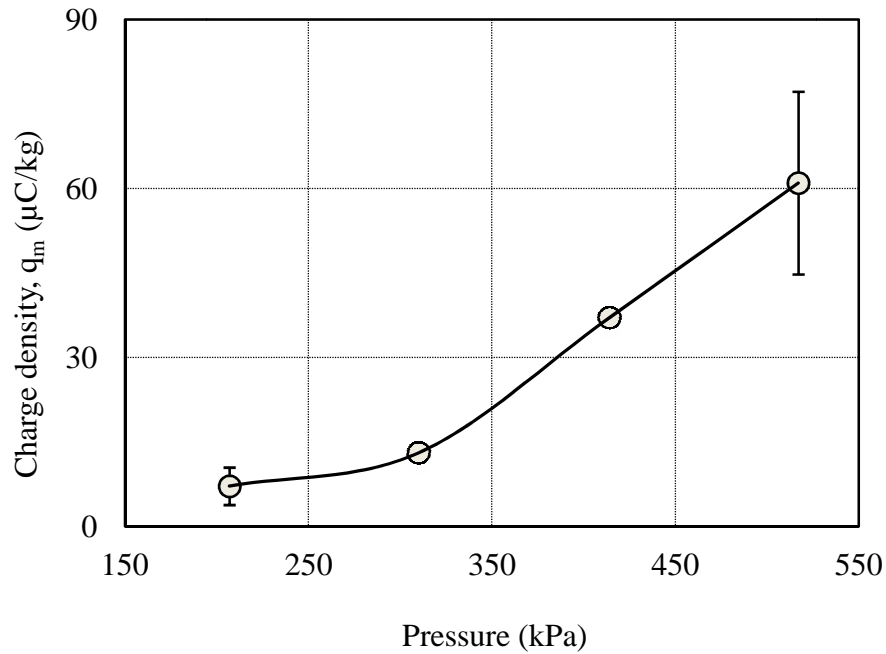


Figure 3.23 Effect of pressure on charge density of fines measured by freeboard sampler in binary mixture M10. $U_g = 0.3 \text{ m/s}$, $T = 20 \pm 2^\circ\text{C}$, $\text{RH} = 12 \pm 2\%$. For physical properties of particles, see Tables 2.1, 2.2 and 2.3. For freeboard sampler details, see Figure 2.5. Error bars correspond to $\pm 90\%$ confidence intervals.

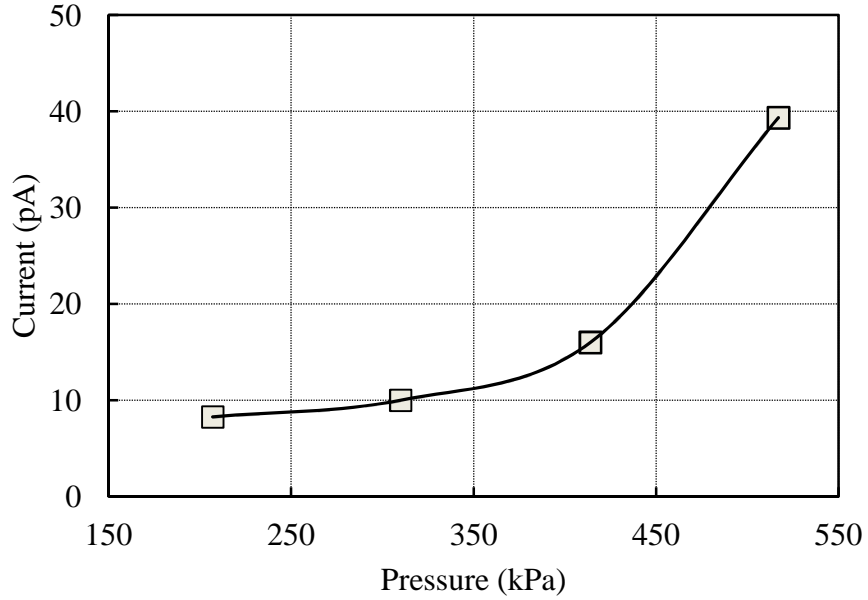


Figure 3.24 Current flow through current detection pipe at column exit in binary mixture M10 as function of pressure. $U_g = 0.3$ m/s, $T = 20 \pm 2^\circ\text{C}$, $\text{RH} = 12 \pm 2\%$. For physical properties of particles, see Tables 2.1, 2.2 and 2.3. For current detecting pipe details, see Figure 2.6.

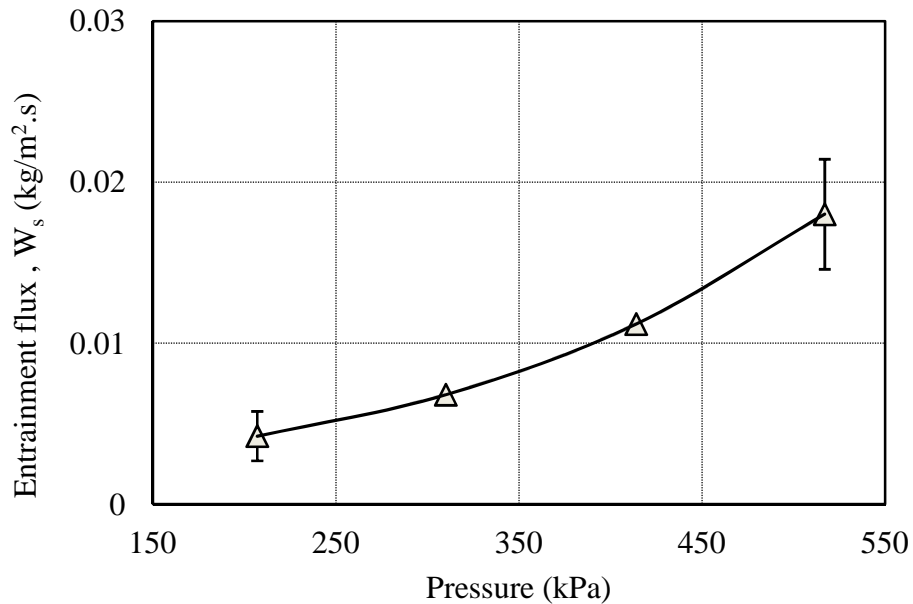


Figure 3.25 Entrainment flux measured for binary mixture M10 as function of pressure. $U_g = 0.3$ m/s, $T = 20 \pm 2^\circ\text{C}$, $\text{RH} = 12 \pm 2\%$. For physical properties of particles, see Tables 2.1, 2.2 and 2.3. Error bars correspond to $\pm 90\%$ confidence intervals.

The results plotted in Figures 3.21–3.25 show that for binary mixture M10, the magnitude of electrostatic charges in the bed and in the freeboard region, as well as the entrainment flux, all increased as the bed operating pressure increased. This is probably for the same reasons as discussed above, i.e., the increase in electrostatic charge and entrainment flux can be attributed to the effects of increasing pressure on bubble behaviour and drag.

Moughrabiah et al. (2009) investigated the effect of pressure on electrostatic charge generation in the same three-dimensional fluidization column (inner diameter 0.15 m; height, 2 m) as in the present study, with mono-sized polyethylene resin particles (mean diameter 450 μm). They used a Faraday cup to measure the charge density of the bed particles at elevated pressures and found that the magnitude of the charge density of particles increased almost linearly as the pressure increased from 101 to 724 kPa.

3.2.3 Effect of Operating Temperature

3.2.3.1. Glass Beads

To investigate the effect of temperature on the electrostatic charges generated inside the fluidized bed, entrainment flux and charge density of entrained fine particles, freely bubbling experiments were conducted in the same three-dimensional elevated-pressure column with collision ball probes at four heights, as shown in Figure 2.9. The fines charge density in the freeboard and the current at the column exit were measured by the freeboard sampler and a current detecting pipe, as illustrated in Figures 2.4 to 2.6. The mono-sized particles were GBL, whereas the added fines for the binary mixture were GBF (M3, in Table 2.3). For physical properties, see Tables 2.1 and 2.2. The static bed height was again ~ 0.54 m in all cases. The superficial gas velocity (U_g) and pressure were maintained nearly constant at 0.3 m/s and 414 kPa, respectively, to isolate the effect of bed temperature. In these experiments, it was difficult to control the air relative humidity within a narrow range as the temperature varied; consequently, the relative humidity of the fluidizing air was in the range of $12\pm 6\%$.

The bed temperature was controlled by electrical heating tapes coiled around the feed line. Three temperature ranges were investigated: 20–25, 50–55 and 70–75°C. In each of these

experiments, the bed temperature was raised over ~ 1.5 h until the desired temperature range was achieved. Then the bed was fluidized for ~1 h to achieve steady state before collecting and recording data.

The net cumulative charge measured by the collision ball probes is plotted versus time in Figure 3.26. Figure 3.27 plots the standard deviation of charge fluctuations measured by probe D in the freeboard region versus bed temperature, after filtering the net cumulative charge curves using a high-pass filter with a cut-off frequency of 0.03 Hz. The particle charge density and current flow through the current-detecting pipe at the column exit due to direct charge transfer are presented as a function of bed temperature in Figures 3.28 and 3.29, respectively. The entrainment flux of the fine particles in the M3 binary mixture is plotted against bed temperature in Figure 3.30.

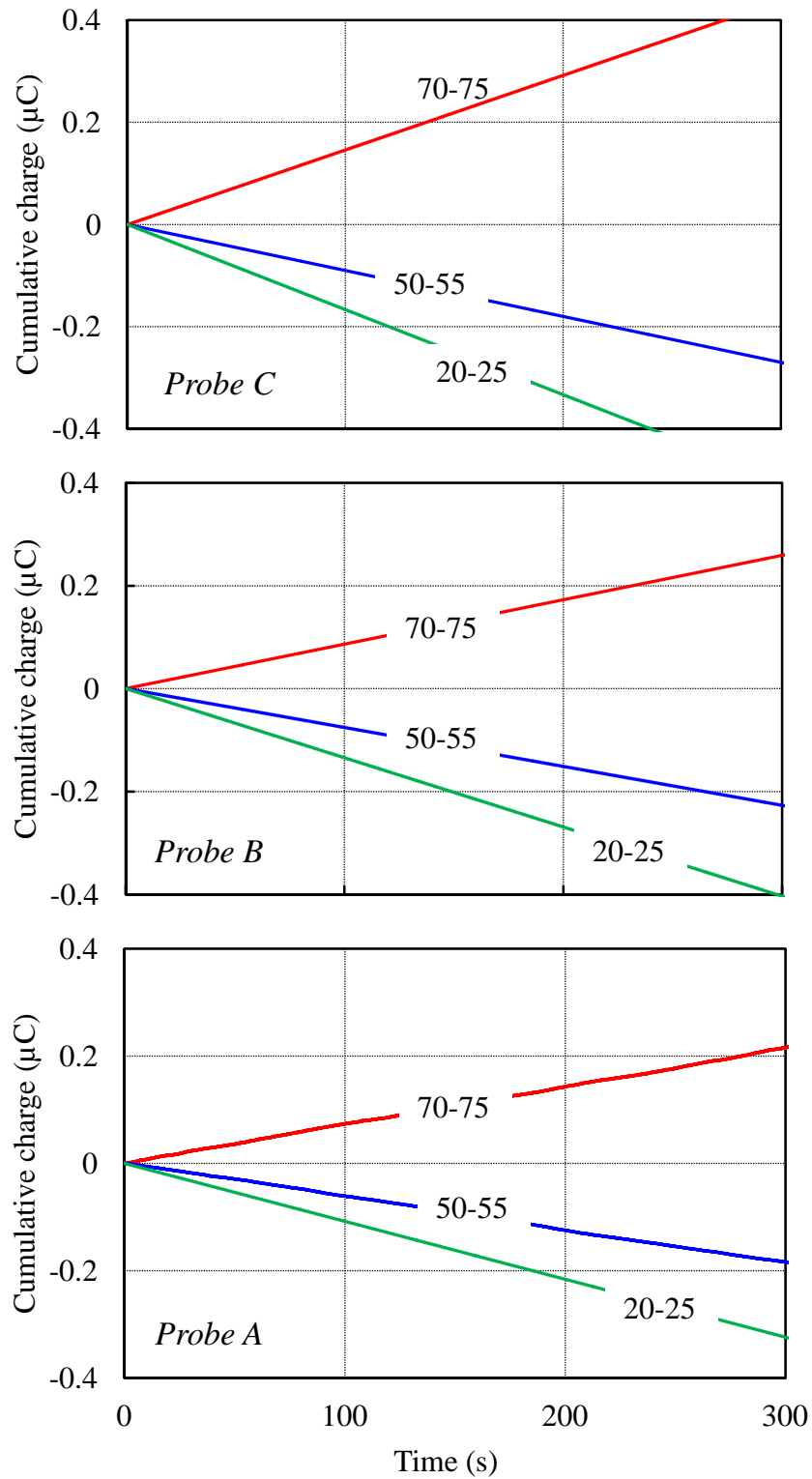


Figure 3.26 Effect of temperature on net cumulative charges as function of time at different axial positions in bed of binary mixture M3. $U_g = 0.3$ m/s, $P = 414$ kPa, $RH = 12 \pm 6\%$. For physical properties of particles, see Tables 2.1, 2.2 and 2.3. Numbers on curves denote bed temperature (in °C). For probe positions, see Figure 2.4.

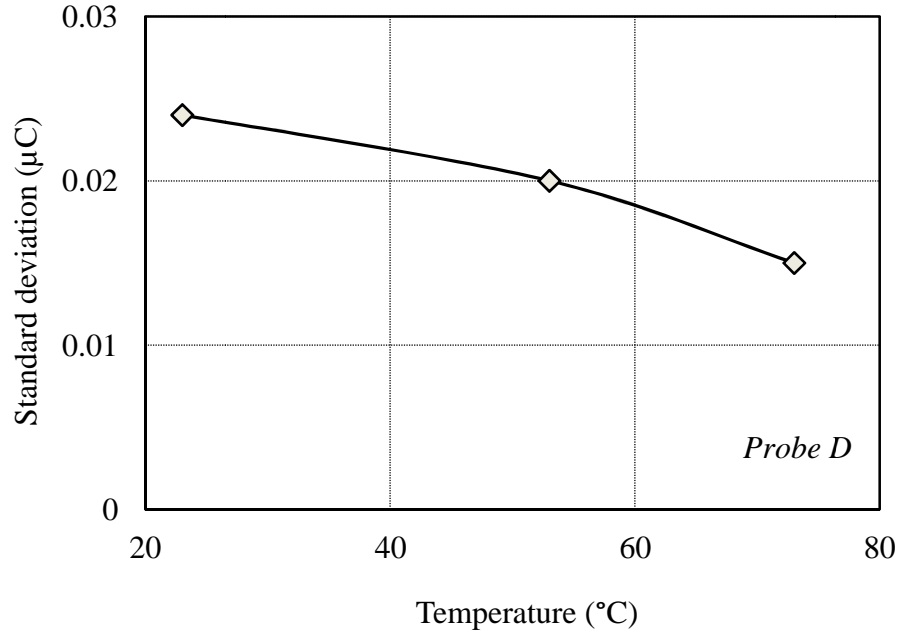


Figure 3.27 Standard deviation of charge fluctuations in freeboard as function of bed temperature for binary mixture M3. $U_g = 0.3$ m/s, $P = 414$ kPa, $RH = 12 \pm 6\%$. For physical properties of particles, see Tables 2.1, 2.2 and 2.2. For position of probe D, see Figure 2.4.

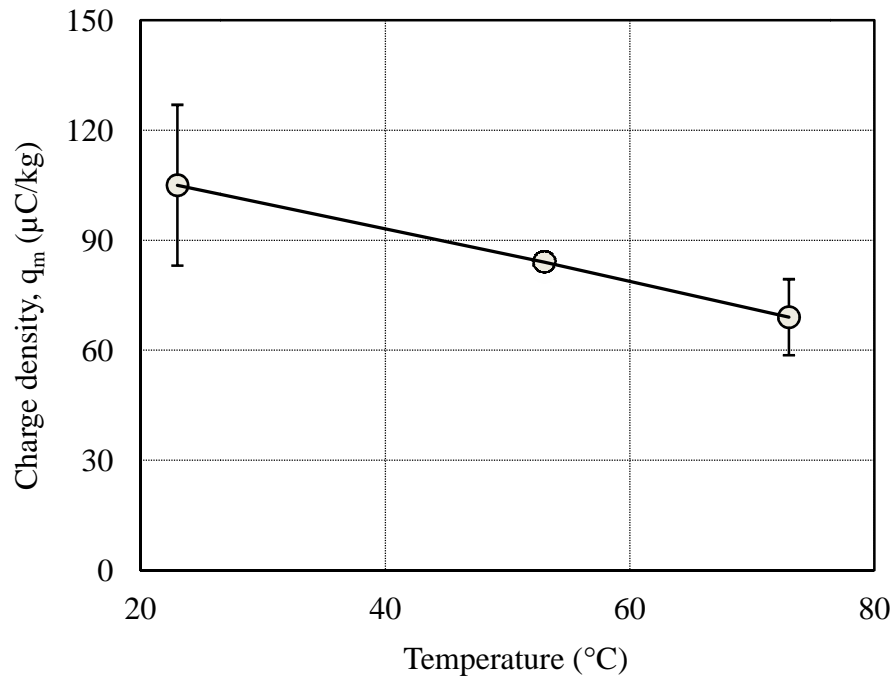


Figure 3.28 Effect of bed temperature on charge density of fines measured by freeboard sampler in binary mixture M3. $U_g = 0.3$ m/s, $P = 414$ kPa, $RH = 12 \pm 6\%$. For physical properties of particles, see Tables 2.1, 2.2 and 2.3. For freeboard sampler details, see Figure 2.5. Error bars correspond to $\pm 90\%$ confidence intervals.

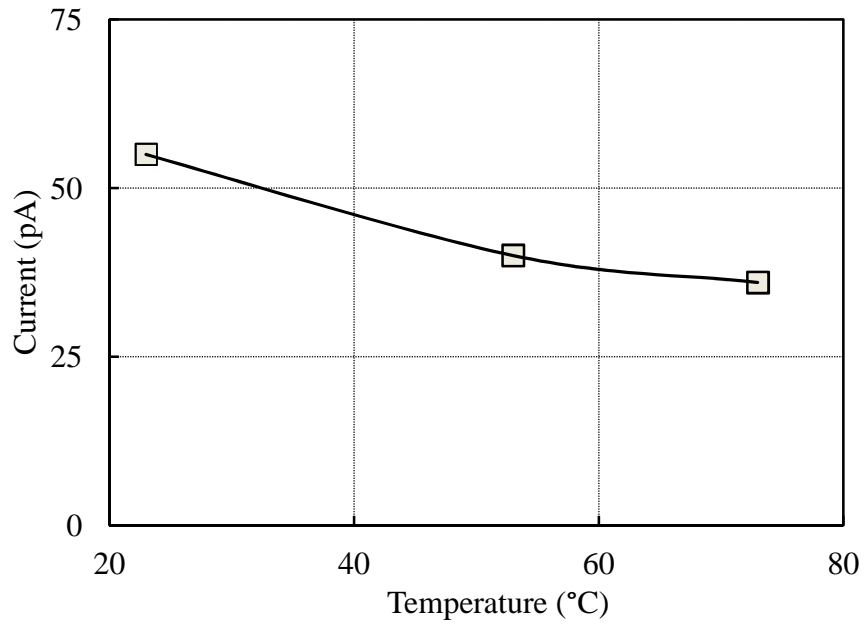


Figure 3.29 Current flow through current detection pipe at column exit in binary mixture M3 as function of bed temperature. $U_g = 0.3$ m/s, $P = 414$ kPa, $RH = 12 \pm 6\%$. For physical properties of particles, see Tables 2.1, 2.2 and 2.3. For current-detecting pipe details, see Figure 2.6.

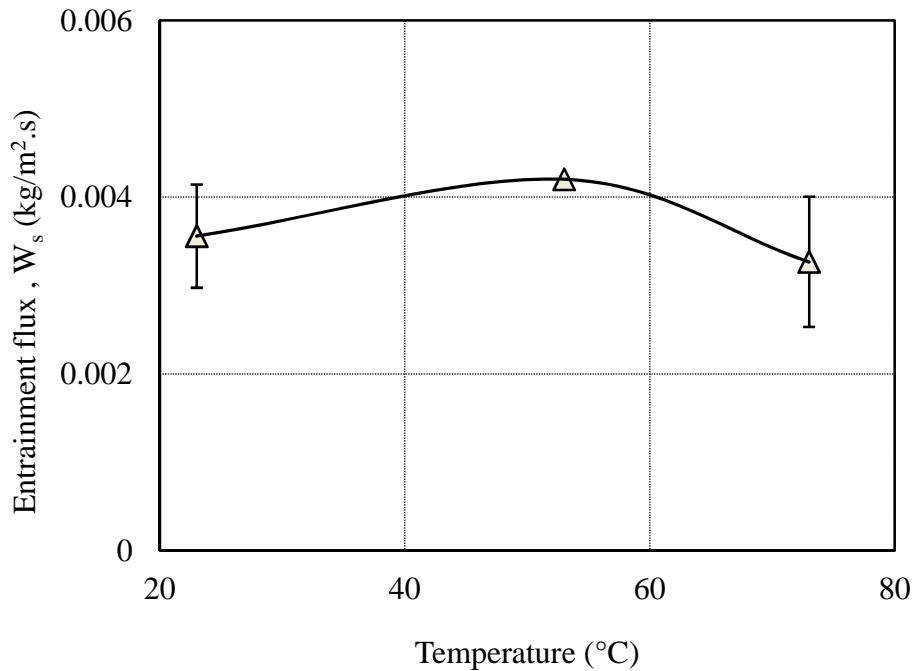


Figure 3.30 Entrainment flux for binary mixture M3 as function of bed temperature. $U_g = 0.3$ m/s, $P = 414$ kPa, $RH = 12 \pm 6\%$. For physical properties of particles, see Tables 2.1, 2.2 and 2.3. Error bars correspond to $\pm 90\%$ confidence intervals.

The experimental results presented in Figure 3.26 show that the magnitude of the accumulation of electrostatic charges measured in the dense fluidized bed at different heights by probes A, B and C for binary mixture M3 decreased slightly as the bed temperature increased. In addition, Figures 3.27 and 3.28 indicate that mean charges and standard deviation of charges of fines in the freeboard measured by both probe D and the freeboard sampler decreased slightly as the temperature increased. Figure 3.29 shows that the current flow through the current-detection pipe at the column exit for binary mixture M3 decreased as the bed temperature increased. This decrease in electrostatics is probably related to the increase in particle electrical conductivity as the temperature increased, enhancing the dissipation rate of electrostatic charge inside the fluidized bed. Jain and Saxena (2009) studied the influence of temperature on the electrical conductivity of glass and found that the electrical conductivity increased as the temperature increased from 27 to 77°C. Similar results were reported by Boggs et al. (2001) who investigated the effect of temperature on the electrical conductivity of polymer material and reported that the conductivity increased as the temperature increased from 20 to 90°C. In our experiments it seems that the increase in temperature over the limited range explored had little or no effect on bubble behaviour, and hence on electrostatics. The effect of temperature on the bubble behaviour has not been investigated extensively, with the available results in the literature indicating that bubble size and frequency are not very sensitive to varying temperature (as long as particles do not become sticky). Wittman et al. (1981) found that bubble size in a fluidization column of 0.19 m inner diameter was not affected when the bed temperature was increased from 50 to 195°C. Similar results reported by Sishtla et al. (1986) indicated that bubble size, frequency and velocity were not appreciably influenced when the temperature increased to 982°C.

Moughrabiah et al. (2009) investigated the influence of temperature (up to 90°C) on the degree of electrification inside the same three-dimensional fluidization column. They conducted freely bubbling experiments with glass beads particles (mean diameter, 693 µm). They found that, as the bed temperature increased, the bed exhibited smoother fluidization, while the magnitude of electrostatic charges in the bed decreased.

In our study, as shown in Figure 3.26, the bed particles were charged negatively at all levels (probe A, B and C), except for the polarity measured in the bed temperature range of

70–75°C, which switched to positive polarity. This switch was probably due to changes in the electrical properties of the particles and the column wall as the bed temperature increased. Varying the temperature of contact surfaces could lead to changes in the charging mechanisms of bed particles. These results are consistent with those reported by Zimmer (1970) who investigated the effect of temperature on the charge polarity of polymers when they were rubbed against a metal. He found that the polymer charge polarity was sensitive to temperature when the temperature increased from 90 to 180 °C. Similar results were reported by Moughrabiah (2009) who found that the charge polarity of glass beads particles inside a fluidized bed changed from negative to positive as the bed temperature increased beyond 45°C. On the other hand, as shown in Figure 3.28, no change in the charge polarity of fine particles was observed as the bed temperature increased. This could be because the temperature in the freeboard region was lower than in the bed, so that the bed particles were at higher temperatures than the fine particles. In addition, the fine particles cooled down as they travelled through the freeboard and recycle loop where the temperature was close to the ambient temperature.

The influence of bed temperature on the solid entrainment flux is portrayed in Figure 3.30. Experimental procedures described in Section 2.5 were followed to measure the entrainment flux. The experimental results show that the bed temperature had little effect on the entrainment flux over the limited temperature range of 20 to 75°C. Although there was a reduction in the charge density of fines as the bed temperature increased (Figure 3.28), which might help reduce agglomeration and increase the entrainment flux, the results indicate that entrainment flux was insensitive to temperature over the limited range examined. These results are consistent with those reported by George and Grace (1981) who found that temperature had negligible effect on the entrainment flux of silica sand in a pilot-scale column of 0.254 m × 0.432 m rectangular cross-section, over a temperature range of 27 to 172°C. Knowlton et al. (1990) studied the effect of temperature on entrainment of group B particles in a pressurized fluidization column of 0.2 m inner diameter. They reported that, at constant gas velocity, the particle entrainment rate increased as the bed temperature increased from 27 to 760°C, and they attributed their results to the decrease in particle terminal velocity as gas viscosity increased with increasing temperature. Choi et al. (1989) investigated the effect of bed temperature on the entrainment rate of sand particles in a

combustor of 0.3 m × 0.3 m cross-section and height 1.7 m. They reported that the entrainment rate decreased as the temperature increased from 700 to 900 °C and attributed these results to a reduction in gas density. The effect of temperature on entrainment is therefore complex. In our experiments, temperature had very little effect on entrainment, probably due to the counteractive effects of the increase in gas viscosity and the decrease in gas density as the temperature increased. With these counteracting dependencies, the effect of the temperature on the terminal velocity of fine particles was negligible for the limited temperature range tested in our experiments.

3.2.3.2. Polyethylene

To investigate the effect of bed temperature on different materials, free-bubbling experiments were also conducted on the binary combination of coarse polyethylene (HDPE) and glass beads fines (GBF) as the mono-sized coarse particles and added fines, respectively. The resulting binary mixture, M10, is detailed in Table 2.3, with individual particle properties are listed in Tables 2.1 and 2.2. The previously described three-dimensional fluidization column with collision ball probes (Figure 2.4), freeboard sampler (Figure 2.5), and current-detecting pipe (Figure 2.6) were again used to investigate the effect of pressure on the electrostatic charges generated inside the fluidized bed as well as the entrainment flux and charge density of entrained fine particles. Experimental conditions were the same as in the previously described experiments, i.e. the static bed height was ~0.54 m in all cases, and the pressure, superficial air velocity and air relative humidity were maintained at 414 kPa, $U_g = 0.3$ m/s and 12±6% respectively to isolate the effect of bed temperature, which was set at 20 and 50°C. The bed was fluidized for approximately for 2 h to stabilize the temperature and then for an additional 1 h to achieve steady state before data were collected.

The net cumulative charge was then measured by the collision ball probes and plotted versus time, as shown in Figure 3.31. Figure 3.32 shows the standard deviation of charge fluctuations measured by probe D in the freeboard region versus bed temperature after filtering the net cumulative charge curves using a high-pass filter with a cut-off frequency of 0.03 Hz. The fine particle charge density and current flow through the current-detecting pipe at the column exit due to direct charge transfer are plotted versus bed temperature in Figures 3.33 and 3.34, respectively. The entrainment flux is plotted against bed temperature in Figure 3.35.

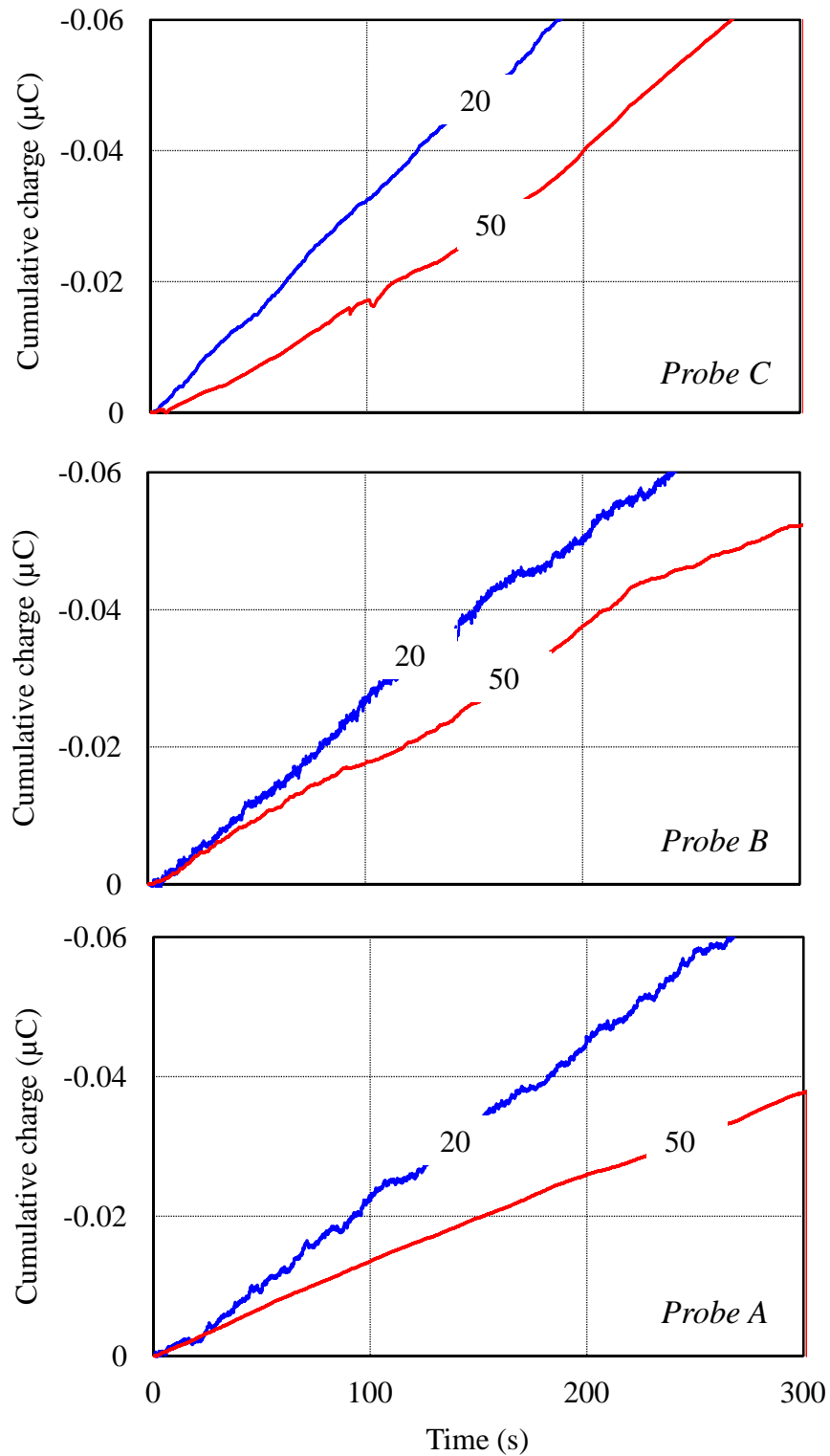


Figure 3.31 Effect of bed temperature on net cumulative charges as function of time at different axial positions in binary mixture M10. $U_g = 0.3$ m/s, $P = 414$ kPa, $RH = 12 \pm 6\%$. For physical properties of particles, see Tables 2.1, 2.2 and 2.3. Numbers on curves denote bed temperature (in °C). For probe positions, see Figure 2.4.

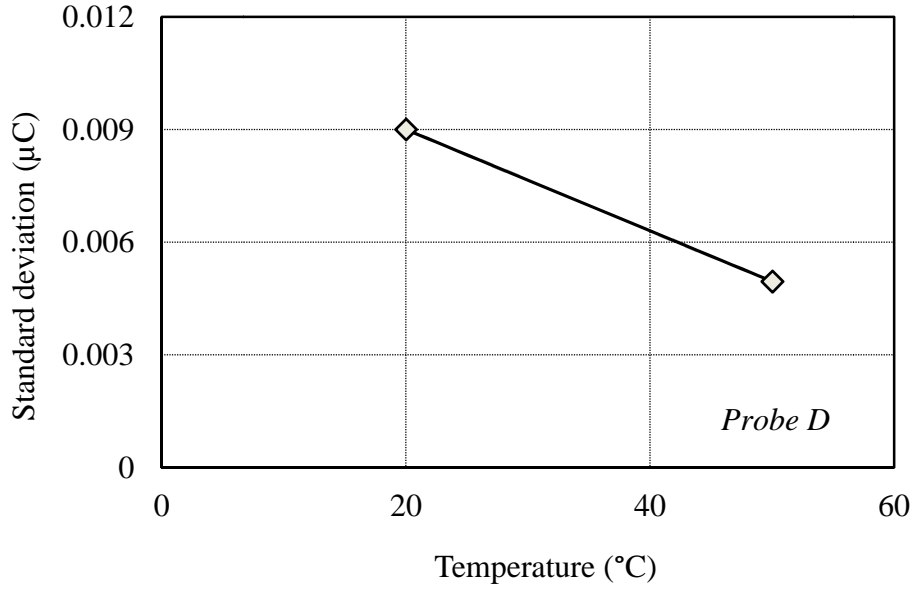


Figure 3.32 Standard deviation of charge fluctuations in freeboard as function of bed temperature for binary mixture M10. $U_g = 0.3$ m/s, $P = 414$ kPa, $RH = 12 \pm 6\%$. For physical properties of particles, see Tables 2.1, 2.2 and 2.2. For position of probe D, see Figure 2.4.

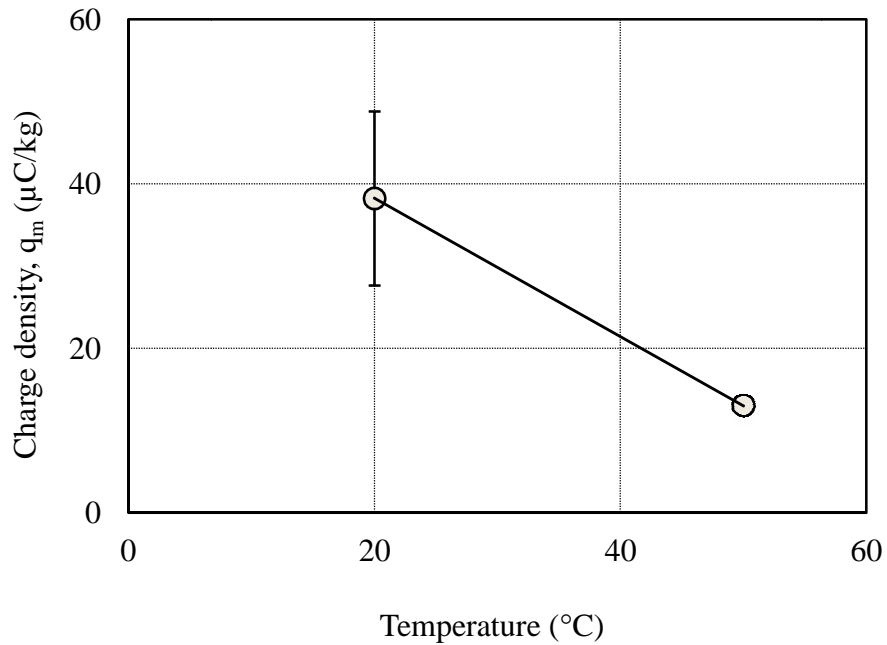


Figure 3.33 Effect of bed temperature on charge density of fines measured by freeboard sampler in binary mixture M10. $U_g = 0.3$ m/s, $P = 414$ kPa, $RH = 12 \pm 6\%$. For physical properties of particles, see Tables 2.1, 2.2 and 2.3. For freeboard sampler details, see Figure 2.5. Error bar corresponds to $\pm 90\%$ confidence interval.

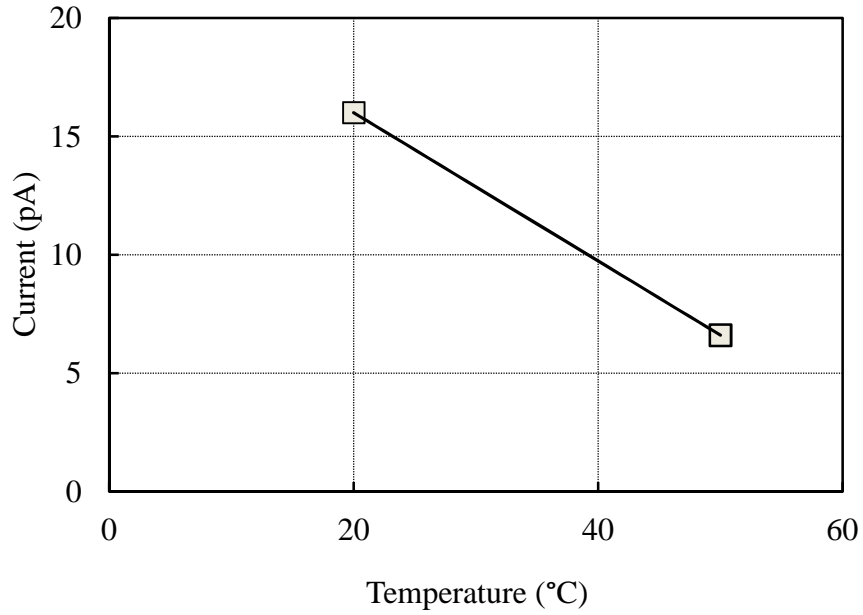


Figure 3.34 Current flow through current detection pipe at column exit in binary mixture M10 as function of bed temperature. $U_g = 0.3$ m/s, $P = 414$ kPa, $RH = 12 \pm 6\%$. For physical properties of particles, see Tables 2.1, 2.2 and 2.3. For current-detection pipe details, see Figure 2.6.

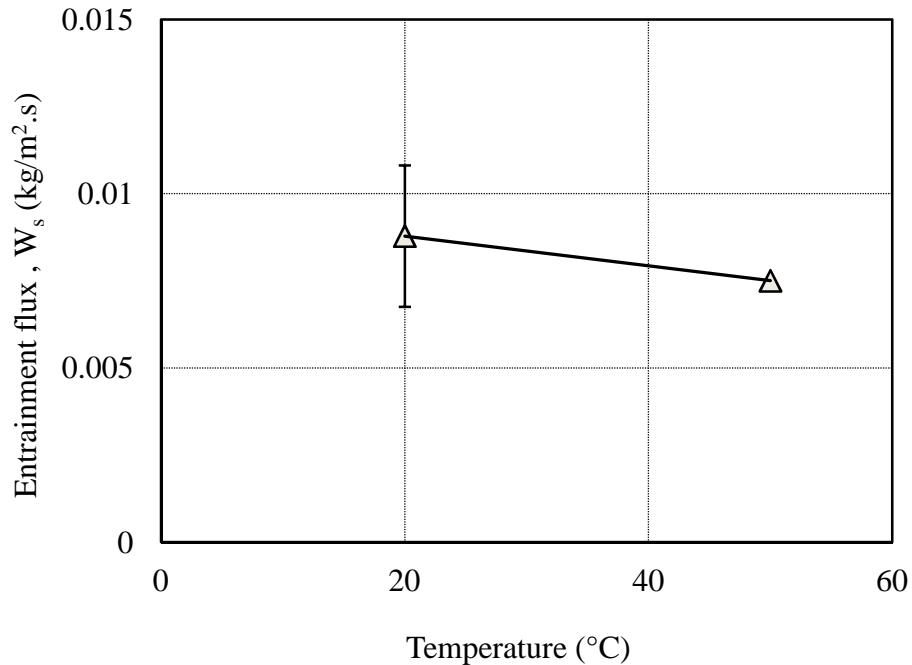


Figure 3.35 Entrainment flux for binary mixture M10 as function of bed temperature. $U_g = 0.3$ m/s, $P = 414$ kPa, $RH = 12 \pm 6\%$. For physical properties of particles, see Tables 2.1, 2.2 and 2.3. Error bar corresponds to $\pm 90\%$ confidence interval.

The experimental results in Figures 3.31 to 3.34 again show that for a binary mixture (M10), magnitude of electrostatic charges in the bed and freeboard region decreased as the bed temperature increased from 20 to 50°C, whereas temperature had very little effect on the entrainment flux (see Figure 3.35.) The decrease in electrostatic charge inside the fluidized bed is probably for the same reasons as discussed in section 3.2.3.1 These results are also consistent with those reported by Moughrabiah et al. (2009) who studied the effect of bed temperature (up to 60°C) on electrostatic charges generated inside the same fluidization column as in this project with polyethylene particles (mean diameter, 642 μm), reporting that the degree of bed electrification decreased as the bed temperature increased.

In our experiments with polyethylene as bed particles, no change in polarity of the bed (probe A, B and C) was observed. The polarity of fine particles in the freeboard region (Figures 3.31 and 3.33) was again positive, the same as observed previously in the glass bead experiments. The relationship between particle entrainment and electrostatic forces over the range of operating variables for different mixtures are discussed in Chapter 6.

3.3 Summary

In this chapter, the effects of superficial gas velocity, operating pressure and bed temperature on electrostatic charges in the bed and freeboard region, and on entrainment flux were investigated in the bubbling bed flow regime. The experiments with glass beads and polyethylene particles (mixtures M3 and M10) showed that as the superficial gas velocity or operating pressure increased, both the magnitude of electrostatic charge inside the fluidized bed and entrainment flux increased, probably due to increases in bubble velocity, frequency and upward drag forces exerted on the particles. It is clear from these experimental results, as well as earlier work in the literature, that both entrainment and electrostatics are greatly affected by the bed hydrodynamics. Free-bubbling experiments with glass beads (M3 mixture) showed that electrostatic charges decreased and the charge polarity reversed as the bed temperature increased, whereas temperature had negligible effect on the entrainment flux over the limited temperature ranges studied. In all experiments, the polarity of fines in the freeboard was to be opposite to that in the bed, indicating that entrained fine particles carry charges, leaving behind a net charge of opposite polarity inside the bed.

Chapter 4: Results and Discussion: Effect of Gas Properties

4.1 Humidification

Increasing gas humidity is one of the common techniques used to prevent or reduce electrostatic charges in gas-solids fluidized beds. The influence of gas relative humidity on electrostatic charges inside fluidized beds has been investigated previously (Ciborowski and Wlodarski, 1962; Boland and Geldart, 1972; Tardos and Pfeffer, 1980; Wolny et al., 1989; Guardiola et al., 1996; Park et al., 2002; Mehrani, 2005; Moughrabiah et al., 2009; Mehrani and Giffin, 2013). The authors have reported that increasing the gas relative humidity (RH) reduces electrostatic effects in gas-solid fluidized beds attributing this result to the increase in the solids' surface conductivity and higher charge dissipation rates. Park et al. (2002) investigated the influence of fluidizing air RH over a wide range (from 6 to 98%) on the degree of bed electrification. They reported that a relative humidity higher than 60% dissipated the bed charges sufficiently to prevent charge accumulation in gas-solids fluidized beds.

Mehrani et al. (2007) investigated the influence of fluidizing gas relative humidity on the charge density (charge-to mass ratio) of fine glass beads. They concluded that, as the gas RH increased, the fines charge density decreased. Moughrabiah et al. (2009) studied the effect of air relative humidity over a range of 5 to 30% on the degree of bed electrification in a three-dimensional fluidized bed. They found that as the relative humidity decreased the accumulation of electrostatic charges increased.

A number of researchers (Geldart and Wong, 1985; Baron et al., 1987; Briens et al., 1992; Kato and Li, 2001; Mehrani and Giffin, 2013) have investigated the effect of gas relative humidity on particle entrainment. Baron et al. (1987) investigated the effect of gas relative humidity on the entrainment of silica sand particles from a bubbling fluidized bed. They concluded that the entrainment rate decreased by 45% when the gas relative humidity was reduced from 30 to 10%, and they attributed this to an increase in pressure drop in the freeboard due to electrostatic forces generated from interactions between particles and the column wall. Kato and Li (2001) studied the effect of gas relative humidity on elutriation of alumina fine particles from a gas-solids fluidized bed. They found that as the gas relative

humidity increased from 0 to 32%, the elutriation rate increased and attributed this to the influence of electrostatic forces. On the other hand, Mehrani and Giffin (2013) reported that humidity had no clear effect on the entrainment of polyethylene particles from a bubbling fluidized bed.

4.2 Effect of Gas Relative Humidity

4.2.1 Fines Material: Glass beads

Free-bubbling experiments were conducted in the three-dimensional fluidized bed column, described in Chapter 2, with collision ball probes at four levels, as shown in Figure 2.4, a freeboard sampler as shown in Figure 2.5, and a current detecting pipe, as shown in Figure 2.6, to investigate the effect of fluidizing gas relative humidity on electrostatic charges inside the fluidized bed, entrainment flux (W_s) and charge density (q_m) of entrained fine particles. Experiments were conducted utilizing relatively large glass beads (GBL) as the mono-sized particles with GBF as added fines for the binary mixture (M3, in Table 2.3). For particle physical properties, see Tables 2.1 and 2.2. The static bed height was ~ 0.54 m in all cases. The temperature, pressure and superficial air velocity were maintained nearly constant at $20 \pm 2^\circ\text{C}$, 414 kPa and $U_g = 0.3$ m/s, respectively, to isolate the effect of gas relative humidity. The relative humidity of the fluidizing air was varied from 3 to 38% by passing the air through a compressor refrigerator dryer and a silica gel dryer upstream of the fluidized bed column.

In each experiment, the bed was first fluidized for approximately an hour to achieve steady state before the data were collected. The net cumulative charge generated inside the bed was then measured by the three collision ball probes during fluidization and plotted versus time, as in Figure 4.1. Figure 4.2 also shows the standard deviation of charge fluctuations registered by probe D in the freeboard region as a function of relative humidity after filtering the net cumulative charge curves using a high-pass filter of cut-off frequency of 0.03 Hz. The charge density of the fine glass bead particles sampled is plotted versus air relative humidity in Figure 4.3. Figure 4.4 shows the effect of air relative humidity on the current flow through the detection pipe due to direct charge transfer. The influence of relative humidity on the solid entrainment flux is shown in Figure 4.5.

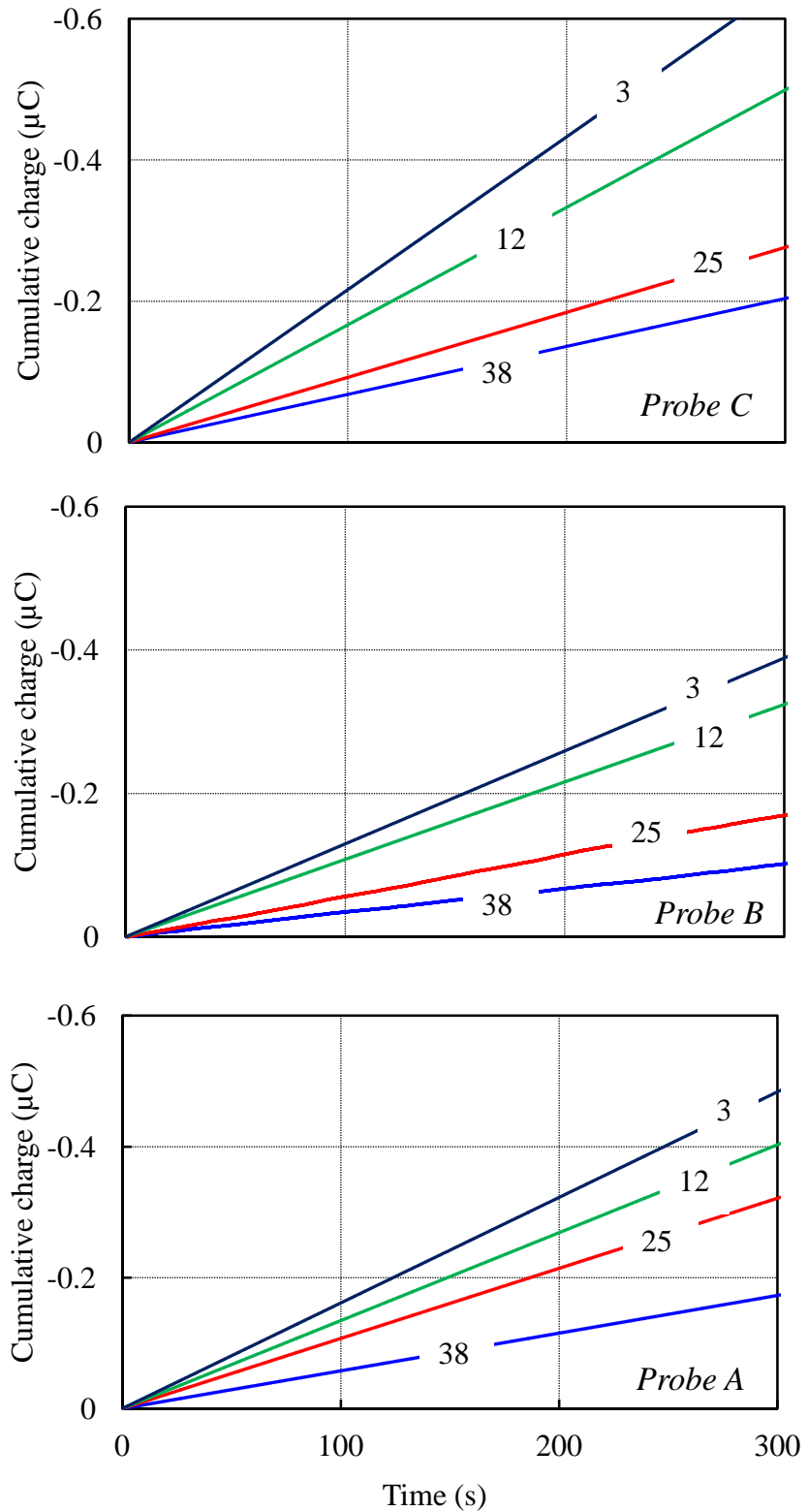


Figure 4.1 Effect of relative humidity of fluidizing air on net cumulative charges as a function of time at different axial positions in a bed of binary mixture M3. For physical properties of particles, see Tables 2.1, 2.2 and 2.3. $P = 414 \text{ kPa}$, $T = 20 \pm 2^\circ\text{C}$, and $U_g = 0.3 \text{ m/s}$. Numbers on curves denote % RH. For probe positions, see Figure 2.4.

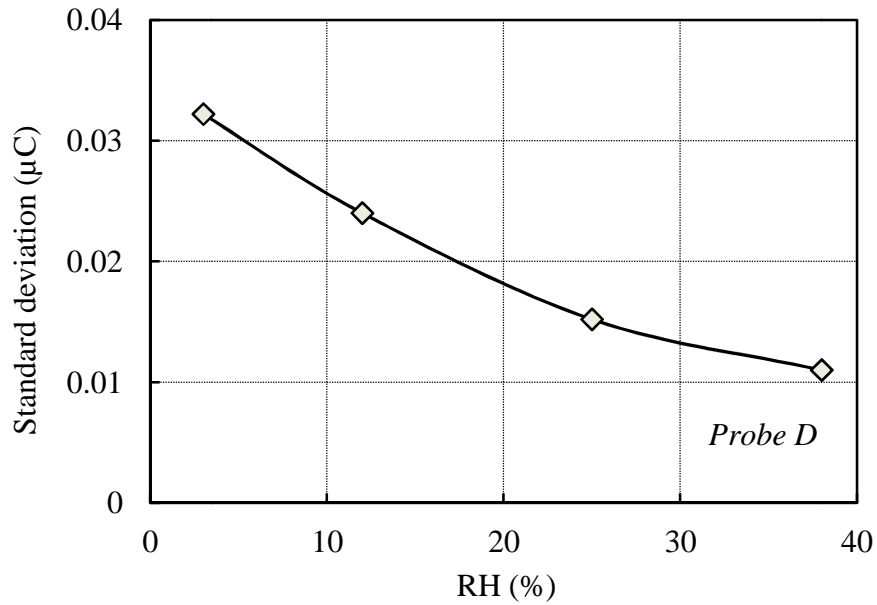


Figure 4.2 Standard deviation of charge fluctuations in the freeboard as a function of air relative humidity for a binary mixture M3. For physical properties of particles, see Tables 2.1, 2.2 and 2.3. $P = 414 \text{ kPa}$, $T = 20 \pm 2^\circ\text{C}$ and $U_g = 0.3 \text{ m/s}$. For position of probe D, see Figure 2.4.

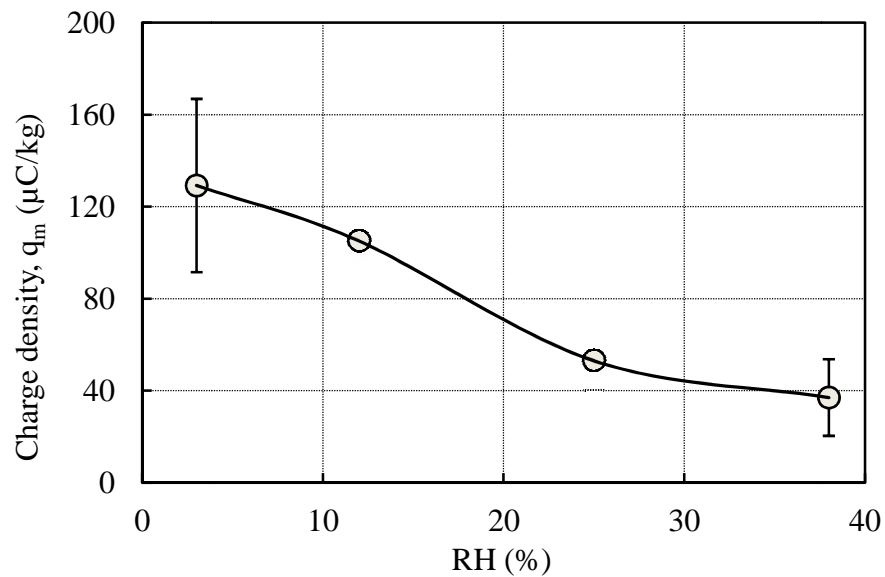


Figure 4.3 Charge density of glass bead fines measured by the freeboard sampler as a function of air relative humidity for a binary mixture M3. $P = 414 \text{ kPa}$, $T = 20 \pm 2^\circ\text{C}$ and $U_g = 0.3 \text{ m/s}$. For physical properties of particles, see Tables 2.1, 2.2 and 2.3. For freeboard sampler details, see Figure 2.5. Error bars correspond to $\pm 90\%$ confidence intervals.

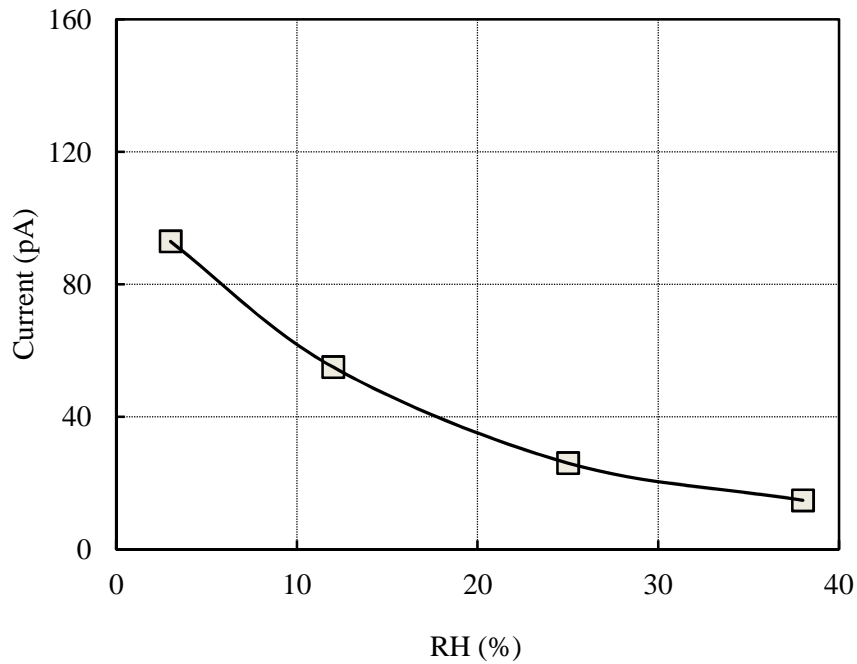


Figure 4.4 Current flow through current detection pipe at column exit for a binary mixture M3 as a function of air relative humidity. $P = 414 \text{ kPa}$, $T = 20 \pm 2^\circ\text{C}$ and $U_g = 0.3 \text{ m/s}$. For physical properties of particles, see Tables 2.1, 2.2 and 2.3. For current-detecting pipe details, see Figure 2.6.

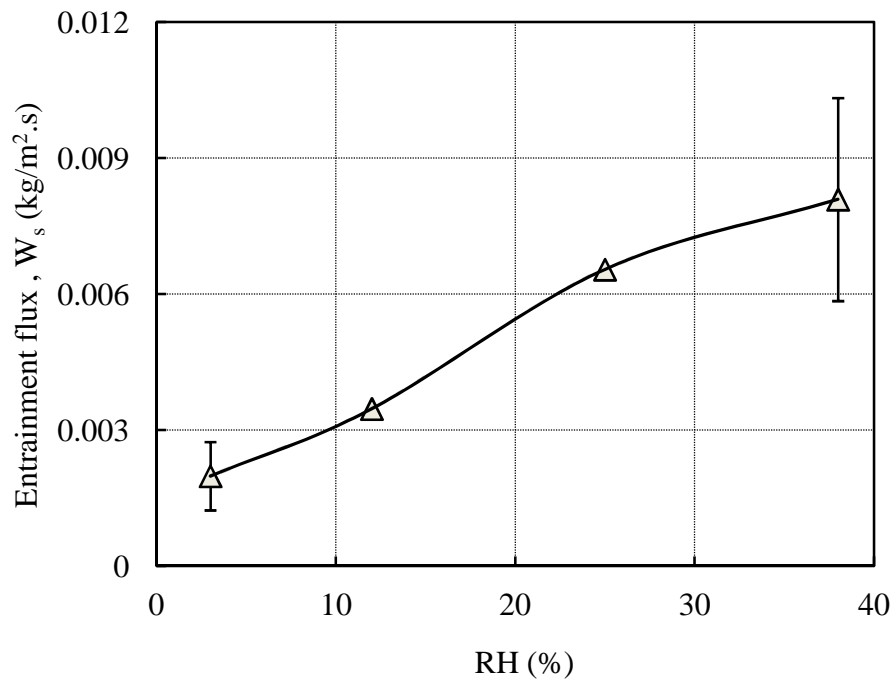


Figure 4.5 Entrainment flux measured from a binary mixture M3 as a function of air relative humidity. $P = 414 \text{ kPa}$, $T = 20 \pm 2^\circ\text{C}$ and $U_g = 0.3 \text{ m/s}$. For physical properties of particles, see Tables 2.1, 2.2 and 2.3. Error bars correspond to $\pm 90\%$ confidence intervals.

As expected, the experimental results shown in Figures 4.1 and 4.2 reveal that as the relative humidity increased, the accumulation of electrostatic charges decreased. This is most likely due to the increase in charge dissipation resulting from increased conductivity around the surfaces of particles as the relative humidity of the fluidizing air increased. Most outer surfaces of solid particles in air are covered by a layer of water ranging in thickness between a monolayer to a macroscopic thin film (Cross, 1987). When the charged solid surface comes in contact with a liquid, an electrical double layer is then formed due to charges on the solid surface and the difference of electrons between the solid surface and liquid. In the region next to the surface (Stern layer), ions are bound to surface due to adsorption and Coulomb interactions. In contrast, in the region next to the Stern layer (diffuse layer), ions can move freely in any direction (Kim, 2005). As adsorbed moisture forms a continuous film on the solid surface, the water provides a medium for dissociation of ions. The results shown in Figure 4.1 indicate that, for the RH range of 3–25%, humidifying the fluidizing air is effective in charge reduction, and the measured electrostatic charges do not vary much with RH in the range of 25–38%.

These results are consistent with those of Mehrani (2005) and Moughrabiah (2009), which indicate that for $RH < 35\%$, the electrostatic charge was clearly influenced by air relative humidity. On the other hand, Guardiola et al. (1996) found that for $RH < 30\%$, electrostatic charge accumulation in a three-dimensional column of 0.044 m inner diameter was slightly affected or not influenced by fluidizing air relative humidity. They attributed these results to the difficulties in measuring the electrostatics in the bed due to adhesion of particles to the probe used to measure the electrostatics.

In the freeboard region, the influence of air relative humidity on the charge density and entrainment flux of fine particles was evaluated. The freeboard sampler described schematically in Figure 2.5 was utilized to measure fine particle charge density by withdrawing particle samples from the freeboard region. The results show that as the air relative humidity increased the fines charge density (q_m) decreased. This was expected since it has been reported previously by several researchers that increasing fluidizing air relative humidity helps to increase the rate of charge dissipation. These results are consistent with those reported by Mehrani (2005) who studied the influence of air RH (0 to 60%) on the charge density of different fine glass beads added to large glass beads in a copper column of

0.1 m inner diameter. They found that the charge density decreased as air relative humidity increased, and the measured charge density values did not vary much when air humidity exceeded 35%. Mehrani and Giffin (2013) studied the effect of gas relative humidity (0 to 80%) on fine polyethylene particles in a bubbling fluidized bed. They reported that in the bubbling flow regime the air relative humidity had no clear effect on the fines charge density. Figure 4.4 shows the effect of air relative humidity on the current flow through the current detection pipe due to direct charge transfer, reflecting the degree of electrification at the column exit. It can be seen that as the air relative humidity increased, the degree of electrification at the column exit decreased, which means that fine particles carried less charge. The influence of relative humidity on the solid entrainment flux was also investigated, with results shown in Figure 4.5. Procedures similar to those described in Section 2.5 were again followed to measure the entrainment flux. The results show that as the air relative humidity increased the entrainment flux increased. From the data presented in Figure 4.3, it can be seen that lower entrainment was measured at low RH. This may be because high electrostatic charges led fine particles to attach to the surface of large particles and become trapped in the bed. It is also possible that the increased magnitude of charge on fine particles promoted adhesion of these particles to the column wall.

Mehrani and Giffin (2013) measured the electrostatic charges of particles at a reactor wall and found that these charges were high. They observed that increasing RH helps to reduce particle charges on the wall and as a result, particle wall adhesion is also reduced. Increasing relative humidity helps to increase charge dissipation, causing fine particles to become less charged in the freeboard. Thus, it is possible that, when particles become less charged, bed particle agglomeration and wall adhesion caused by electrostatic forces were reduced and particles became free and more easily entrained from the column.

The results in Figure 4.5 indicate that when relative humidity increased from 3 to 38%, the entrainment flux increased substantially. This result is consistent with those of Baron et al. (1987) and Kato and Li (2001), which indicate that for $RH < 30\%$ the entrainment flux was clearly influenced by the fluidizing air relative humidity. Baron et al. (1987) studied the effect of air relative humidity on the entrainment of silica sand from a 0.61 m inner diameter carbon steel column. They reported that the entrainment flux increased as the air RH increased from 7 to 30%. Their results were attributed to increased pressure drop in the

freeboard due to electrostatic interactions between the particles and column wall. Kato and Li (2001) investigated the effect of air humidity on the elutriation rate constant of fine alumina particles mixed with large PVC particles in a transparent column of 0.103 m inner diameter. They found that for $RH \leq 32\%$, the fines elutriation constant increased as the relative humidity increased. They attributed these results to electrostatic forces, which were mitigated by increasing air humidity. They also found that if the relative humidity continuously increased from 32 to 68%, this had no effect on the elutriation rate constant. For relative humidity greater than 68%, the elutriation constant decreased as a result of capillary forces. Mehrani (2005) studied the effect of relative humidity on the fines entrainment for a binary mixture of fines and large glass beads in a fluidized bed. The results showed that the entrainment rate of fines increased when the relative humidity increased.

In contrast, Mehrani and Giffin (2013) reported that relative humidity had no effect on the amount of fines collected from the freeboard region. Hemery et al. (2009) investigated the effect of air humidity on electrostatic properties of different hydrophobic materials and found that those materials were not influenced by changes in moisture content. However, the particles materials used by Baron et al. (1987), Kato and Li (2001) and in this work were silica sands, alumina and glass beads, respectively, all of which are hydrophilic in nature (Castricum et al., 2005 and Siddique, 2007), whereas polyethylene is hydrophobic (Harper, 1967).

To gain a better understanding of the effect of air relative humidity and the interactions between humidity and particulate materials, additional particles, such as alumina and polyethylene fine particles, were tested. The results are presented and discussed in sections 4.2.2 and 4.2.3.

The above experiments were conducted at elevated pressure (414 kPa) and a superficial gas velocity, U_g , of 0.3 m/s. To verify the effect of air humidity at different operating conditions, freely bubbling experiments were performed by fluidizing a bed of the same binary mixture (M3) at a lower pressure (210 kPa) and higher superficial gas velocity ($U_g = 0.6$ m/s), following the same experimental procedure as above. Figure 4.6 shows the effect of air relative humidity on the current flow through the ball probe, reflecting the degree of electrification at different levels in the bed, whereas Figure 4.7 shows the influence of air

relative humidity on the charge density of entrained fines in the freeboard. The fines entrainment flux is plotted versus the air relative humidity in Figure 4.8.

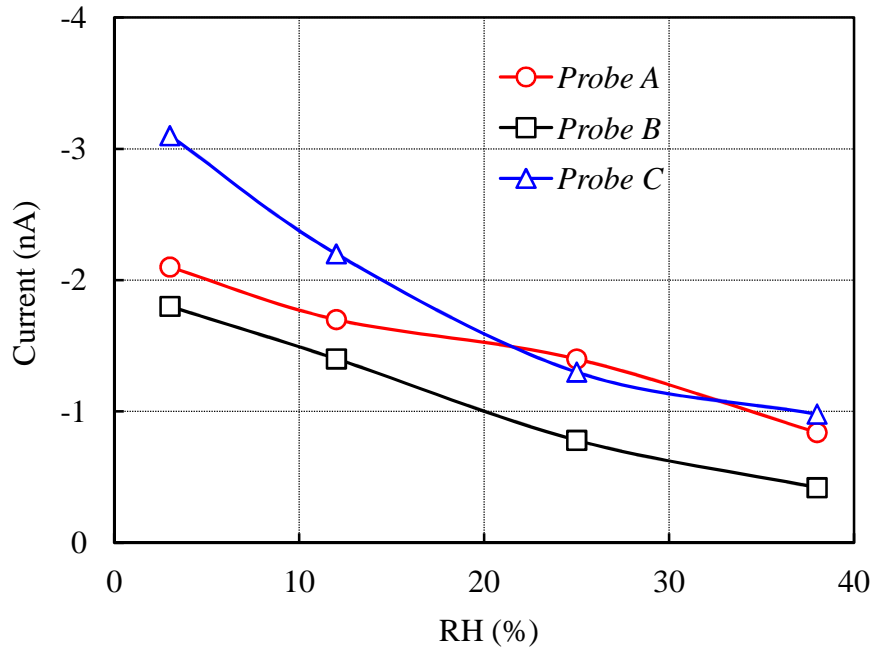


Figure 4.6 Current flow through collision ball probes in a bed of binary mixture M3 as a function of air relative humidity. $P = 210$ kPa, $T = 20 \pm 2^\circ\text{C}$ and $U_g = 0.6$ m/s. For physical properties of particles, see Tables 2.1, 2.2 and 2.3. For probe positions, see Figure 2.4.

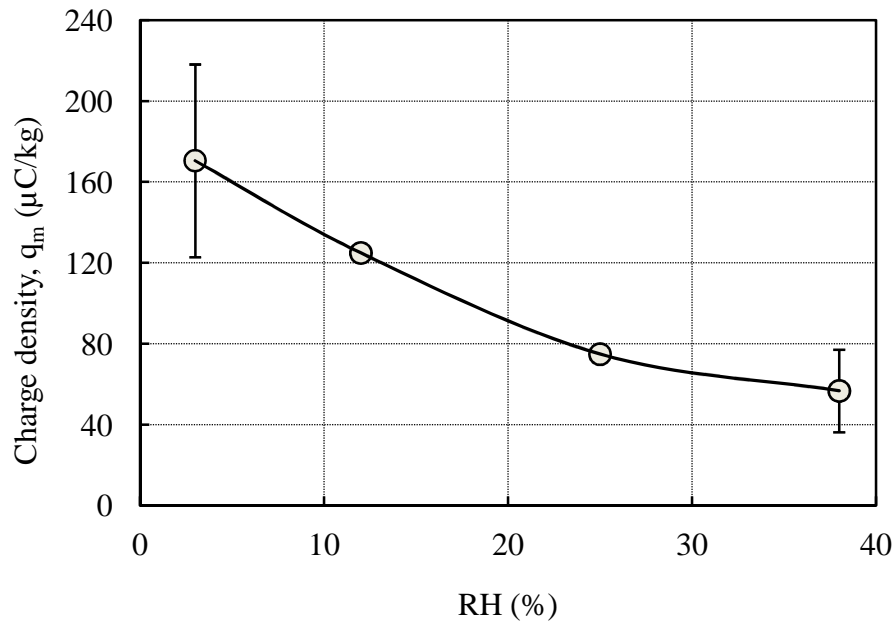


Figure 4.7 Charge density of fine glass beads measured by freeboard sampler as a function of air relative humidity in a binary mixture M3. $P = 210$ kPa, $T = 20 \pm 2^\circ\text{C}$ and $U_g = 0.6$ m/s. For physical properties of particles, see Tables 2.1, 2.2 and 2.3. For freeboard sampler details, see Figure 2.5. Error bars correspond to $\pm 90\%$ confidence intervals.

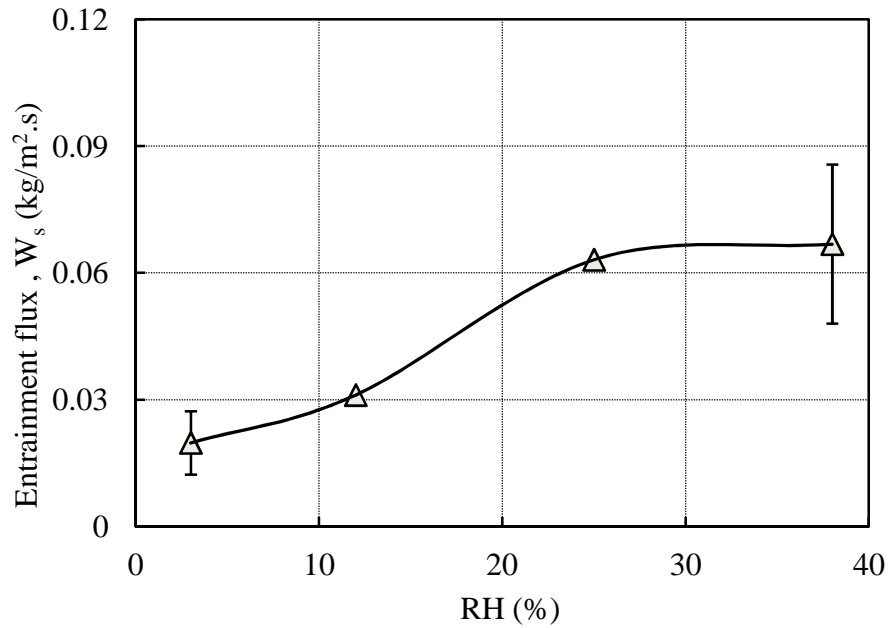


Figure 4.8 Entrainment flux measured from a binary mixture M3 as a function of air relative humidity. $P = 210$ kPa, $T = 20 \pm 2^\circ\text{C}$ and $U_g = 0.6$ m/s. For physical properties of particles, see Tables 2.1, 2.2 and 2.3. Error bars correspond to $\pm 90\%$ confidence intervals.

Figures 4.6–4.8 demonstrate that air relative humidity had effects similar to those indicated in Figures 4.1–4.5, despite changes in the pressure and superficial gas velocity. The increase in superficial gas velocity apparently did not destroy the conductive water films formed around particle surfaces in the bed. Thus, these results show that as the air relative humidity increased from 3 to 38%, the electrostatic charges in the column decreased, and the fine particle entrainment flux increased.

In this set of experiments at 210 kPa and $U_g = 0.6$ m/s, the degree of electrification in the column and the fines entrainment flux were higher than in the previous experiments at 414 kPa and $U_g = 0.3$ m/s. This is probably due to the significant impact of superficial gas velocity on both electrostatics and entrainment flux. As the superficial gas velocity increased, the motion and interactions between particles in the fluidized bed are enhanced, leading to increased electrostatic charge generation. At the same time, increasing superficial gas velocity resulted in higher bubble velocity and greater ejection velocities at the bed surface, resulting in higher upwards drag on the particles in the freeboard, which in turn resulted in

increased entrainment flux. However, in this case the pressure was also reduced from 414 to 210 kPa, which means that the electrostatic charge decreases, based on the results presented in Chapter 3; in these experiments covered in this chapter, the net increase in electrostatic charges probably reflected the effect of increased superficial gas velocity being greater than the counter effect of decreasing pressure.

4.2.2 Fines Material: Alumina (Al_2O_3)

Free-bubbling experiments were also conducted utilizing GBL as the mono-sized coarser particles and Al_2O_3 as the added fines, giving the binary mixture (M6, in Table 2.3). For physical properties, see Tables 2.1 and 2.2. The experiments were conducted in the three-dimensional fluidized bed with collision ball probes at four levels, a freeboard sampler, and a current detecting pipe (illustrated in Figures 2.4–2.6, respectively) to investigate the effect of fluidizing air relative humidity on the electrostatic charge generated inside the fluidized bed, the entrainment flux, and the charge density of entrained fine particles. The static bed height was ~ 0.54 m in all cases. To isolate the effect of gas relative humidity, temperature, pressure and superficial air velocity were maintained as constant as possible at $20 \pm 2^\circ\text{C}$, 414 kPa and $U_g = 0.3$ m/s, respectively. The relative humidity of the fluidizing air was varied from 3 to 38%. The bed was again fluidized for approximately one hour to achieve steady state before data were collected.

The net cumulative charge generated in the bed, measured by the collision ball probes, is plotted versus time in Figure 4.9. The standard deviation of charge fluctuations registered by probe D in the freeboard region is presented in Figure 4.10 as a function of air relative humidity after filtering the net cumulative charge curves using a high-pass filter with cut-off frequency 0.03 Hz. The fine particles charge density and entrainment flux are plotted as a function of air relative humidity in Figures 4.11 and 4.12, respectively. The current flow through the current-detecting pipe in the column exit due to direct charge transfer is plotted versus air relative humidity in Figure 4.13.

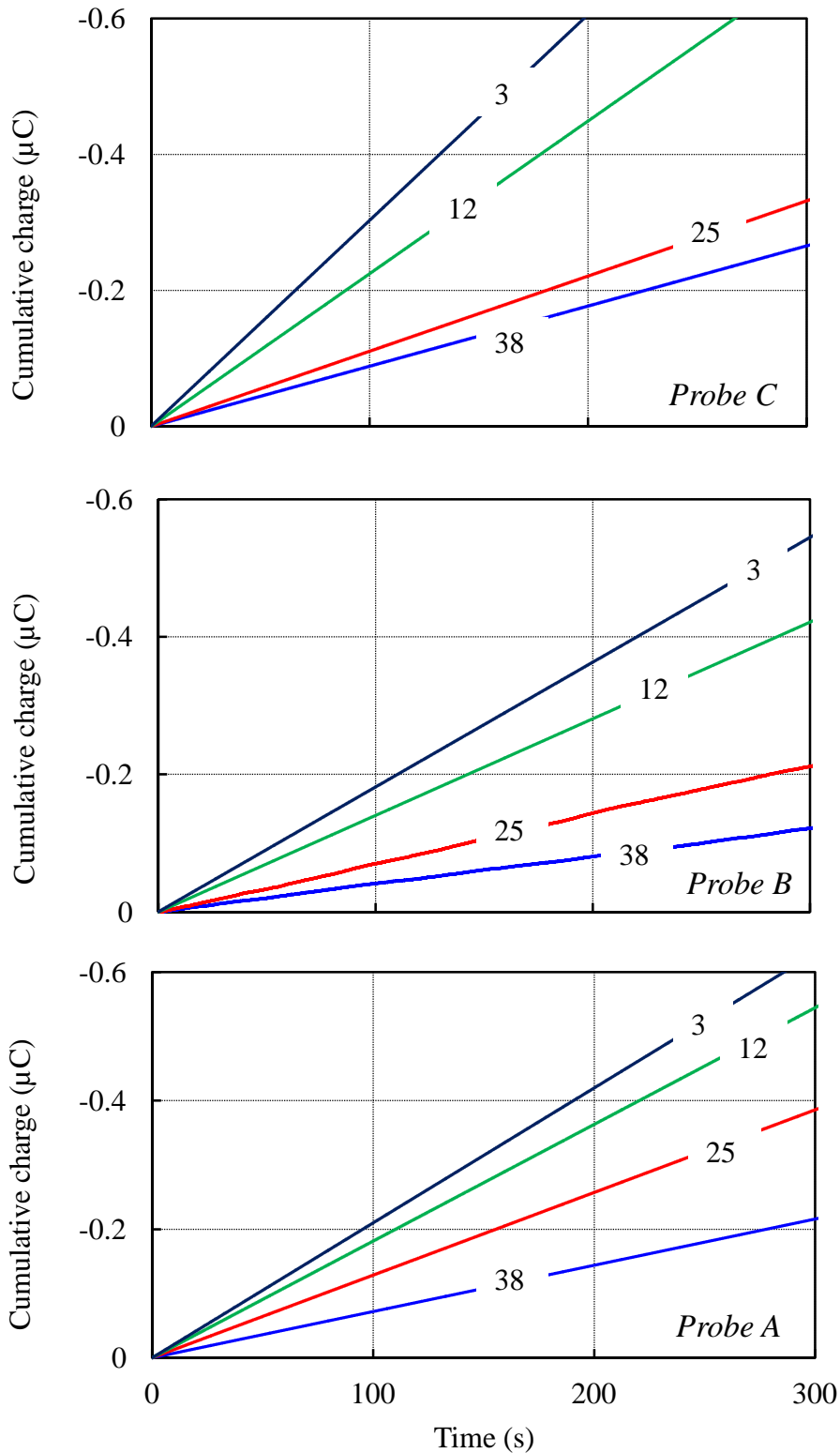


Figure 4.9 Effect of relative humidity of fluidizing air on net cumulative charges as a function of time at different axial positions in a bed of binary mixture M6. For physical properties of particles, see Tables 2.1, 2.2 and 2.3. $P = 414 \text{ kPa}$, $T = 20 \pm 2^\circ\text{C}$, and $U_g = 0.3 \text{ m/s}$. Numbers on curves denote % RH. For probe positions, see Figure 2.4.

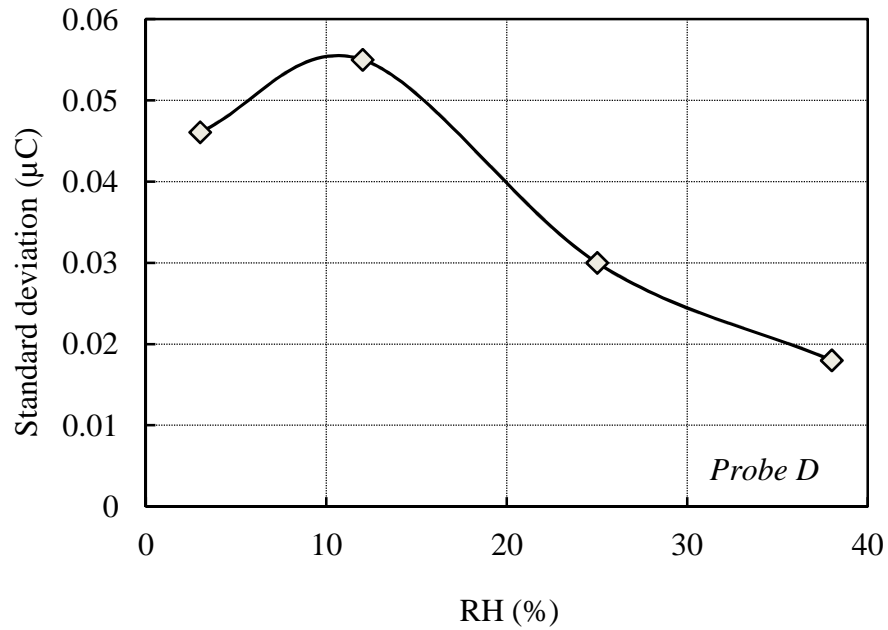


Figure 4.10 Standard deviation of charge fluctuations in the freeboard as a function of air relative humidity for a binary mixture M6. For physical properties of particles, see Tables 2.1, 2.2 and 2.2. $P = 414$ kPa, $T = 20 \pm 2^\circ\text{C}$ and $U_g = 0.3$ m/s. For position of probe D, see Figure 2.4.

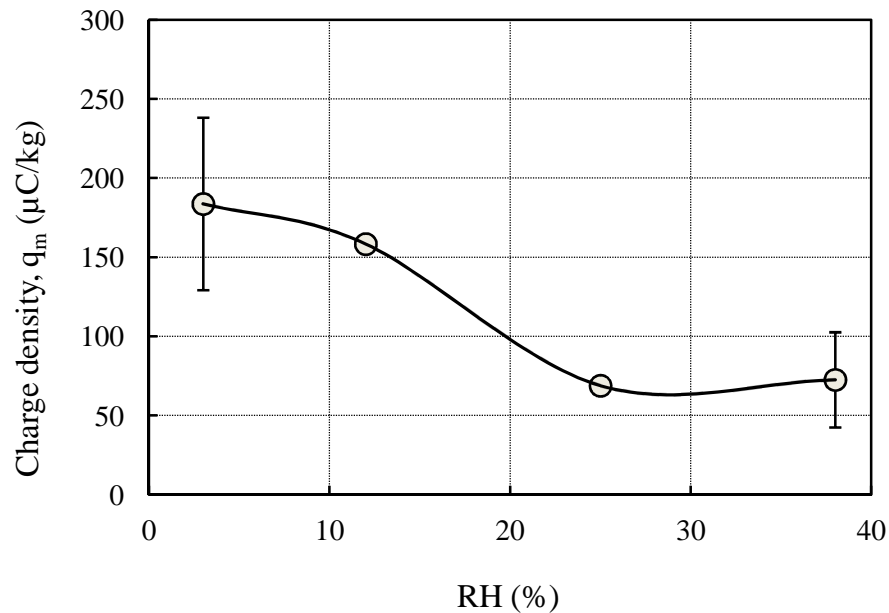


Figure 4.11 Charge density of Al_2O_3 fines measured by freeboard sampler as a function of air relative humidity in a binary mixture M6. $P = 414$ kPa, $T = 20 \pm 2^\circ\text{C}$ and $U_g = 0.3$ m/s. For physical properties of particles, see Tables 2.1, 2.2 and 2.3. For freeboard sampler details, see Figure 2.5. Error bars correspond to $\pm 90\%$ confidence intervals.

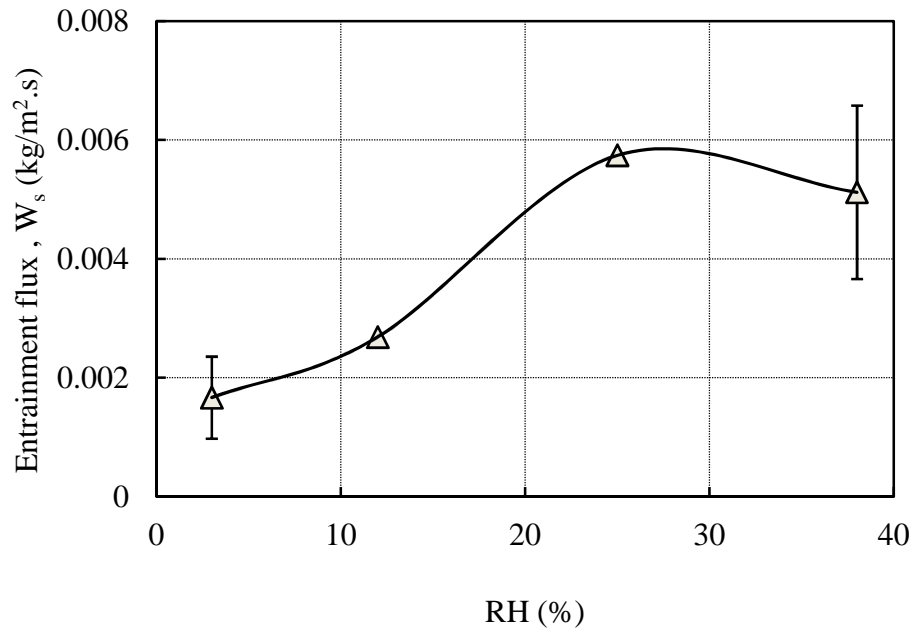


Figure 4.12 Entrainment flux from binary mixture M6 as a function of air relative humidity. $P = 414$ kPa, $T = 20 \pm 2^\circ\text{C}$ and $U_g = 0.3$ m/s. For physical properties of particles, see Tables 2.1, 2.2 and 2.3. Error bars correspond to $\pm 90\%$ confidence intervals.

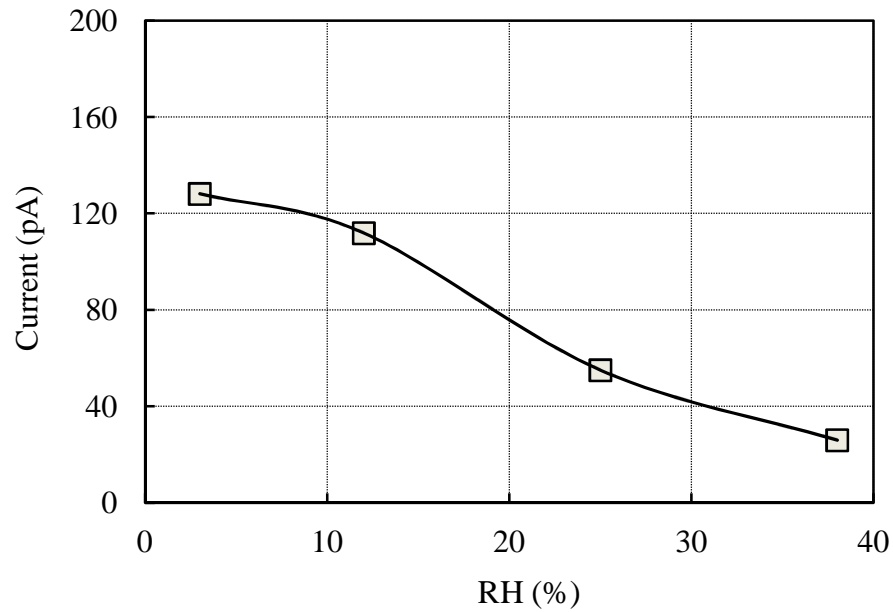


Figure 4.13 Current flow through current detection pipe at column exit in binary mixture M6 as a function of air relative humidity. $P = 414$ kPa, $T = 20 \pm 2^\circ\text{C}$ and $U_g = 0.3$ m/s. For physical properties of particles, see Tables 2.1, 2.2 and 2.3. For current-detecting pipe details, see Figure 2.6.

Figure 4.9 shows that the magnitude of electrostatic charges in the bed measured at different levels by probes A, B and C and the charges of Al_2O_3 fines measured in the freeboard region by probe D decreased as the air relative humidity increased, very likely for the same reasons as discussed above for the GBF experiments. In Figure 4.10, the standard deviation of charge fluctuations decreased as RH increased. Figure 4.11 indicates that the charge density of Al_2O_3 fines measured by the freeboard sampler decreased as the air relative humidity increased. The results in Figures 4.9–4.11 indicate again that, for the RH range of 3–25%, humidifying the fluidizing air is effective in charge reduction, with the measured electrostatic charges varying less with RH in the range of 25–38%. Figure 4.12 indicates that the fine particle entrainment flux increased as the air relative humidity increased from 3 to 25%, a similar finding to the results obtained previously for fine glass beads particles (GBF). The increase in entrainment flux is possibly because Al_2O_3 is hydrophilic, following the same pattern as GBF, with the formation of a water film around the Al_2O_3 particle surface helping to dissipate the electrostatic charges and leading to less fines-coarse particle adhesion and fines-wall adhesion; as a result fines became free and were entrained from the column. It can be seen from Figure 4.13 that, as the air relative humidity increased, the degree of electrification at the column exit decreased, indicating that the entrained Al_2O_3 fine particles carried less charge.

These results are consistent with those of Kato and Li (2001) who studied the effect of air relative humidity on the elutriation of Geldart group A particles and found that at constant gas velocity the electrostatic potential of bed particles decreased, whereas the elutriation constant increased, as the air relative humidity increased from 10 to 32%.

4.2.3 Fines Material: Polyethylene (PEF)

Similar free-bubbling experiments were also conducted utilizing GBL and polyethylene fines (PEF) as the mono-sized particles and added fines, respectively. The resulting binary mixture, M9, is detailed in Table 2.3, and individual particle properties are listed in Tables 2.1 and 2.2. The previously described three-dimensional fluidization column with collision ball probes (Figure 2.4), freeboard sampler (Figure 2.5), and current-detecting pipe (Figure 2.6) were again used to investigate the effect of fluidizing gas relative humidity on the

electrostatic charges generated inside the fluidized bed, entrainment flux, and charge density of entrained fine particles.

Experimental conditions were the same as those previously described. The static bed height was ~ 0.54 m in all experiments. The temperature, pressure and superficial air velocity were maintained as constant as possible at $20 \pm 2^\circ\text{C}$, 414 kPa and $U_g = 0.3$ m/s respectively to isolate the effect of gas relative humidity of the fluidizing air which was again varied from 3 to 38%. The bed was again fluidized for approximately one hour to achieve steady state before data were recorded. The net cumulative charges at three levels were then measured by the collision ball probes and are plotted versus time, as shown in Figure 4.14. Figure 4.15 shows the standard deviation of charge fluctuations measured by probe D in the freeboard region versus air relative humidity after filtering the net cumulative charge curves using a high-pass filter of cut-off frequency 0.03 Hz. The fine particle charge density and entrainment flux are plotted in Figures 4.16 and 4.17, respectively as a function of air relative humidity. Current flow through the current detecting pipe in the column exit due to direct charge transfer is plotted against air relative humidity in Figure 4.18.

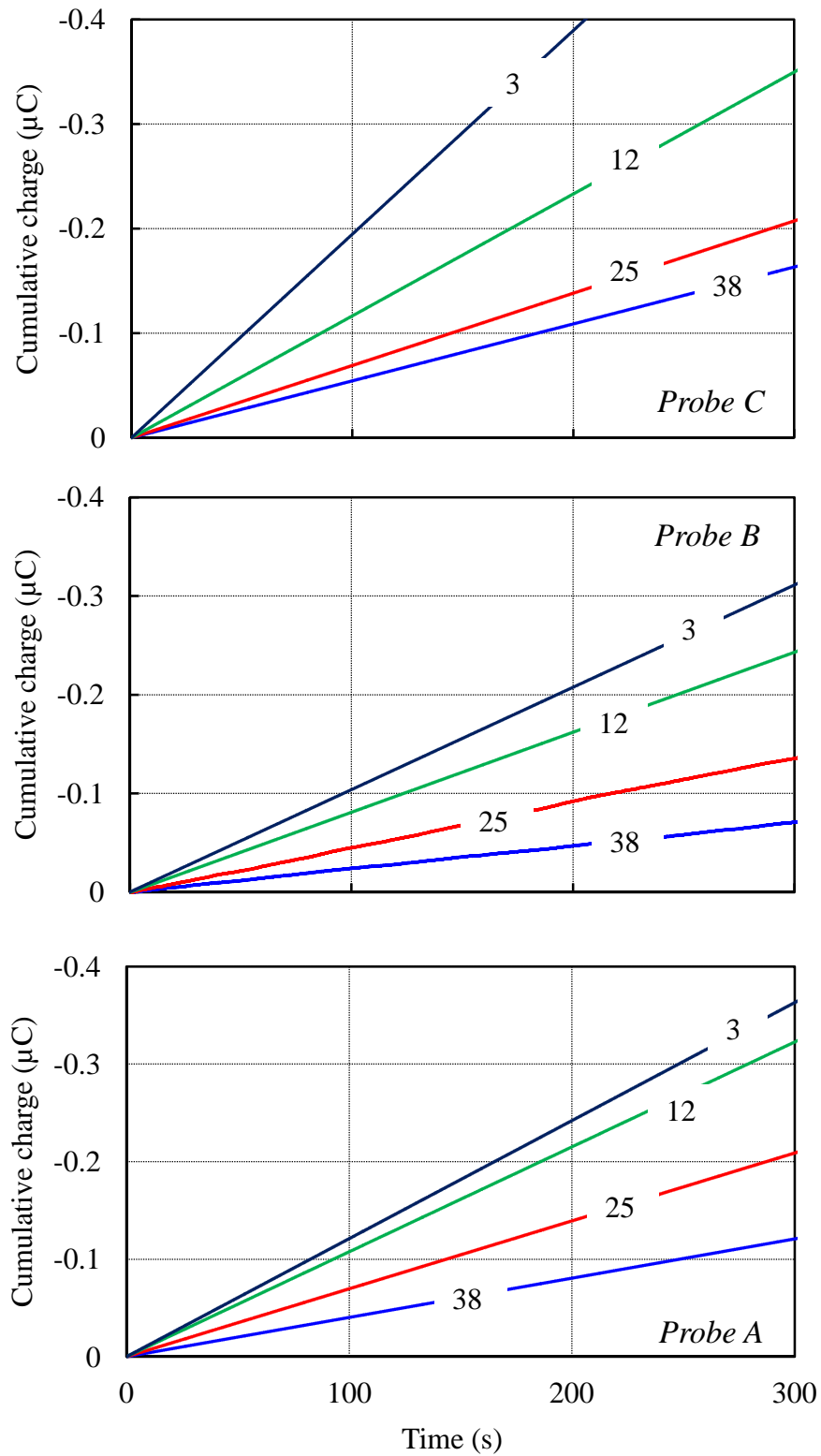


Figure 4.14 Effect of relative humidity of fluidizing air on net cumulative charges as a function of time at different axial positions in bed of binary mixture M9. For physical properties of particles, see Tables 2.1, 2.2 and 2.3. $P = 414$ kPa, $T = 20 \pm 2^\circ\text{C}$, and $U_g = 0.3$ m/s. Numbers on curves denote % RH. For probe positions, see Figure 2.4.

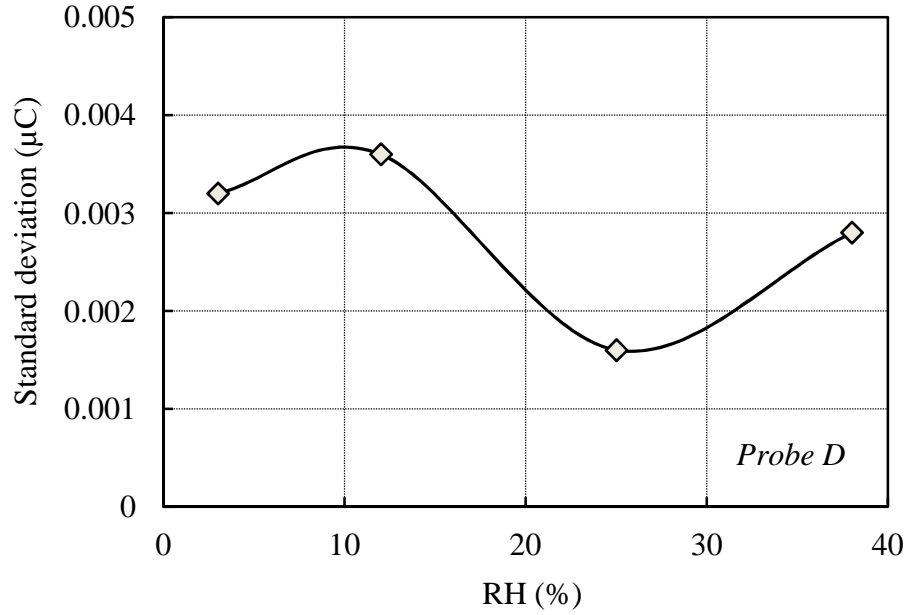


Figure 4.15 Standard deviation of charge fluctuations in the freeboard as a function of air relative humidity for a binary mixture M9. For physical properties of particles, see Tables 2.1, 2.2 and 2.3. $P = 414$ kPa, $T = 20 \pm 2^\circ\text{C}$ and $U_g = 0.3$ m/s. For position of probe D, see Figure 2.4.

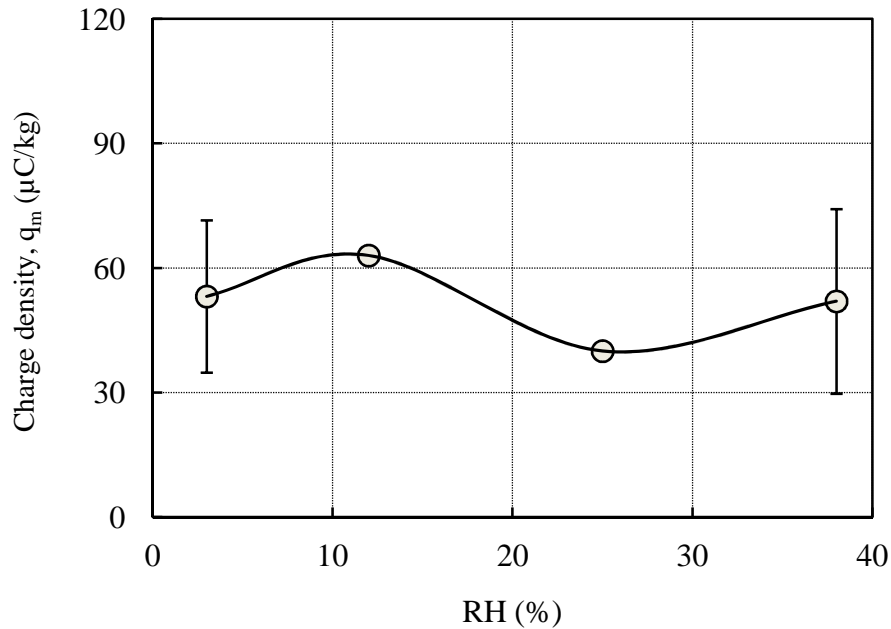


Figure 4.16 Charge density of polyethylene fines measured by freeboard sampler as a function of air relative humidity for binary mixture M9. $P = 414$ kPa, $T = 20 \pm 2^\circ\text{C}$ and $U_g = 0.3$ m/s. For physical properties of particles, see Tables 2.1, 2.2 and 2.3. Error bars correspond to $\pm 90\%$ confidence intervals. For freeboard sampler details, see Figure 2.5.

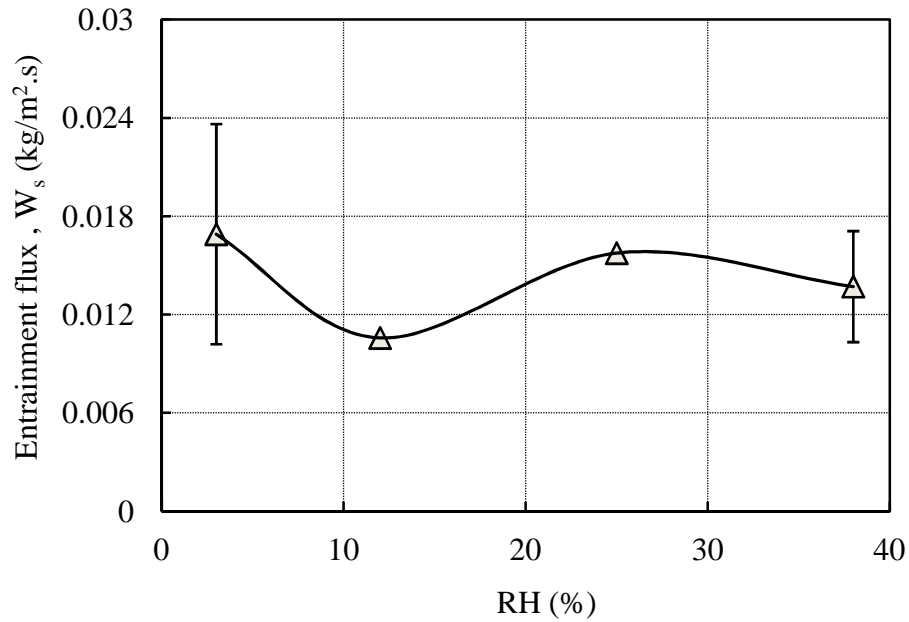


Figure 4.17 Entrainment flux measured from a binary mixture M9 as a function of air relative humidity. $P = 414$ kPa, $T = 20 \pm 2^\circ\text{C}$ and $U_g = 0.3$ m/s. For physical properties of particles, see Tables 2.1, 2.2 and 2.3. Error bars correspond to $\pm 90\%$ confidence intervals.

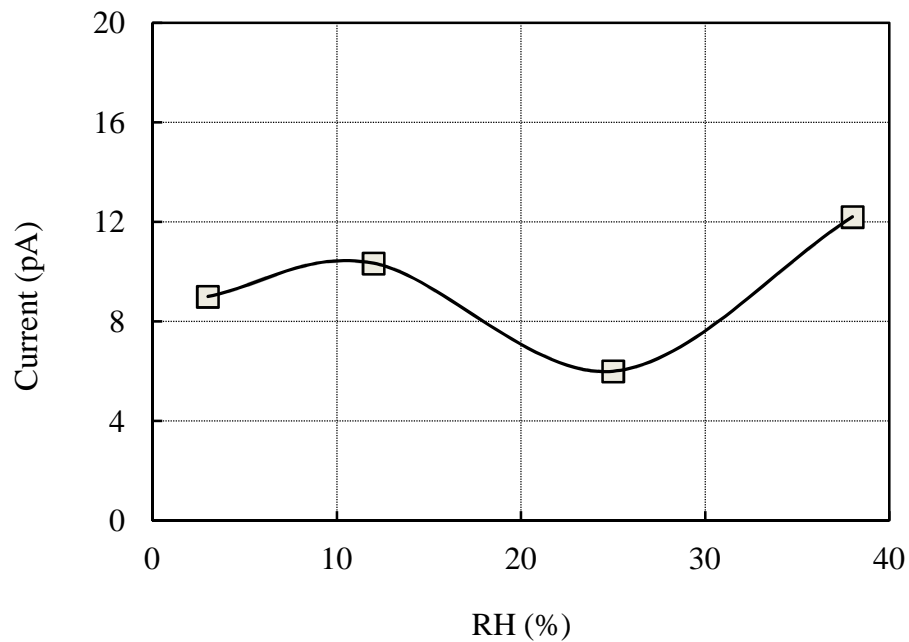


Figure 4.18 Current flow through current detection pipe at column exit for binary mixture M9 as a function of air relative humidity. $P = 414$ kPa, $T = 20 \pm 2^\circ\text{C}$ and $U_g = 0.3$ m/s. For physical properties of particles, see Tables 2.1, 2.2 and 2.3. For current detecting pipe details, see Figure 2.6.

Figure 4.14 shows that, once again, the magnitude of electrification in the fluidized bed column measured at different levels by probes A, B and C decreased as the air relative humidity increased, probably for the same reasons as discussed previously. The formation of a water film around the GBL particle surface helps to dissipate electrostatic charges. On the other hand, as shown in Figures 4.15–4.18, there were no clear trends of fine charge density (q_m) and entrainment flux (W_s) with respect to the air relative humidity (3-38%). This could be because polyethylene is hydrophobic; so that, a stable water film does not form on the surface of the fine polyethylene particles. Thus, moisture did not affect the charge dissipation, and it is also possible that fines-coarse particle adhesion and fines-wall adhesion caused by electrostatic forces were not affected. However, in this mixture (M9), the figures indicate that the fine particles almost maintained their charges while the bed particles (GBL) lost charges as the RH increased. One possible explanation is that the GBL had reduced charges through contact with the column inner wall. Previous work that considered RH showed that a film may developed on particles and/or the inner column wall and may influence charge generation and dissipation rate (Harper, 1967). In this work, it is possible that a film formed on the inner stainless steel column wall leading to dissipation of the charges on the GBL particles near the wall when they come in contact with the wall.

Our results are similar to those of Mehrani and Giffin (2013) who investigated the effect of air relative humidity on entrainment rate and charge of fine and large polyethylene particles in a 0.1 m inner diameter carbon steel column in which was a bubbling fluidized bed. They reported that the air relative humidity had no effect on the fines charge density and entrainment rate. They attributed these results to the hydrophobic nature of polyethylene and concluded that it was unlikely that the agglomerates caused by electrostatic forces were broken apart. Therefore, it seems that fine polyethylene particles behaved in a similar manner, regardless of the type of bed particles. On the other hand, Mehrani and Giffin (2013) observed that RH had no appreciable effect on the charges of polyethylene bed particles unless the relative humidity exceeded 65%.

The charge density (q_m), charge-to-surface area ratio (Q_s) and entrainment flux (W_s) measured for different added fines and different air relative humidities with large glass beads particles (GBL) as the major bed component is compared in Table 4.1.

Table 4.1 Charge density, q_m ($\mu\text{C}/\text{kg}$), charge/surface ratio, Q_s ($\mu\text{C}/\text{m}^2$) and entrainment flux, W_s ($\text{kg}/\text{m}^2\text{s}$) for different fines and different air relative humidities with large glass beads particles (GBL) as the major bed component. $P = 414$ kPa, $T = 20 \pm 2^\circ\text{C}$ and $U_g = 0.3$ m/s.

Fine Particles	RH = 3%		RH = 12%		RH = 25%		RH = 38%		W_s (RH=12%)
	q_m	Q_s	q_m	Q_s	q_m	Q_s	q_m	Q_s	
GBF	129	2.206	105	1.796	53	0.906	37	0.633	0.0035
Al_2O_3	184	3.709	158	3.185	69	1.391	73	1.472	0.0024
PEF	53	0.298	71	0.399	40	0.225	52	0.292	0.011

The added fines in these experiments had different densities. To better analyze the results discussed previously, the charge-to-surface area ratio was also determined for each fine particle and the results are presented in Table 4.1. For detailed calculations of fine surface areas, see the Appendix C.

It can be seen from Table 4.1 that the results of charge-to-surface area are consistent with previous findings based on charge density. These data show that charge-to-surface ratio decreased as the air relative humidity increased. In addition, the charge-to-surface ratios for the Al_2O_3 and GBF fine particles are higher than for the PEF particles, possibly due to different particle surface properties and sphericities.

Bipolar charging was observed in all experiments, with fine particles carrying positive charges, whereas large particles carried negative charges. The gas relative humidity (in the range 3–38%) had no effect on the polarity of either the large or fine particles. Bipolar charging is discussed in Chapter 5.

4.3 Summary

In this chapter, the effect of air relative humidity on bed electrification, fines charge density and entrainment flux were studied in the bubbling bed flow regime. In all experiments, the degree of electrification in the bed decreased with increasing air relative humidity. For the fine glass beads and fine Al_2O_3 experiments, the fluidizing air was effective for a range of relative humidities (3–25%), and relative humidity influenced the fines charge density and entrainment flux. As the air relative humidity increased, the charge density of fines decreased, and entrainment increased. This may be due to the hydrophilic nature of glass beads and Al_2O_3 ; the formation of thin water films around the particle surface enhances the charge dissipation rate and reduces fines-coarse particle adhesion and fines-wall adhesion. The effect of air humidity on polyethylene particles was also investigated, with results showing that humidity had no clear effect on the fines charge density and entrainment flux. This is likely due to the hydrophobic nature of polyethylene which prevents the formation of water films around the surface of particles. As a result, fine particle adhesion to the bed particles and column wall was unaffected since charge dissipation was not increased and the fine particles maintained their charges.

Chapter 5: Results and Discussion: Effects of Particle Properties

As mentioned in Chapter 1, several researchers have reported that electrostatics and particle entrainment rates are influenced by the properties of the particles. To gain a better understanding of the effects of coarse and fine particle properties on electrostatic behaviour and entrainment flux in a fluidized bed operated in the bubbling flow regime, three types of coarse particles (glass beads, HDPE and LDPE) and three types of fine particles (glass beads, alumina and polyethylene) were tested. In addition, the effects of different fines concentrations (5, 10 and 15% by mass) were investigated. The results are presented and discussed in this chapter.

5.1 Effect of Coarse Particle Properties

5.1.1 Effect of Average Particle Size

Free-bubbling experiments were conducted in a three-dimensional elevated-pressure fluidized bed to investigate the effect of coarse particle average size on the electrostatic behavior and entrainment rate. Experiments were conducted utilizing GBL, GBM and GBS as the larger mono-sized particles, with GBF as added fines to prepare the binary mixtures (M1, M2 and M3, in Table 2.3). For physical properties of the individual species, see Tables 2.1 and 2.2. The relative humidity of the fluidizing air was maintained at $12\pm 2\%$. The static bed height was ~ 0.54 m in all cases. The temperature, pressure and superficial air velocity were maintained nearly constant at $20\pm 2^\circ\text{C}$, 414 kPa and $U_g = 0.3$ m/s, respectively, to isolate the influence of coarse particle properties.

In each experiment, the bed was first fluidized for approximately an hour to achieve steady state before collecting data. Figure 5.1 compares the net cumulative charges measured by the electrostatic collision ball probes (see Figure 2.3) in beds of binary mixtures M1, M2 and M3. Figure 5.2 shows the standard deviation of charge fluctuations registered by probe D in the freeboard region after filtering the net cumulative charge curves using a high-pass filter of cut-off frequency 0.03 Hz for different binary mixtures as a function of superficial air velocity. The charge density and current flow through the detection pipe are compared for different binary mixtures and plotted versus superficial air velocity in Figures 5.3 and 5.4, respectively. The influence of coarse particle average size on the solid entrainment rate is shown in Figure 5.5.

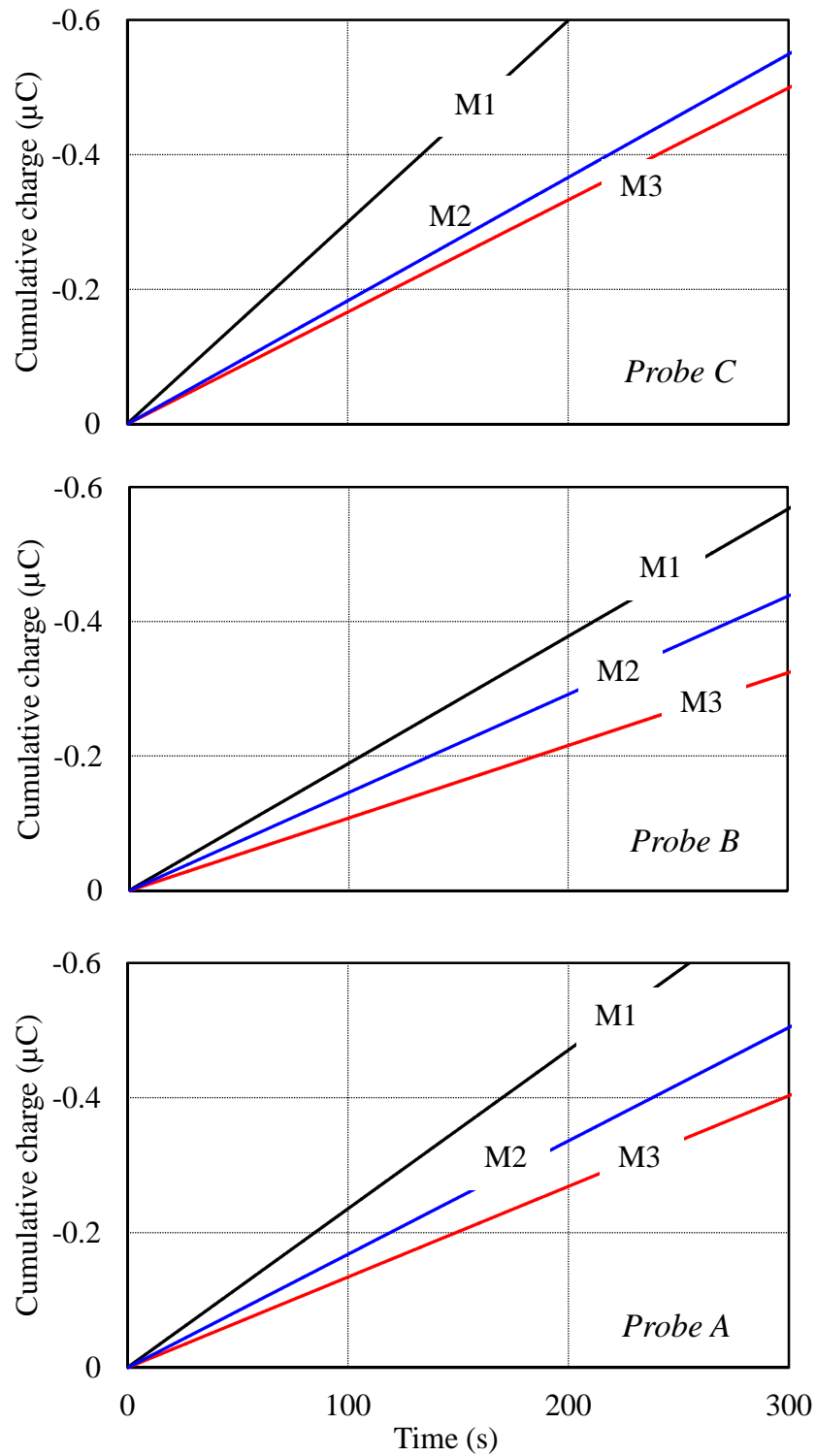


Figure 5.1 Effect of coarse particle size on net cumulative charges as a function of time at different axial positions in beds of binary mixtures M1, M2 and M3. For physical properties of particles, see Tables 2.1, 2.2 and 2.3. $P = 414$ kPa, $T = 20 \pm 2^\circ\text{C}$, and $U_g = 0.3$ m/s. Letters on curves denote mixture types. For probe positions, see Figure 2.4.

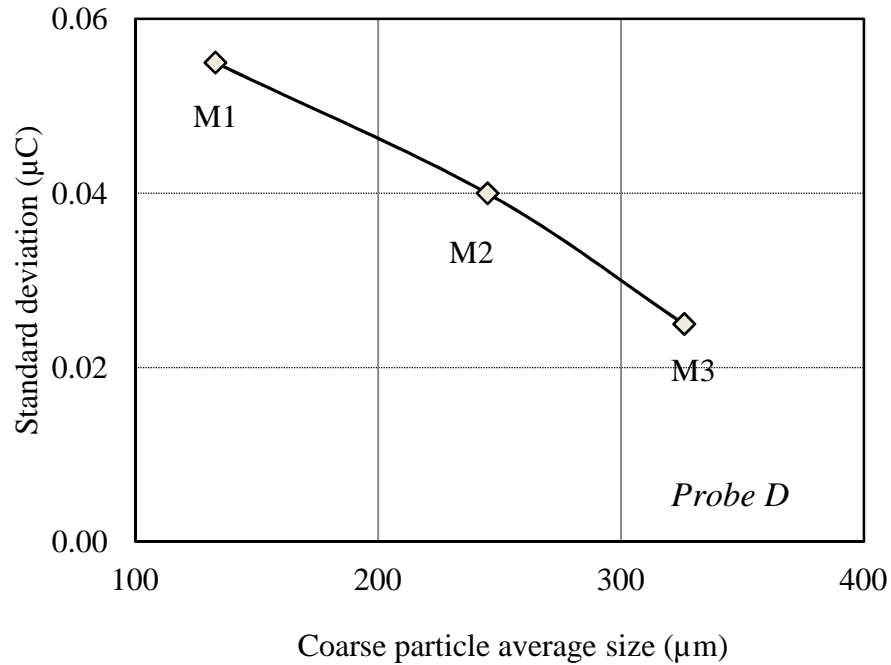


Figure 5.2 Standard deviation of charge fluctuations in the freeboard as a function of coarse particle average size in beds of binary mixtures M1, M2 and M3. For physical properties of particles, see Tables 2.1, 2.2 and 2.3. $P = 414$ kPa, $T = 20 \pm 2^\circ\text{C}$ and $U_g = 0.3$ m/s. For position of probe D, see Figure 2.4.

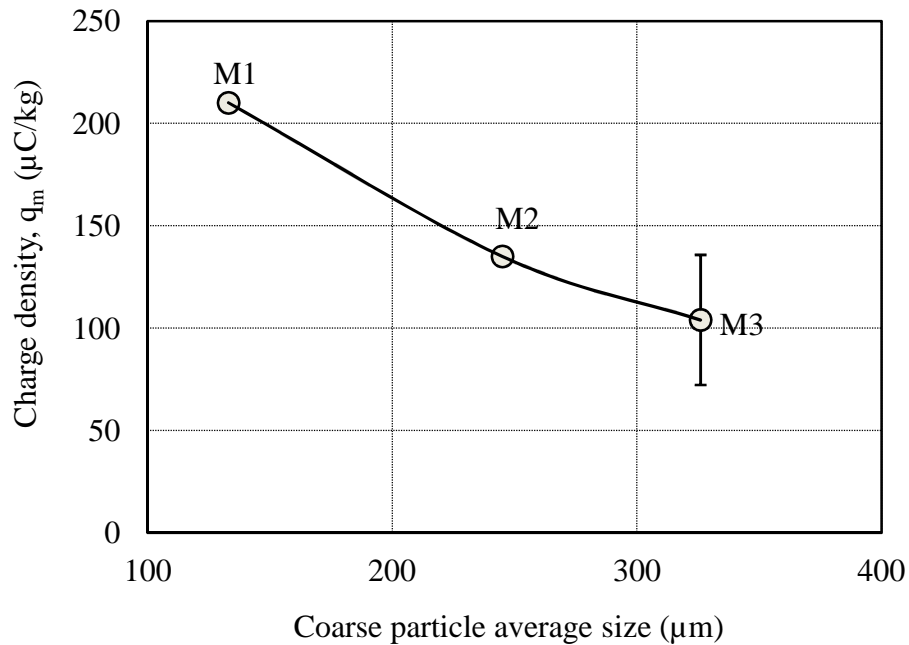


Figure 5.3 Charge density measured by freeboard sampler as a function of coarse particle average size in beds of binary mixtures M1, M2 and M3. For physical properties of particles, see Tables 2.1, 2.2 and 2.3. $P = 414$ kPa, $T = 20 \pm 2^\circ\text{C}$ and $U_g = 0.3$ m/s. Error bar corresponds to $\pm 90\%$ confidence interval. For freeboard sampler details, see Figure 2.5.

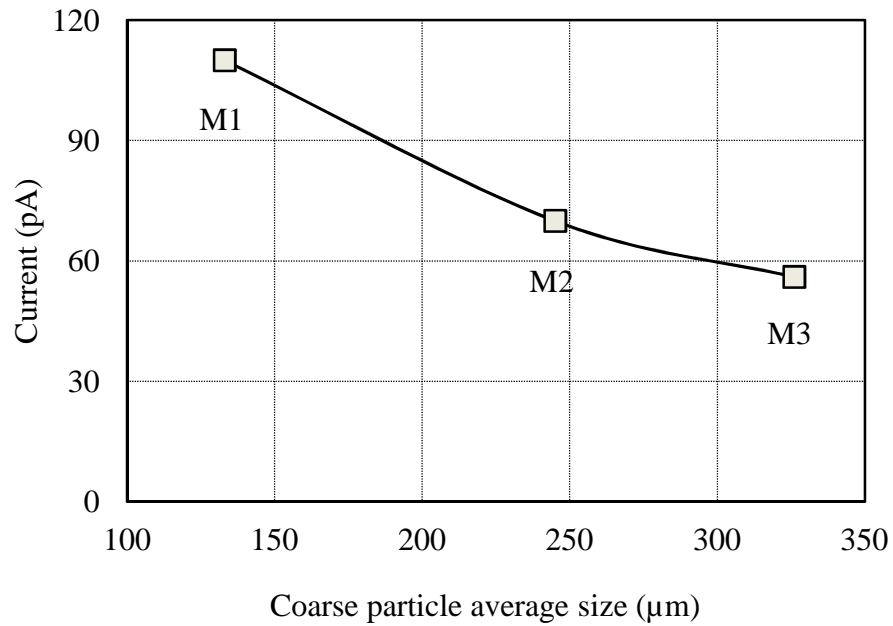


Figure 5.4 Current flow through current detection pipe at column exit as a function of coarse particle average size in beds of binary mixtures M1, M2 and M3. For physical properties of particles, see Tables 2.1, 2.2 and 2.3. $P = 414$ kPa, $T = 20 \pm 2^\circ\text{C}$ and $U_g = 0.3$ m/s. For current detecting pipe details, see Figure 2.6.

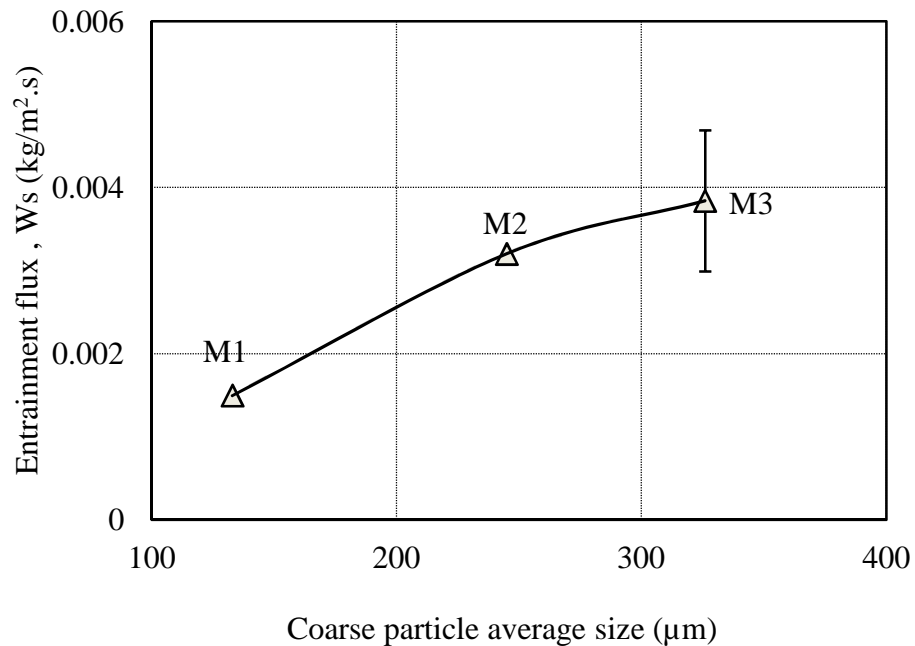


Figure 5.5 Entrainment flux measured from beds of binary mixtures M1, M2 and M3 as a function of coarse particle average size, $P = 414$ kPa, $T = 20 \pm 2^\circ\text{C}$ and $U_g = 0.3$ m/s. For physical properties of particles, see Tables 2.1, 2.2 and 2.3. Error bar corresponds to $\pm 90\%$ confidence interval.

The experimental results presented in Figure 5.1 show that the degree of bed electrification measured in the bed at different levels by probes A, B and C for mixtures M1, M2 and M3 increased as the average diameter of the coarse particles decreased. As well, Figures 5.3, shows that the charges on fines in the freeboard measured the freeboard sampler increased as the average diameter of the coarse particles decreased. It can be seen that the charge density is approximately 2.2 times greater for GBF particles in mixture M1 than for GBF particles in mixture M3 where the coarse particles are larger. Figure 5.4 shows that the current flow through the current detection pipe at the column exit for binary mixture M1 is higher than for mixtures M2 and M3.

These increases in electrostatic charges are likely due to the increase in total surface area of bed particles. As shown in Table 2.3, the specific surface area of particles in mixture M1 is approximately twice that of the particles in mixtures M2 and M3. This higher total surface area is likely to enhance particle-particle and particle-probe collisions and charge generation in the column.

These findings are similar to those reported by Moughrabiah (2009), who investigated the effect of average particle size on electrostatic charge buildup inside the same three-dimensional fluidization column of 0.15 m inner diameter. In his experiments, Moughrabiah used collision ball probes to measure the net cumulative charge locally at different locations in beds of mono-sized glass beads of diameter 693, 574, 365 and 65 μm . The results showed that charge generation in the bed increased as the average particle size decreased. In contrast, Guardiola et al. (1996) studied the effect of average particle size on the degree of bed electrification in a column of 0.044 m inner diameter, with a capacitance probe to measure the average overall electrical potential of the bed for glass beads of diameter 250–297, 297–350 and 350–420 μm . They found that at constant gas velocity, the average electrical potential increased as the particle size increased. These differences in reported results are probably due to differences in experimental conditions such as column diameter, particle size distribution and electrostatic measurement technique.

Figure 5.5 shows that the entrainment flux was lower for M1 than for the M2 and M3 binary mixtures. This could be because the GBF particles in mixture M1 carried higher charges in the freeboard than in mixtures M2 and M3, as shown in Figure 5.3. As a result, particles in M1 have greater fine-coarse particles and fine-wall adhesion, causing a reduction in entrainment flux. Another possible explanation for the lower entrainment flux of M1 is that the average diameter of the coarse particles (GBS) is smaller; therefore, their terminal velocities are lower than for GBM and GBL, increasing the residence time of GBS in the freeboard and leading to more interactions between fast-moving GBF and the slower moving GBS.

Nakazato et al. (2004) investigated the effect of coarse particle size on the entrainment rate of fines at constant superficial gas velocity from a fluidization column containing a binary mixture of FCC particles (group A) and alumina fines (group C). They found that the fines entrainment decreased as the coarse particle size increased. Kato and Li (2001) studied the effect of the mean diameter of bed particles on the entrainment rate of fines in a fluidization column of 0.103 m inner diameter and 2.55 m height containing binary mixtures of alumina (group B) and FCC fines (group C), and another mixture of alumina (group B) and fine alumina (group A). Their results showed that at constant superficial gas velocity the fines entrainment rate decreased as the mean diameter of bed particles increased up to 200 μm . However, when the diameter exceeded 200 μm , the entrainment rate was no longer affected by the mean diameter of the bed particles.

On the other hand, Geldart et al. (1979) performed experiments in a fluidized bed column of 0.076 m inner diameter containing a mixture of sand particles (coarse) and alumina (fines), finding at constant gas velocity that fines entrainment was unaffected by the coarse particles. These findings were similar to those observed by Sanari and Kunii (1962).

5.1.2 Effect of Particle Density and Type

To verify the effect of coarse particle type and density on entrainment rate and electrostatic charge buildup in a fluidized bed, freely bubbling experiments were performed in an elevated-pressure fluidized bed. Experiments were conducted utilizing GBL, HDPE and LDPE as the mono-sized coarser particles and GBF as added fines for binary mixtures M3, M10 and M11 in Table 2.3. For physical properties of the individual particle species, see Tables 2.1 and 2.2.

Experimental conditions were the same as those for the experiments investigating the effect of average particle size. The static bed height was ~ 0.54 m in all cases. To isolate the effect of particle properties, temperature, pressure and superficial air velocity were maintained nearly constant at $20 \pm 2^\circ\text{C}$, 414 kPa and $U_g = 0.3$ m/s, respectively, and relative humidity of the fluidizing air was maintained at $12 \pm 2\%$.

As before, in each experiment, the bed was first fluidized for approximately an hour to achieve steady state before collecting data. Figure 5.6 compares the net cumulative charges measured by the probes in beds of binary mixtures M3 and M10. Figure 5.7 shows the standard deviation of charge fluctuations measured by probe D in the freeboard region after filtering the net cumulative charge curves (high-pass filter, cut-off frequency 0.03 Hz) for different binary mixtures as a function of the superficial gas velocity. The charge density and current flow through the detection pipe are compared for different binary mixtures in Figures 5.8 and 5.9, and plotted versus superficial gas velocity. The influence of particle properties on the solid entrainment flux is shown in Figure 5.10.

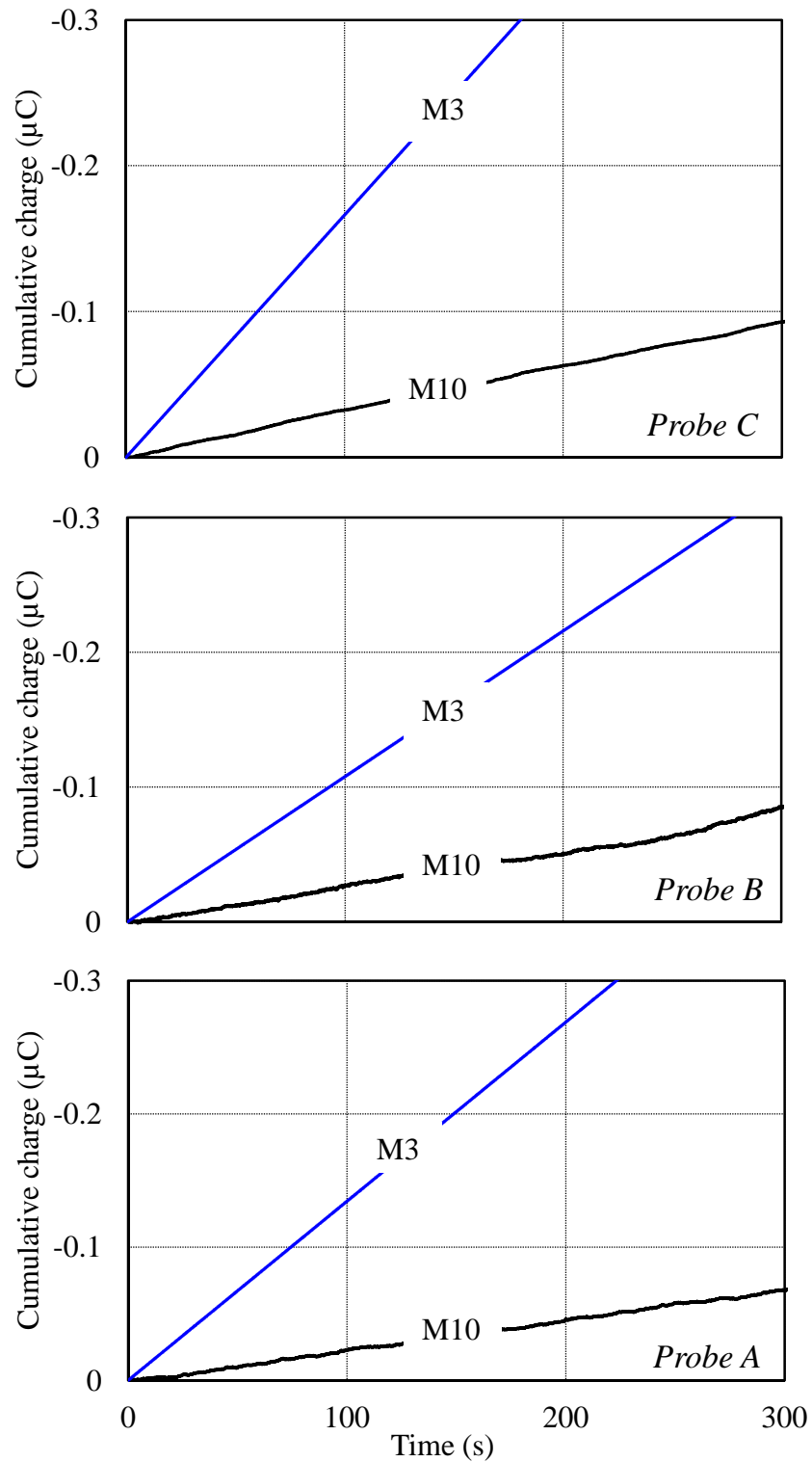


Figure 5.6 Effect of coarse particle type on net cumulative charges as a function of time at different axial positions in beds of binary mixtures M3 and M10. For physical properties of particles, see Tables 2.1, 2.2 and 2.3. $P = 414$ kPa, $T = 20 \pm 2^\circ\text{C}$, and $U_g = 0.3$ m/s. Letters on curves denote mixture types. For probe positions, see Figure 2.4.

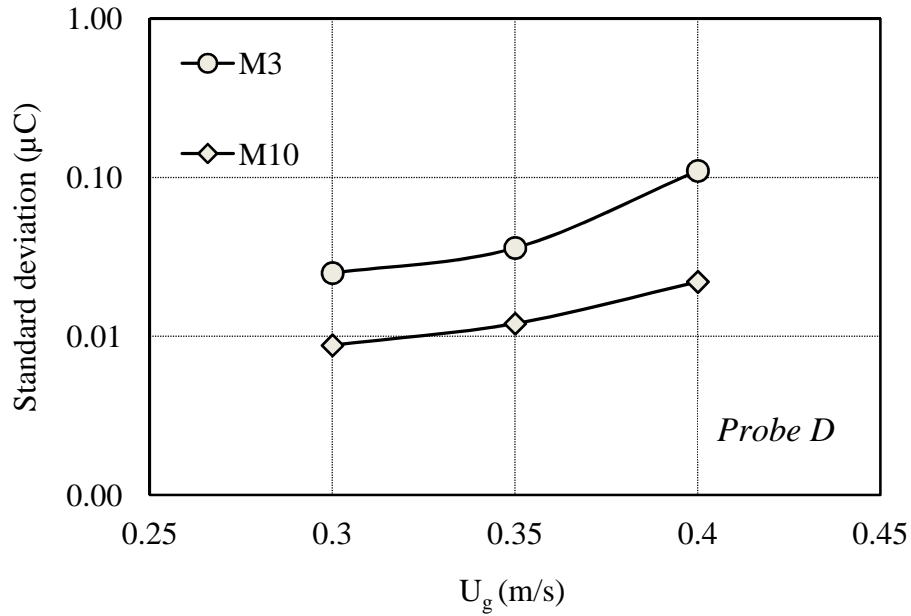


Figure 5.7 Standard deviation of charge fluctuations in the freeboard as a function superficial gas velocity in beds of binary mixtures M3 and M10. For physical properties of particles, see Tables 2.1, 2.2 and 2.3. $P = 414 \text{ kPa}$, $T = 20 \pm 2^\circ\text{C}$. For position of probe D, see Figure 2.4.

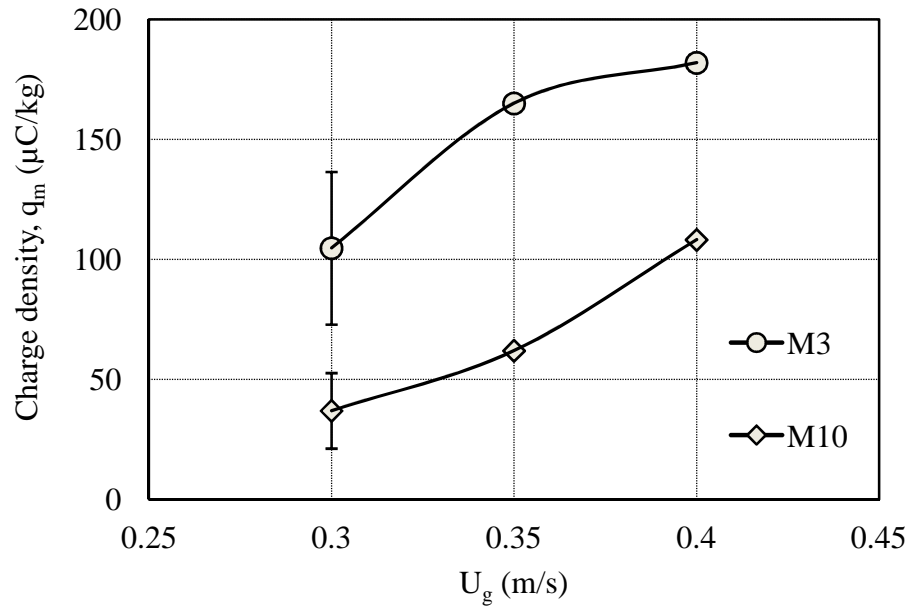


Figure 5.8 Charge density measured by freeboard sampler as a function of superficial gas velocity in beds of binary mixtures M3 and M10. For physical properties of particles, see Tables 2.1, 2.2 and 2.3. $P = 414 \text{ kPa}$, $T = 20 \pm 2^\circ\text{C}$. Error bars correspond to $\pm 90\%$ confidence intervals. For freeboard sampler details, see Figure 2.5.

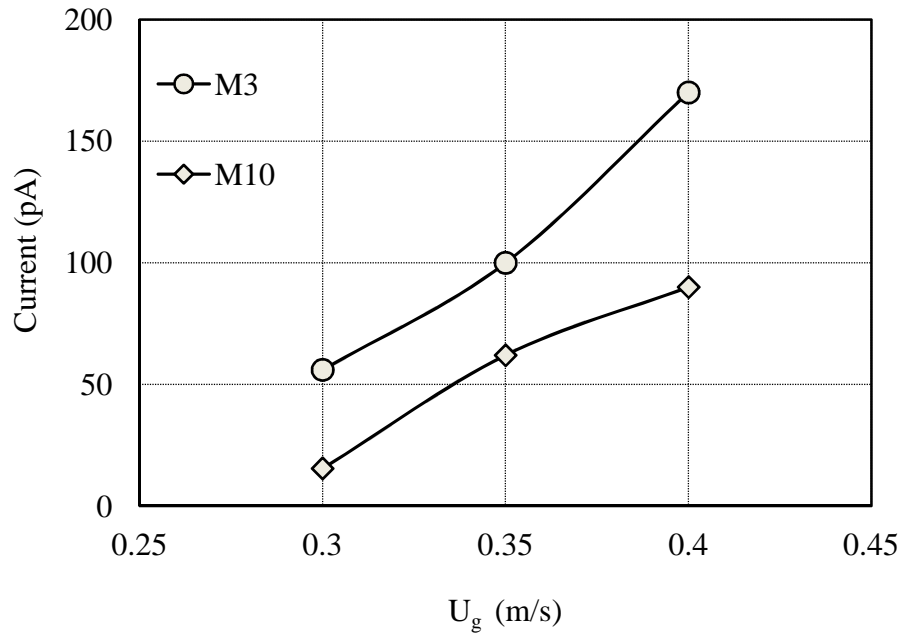


Figure 5.9 Current flow through current detection pipe at column exit as a function of superficial gas velocity in beds of binary mixtures M3 and M10. For physical properties of particles, see Tables 2.1, 2.2 and 2.3. $P = 414$ kPa, $T = 20 \pm 2^\circ\text{C}$. For current detecting pipe details, see Figure 2.6.

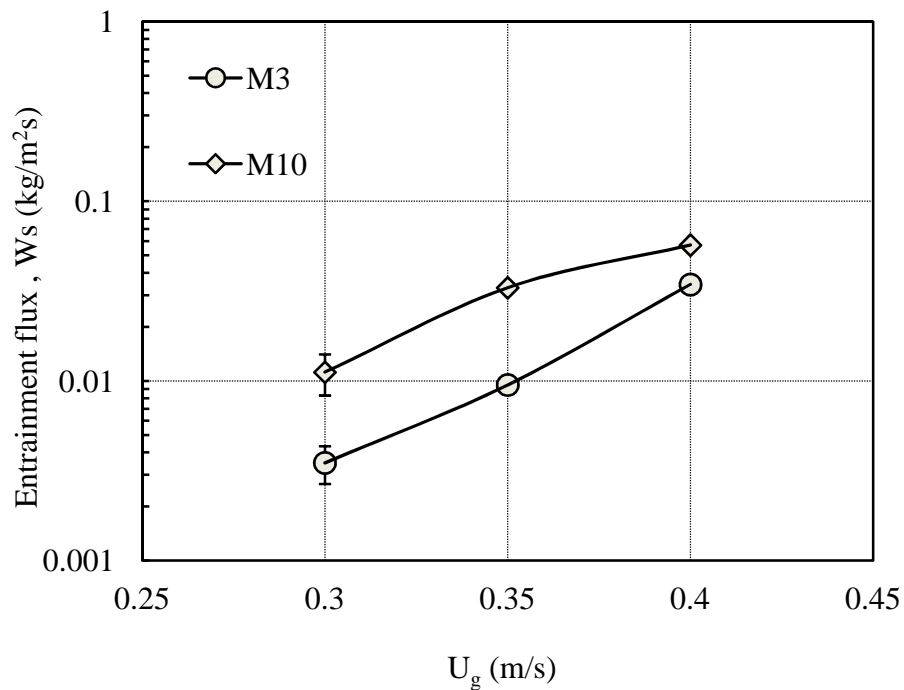


Figure 5.10 Entrainment flux measured from beds of binary mixtures M3 and M10 as a function of superficial gas velocity. $P = 414$ kPa, $T = 20 \pm 2^\circ\text{C}$. For physical properties of particles, see Tables 2.1, 2.2 and 2.3. Error bars correspond to $\pm 90\%$ confidence intervals.

The experimental results presented in Figures 5.6 show that the magnitudes of bed electrification in the bed at different levels for mixture M3 are higher than for mixture M10. Figures 5.7 and 5.8 indicate that charges on the fines in the freeboard measured by probe D and freeboard sampler for mixture M3 are higher than for mixture M10. Figure 5.9 shows that the current flow through the current detection pipe at the column exit for binary mixture M3 is higher than for the M10 mixture. As explained above, this could be due to the sizeable difference between the densities of the coarse particles in the two mixtures. As shown in Table 2.1, the density of GBL in mixture M3 is approximately three times that of the HDPE particles in mixture M10. The high density of GBL likely resulted in higher collision force and, as a result, more electrostatic charge generation. Another possible explanation is that for mixture M3, the coarse particles (GBL) and fines (GBF) were spherical with smooth surfaces, whereas the HDPE particles were non-spherical, with uneven surfaces. This would result in more points of contact between GBL and GBF in mixture M3 than for HDPE and GBF particles in mixture M10, probably enhancing electrostatic charge generation or transfer between the GBL and GBF particles.

The HDPE and GBL coarse particles tested in the above experiments are both dielectric materials. However, based on the material electrical properties, the HDPE is less conductive than the GBL. From Figures 5.3 and 5.8, it can be seen that the electrostatic charges generated inside a bed of GBL/GBF binary mixture were higher than for the HDPE/GBF binary mixture. GBL, being more conductive than HDPE, would dissipate and reduce charge accumulation in the fluidized bed. Guardiola et al. (1992) investigated the effect of added conductive and dielectric materials on the degree of electrification in a fluidized bed. Their results showed that if a conducting material, such as steel, is added to a fluidized bed of a dielectric material, such as glass beads, the charge build-up in the fluidized bed is greatly reduced.

Moughrabiah (2009) investigated the effect of bed particle density on the degree of electrification inside a fluidized bed. He found that the charge generation in the bed was larger for glass beads than for polyethylene particles, and he attributed this result to the sizeable difference between particle densities.

The results in Figure 5.10 show that the entrainment flux was higher for the M10 mixture than for the M3 mixture. This is likely because GBF particles in the M10 mixture carried less charge in the freeboard than the GBF particles in mixture M3, as shown in Figure 5.8. As a result, GBF particles are likely to have formed fewer agglomerates with bed particles, and to have had fewer particles attached to the column wall, with the result that their entrainment flux increased. These results are consistent with those reported by Nakazato et al. (2004) who studied the effect of coarse particle density on the entrainment of fines from a fluidized bed containing binary mixtures of different coarse particles (group A), such as FCC, alumina, limestone, silica, $\text{Al}(\text{OH})_3$ and SiC with densities of 1350, 1400, 2400, 2600, 2300 and 3170 kg/m^3 , respectively, mixed with $\text{Al}(\text{OH})_3$ fines (group C). They found that at constant superficial gas velocity the fines entrainment decreased as the coarse particle density increased. Kato and Li (2001) investigated the effect of coarse particle density on the entrainment rate of fines from a fluidization column. They tested different binary mixtures of coarse particles, such as PVC, alumina, silica and SiC with densities of 950, 1350, 2600 and 3880 kg/m^3 , respectively, mixed with alumina fines. At constant gas velocity the fines entrainment rate was hardly affected by the density of the coarse particles. These different results indicate that different particles behave differently, depending on their properties.

During our experiments, it was observed that charge fluctuations measured by the collision ball probes for mixture M10 was larger than for mixture M3, as shown in Figure 5.6. This is probably due to the effect of the particle surface condition. As mentioned previously, roughness or the condition of particle surfaces is one of the factors influencing electrostatic charge generation and transfer in gas-solids fluidized beds. The SEM images in Figure 2.8 show that GBL particles in mixture M3 have smooth surfaces, whereas the HDPE particles in mixture M10 have uneven surfaces.

To further investigate the effect of particle density on the electrostatic charge buildup and entrainment flux in a fluidized bed containing polyethylene particles of different densities (e.g. HDPE and LDPE), freely bubbling experiments were conducted in our three-dimensional elevated-pressure fluidized bed with HDPE and LDPE as the mono-sized particles and GBF as added fines (binary mixtures M10 and M11, in Table 2.3). For physical properties of particles, see Tables 2.1 and 2.2. Experimental conditions were the same as for

the experiments in which the effects of average particle size and particle density and type were investigated. Static bed height was ~ 0.54 m in all cases. Temperature ($20 \pm 2^\circ\text{C}$) pressure (414 kPa), superficial air velocity ($U_g = 0.3$ m/s) and RH of the fluidizing air ($12 \pm 2\%$) were all maintained nearly constant to isolate the effect of particle properties. In each experiment, the bed was first fluidized for approximately an hour to achieve steady state before collecting data.

Figure 5.11 compares the net cumulative charges measured by the probes in beds of binary mixtures M10 and M11. Figure 5.12 shows the standard deviation of charge fluctuations registered by probe D in the freeboard region after filtering the net cumulative charge curves using a high-pass filter of cut-off frequency 0.03 Hz for both binary mixtures as a function of superficial gas velocity. The charge density and current flow through the detection pipe are compared for different binary mixtures and plotted against superficial gas velocity in Figures 5.13 and 5.14, respectively. Figure 5.15 shows the influence of particle density on the solids entrainment flux.

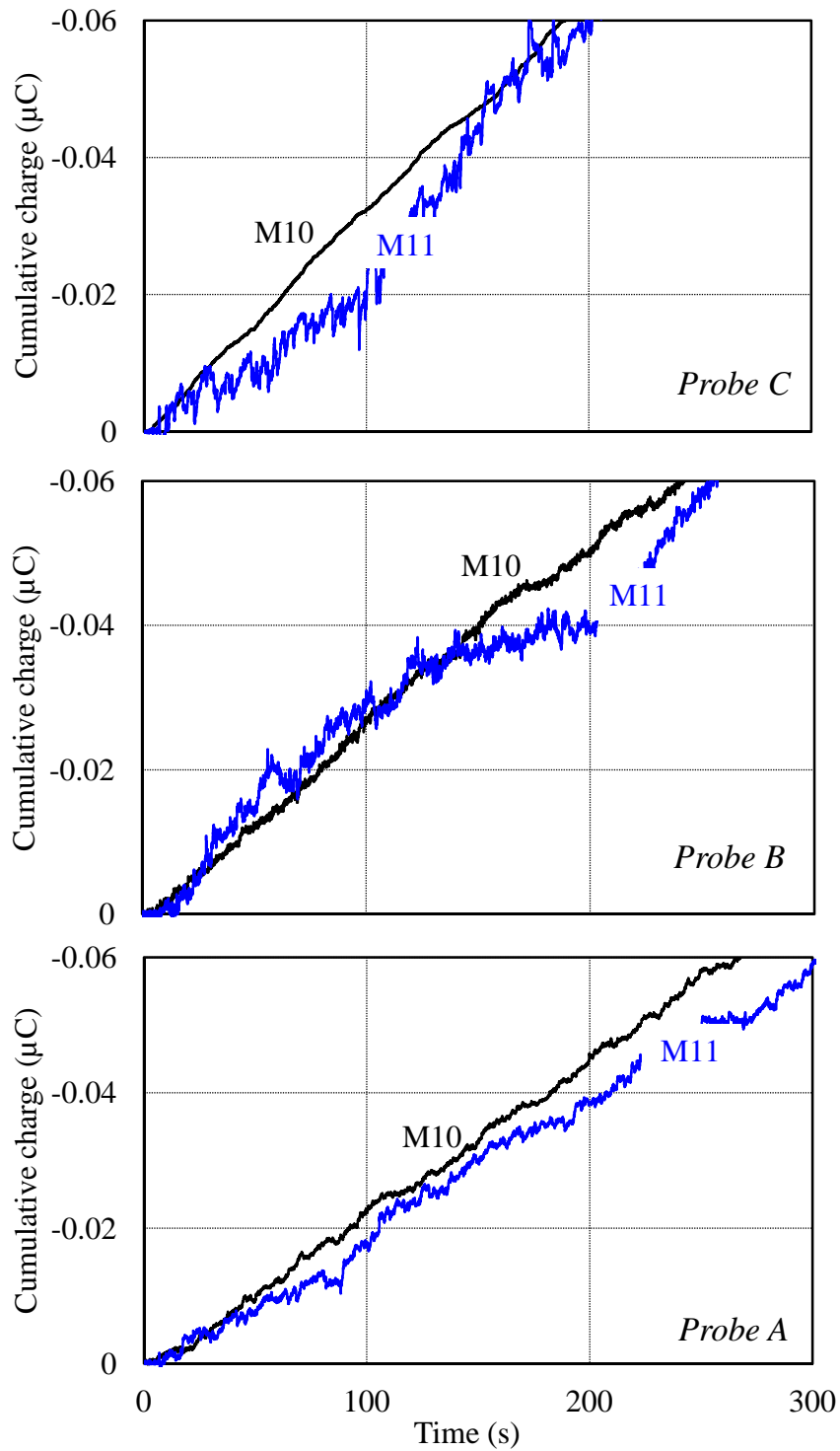


Figure 5.11 Effect of coarse particle type on net cumulative charges as a function of time at different axial positions in beds of binary mixtures M10 and M11. For physical properties of particles, see Tables 2.1, 2.2 and 2.3. $P = 414$ kPa, $T = 20 \pm 2^\circ\text{C}$, and $U_g = 0.3$ m/s. Letters on curves denote mixture types. For probe positions, see Figure 2.4.

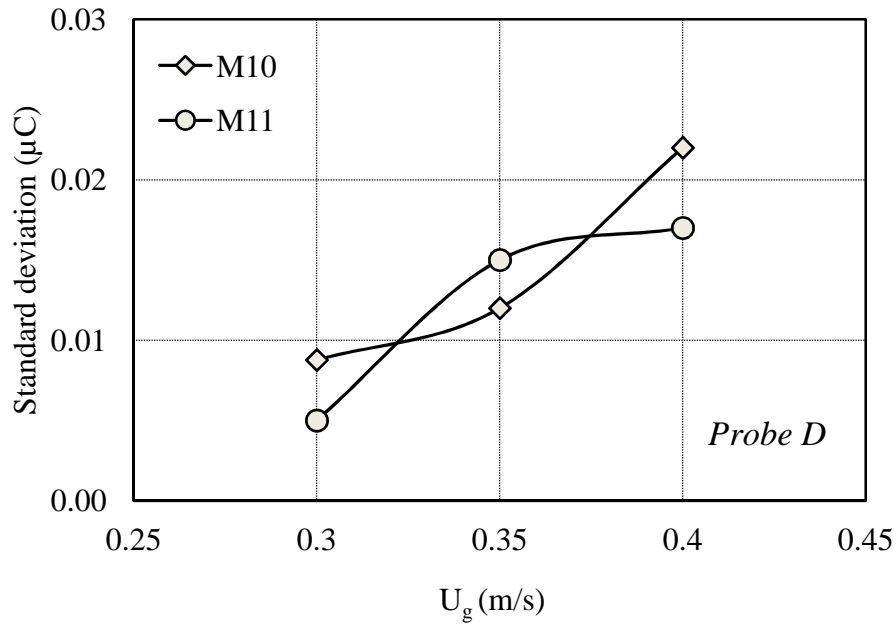


Figure 5.12 Standard deviation of charge fluctuations in the freeboard as a function of superficial gas velocity in beds of binary mixtures M10 and M11. For physical properties of particles, see Tables 2.1, 2.2 and 2.3. $P = 414$ kPa, $T = 20 \pm 2^\circ\text{C}$. For position of probe D, see Figure 2.4.

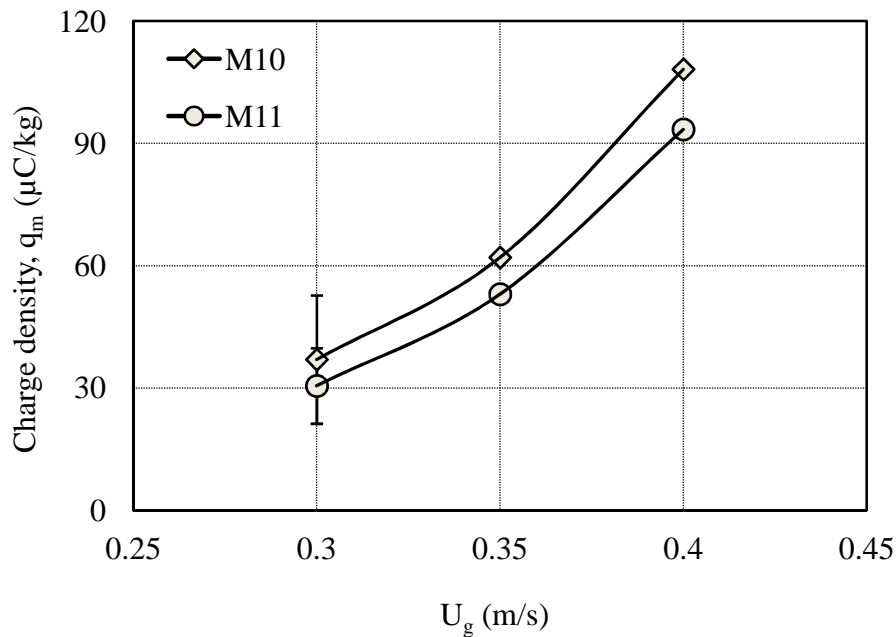


Figure 5.13 Charge density measured by freeboard sampler as a function of superficial gas velocity in beds of binary mixtures M10 and M11. For physical properties of particles, see Tables 2.1, 2.2 and 2.3. $P = 414$ kPa, $T = 20 \pm 2^\circ\text{C}$. Error bars correspond to $\pm 90\%$ confidence intervals. For freeboard sampler details, see Figure 2.5.

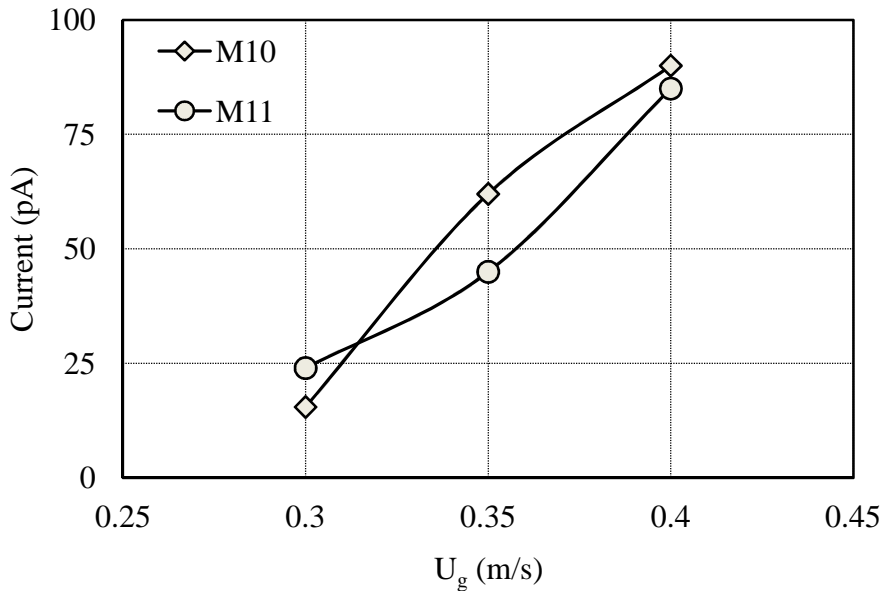


Figure 5.14 Current flow through current detection pipe at column exit as a function of superficial gas velocity in beds of binary mixtures M10 and M11. For physical properties of particles, see Tables 2.1, 2.2 and 2.3. $P = 414$ kPa, $T = 20 \pm 2^\circ\text{C}$. For current detecting pipe details, see Figure 2.6.

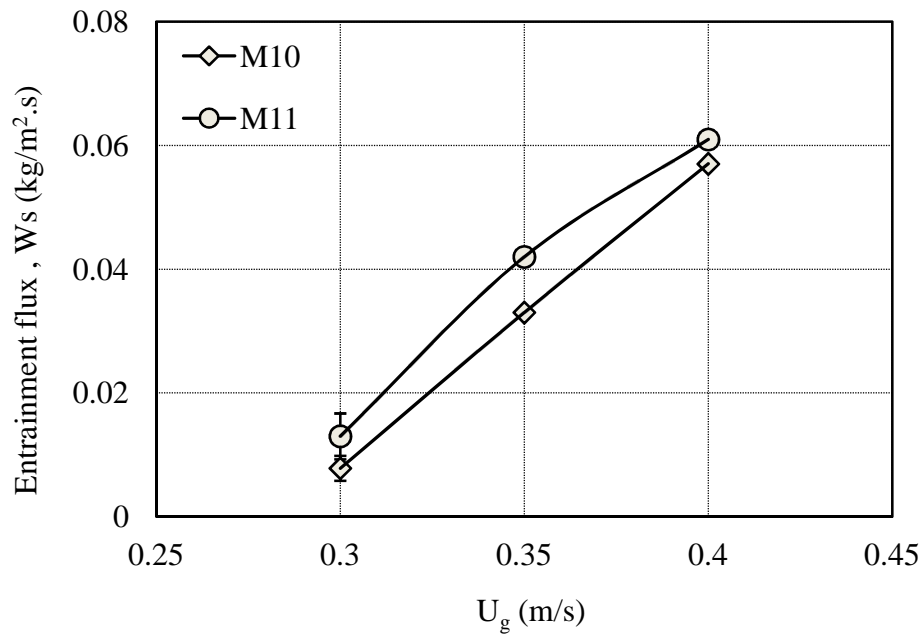


Figure 5.15 Entrainment flux measured from beds of binary mixtures M10 and M11 as a function of superficial gas velocity. $P = 414$ kPa, $T = 20 \pm 2^\circ\text{C}$. For physical properties of particles, see Tables 2.1, 2.2 and 2.3. Error bars correspond to $\pm 90\%$ confidence intervals.

The experimental results presented in Figure 5.11 show that the degree of bed electrification measured in the bed at different levels by probes A, B and C for the M10 and M11 mixtures are similar. Figures 5.12 and 5.13 indicate that charges of fines in the freeboard measured by probe D and freeboard sampler for M10 and M11 mixtures were not significantly affected by the density of polyethylene coarse particles. From Figure 5.14, we see that the currents measured by the current detection pipe at the column exit for binary mixtures M10 and M11 were almost equal. The results in Figure 5.15 show that the entrainment flux for the M10 and M11 mixtures was hardly affected by the coarse particle density.

Overall, the results in Figures 5.11–5.15 suggest that the electrostatic charges and entrainment flux are nearly independent of the density of the polyethylene coarse particles. This result may be attributed to the small difference in density between the experimental HDPE and LDPE in the M10 and M11 binary mixtures.

5.1.3 Summary

The influences of coarse particle average size, type and density on cumulative charge, charge density and entrainment flux were investigated. Freely bubbling experiments in fluidized beds of binary mixtures of group A fines with different sizes of group B particles indicate that the magnitude of net cumulative charges generated inside a fluidized bed increased slightly as the size of the coarse particles decreased. This is probably due to the increase in total surface area of the bed particles. However, since GBF particles in mixture M1 carried more charge and coarse particles had higher residence time in the freeboard, the entrainment from the M1 mixture was slightly lower than for M2 and M3 mixtures. In experiments with binary mixtures of group A and different types of group B particles, the experimental data showed that electrostatic charges increased and entrainment flux decreased as the coarse particle density increased. This is likely due to the sizeable difference between coarse particle densities and surface properties. The entrainment fluxes for the M10 and M11 mixtures were higher than for the M3 mixture. This is probably because GBF particles in M10 and M11 mixtures carried less charge, leading to reduced agglomeration and fewer particles clinging to the inner wall of the column.

5.2 Effect of Fine Particle Properties

5.2.1 Effect of Fines Density and Type

To investigate the effect of fines density and type on the electrostatic behavior and entrainment flux, free-bubbling experiments were conducted in an elevated-pressure fluidized bed with GBL as the mono-sized coarse particles and GBF, Al_2O_3 and PEF fines were added to provide binary mixtures M3, M6 and M9, in Table 2.3. For physical properties, see Tables 2.1 and 2.2. As before, experimental conditions did not change. The static bed height was ~ 0.54 m in all experiments. To isolate the effect of particle properties, the temperature, pressure and superficial air velocity were maintained as constant as possible at $20 \pm 2^\circ\text{C}$, 414 kPa and $U_g = 0.3$ m/s, respectively, and the relative humidity of the fluidizing air was maintained at $12 \pm 2\%$. Before collecting data, the bed was again fluidized for approximately an hour to achieve steady state.

Figure 5.16 compares the net cumulative charges measured by the probes in beds of binary mixtures M3, M6 and M9. Figure 5.17 plots the standard deviation of charge fluctuations registered by probe D in the freeboard region. The net cumulative charge curves for different binary mixtures as a function of superficial gas velocity were filtered using a high-pass filter of cut-off frequency of 0.03 Hz. The charge density and the current flow through the detection pipe are compared for different binary mixtures and plotted versus superficial gas velocity in Figures 5.18 and 5.19, respectively. The influence of particle properties on the solid entrainment flux is shown in Figure 5.20.

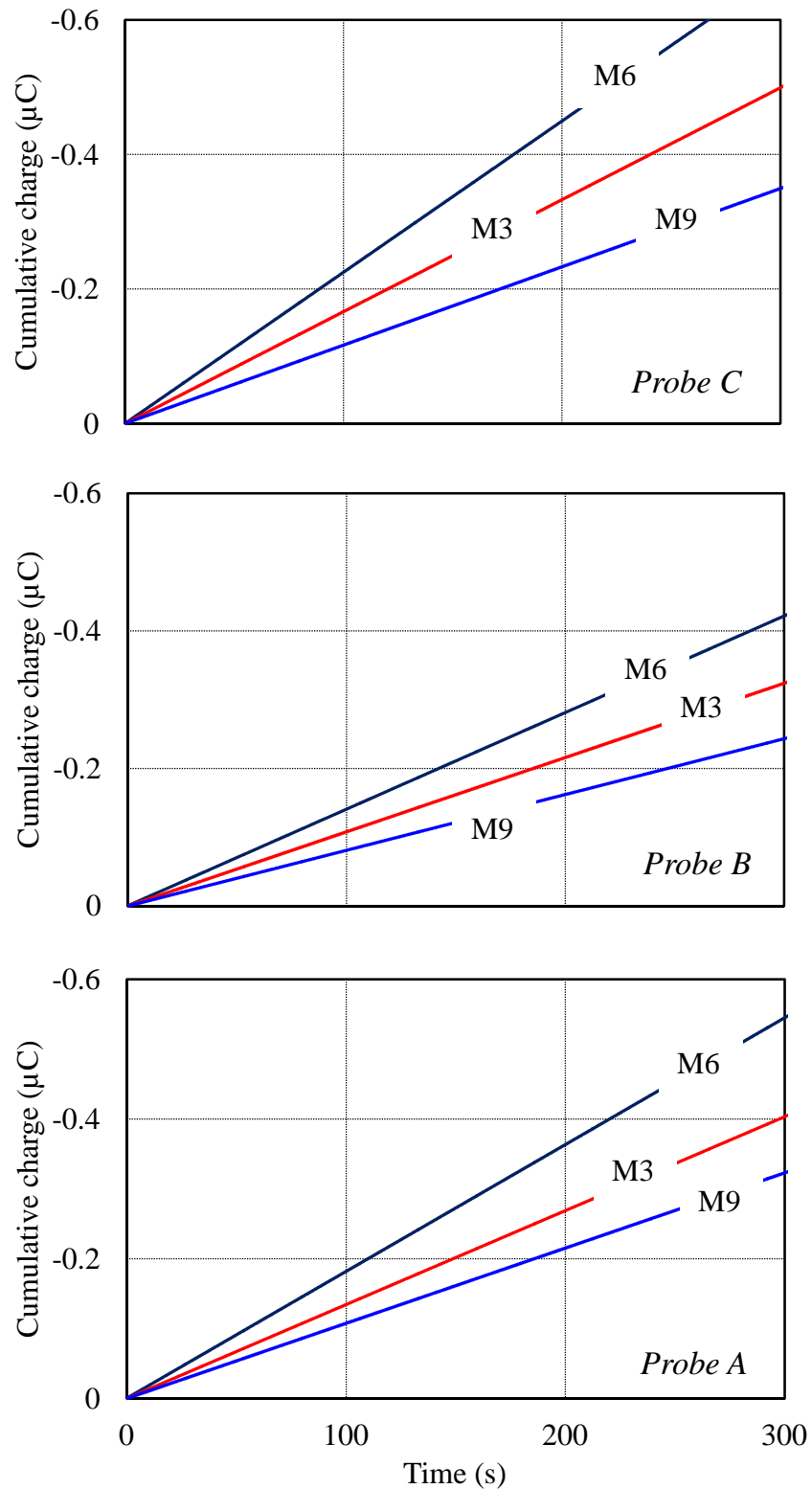


Figure 5.16 Effect of fine types on net cumulative charges as a function of time at different axial positions in beds of binary mixtures M3, M6 and M9. For physical properties of particles, see Tables 2.1, 2.2 and 2.3. $P = 414 \text{ kPa}$, $T = 20 \pm 2^\circ\text{C}$, and $U_g = 0.3 \text{ m/s}$. Letters on curves denote mixture types. For probe positions, see Figure 2.4.

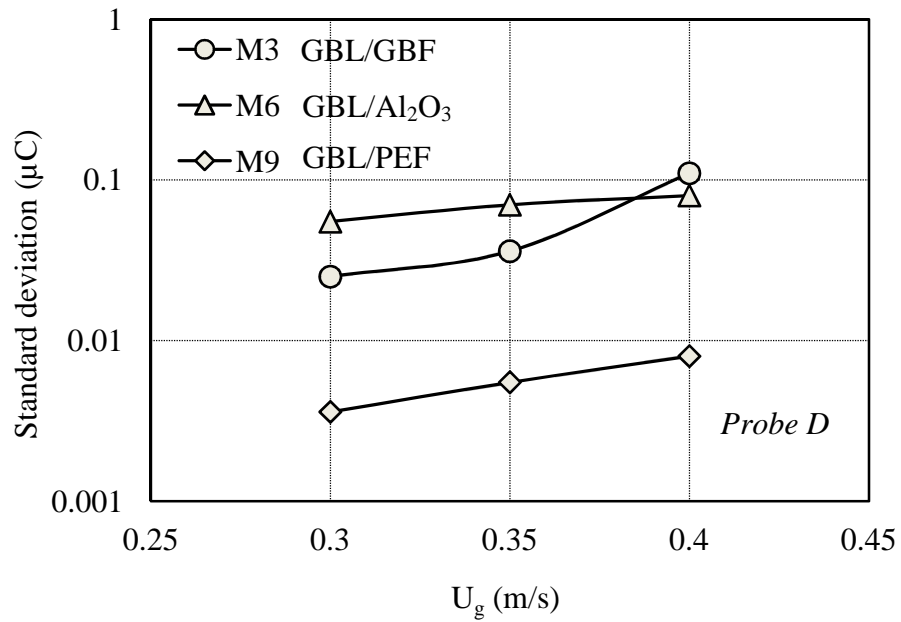


Figure 5.17 Standard deviation of charge fluctuations in the freeboard as a function of superficial gas velocity in beds of binary mixtures M3, M6 and M9. For physical properties of particles, see Tables 2.1, 2.2 and 2.3. $P = 414$ kPa, $T = 20 \pm 2^\circ\text{C}$. For position of probe D, see Figure 2.4.

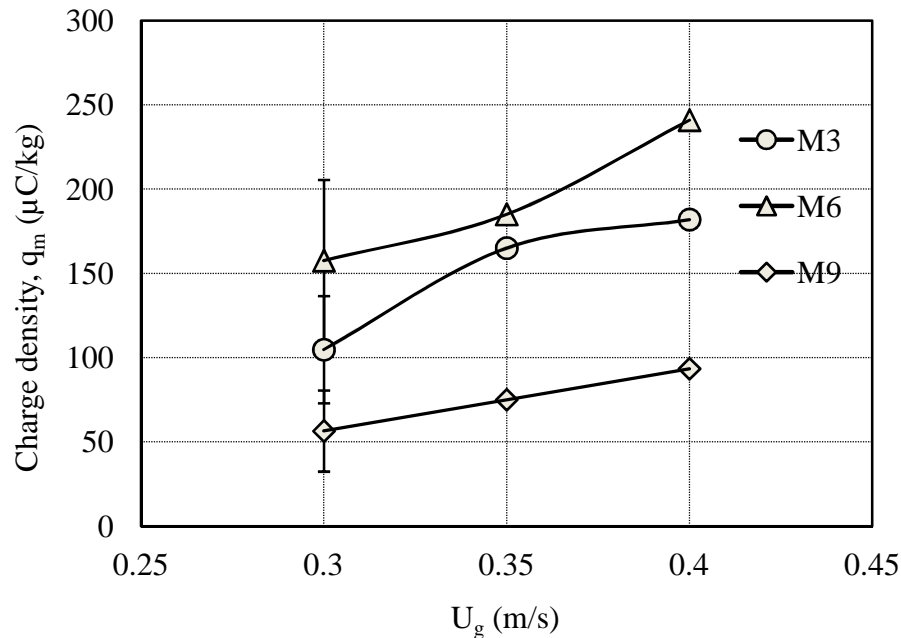


Figure 5.18 Charge density measured by freeboard sampler as a function of superficial gas velocity in beds of binary mixtures M3, M6 and M9. For physical properties of particles, see Tables 2.1, 2.2 and 2.3. $P = 414$ kPa, $T = 20 \pm 2^\circ\text{C}$. Error bars correspond to $\pm 90\%$ confidence intervals. For freeboard sampler details, see Figure 2.5.

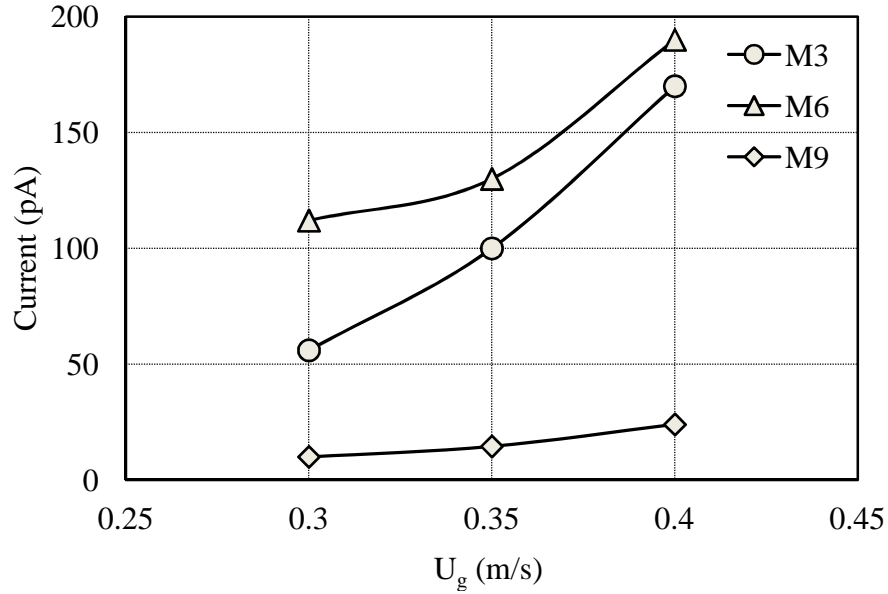


Figure 5.19 Current flow through current detection pipe at column exit as a function of superficial gas velocity in beds of binary mixtures M3, M6 and M9. For physical properties of particles, see Tables 2.1, 2.2 and 2.3. $P = 414 \text{ kPa}$, $T = 20 \pm 2^\circ\text{C}$. For current detecting pipe details, see Figure 2.6.

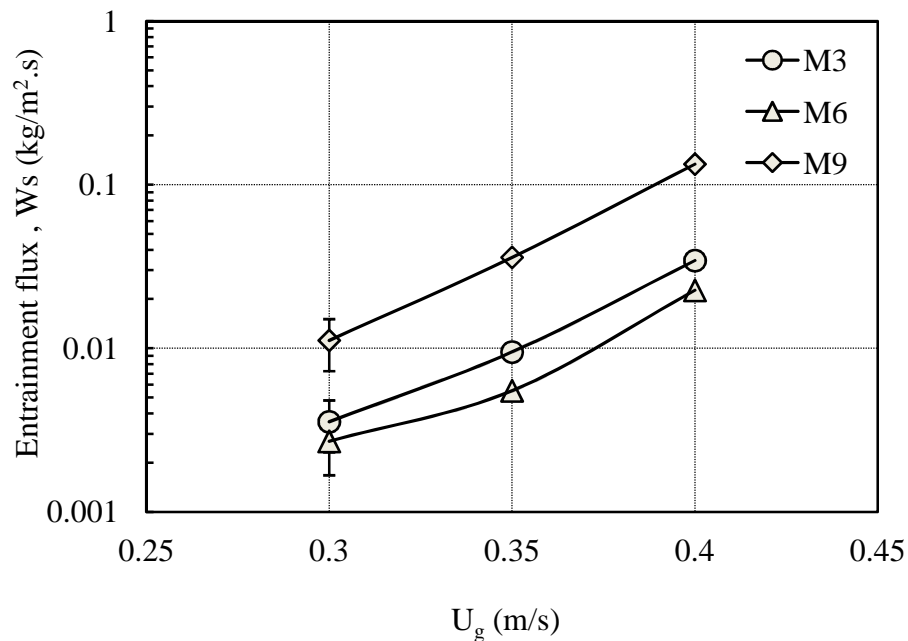


Figure 5.20 Entrainment flux from beds of binary mixtures M3, M6 and M9 as a function of superficial gas velocity. $P = 414 \text{ kPa}$, $T = 20 \pm 2^\circ\text{C}$. For physical properties of particles, see Tables 2.1, 2.2 and 2.3. Error bars correspond to $\pm 90\%$ confidence intervals.

The experimental results in Figures 5.16 show that the magnitude of bed electrification in the bed at different levels for mixtures M3 and M6 are higher than for mixture M9. As well, Figures 5.17 and 5.18 indicate that charges of fines in the freeboard measured by probe D and freeboard sampler for mixtures M3 and M6 are higher than for mixture M9, with the charge density approximately 2.3 times greater for GBF particles (mixture M3) than for the PEF particles (mixture M9). Figure 5.19 shows that the current flow through the current detection pipe at the column exit for binary mixtures M3, M6 are much higher than for mixture M9. These differences could be due to the sizeable differences among the densities of the fine particles in each mixture. As shown in Table 2.2, the densities of GBF and Al_2O_3 in mixtures M3 and M6 are approximately three times that of the PEF fines in mixture M9. As noted previously, gas-solids fluidized beds are subject to continuous collisions among particles and between particles and the column wall. Senior (1992) found that the collision force between two particles is a function of particle density, with the collision force increasing as the particle density increases. In general, as the force at the point of contact between two particles increases, charge transfer also increases (Montgomery, 1959). Therefore, in our experiments, the higher density of GBF and Al_2O_3 resulted in higher collision forces and, as a result, higher electrostatic charge generation than for the less dense PEF fines. It is also possible that the higher electrostatic charges in the bed and freeboard for mixtures M3 and M6 may be partially due to different physical surface structures of GBF and Al_2O_3 , as portrayed in Figure 2.8 where SEM images show that GBF and Al_2O_3 particles are nearly spherical and have smooth surfaces, whereas the PEF particles are non-spherical with uneven surfaces. In these experiments, it was observed that GBF and Al_2O_3 fine particles behaved in a similar manner, which was expected because they have similar surface conditions and sphericity, with little difference between their particle densities. In addition, from Figure 2.7, it can be seen that the bed particles (GBL) are spherical with smooth surfaces, resulting in fewer points of contact between them and PEF than for the GBF and Al_2O_3 fine particles. Therefore, there is probably less electrostatic charge generation or transfer between the GBL and PEF particles.

In the above experiments, all the fines tested are classified as dielectric materials. The dielectric constants of GBF and Al_2O_3 are higher than for PEF, meaning they have more ability to hold large quantities of electrical charge for longer periods. From Figure 5.18, it

can be seen that the charge densities of the GBF and Al_2O_3 fine particles were higher than for the PEF particles. Wolny et al. (1983) studied the effect of electrical properties of fines by adding conductive, semi-conductive and dielectric fine materials to beds of polystyrene, finding that the electrical nature of the fines had negligible impact on the charge of the bed.

Mehrani et al. (2007b) studied the electrostatic behaviour of different fines (glass beads, silica and polyethylene catalyst) added to a Faraday cup fluidized bed and found that the charges carried by the fines depended on the physical properties and size of the fine particles.

The results in Figure 5.20 show that the entrainment flux was nearly one order of magnitude larger for PEF than for the GBF and Al_2O_3 fine particles. This could be because PEF particles carried less charge in the freeboard compared to the GBF and Al_2O_3 particles, as shown in Figure 5.18. As a result, the PEF particles formed fewer agglomerates with bed particles and possibly fewer fine particles would cling to the column wall, resulting in greater entrainment flux. In the experiments with the GBF, Al_2O_3 and PEF particles, after discharging the particles from the column, a thin layer of fines was observed in each case adhering to the inner surface of the column wall.

Briens et al. (1992) measured the entrainment flux from a bed of polyethylene particles and found that the entrainment flux increased after neutralizing the bed charges, indicating that particle charges affected the entrainment flux.

Another possible explanation for the higher entrainment flux of PEF is that PEF fine particles are less dense; therefore, their terminal velocities are less than for GBF and Al_2O_3 , making them more entrainable. Geldart et al. (1979) investigated the effect of particle density on the entrainment flux in a fluidization column of 0.076 m inner diameter and found that at constant gas velocity, heavier particles had smaller entrainment rates. Wen and Chen (1982) observed a similar trend when studying the effect of the physical properties of sand particles on entrainment flux. On the other hand, Nakazato et al. (2004) investigated the effect of fine particle (group C) density on fines entrainment from a fluidization column of 0.103 m inner diameter containing different binary mixtures of FCC particles (group A) and fines such as $\text{Al}(\text{OH})_3$, alumina and TiO_2 with densities of 2300, 1400 and 3880 kg/m^3 , respectively. They

found that at constant gas velocity the fines entrainment constants were hardly affected by the density of the fine particles.

5.2.2 Effect of Fines Concentration

(a) GBL/GBF Systems

To determine the effect of fines concentration on electrostatic charge buildup in a fluidized bed and entrainment flux, freely bubbling experiments were conducted in the same elevated-pressure column with GBL as the mono-sized coarse particles and GBF as added fines (5, 10 and 15 wt%) for binary mixtures (M3, M4 and M5, in Table 2.3). For physical properties, see Tables 2.1 and 2.2. As before, the static bed height was ~ 0.54 m in all cases. The temperature, pressure and superficial air velocity were maintained nearly constant at $20 \pm 2^\circ\text{C}$, 414 kPa and $U_g = 0.3$ m/s respectively to isolate the effect of particle properties. The relative humidity of the fluidizing air was maintained at $12 \pm 2\%$.

In each experiment, the bed was fluidized for approximately an hour to achieve steady state before collecting data. Then, the net cumulative charge in the bed was measured, as plotted versus time in Figure 5.21. Figure 5.22 shows the standard deviation of charge fluctuations registered by probe D in the freeboard region versus the wt% of GBF particles in the binary mixtures after filtering the net cumulative charge curves using a high-pass filter (cut-off frequency 0.03 Hz). The fines charge density measured in the freeboard is plotted versus the wt% of GBF particles in the mixtures in Figure 5.23. Figure 5.24 shows the current flow through the current detection pipe due to direct charge transfer, as a function of the wt% of GBF particles in the mixtures. The measured entrainment flux is plotted against the wt% of GBF particles in the mixtures in Figure 5.25.

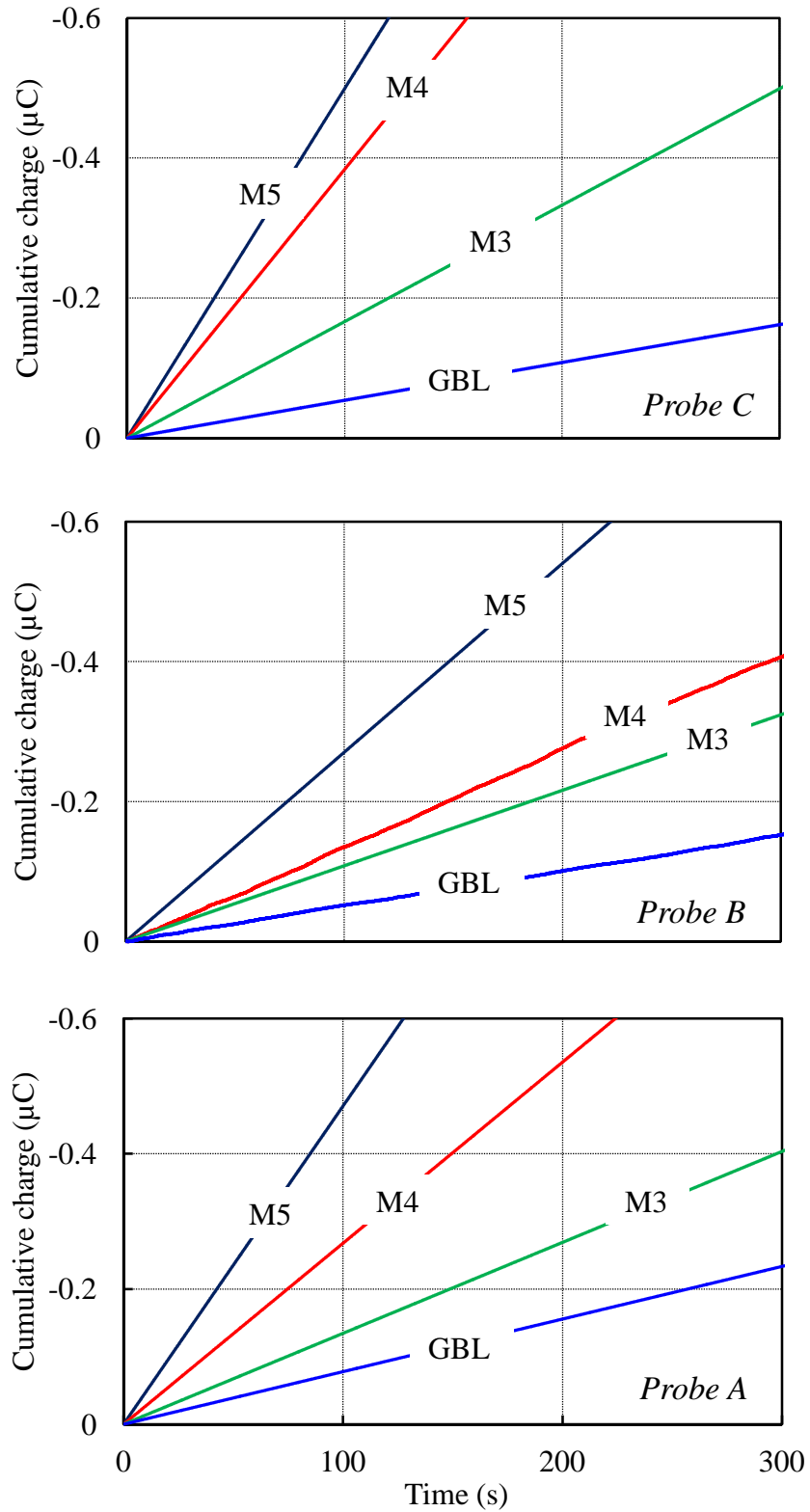


Figure 5.21 Effect of fines concentration on net cumulative charges as a function of time at different axial positions in beds of binary mixtures M3, M4, M5 and mono-size GBL. For physical properties of particles, see Tables 2.1, 2.2 and 2.3. $P = 414 \text{ kPa}$, $T = 20 \pm 2^\circ\text{C}$, and $U_g = 0.3 \text{ m/s}$. Letters on curves denote mixture types. For probe positions, see Figure 2.4.

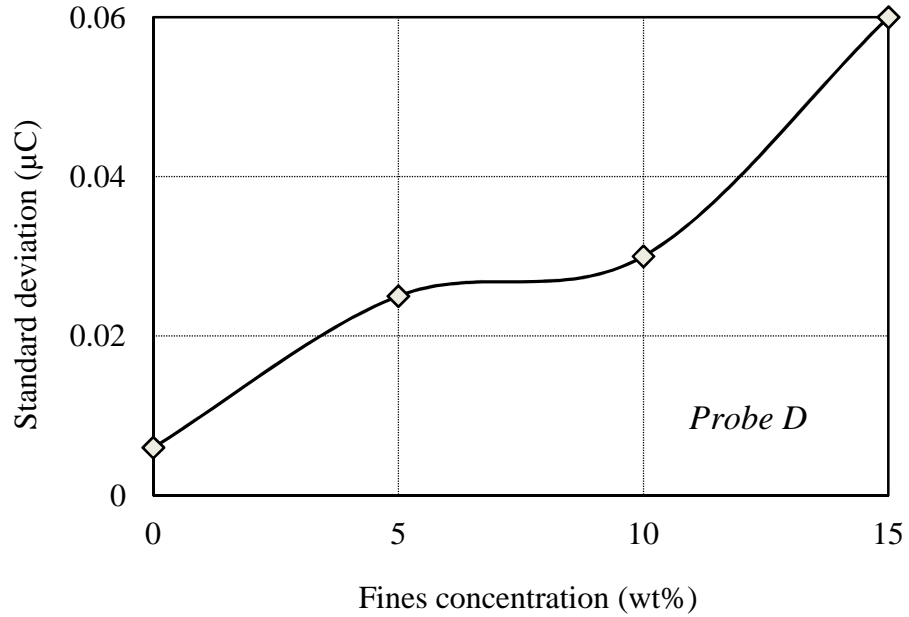


Figure 5.22 Standard deviation of charge fluctuations in the freeboard as a function of fines concentration in beds of binary mixtures M3, M4, M5 and mono-size GBL. For physical properties of particles, see Tables 2.1, 2.2 and 2.3. $P = 414$ kPa, $T = 20 \pm 2^\circ\text{C}$ and $U_g = 0.3$ m/s. For position of probe D, see Figure 2.4.

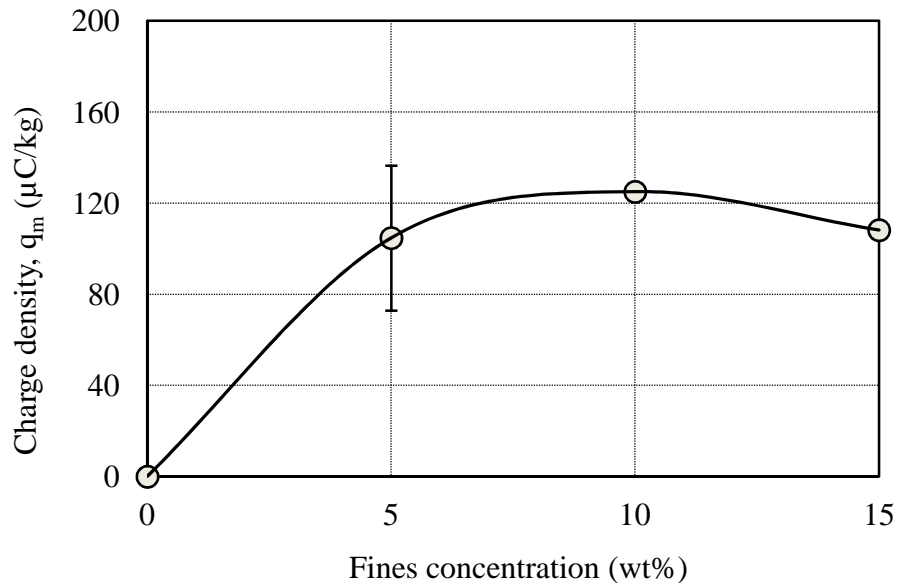


Figure 5.23 Charge density measured by freeboard sampler as a function of fines concentration in beds of binary mixtures M3, M4, M5 and mono-size GBL. For physical properties of particles, see Tables 2.1, 2.2 and 2.3. $P = 414$ kPa, $T = 20 \pm 2^\circ\text{C}$ and $U_g = 0.3$ m/s. Error bar corresponds to $\pm 90\%$ confidence interval. For freeboard sampler details, see Figure 2.5.

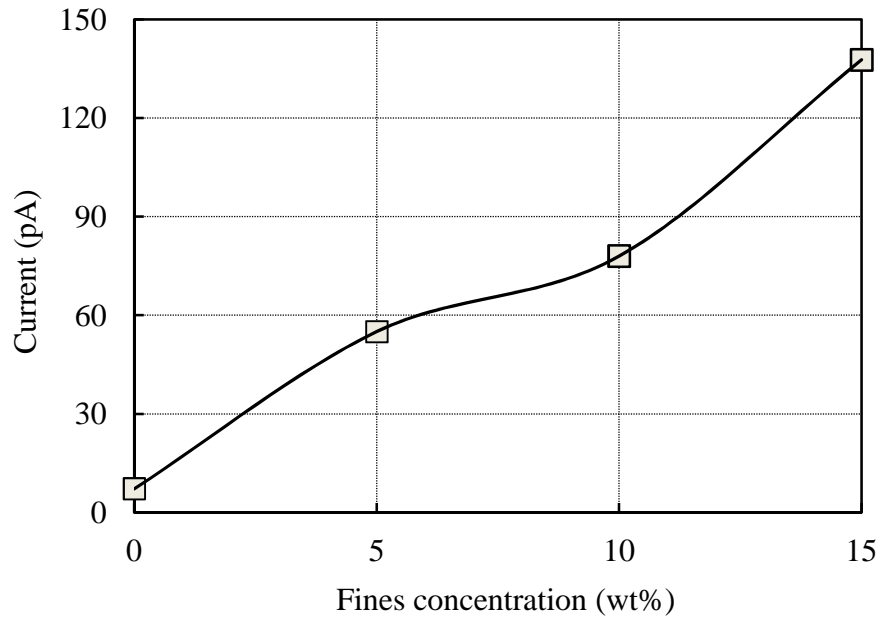


Figure 5.24 Current flow through current detection pipe at column exit as a function of fines concentration in beds of binary mixtures M3, M4, M5 and mono-size GBL. For physical properties of particles, see Tables 2.1, 2.2 and 2.3. $P = 414$ kPa, $T = 20 \pm 2^\circ\text{C}$ and $U_g = 0.3$ m/s. For details of current-detecting pipe, see Figure 2.6.

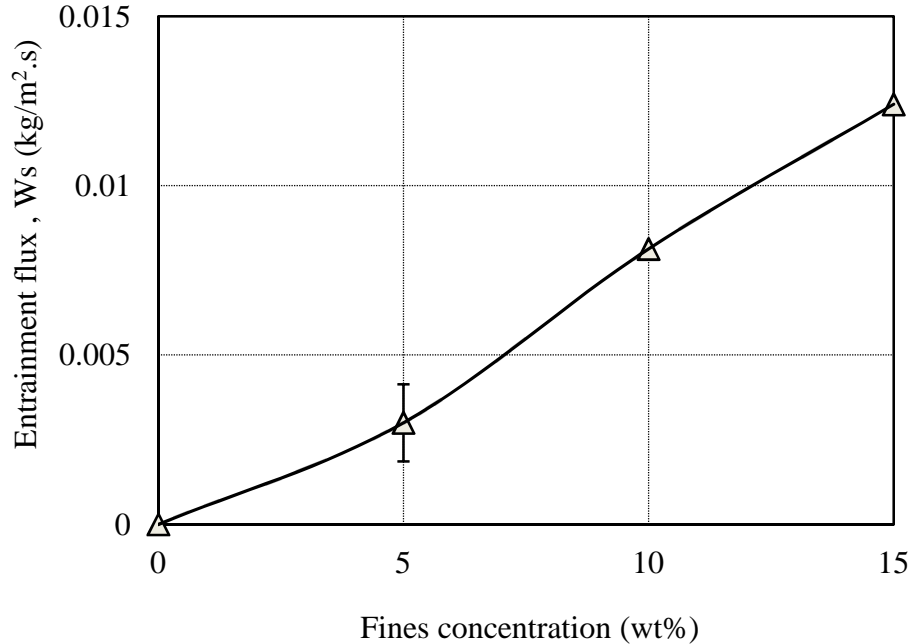


Figure 5.25 Entrainment flux from beds of binary mixtures M3, M4, M5 and mono-size GBL as a function of fines concentration. $P = 414$ kPa, $T = 20 \pm 2^\circ\text{C}$ and $U_g = 0.3$ m/s. For physical properties of particles, see Tables 2.1, 2.2 and 2.3. Error bar corresponds to $\pm 90\%$ confidence interval.

The results in Figures 5.21 and 5.22 indicate that the magnitude of electrostatic charges in the bed measured at different levels by probes A, B and C and the charges of GBF fines in the freeboard region from probe D increased as the proportion of fines in the binary mixtures increased. The higher charges measured for coarse and fine particles in mixtures M5 and M4 than for mixture M3 are probably related to the increase in the surface areas of mixtures as the proportion of GBF particles increased. As shown in Table 2.3, the surface area is approximately twice as large for the M5 mixture as for the M3 mixture. This increase in the surface area is likely to have enhanced the number of particle-particle and particle-wall collisions. The results in Figures 5.21 and 5.22 show that the mono-sized (GBL) particles gain less charges than the binary mixtures, likely because GBL is comprised entirely of large glass beads particles with negligible fines.

These results are consistent with those reported by Moughrabiah et al. (2012) who investigated the effect of increasing the proportion of small particles (10–90 wt %) in binary mixtures of small (group A) and large (group B) glass beads on the degree of bed electrification inside a three-dimensional fluidized bed and reported that the degree of electrification in the bed increased as the proportion of small particles increased. They attributed these results to an increase in collisions among particles and between particles and the column wall.

Figure 5.23 shows that the proportions of GBF particles had little or no impact on the particle charge densities measured in the freeboard region. This is probably because the fine charge and mass increased simultaneously as the fine proportion increased, and as a result the charge density remained constant. In addition, as shown in Figure 5.24, the current flow through the current detection pipe increased as the wt% of fines (GBF particles) in the mixtures increased, indicating an increase in entrainment and particle concentration at the column exit.

The experimental results presented in Figures 5.25 show that, as the proportion of GBF tripled from 5 to 15 wt%, the entrainment flux of fines increased approximately four-fold. Although there was no significant change in the fines charge densities, the increase in entrainment flux was expected because, as noted by Werther and Hartge (2003), it is

commonly held that the entrainment rate of a given size fraction from a gas-solids fluidized bed is proportional to its weight fraction in the bed.

These findings are consistent with those reported by Geldart et al. (1979), who studied the effect of fine weight fractions (0 to 1) on the entrainment flux in a fluidized bed column of 0.076 m inner diameter containing a binary mixture of fine alumina (group A) and larger particles of sand (group B). It was found that at a constant gas velocity the fines entrainment flux increased as the fines weight fraction increased.

Similar results were published by Ma et al. (1996) for a mixture of silica sand and limestone, by Tasirin and Geldart (1998) for a FCC mixture and by Kato and Li (2001) for a mixture of alumina and PVC particles. Each set of authors reported that at constant gas velocity, fines entrainment flux increased as the fines concentration increased. On the other hand, Nakazato et al. (2004) investigated the effect of fines concentrations (1.65 to 30 wt%) on entrainment from a transparent column of 0.103 m inner diameter containing a binary mixture of fines (group C) and group A bed particles. They found that at constant gas velocity the entrainment flux decreased as the fines concentration increased and attributed this to interparticle adhesion forces.

Other researchers (Sycheva and Donat, 1975; Bachovchin et al., 1981; Kage et al., 1992; Baeyens et al., 1992 and Ma and Kato, 1998) reported similar results, finding that the fines concentration has a small effect on the fines entrainment flux. When the fines concentration increased beyond ~ 25%, the entrainment flux decreased as the fines concentration increased. Tasirin and Geldart (1998) attributed the decrease in the entrainment flux observed in their experiments as the fines concentration increased to higher fines hold-up in the freeboard, preventing particles from being entrained.

(b) GBL/Al₂O₃ Systems

Freely bubbling experiments were also conducted in the three-dimensional elevated-pressure column to test the reproducibility of fines concentration results when the coarse particles are composed of different materials. These experiments were performed with GBL as the mono-

sized coarse particles and Al_2O_3 added as the fines (5, 10 and 15 wt%) corresponding to binary mixtures M6, M7 and M8, in Table 2.3. For physical properties, see Tables 2.1 and 2.2. Consistent with previous experiments, static bed height was ~ 0.54 m, and temperature, pressure and superficial air velocity were maintained nearly constant at $20 \pm 2^\circ\text{C}$, 414 kPa and $U_g = 0.3$ m/s respectively to isolate the effect of particle properties. The relative humidity of the fluidizing air was maintained at $12 \pm 2\%$.

In each experiment, the bed was fluidized for approximately an hour to achieve steady state before collecting data. Figure 5.26 shows the net cumulative charge in the bed plotted against time. Figure 5.27 shows the standard deviation of charge fluctuations measured by probe D in the freeboard region versus the wt% of Al_2O_3 particles in the binary mixtures after filtering the net cumulative charge curves using a high-pass filter (cut-off frequency 0.03 Hz). The fines charge density measured in the freeboard is plotted versus the wt% of Al_2O_3 particles in the mixtures in Figure 5.28. Figure 5.29 shows the current flow through the current detection pipe due to direct charge transfer as a function of the wt% of Al_2O_3 particles in the mixtures. Figure 5.30 plots the measured entrainment flux against the wt% of Al_2O_3 particles in the mixtures.

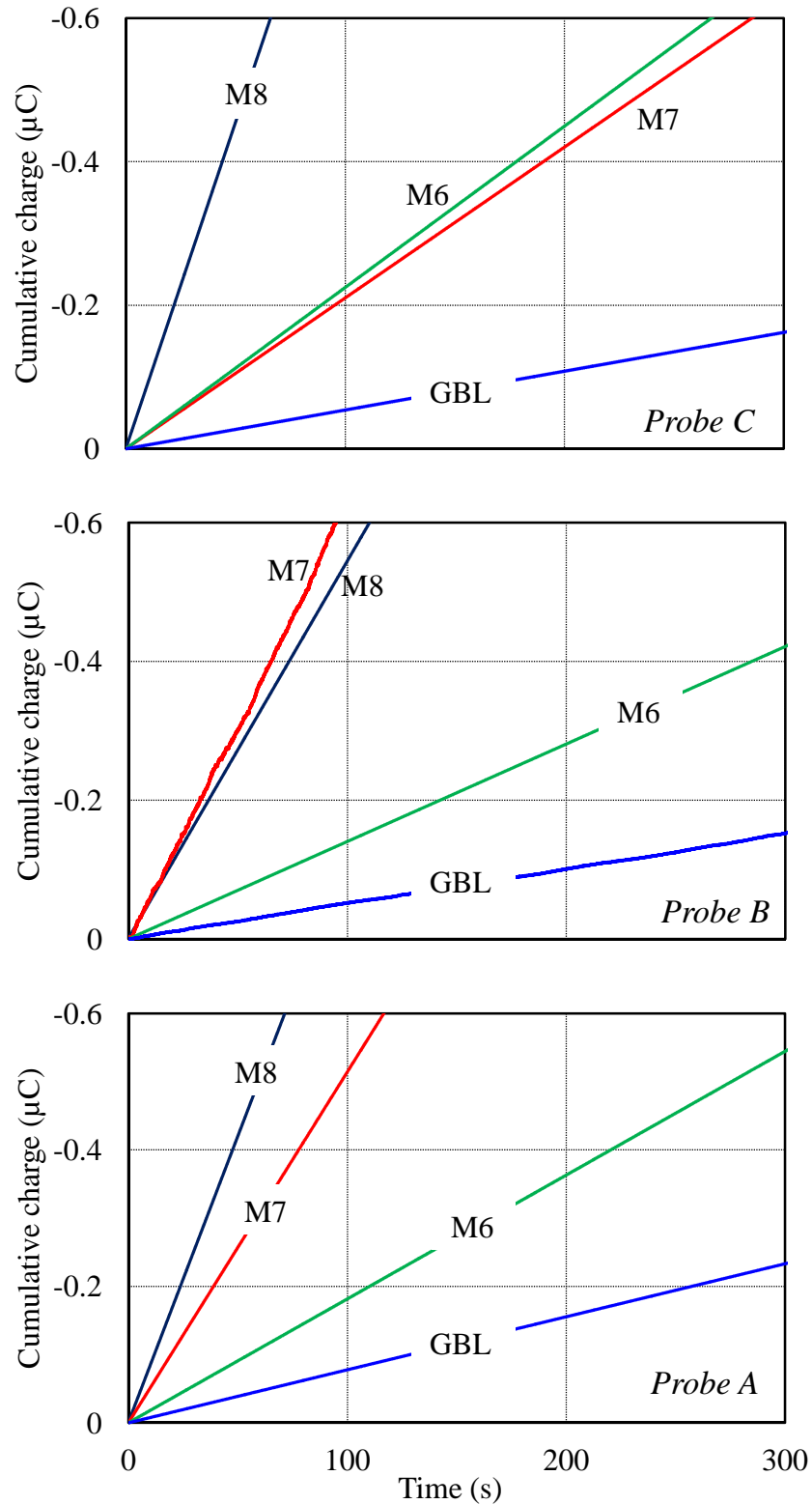


Figure 5.26 Effect of fines concentration on net cumulative charges as a function of time at different axial positions in beds of binary mixtures M6, M7, M8 and mono-size GBL. For physical properties of particles, see Tables 2.1, 2.2 and 2.3. $P = 414 \text{ kPa}$, $T = 20 \pm 2^\circ\text{C}$, and $U_g = 0.3 \text{ m/s}$. Letters on curves denote mixture types. For probe positions, see Figure 2.4.

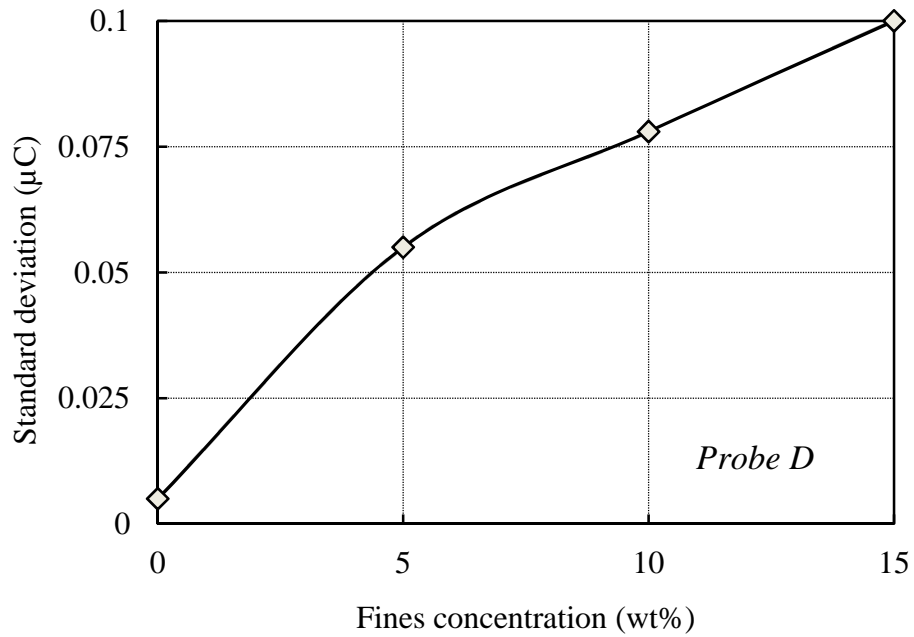


Figure 5.27 Standard deviation of charge fluctuations in the freeboard as a function of fines concentration in beds of binary mixtures M6, M7, M8 and mono-size GBL. For physical properties of particles, see Tables 2.1, 2.2 and 2.3. $P = 414$ kPa, $T = 20 \pm 2^\circ\text{C}$ and $U_g = 0.3$ m/s. For position of probe D, see Figure 2.4.

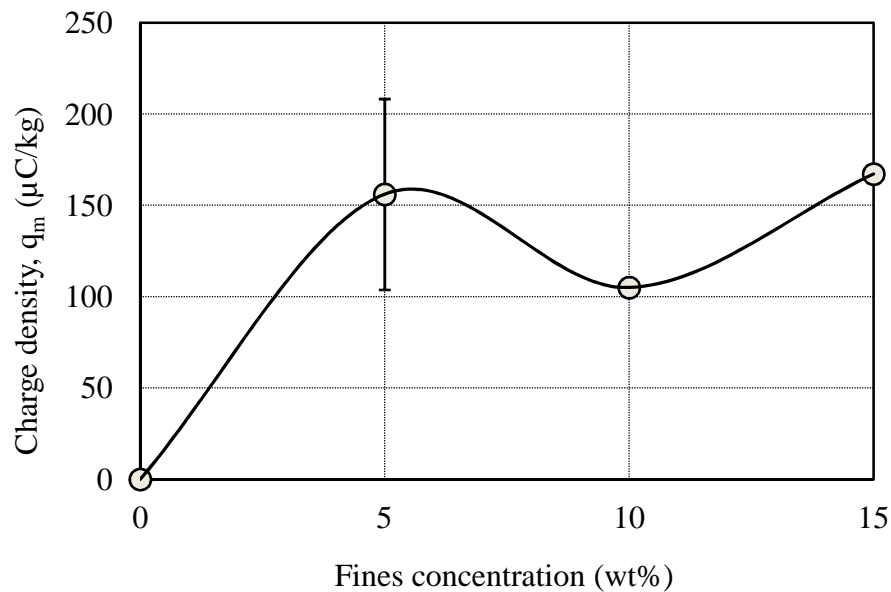


Figure 5.28 Charge density measured by the freeboard sampler as a function of fines concentration in beds of binary mixtures M6, M7, M8 and mono-size GBL. For physical properties of particles, see Tables 2.1, 2.2 and 2.3. $P = 414$ kPa, $T = 20 \pm 2^\circ\text{C}$ and $U_g = 0.3$ m/s. Error bar corresponds to $\pm 90\%$ confidence interval. For freeboard sampler details, see Figure 2.5.

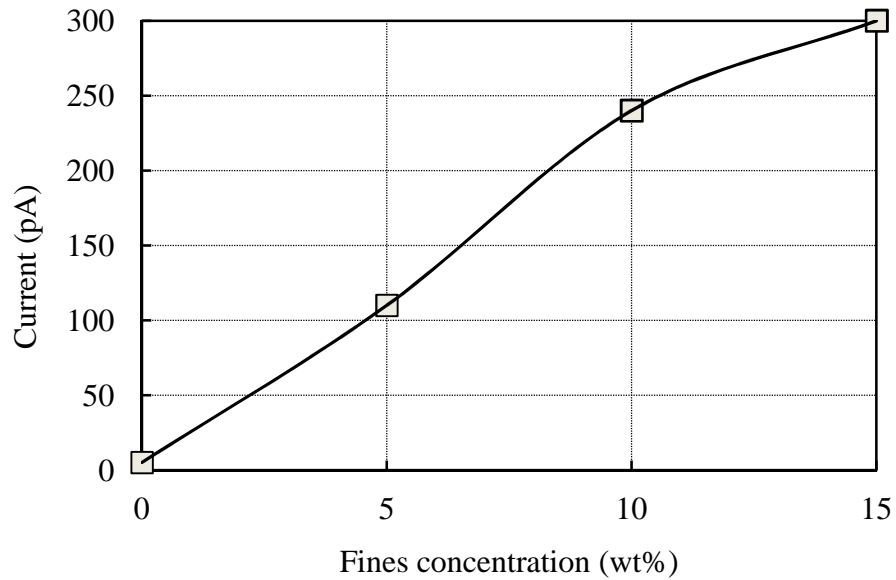


Figure 5.29 Current flow through current detection pipe at column exit as a function of fines concentration in beds of binary mixtures M6, M7, M8 and mono-size GBL. For physical properties of particles, see Tables 2.1, 2.2 and 2.3. $P = 414$ kPa, $T = 20 \pm 2^\circ\text{C}$ and $U_g = 0.3$ m/s. For current detecting pipe details, see Figure 2.6.

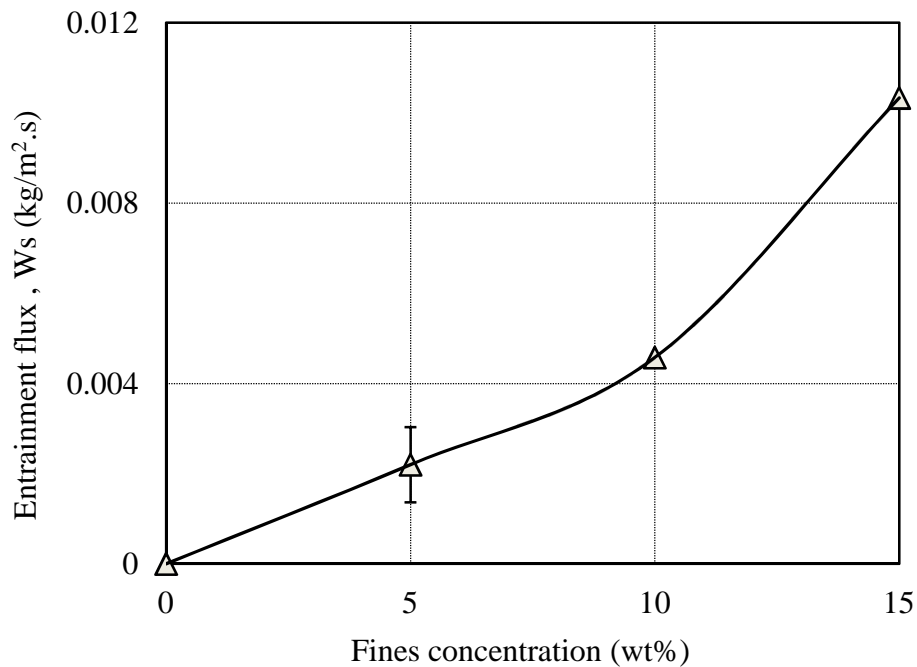


Figure 5.30 Entrainment flux measured from beds of binary mixtures M6, M7, M8 and mono-size GBL as a function of fines concentration. $P = 414$ kPa, $T = 20 \pm 2^\circ\text{C}$ and $U_g = 0.3$ m/s. For physical properties of particles, see Tables 2.1, 2.2 and 2.3. Error bar corresponds to $\pm 90\%$ confidence interval.

It can be seen from the results in Figures 5.26–5.30 that the trends were similar to those for the GBL/GBF experiments, i.e. the GBL/Al₂O₃ system, behaved in a similar manner in these experiments. The experimental results in Figures 5.26 and 5.27 indicate that the electrostatic charges in the bed measured at different levels by probes A, B and C and the charges of Al₂O₃ fines measured in the freeboard region by probe D increased somewhat as the proportion of fines in the mixture increased. The charges measured for coarse and fine particles in mixtures M8 and M7 were higher than for mixture M6. This is probably due to the increase in the surface areas of mixtures as the proportion of Al₂O₃ particles increased, which enhanced the number of particle-particle and particle-wall collisions. Figure 5.28 shows again that increasing the proportion of Al₂O₃ particles had little effect on the particle charge densities measured in the freeboard region. As explained previously, this is probably because the fine charge and mass increased simultaneously as the fine proportion increased, causing the charge density to remain nearly constant.

The results in Figure 5.29 show that the current flow through the current detection pipe increased as the wt% of Al₂O₃ fines in the mixtures increased, indicating an increase in entrainment and particle concentration at the column exit.

In similar manner to Figure 5.25, the experimental results presented in Figures 5.30 show that, as the proportion of Al₂O₃ increased from 5 to 15 wt%, the entrainment flux of fines increased sharply in this case by a factor of approximately 4.6. The results discussed in section 5.2.1 show that the entrainment flux decreased as charge density increased, while in the experiments to test the influence of fines concentration the results show that as the fines concentration increased, the entrainment flux increased even though the charge density did not change. This increase in entrainment flux with constant charge density is probably due to the increase in fines concentration, leading to higher entrainment flux, i.e., due to the presence of more entrainable fine particles.

5.2.3 Bipolar Charging

The charging mechanisms and the charge polarity of contacting surfaces are complex phenomena. Bipolar charging is contact charging between solid particles of the same material, but different sizes. Ali et al. (1998) and Zhao et al. (2000) found that for the same particle material, small particles charged negatively and large ones positively. On the other hand, when Mehrani (2005) and Moughrabiah et al. (2009) performed experiments in fluidized beds involving binary mixtures of large and fine glass beads, they found that the entrained fines were positively charged, whereas the large particles were negatively charged. These differences in findings can be attributed to differences between experiments in terms of particles sizes, structure, physical and chemical surface properties and gas moisture content, which, according to Cross (1987), can influence the charging mechanisms and charge polarity.

In our work, bipolar charging was observed in all experiments. Results for the experiments with binary mixtures of large glass beads (560 μm mean diameter) and fine glass beads (38 μm mean diameter), presented in Figures 5.16–5.19, indicate bipolar charging. From probe A, B and C measurements in the bed; large particles were charged negatively, whereas probe D and current detection measurements in the freeboard region show that fine particles were charged positively. According to the charging mechanisms for binary systems identified by Mehrani (2005), large particles charged negatively due to charge separation between particles and charge separation among the particles and the wall, whereas the fines charged positively due to charge transfer between fines and the wall and charge separation between fines and the large particles in the bed.

Similar results were observed in the experiments with different types of fine particles (Al_2O_3 vs. polyethylene) added to large glass beads, as shown by the results in Figures 5.16–5.19, indicating that although the fines used in this work had different chemical and physical surface properties, they were similar in polarity. Also, the fluidizing gas relative humidity (3–38%) and the fines concentrations (5–15 wt%) of the binary mixtures of large and fine particles did not affect the fines charge polarity, as shown in Figures 4.1-4.4 and 5.26-5.29, respectively.

According to the triboelectric series presented by Cross (1987), when large glass beads (GBL) rub against Al_2O_3 particles, the GBL should be charged positively whereas the Al_2O_3 particles should be charged negatively. In addition, when a GBL particle rubs against a polyethylene fine (PEF) particle, the GBL should be charged positively whereas the PEF particle should be charged negatively. The triboelectric series ranking is surprisingly opposite to what was found in our experiments. As noted previously, the tribocharging mechanism and charge polarity depend on several factors, such as the physical and chemical properties of particles, as well as size, shape and surface impurities. These factors are thought to account for the differences in charge polarity obtained in our experiments compared to the triboelectric series.

5.2.4 Summary

The influences of fine particle type, density and concentrations are investigated in this chapter. Freely bubbling experiments in fluidized beds with binary mixtures of group B and different types of group A particles indicate that the magnitude of net cumulative charges generated inside a fluidized bed with glass and Al_2O_3 fines are higher than for polyethylene fines, probably due to the sizeable difference between the densities and surface properties of these particles. Although PEF fines carried less charge, their entrainment flux was much higher than for GBF and Al_2O_3 . In experiments with binary mixtures of group B and A particles, electrostatic charges and entrainment flux increased as the fines concentration increased, while the proportion of fines had little or no effect on fines charge densities. Bipolar charging was observed in all experiments using large glass beads (GBL) and different fines (GBF, Al_2O_3 and PEF), with the fine particles always charged positively, whereas the large particles were charged negatively. The gas relative humidity (3–38%) and fines concentration (5–15 wt%) had no effect on the polarity of either the large or the fine particles.

Chapter 6: Relationship between Electrostatics and Entrainment

The experimental results presented in Chapters 3, 4 and 5 show that both electrostatics and entrainment are affected by the operating conditions, as well as by particle properties. Entrainment phenomena are extremely complex because they can be affected by a great many parameters. This explains why an accurate model for entrainment from gas-solid fluidized beds has not yet been developed. As noted in Chapter 1, the electrostatic charges generated in fluidized beds could affect the entrainment, but none of the previous correlations in the literature makes any allowance for electrostatic effects. Therefore, in this chapter, we investigate the importance of electrostatics as a factor affecting entrainment, based on the experimental results presented in the earlier chapters. This chapter therefore addresses the last of the five thesis objectives expressed in Chapter 1.

6.1 Comparison of Forces on Particles

In gas-solid fluidized beds, different forces, such as gravitational, drag, electrostatic, and van der Waals forces, act on the particles in the freeboard region. The motion of particles in the freeboard is controlled by the balance of forces exerted on the particle. For large particles, the gravitational force becomes dominant, and those particles tend to fall back to the bed. In contrast, for fine particles, the gravitational forces are less dominant, and other forces, including electrostatic force and drag, become more significant.

Table 6.1 compares the gravitational forces (F_g) and magnitude of the electrostatic forces (F_e) calculated for a pair of particle in contact with each other for different binary mixtures. The electrostatic force magnitudes are calculated based on the electrostatic charges measured in our experiments presented in Chapters 3 and 5 for large and fine particles. F_e is the magnitude of the electrostatic force on a particle in contact with a second particle, where the charge densities are the experimentally measured values, while the separation distances are taken as the sums of the radii of the two particles (see Appendix C for the calculations).

It can be seen from the table that the electrostatic forces resulting from fine-fine and fine-coarse particle interactions are of comparable magnitude to the gravitational force exerted on fine particles in the fluidized bed. This indicates that electrostatic forces can play a major

role and suggests that the presence of fine particles in the fluidized bed results in electrostatic forces, which can greatly influence fine particle motion. On the other hand, the electrostatic forces generated from the interaction between pairs of coarse particles are orders of magnitude lower than the corresponding gravitational force. The lack of importance of electrostatics for coarse particles is due to their relatively low electrostatic charges and the high mass of the large particles compared to the fine particles.

In gas-solid fluidized beds, continuous particle-particle interactions result in electrostatic forces between particles becoming significant compared to gravitational and drag forces. The relatively large electrostatic forces between pairs of fine particles and between fine and coarse particles affect the motion of the fine particle, very likely altering the rate of entrainment. The electrostatic charges can also cause the fine particles to adhere to the column inner wall, as observed in our experiments, once again influencing the entrainment of fine particles from the fluidized bed.

Table 6.1 Comparison of interparticle forces in a fluidized bed for different binary mixtures ($P = 414$ kPa, $T = 20 \pm 2^\circ\text{C}$ and $U_g = 0.3$ m/s).

Binary mixture	Contact between	Force type	F_e , N	F_g , N	$ F_e /F_g$
M3	GBF-GBF	Repulsive	2.29E-09	7.60E-10	3.02E+00
	GBF-GBL	Attractive	-3.55E-10	7.60E-10	4.67E-01
	GBL-GBL	Repulsive	1.02E-09	2.13E-06	4.77E-04
M6	Al2O3-Al2O3	Repulsive	5.71E-09	1.22E-09	4.70E+00
	Al2O3-GBL	Attractive	-9.88E-10	1.22E-09	8.12E-01
	GBL-GBL	Repulsive	2.70E-09	2.13E-06	1.27E-03
M9	PEF-PEF	Repulsive	2.29E-10	4.39E-10	5.21E-01
	PEF-GBL	Attractive	-9.49E-11	4.39E-10	2.16E-01
	GBL-GBL	Repulsive	5.76E-10	2.13E-06	2.70E-04
M10	GBF-GBF	Repulsive	3.10E-10	7.60E-10	4.08E-01
	GBF-HDPE	Attractive	-2.73E-11	7.60E-10	3.59E-02
	HDPE-HDPE	Repulsive	4.62E-11	8.02E-07	5.75E-05

6.2 Relationship between Entrainment and Electrostatics

6.2.1 Derivation of Correlation

As mentioned previously, the entrainment phenomena are complex, with many different parameters playing different roles in determining the number of particles entrained from the fluidized bed. The experimental findings from earlier chapters for different binary mixtures are summarized in Table 6.2. It can be seen that, as the pressure and superficial gas velocity increased, the magnitude of electrostatic charges and entrainment both increased. The bed temperature had relatively little effect on either electrostatics or on entrainment for the limited range of temperature examined.

Table 6.2 Summary of experimental findings from earlier chapters for different binary mixtures. For particle properties, see Tables 2.1, 2.2 and 2.3.

Variable	Operating range	Effect of increasing variable on	
		Electrostatics	Entrainment
Pressure, P (kPa)	207 - 517	Increased	Increased
Superficial gas velocity, U_g (m/s)	0.2 - 0.6	Increased	Increased
Temperature, T (°C)	20 - 75	Negligible	Negligible
RH (%)	3 - 38	Decreased	Increased

From the experimental results presented in Chapter 4 for mixture M3 where only the relative humidity (RH) was varied, a nonlinear regression analysis was performed using a numerical computation package (Polymath 6.1 software- algorithm: Levenberg-Marquardt) to investigate the direct effect of electrostatic forces (F_e) on entrainment while all other operating parameters were held constant. The following correlation was found to provide the best fit to these experimental data ($R^2=0.93$):

$$W_s = 1.3 \times 10^{-7} (F_e)^{-0.464} \quad (6.1)$$

The above correlation shows that there is a direct relationship between electrostatics and entrainment; as electrostatic forces increase, entrainment decreases. The exponent of -0.464 on the (F_e) term indicates a substantial role of electrostatics.

To determine the effect of other operating parameters and electrostatics on entrainment in the fluidized bed, a nonlinear regression analysis was performed (Polymath 6.1) on all the experimental data presented in earlier chapters for different binary mixtures (see Table 2.3). The effect of operating variables, such as pressure, superficial gas velocity, and temperature, in addition to the effect of electrostatics and gravitational forces, were considered in the analysis. The following dimensionless correlation was found to provide the best fit to the experimental data ($R^2=0.84$):

$$\frac{W_s}{\rho_g U_t} = 1.8 \times 10^{-3} \left(\frac{P}{P^\circ}\right)^{1.434} \left(\frac{U_g}{U_t}\right)^{5.071} \left(\frac{T}{T^\circ}\right)^{-0.121} \left(\frac{F_e}{F_g}\right)^{-0.628} \quad (6.2)$$

where W_s , ρ_g , U_t , P° and T° denote the entrainment flux, gas density, particle terminal velocity, ambient pressure, and ambient temperature, respectively. Here P° and T° were taken as 101.3 kPa and 293 K, respectively.

Figure 6.1 compares the entrainment flux calculated from Equation 6.2 with the entrainment flux measured in our experiments. When the electrostatic effects in Equation 6.2 are not considered, the equation gives a poor fit ($R^2 < 0.5$) to the experimental data. This indicates that electrostatic forces play a significant role in determining the entrainment and that the effect of electrostatics on entrainment needs to be recognized. Note that the F_e term in Equation 6.2 is based solely on fine-fine particle interactions. It is likely that fine-coarse particle interactions also affect entrainment, in fact reducing entrainment. However, since the charges on the coarse particles were difficult to measure accurately and were only measured roughly in a few cases, here F_e is based solely on the fine-fine particle electrostatic forces. The amplitude of F_e between fine particles is thus used to represent the magnitude of electrostatic forces between fine and coarse particles in the fluidized bed, which directly link to fine particle entrainment.

Equation 6.2 successfully describes the effect of superficial velocity and pressure and shows that the entrainment increases with both pressure and superficial gas velocity. The correlation also shows that the temperature had very little effect on the entrainment over the temperature range examined. On the other hand, the correlation shows that there is a relationship between electrostatics and entrainment; as electrostatic forces increase, entrainment decreases. The exponent of -0.628 on the (F_e/F_g) term indicates an appreciable role of electrostatics, much more important than the role of temperature, whose exponent is only -0.121. Electrostatics promote attractive forces between fine and coarse particles. Electrostatics also cause fines to adhere to the column inner wall. In this thesis, the goal is not to develop a new generalized correlation for entrainment prediction, given the lack of measurements of electrostatics in previously reported entrainment literature, but rather to find whether or not electrostatics have an appreciable influence on entrainment. The results clearly show that electrostatic charges on entrained particles affect the entrainment of fines.

Clearly, it is difficult to incorporate all relevant factors — the extent of grounding of the reactor and cyclones, dielectric constants, electrical conductivity, etc. — in correlations to predict entrainment. However, designers and operators of fluidized bed processes need to recognize that such factors are likely to affect the extent of entrainment through their influence on electrical charge generation and dissipation.

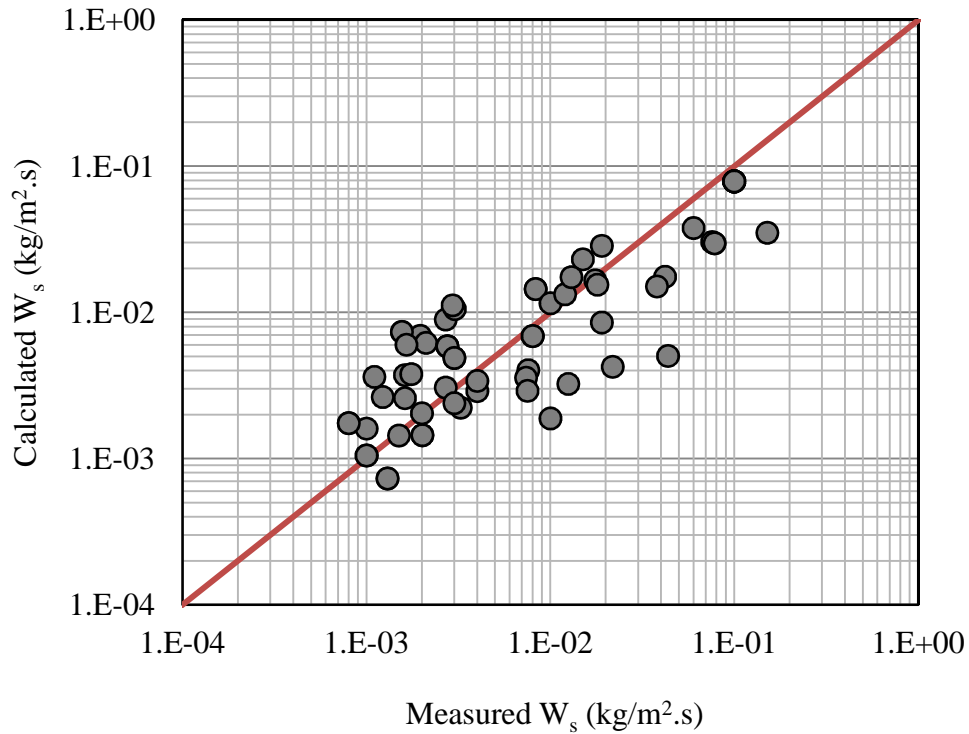


Figure 6.1 Comparison of entrainment flux predicted by empirical correlation (Equation 6.2) with experimentally measured values for different binary mixtures. For physical properties of particles, see Tables 2.1, 2.2 and 2.3.

6.2.2 Comparison of Correlation

As mentioned previously, previous empirical correlations in the literature appear to be inadequate to predict entrainment from fluidized beds. They differ by several orders of magnitude in their predictions, and all of these previous correlations neglect the important effect of electrostatic forces. To further study the effect of electrostatic forces on the entrainment, the measured data in our experiments were compared to the correlation reported by Choi et al. (1999), believed to be the most comprehensive empirical correlation, as it is based on more than 1000 experimental data, and covers a wide range of variables, as shown in Table 6.3.

Table 6.3 Range of variables for the data on which the Choi et al. (1999) correlation is based.

Variable	Choi et al range	Range in this project
Particle diameter, d_p (μm)	21 - 710	38 - 573
Particle density, ρ_p (kg/m^3)	2400 - 6158	797 - 3200
Superficial gas velocity, U_g (m/s)	0.15 - 2.8	0.2 - 0.6
Pressure, P (kPa)	101 - 3200	207 - 517
Temperature, T ($^{\circ}\text{C}$)	12 - 600	22 - 75

Choi et al. (1999) considered the drag and gravity force effects on particle entrainment in their correlation (Equation 6.3), but neglected the effect of electrostatics. Their equation is

$$\frac{W_s d_p}{\mu} = \text{Ar}^{0.5} \exp\left(6.92 - 2.11 F_G^{0.303} - \frac{13.1}{F_d^{0.902}}\right) \quad (6.3)$$

where

$$\text{Ar} = g d_p^3 \rho_g \frac{(\rho_p - \rho_g)}{\mu^2} \quad (6.4)$$

$$F_G = g d_p (\rho_p - \rho_g) \quad (6.5)$$

$$F_d = \rho_g C_d \frac{U_g^2}{2} \quad (6.6)$$

Ar , F_G , and F_d are the Archimedes number, gravitational force, and drag force divided by the projected area, respectively. Figure 6.2 compares the entrainment flux predicted by the Choi et al. (1999) correlation with the experimental values measured in our work. It can be seen that the correlation in most cases overestimates the entrainment flux compared with our measured values.

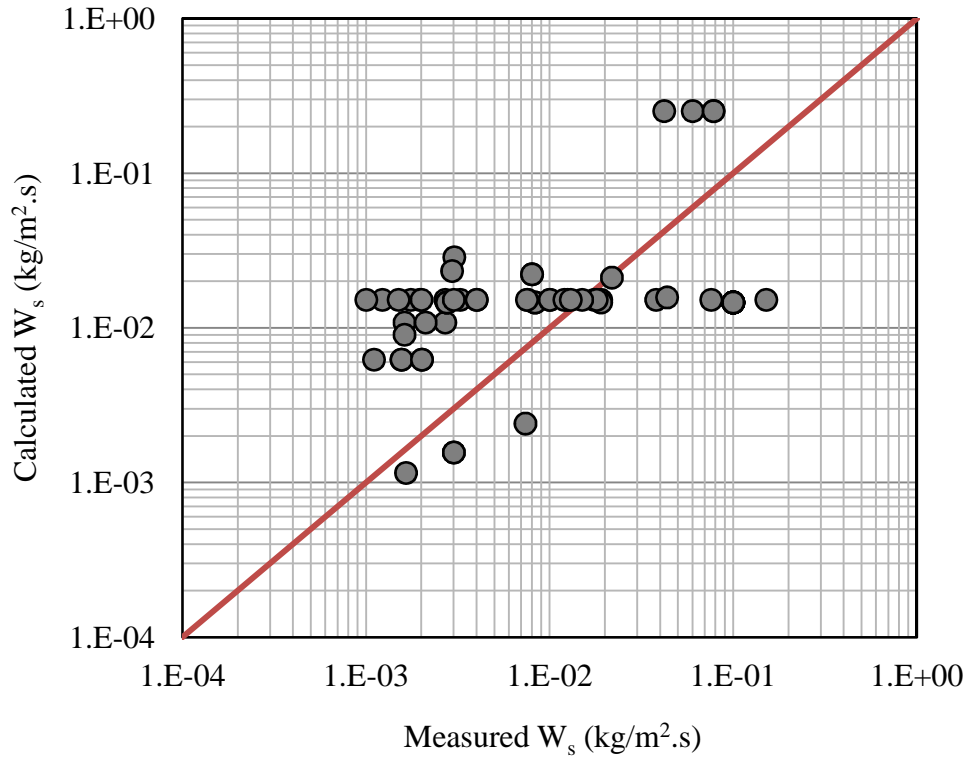


Figure 6.2 Comparison of entrainment flux predicted by Choi et al. (1999) correlation (Equation 6.3) with experimentally measured values for different binary mixtures in this project. For physical properties of particles, see Tables 2.1, 2.2 and 2.3.

The data obtained from our experiments were next refitted to the correlation reported by Choi et al. (1999) using nonlinear regression (using Polymath 6.1 software). The following correlation was found to provide the best fit to our experimental data for an equation of this form ($R^2 < 0.5$).

$$\frac{W_s d_p}{\mu} = Ar^{2.21} \exp \left(12.17 - 2.11 F_G^{0.303} - \frac{22.15}{F_d^{0.218}} \right) \quad (6.7)$$

Figure 6.3 shows the entrainment flux predicted by Choi et al. (1999) after data refitting compared with the experimental values measured in our work. Equation 6.7, which does not consider electrostatic effects, returned significantly less accurate prediction results for our experimental data than Equation 6.2, which included allowance for electrostatic forces.

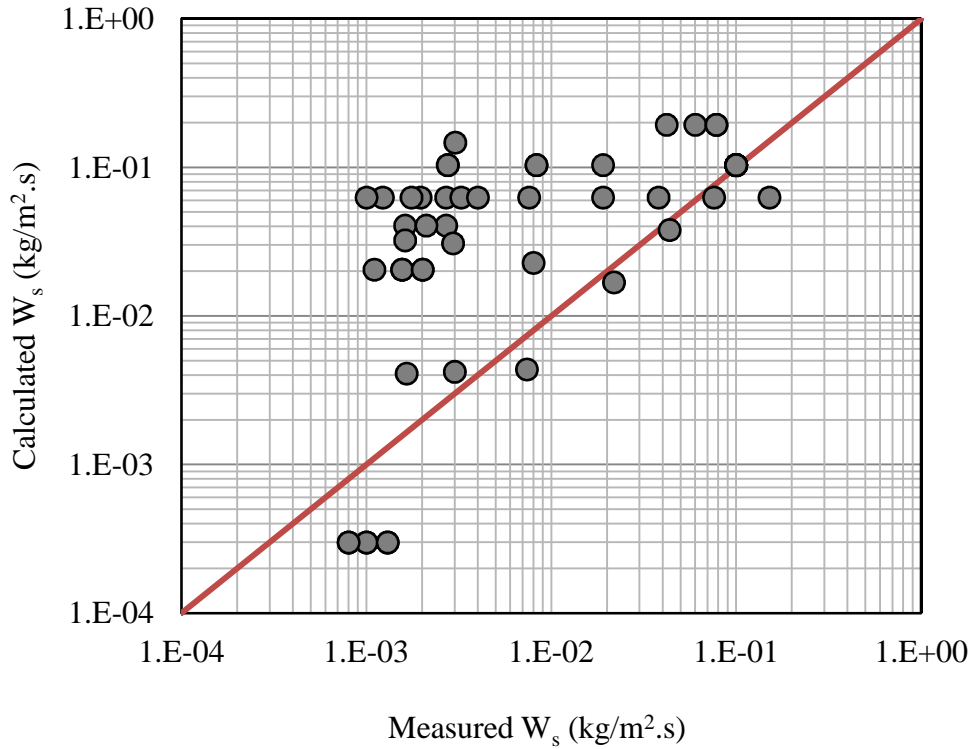


Figure 6.3 Comparison of entrainment fluxes predicted by refitted Choi et al. (1999) correlation (Equation 6.7) and experimentally measured values for different binary mixtures. For physical properties of particles, see Tables 2.1, 2.2 and 2.3.

To verify the effect of electrostatic forces on the Choi et al. (1999) correlation prediction for our experimental data, the electrostatic force (F_e) from Table 6.1 was next incorporated in Equation 6.3 and new nonlinear regression fitting was conducted to improve the performance of the correlation. The following correlation was found to provide a significantly better fit to the experimental data ($R^2=0.83$).

$$\frac{W_s d_p}{\mu} = Ar^{-0.34} \exp \left(10.75 - 2.11 F_G^{0.303} - \frac{12.78}{F_d^{1.714}} - 13.76 F_e^{0.121} \right) \quad (6.8)$$

where

$$F_e = \frac{1}{4\pi k \epsilon_0} \frac{q_F^2}{d^2} \quad (6.9)$$

with, q being the measured charge carried by the fine particles, d is the distance between particle centers when in contact, k is the dielectric constant of the particles, and ϵ_0 is the electric constant.

It can be seen that the new correlation successfully includes the effects of gravity, drag, and electrostatic forces, showing that the entrainment flux decreases with gravity and electrostatic forces, and increases with drag force. Figure 6.4 shows that the entrainment flux prediction for measured values was improved for the correlation presented by Choi et al. (1999) by the incorporation of the electrostatic force term. Overall, when electrostatic forces are appreciable in the fluidized bed, their effect needs to be recognized and considered, since they are likely to affect the extent of entrainment. For Equation 6.8 to be fully predictive, one would need to correlate the magnitude of q , the electrostatic charge, as a function of particle properties, operating conditions and equipment variables. This is beyond the scope of the present work.

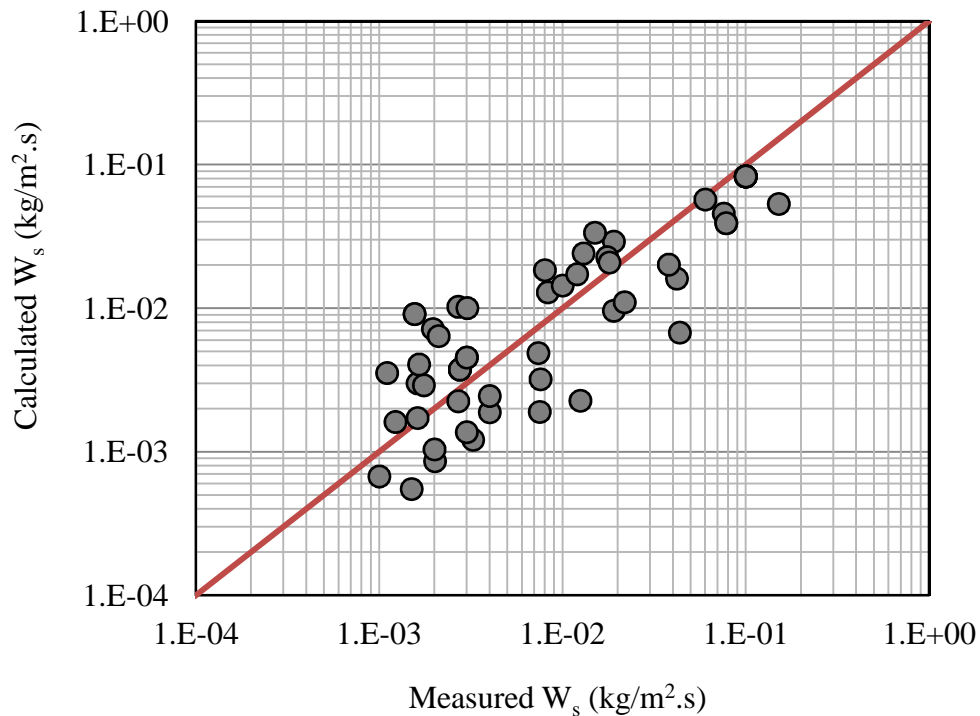


Figure 6.4 Comparison of entrainment flux predicted by modified Choi et al. (1999) correlation (Equation 6.8) incorporating an electrostatics term with experimentally measured values for different binary mixtures. For physical properties of particles, see Tables 2.1, 2.2 and 2.3.

Table 6.4 compares the empirical correlations developed and refitted in this work based on R^2 and the relative deviations of predictions from experimental data.

Table 6.4 Summary of empirical correlations investigated in this chapter.

Equation	R^2	Percent deviation (%)*
6.2	0.84	14
6.3	0.22	44
6.7	0.45	155
6.8	0.83	19

$$*\text{Percent deviation (\%)} = \sqrt{\frac{\sum (W_{\text{measured}} - W_{\text{predicted}})^2}{W_{\text{measured}}^2}} \times 100$$

It is clear that electrostatic forces play an important role with respect to entrainment. However, in most industrial processes, electrostatics are likely to be detrimental; consequently, it may not be feasible to utilize electrostatics to assist in reducing the entrainment flux. Utilization of electrostatics in control of entrainment should be considered on a case-by-case basis.

6.3 Summary

The effect of electrostatics on particle entrainment has been investigated in this chapter for different binary mixtures. The calculated electrostatic forces resulting from fine-fine and fine-large particle interactions are comparable in magnitude to, or greater than, the gravitational force exerted on the fine particles in the fluidized bed freeboard. This indicates that electrostatic forces are bound to play an important role in influencing motion of fine particles in the freeboard region.

New empirical correlations developed in this work show much better agreement with fitted data after the effect of electrostatic forces is taken into consideration. These correlations show that the entrainment flux decreases as electrostatic forces increase. This is probably because, under high electrostatic force conditions, fine particles tend to attach to the large particles of opposite polarity, as well as electrostatics causing fine particles to adhere to the column inner wall, resulting in less entrainment. The Choi et al. (1999) correlation shows

significantly better predictions for the entrainment in our system after the effect of electrostatics is taken into consideration.

Overall, when a fluidized bed contains fine particles, electrostatic forces become appreciable and should not be neglected because they can greatly affect the extent of entrainment. Neglecting the effects of electrostatics is likely responsible for much of the serious deficiency in empirical correlations in the literature for predicting entrainment from gas fluidized beds. However, taking electrostatics into account is difficult, as charge depends on particle properties and a host of factors, such as the extent of grounding and the dielectric properties of the particles, which have rarely (if ever) been reported or considered to be of importance in the many studies where entrainment has been measured.

Chapter 7: Conclusions and Recommendations

Understanding and controlling particle entrainment in fluidized bed reactors is a challenging problem. Entrainment phenomena are still not well understood since many parameters, such as particle properties, pressure, gas velocity, temperature, and, as proven in the previous chapter, electrostatics affect the entrainment rate. High gas velocities in fluidized beds result in fine particles becoming entrained in the fluid. Pollution control regulations and high costs, e.g., for catalytic reactor solids, make it necessary to recover the solid particles entrained from the fluidized bed. Proper design of solids recovery equipment, such as cyclones, requires accurate prediction of both the solid flux and the size distribution of the entrained solids. Numerous empirical correlations have been proposed to predict the flux of entrained solids. However, these are of very limited utility as predictions derived from these correlations commonly differ by several orders of magnitude, and no reliable generalized accurate model is available.

Electrostatic phenomena in gas-solid fluidization have been reported for many years and need to be better understood. Electrostatic charges in fluidization processes resulting from the continuous motion and rubbing among bed particles lead to the increased generation of electrostatic charges. The electrostatic charges in fluidized systems can cause problems, such as particle agglomeration, wall sheeting, and even explosions, all of which can affect plant safety and economic efficiency, but they also affect particle motion in the freeboard and downstream separation equipment.

Most industrial gas-solid fluidized bed reactors operate over a range of superficial gas velocities at pressures and temperatures well above ambient. Therefore, in this study, the goal was to investigate the simultaneous influence of particle properties, gas relative humidity, and operating variables, such as pressure, temperature, and fluidizing air velocity, on both particle entrainment and electrostatic charges generated in the bed and freeboard region to gain a better understanding of the entrainment and electrostatic phenomena in gas-solid fluidized beds. An elevated-pressure fluidization facility was modified, and appropriate electrostatic charges and entrainment measurement techniques were developed and used to achieve this goal. Experiments were then performed in gas-solid fluidized beds operating in the bubbling flow regime.

7.1 Conclusions

Experiments to determine the effects of superficial gas velocity, pressure, and temperature on entrainment flux and electrostatic charges were performed with glass beads and polyethylene as coarse bed particles with the superficial gas velocity varied from 0.2 to 0.6 m/s, and other operating parameters maintained nearly constant. The results showed that both the entrainment increased and magnitude of electrostatic charge at different levels inside the bed as well in the freeboard region increased as the superficial gas velocity increased. Different entrainment correlations from the literature were examined to predict the entrainment flux over a range of superficial gas velocities. Wide divergence among correlation predictions was found, with these correlations consistently over-predicting the experimental entrainment flux. The wide divergence of entrainment correlation predictions indicated that many factors influence entrainment and confirmed the complexity of the entrainment phenomena.

In experiments to investigate the influence of operating pressure on entrainment and electrostatics, the freeboard absolute pressure was varied from 207 to 517 kPa while other operating parameters were maintained virtually constant. The results showed that the entrainment flux and electrostatic charges at different levels in the bed and the freeboard region increased as the pressure increased. It is clear from these experimental results and earlier reported studies that both entrainment and electrostatics are greatly affected by the bed hydrodynamics.

Free-bubbling experiments showed that temperature had negligible effect on the entrainment flux over the limited temperature range studied (20 to 75°C). However, electrostatic charges decreased and the charge polarity reversed as the bed temperature increased from 20 to 75°C. In all experiments, the polarity of fines in the freeboard was positive, opposite to that in the bed.

In all experiments, the electrostatic charges in the bed decreased with increasing air relative humidity for a range of relative humidity of (3–38%) for fine glass beads and fine Al_2O_3 . Both the charge density of fines decreased and entrainment increased as the air relative humidity increased. However, there was no clear effect on the fines charge density and

entrainment flux for fine polyethylene particles, probably due to the hydrophobic nature of polyethylene.

The influences of coarse particle type, average size, and density on cumulative charge, charge density, and entrainment flux were studied. Experiments with binary mixtures of relatively coarse (group B) particles and different types of fine (group A) particles indicate that the magnitude of electrostatic charges generated inside a fluidized bed increase as the size of the coarse particles decreases. The experimental data showed that as the coarse particle density increased, electrostatic charges increased and entrainment flux decreased.

Experimental results indicate that the magnitude of electrostatic charges generated inside a fluidized bed with glass and alumina fines are higher than when polyethylene particles constitute the fines, while the polyethylene fines carried less charge, their entrainment flux was much higher than for fine glass beads and alumina. As the fines concentration increased, the electrostatic charges and entrainment flux also increased. However, the fines concentration had little or no effect on fines charge densities. Bipolar charging was observed in all experiments, with the fine particles charged positively, whereas large particles charged negatively. The fines concentration (5–15 wt%) had no effect on the polarity of either the large or fine particles.

The effect of electrostatics on particle entrainment was analysed for binary glass bead systems. The electrostatic forces resulting from fine-fine and fine-large particle interactions were shown to be comparable in magnitude to the gravitational force exerted on fine particles in the fluidized bed, which gives an indication of the importance of electrostatic force. An empirical correlation developed in this work showed significantly better performance when the effect of electrostatic forces was taken into account. The empirical correlation showed that the entrainment flux decreases as electrostatic forces increase. The Choi et al. (1999) correlation, based on more than 1000 experimental data and covering a wide range of variables, shows better prediction for the entrainment in our system after the effect of the electrostatic force is included. When the fluidized bed contains fine particles, electrostatic forces become appreciable and need to be considered when predicting entrainment.

7.2 Recommendations for Future Work

In this work, an attempt has been made to gain a better understanding of the complexity of the entrainment phenomena in gas-solid fluidized beds by investigating the effect of different operating variables, particle properties and electrostatics. However, more extensive experimental measurements of particle entrainment over a wider range of operating variables, such as pressure and temperature, are required. In addition, since our work was limited to the bubbling flow regime and most industrial fluidization units operate in the turbulent flow regime, it is important to study how the entrainment is influenced by operating variables and electrostatics at higher superficial gas velocities.

Future work should be carried out to investigate different particle mixtures, for example, polyolefin and FCC particles, from industrial reactors over industrial operating conditions.

From the extensive data that will be collected from the proposed future work, further work can be undertaken to incorporate the effect of electrostatics into entrainment models to predict particle entrainment from gas-solid fluidized beds accurately. Improving the understanding of electrostatic charge generation and dissipation is important in this respect.

References

- Alan, S. and Hamdullahpur, F., Effect of bubble coalescence on entrainment in gas fluidized beds. *Powder Technology*, 77, (1993), 251-265.
- Ali, F. S., Ali, M. A., Ali, R. A. and Inculet, I. I., Minority charge separation in falling particles with bipolar charge. *Journal of Electrostatics*, 45, (1998), 139-155.
- Anderson, B. and Leckner, B., Particle mass flux in the freeboard of a fluidized bed boiler. *Powder Technology*, 58, (1989), 25-37.
- Bachovchin, D, Beer, J. and Sarofim, A., An Investigation into the steady-state elutriation of fines from a fluidized Bed. *AIChE Symp. Ser.*, 77, (1981), 76.
- Baeyens, J., Geldart, D., Wu, S.Y., Elutriation of fines from gas fluidized bed of Geldart A-type powders-effect of adding superfines. *Powder Technology*, 71, (1992), 71-80.
- Baron, T., Briens, C.L. and Bergougnou, M.A., Measurement of the flux of clusters ejected from a fluidized bed. *Powder Technology*, 55, (1988), 115-125.
- Baron, T., Briens, C.L., Bergougnou, M.A. and Hazlett, J.D., Electrostatic effects on entrainment from a fluidized bed. *Powder Technology*, 57, (1987), 55-67.
- Baron, T., Briens, C.L., Bergougnou, M.A., Inculet, I.I. and Hazlett, J.D., Size distribution of particles entrained from fluidized beds: Electrostatic effects. *Powder Technology*, 70, (1992), 57-62.
- Baron, T., Briens, C.L., Galtier, P. and Bergougnou, M., Effect of bed height on particle entrainment from gas-fluidized beds. *Powder Technology*, 63, (1990), 149-156.
- Barretto G.F., Yates, J.G. and Rowe, P.N., The effect of pressure on the flow of gas in fluidized beds of fine particles. *Chemical Engineering Science*, 38, (1983), 1935-1945.
- Boggs, S., Damon, D., Hjerrild, J., Holboll, J. and Henriksen, M., Effect of insulation properties on the field grading of solid dielectric DC cable. *IEEE Transaction on Power Delivery*, 16, (2001), 456-461.
- Boland, D. and Geldart, D., Electrostatic charging in gas fluidized beds. *Powder Technology*, 5, (1971/1972), 289-297.
- Botterill, J.S., and Desai, M., Limited factors in gas-fluidized bed heat transfer. *Powder Technology*, 6, (1972), 231-238.

- Briens, C. L., Baron, T., Hazlett, J.D., Bergougnou, M.A. and Galtier, P., Size distribution of the particles entrained from fluidized beds: Gas humidity effects. *Canadian Journal of Chemical Engineering*, 70, (1992), 631-635.
- Cai, P., Schiavetti, M., De Michlle, G., Grazzini, G.C. and Miccio, M., Quantitative estimation of bubble size in PFBC. *Powder Technology*, 80, (1994), 99-109.
- Cartwright, P., Singh, S., Bailey, A., and Rose, L., Electrostatic Charging Characteristics of Polyethylene Powder During Pneumatic Conveying. *Industry Applications, IEEE Transactions*, IA-21, (1985), 541-546.
- Castricum, H., Sah, A., Mittelmeijer-Hazeleger, M., and ten Elshof, J., Hydrophobisation of mesoporous γ -Al₂O₃ with organochlorosilanes—efficiency and structure. *Microporous and Mesoporous Materials*, 83, (2005), 1-9.
- Chan, I.H. and Knowlton, T.M., The effect of pressure on entrainment from bubbling gas-fluidized beds. In *Fluidization IV*, Engineering Foundation, (1984), 283-290.
- Chen, A.H., Bi, H.T. and Grace, J.R., Measurements of particle charge-to-mass ratios in a gas-solid fluidized bed by a collision probe. *Powder Technology*, 135-136, (2003a), 181-191.
- Chen, A.H., van Willigen, F.K., Bi, H.T., Grace, J.R. and van Ommen, J.R., Measurements of charge distribution around a rising bubble in a 2-D fluidized bed. *AIChE Journal*, 52, (2006), 174-184.
- Chiba, S., Chiba, T., Nienow, A.W. and Kobayashi, H., The minimum fluidization velocity, bed expansion and pressure-drop profile of binary particle mixtures. *Powder Technology*, 22, (1979), 255-269.
- Chitester, D.C., Kornosky, R.M., Fan, L.S. and Danko, Characteristics of fluidization at high pressure. *Chemical Engineering Science*, 39, (1984), 253-261.
- Choi, J., Chang, I., Shun, D., Yi, C., Son, J. and Kim, S., Correlation on the particle entrainment rate in gas fluidized beds. *Industrial Engineering Chemical*, 38, (1999), 2491-2496.
- Choi, J., Ryn, H., Shun, D., Son, J. and Kim, S., Temperature effect on the particle entrainment rate in a gas fluidized bed. *Industrial Engineering Chemical*, 37, (1998), 1130-1135.
- Choi, J.H., Son, J.E and Kim, S.D., Solid entrainment in fluidized bed combustors. *Journal of Chemical Engineering of Japan*, 22, (1989), 597-606.

- Choi, J.H., Suh, J.M., Chang, I.Y., Shun, D.W., Yi, C.K., Son, J.E. and Kim, S.D., The effect of fine particles on elutriation of coarse particles in a gas fluidized bed. *Powder Technology*, 121, (2001), 190-194.
- Ciborowski, J.S. and Wlodarski, A., On electrostatic effects on fluidized bed. *Chemical Engineering Science*, 17, (1962), 23-32.
- Cross, J.A, *Electrostatics, principles, problems and applications*, Adams Higler, Bristol, (1987).
- Darton, R.C., Lanauze, J.F., Davidson, J.F. and Harrison, D., Bubble growth due to coalescence in fluidized beds, *Transactions Institution of Chemical Engineers*, 55, (1977), 274-280.
- Davidson, J.F., Harrison, D., *Fluidized particles*, Cambridge University Press, Cambridge, 1963.
- Fan, L. and Zhu, C., *Principles of gas-solid flows*. Cambridge University Press, NY, (1998), 66-70.
- Fujino, M., Ogata, S. and Shinohara, H., The electric potential distribution profile in a naturally charged fluidized bed and its effects. *International Chemical Engineering*, 25, (1985), 149-159.
- Gajewski, J., Continuous non-contact measurement of electric charges of solid particles in pipes of pneumatic transport. I. Physical and mathematical models of a method. *Industry Applications Society Annual Meeting*, 2, (1989), 1958-1963.
- Geldart, D. and Wong, A.C., Effect of intraparticle forces. *AIChE Journal*, 83, (1987), 255-260.
- Geldart, D. and Wong, A.C., Entrainment of particles from fluidized beds of fine powders. *AIChE Journal*, Chicago, (1985), 10-15.
- Geldart, D., Cullinan, J., Georghiades, S., Gilvary, S. and Pope, D., The effect of fines on entrainment from gas fluidized beds. *Trans. Inst. Chem. Eng.*, 57, (1979), 269-275.
- Geldart, D., The effect of particle size and size distribution on the behaviour of gas-fluidized beds. *Powder Technology*, 6, (1972), 201-205.
- Geldart, D., Types of gas fluidization. *Powder Technology*, 7, (1973), 285-292.
- George, S.E and Grace, J.R, Entrainment of particles from a pilot scale fluidized bed. *Canadian Journal of Chemical Engineering*, 59, (1981), 279-284.
- Giffin, A., Mehrani, P, Effect of gas relative humidity on reactor wall fouling generated due to bed electrification in gas-solid fluidized beds. *Powder Technology*, 235, (2013), 368-375.
- Goossens, W.R.A., Dumont, G.L., Spaepen G.L., Fluidization of binary mixtures in laminar flow region. *Chem Eng Prog Symp Ser*, 67,116, (1971), 38-45.

- Grace, J.R., Contacting modes and behavior classification of gas-solid and other two-phase suspensions. *Canadian Journal of Chemical Engineering*, 64, (1986), 353-363.
- Guardiola, J., Rajo, V. and Ramos, G., Influence of particle size, fluidization velocity and relative humidity on fluidized bed electrostatics. *Journal of Electrostatics*, 37, (1996), 1-20.
- Guardiola, J., Ramos, G. and Romero, A., Electrostatic behavior in binary dielectric/conductor fluidized beds. *Powder Technology*, 73, (1992), 11-19.
- Harper, W.R., *Contact and Frictional Electrification*, Oxford University Press, London, 1967.
- Hemery, Y., Rouau, X., Dragan, C., Bilici, M., Beleca, R., Dascalescu, L., Electrostatic properties of wheat bran and its constitutive layers: influence of particle size, composition, and moisture content. *Journal of Food Engineering*, 93, (2009), 114–124.
- Inculet, I.I., Castle, G.S.P. and Aartsen, G., Generation of bipolar electric fields during industrial handling of powders. *Chemical Engineering Science*, 61, (2006), 2249-2253.
- Jain, P. and Saxena, N., Temperature and composition dependence of electrical conductivity of $\text{Se}_{90}\text{In}_{10-x}\text{Sb}_x$ ($x=0, 2, 4, 6, 8, 10$) chalcogenide glasses. *Journal of non-oxide and photonic glasses*, 1, (2009), 43-52.
- Jiang, P., Bi, H., Liang, S. and Fan L., Hydrodynamic behavior of circulating fluidized bed with polymeric particles. *AIChE Journal*, 40, 2, (1994), 193-206.
- Jones, T.B., Electrostatic and dust explosions in powder handling, in selected topics on fluidization ,solids handling and processing, Noyes publications, Park Ridge, NJ, (1997), 817-871.
- Kage, H., Tsumori, M., Sasaki, A., and Matsuno, Y., Application of the obstruction model to elutriation of more than one species of particles from multicomponent fluidized bed. *Journal of Chemical Engineering of Japan*, 25, (1992), 672-677.
- Kato, K. and Ito, U., The elutriation rate from a packed fluidized bed. *Journal of Chemical Engineering of Japan*, 5, (1972), 46-51.
- Kato, K. and Li, J., A correlation of elutriation rate constant for adhesion particles (group C particles). *Powder Technology*, 118, (2001), 209-218.
- Kato, K., Tajima, T., Mao, M., Iwamoto, H., In: Kwauk, M., Kunii, D., Zheng, J., Hasatani, M. eds. *Fluidization'85 Science and Technology*, Amsterdam, Elsevier, (1985), 134–147.

- Kawabata, J., Yumiyama, M., Tazaki, Y., Honma, S., Chiba, T., Sumiya, T., and Ehdo, K., Characteristics of gas fluidized beds under pressure. *Journal of Chemical Engineering Japan*, 14, (1981), 85-89.
- Kim, J.U., Electrical double layer: revisit based on boundary conditions. *ArXiv Physics e-prints*, (2005).
- Knowlton, T.M., Findlay, J. and Sishla, C., Attrition and entrainment studies related to fluidized bed gasifiers. Final report for U.S. Dept. of energy, project DE-AC21-85MC22061, (1990).
- Kunii, D. and Levenspiel, O., *Fluidization engineering*, 2nd Edition, Butterworth-Heinemann, (1991).
- Lee, J.L., Hu, C.G., Shin, Y.S., Chun, H.S., Combustion characteristics of a two-stage swirl-flow fluidized bed combustor. *Canadian Journal of Chemical Engineering*, 68, (1990), 824-830.
- Lee, W.J., Chao, Y.J., Kim, J.R. and Kim, S.D., Coal combustion characteristics in an internally circulating fluidized bed combustor. *The 3rd Asian Conference on Fluidized bed*, (1992), 126-131.
- Levy, L., Sears, J.T. and Wen, C.Y., Elutriation and attrition of char from a large fluidized bed. *Powder Technology*, 27, (1983), 105-115.
- Lewis, W.K., Gilliland, E.R. and Bauer, W.C., Characteristics of fluidized particles. *Industrial and Engineering Chemistry*, 41, (1949), 1104-1117.
- Li, J., and Kuipers, J.A., Effect of pressure on gas-solid flow behavior in dense gas-fluidized beds: a discrete particle simulation study. *Powder Technology*, 127, (2002), 173-184.
- Lin, L., Sears, J. and Wen, C., Elutriation and attrition of char from a large fluidized bed. *Powder Technology*, 72, (1980), 105-115.
- Ma, X. and Kato, K., Effect of interparticle adhesion forces on elutriation of fine powders from a fluidized bed of a binary particle mixture. *Powder Technology*, 95, (1998), 93-101.
- Ma, X., Honda, Y., Nakagawa, N. and Kato, K., Elutriation of fine powders from a fluidized bed of a binary particle-mixture. *Journal of Chemical Engineering of Japan*, 29, (1996), 330-335.
- Masuda, H., Komatsu, T. and Linoya, K., The static electrification of particles in gas-solids pipe flow. *AIChE Journal*, 22, (1976), 558-564.

- Masuda, H., Matsusaka, S. and Nagatani, S., Measurements of powder flow rate in gas-solids pipe flow based on the static electrification of particles. *Advanced Powder Technology*, 5, (1994), 241-254.
- Matsusaka, S. and Masuda, H., Simultaneous measurement of mass flow rate and charge-to-mass ratio of particles in gas-solid pipe flow. *Chemical Engineering Science*, 61, (2006), 2254-2261.
- Matsusaka, S., Maruyama, H., Matsuyama, T. and Ghadiri, M., Triboelectric charging of powders: A review. *Chemical Engineering Science*, 65, (2010), 5781–5807.
- May, W.G. and Russel, F.R., Effect of pressure on solid entrainment. Paper presented at the north jersey section of ACS, (1954).
- Mehrani, P., Bi, H.T. and Grace, J.R., Electrostatic behavior of different fines added to a Faraday cup fluidized bed. *Journal of Electrostatics*, 65, (2007b), 1-10.
- Mehrani, P., Bi, T.H. and Grace, J.R., Electrostatic charge generation in gas-solid fluidized beds. *Journal of Electrostatics*, 63, (2005), 165-173.
- Mehrani, P., Characterization of electrostatic charges in gas-solid fluidized beds, Ph.D. Dissertation, University of British Columbia, 2005.
- Mehrani, P., M., Bi, H.T. and Grace, J.R., Bench-scale tests to determine mechanisms of charge generation due to particle–particle and particle–wall contact in binary systems of fine and coarse particles. *Powder Technology*, 173, (2007a), 73-81.
- Mehrani, P., Sowinski, A. and Mayne, A., Effect of fluidizing particle size on electrostatic charge generation and reactor wall fouling in gas-solids fluidized beds. *Chemical Engineering Science*, 71, (2012), 552–563.
- Merrick, D. and Highley, J., Particle size reduction and elutriation in a fluidized bed process. *AIChE Journal*, 70, (1974), 366-378.
- Mii, T., Yoshida, K. and Kunii, D., Temperature effect on the characteristics of fluidized beds. *Journal of Chemical Engineering Japan*, 6, (1973), 100-102.
- Miller, C.O. and Logwinuk, A.K., Fluidization studies of solid particles. *Industrial and Engineering Chemistry*, 43, (1951), 1220-1226.
- Milne, B.J., Berruti, F. and Behie, L.A., The hydrodynamic of the internally circulating fluidized bed at high temperature. *Fourth International Conference on Circulating Fluidized beds*, (1993), 29-34.

- Montgomery, D.J., Static electrification of solids. *Solid state physics*, 9, (1959), 139-196.
- Mori, S., Wen, C.Y., Estimation of bubble diameter in gaseous fluidized beds. *AIChE Journal*, 21, (1975), 109-115.
- Moughrabiah, W., Effect of operating parameters and particles properties on electrostatics in gas-solid fluidized beds, Ph.D. Dissertation, University of British Columbia, 2009.
- Moughrabiah, W.O., Grace, J.R. and Bi, T.H., Effect of pressure, temperature and gas velocity on electrostatics in gas-solid fluidized beds. *Industrial Engineering Chem. Res.*, 48, (2009), 320-325.
- Moughrabiah, W.O., Grace, J.R. and Bi, T.H., Electrostatics in gas-solid fluidized beds for different particle properties. *Chemical Engineering Science*, 75, (2012), 198-208.
- Nakagawa, N., Arita, S., Vchida, H., Takamura, N., Takarda, T. and Kato, K., Particle hold-up and elutriation rate in the freeboard of fluid beds. *Journal of Chemical Engineering of Japan*, 27, (1994), 79-84.
- Nakazato, T., Li, J. and Kato, K., Effect of cohesive powders on the elutriation of particles from a fluid bed. *Chemical Engineering Science*, 59, (2004), 2777-2782.
- Newton, D., Fiorention, M. and Smith, G.B., The application of X-ray imaging to the developments of fluidized bed processes. *Powder Technology*, 120, (2001), 70-75.
- Nieh, S. and Nguyen, T., Effect of humidity, conveying velocity and particle size on electrostatic charges of glass beads in a gaseous suspension flow. *Journal of Electrostatics*, 21, (1988), 99-114.
- Obsberg, G.L. and Charlesworth, D.H., Elutriation in a fluidized bed. *Chemical Engineering Progress*, 47, (1951), 566-570.
- Olowson, P.A., and Almstedt, A.E., Influence of pressure and fluidization velocity on the bubble behaviour and gas flow distribution in a fluidized bed. *Chemical Engineering Science*, 45, (1990), 1733-174.
- Olssen, S.E., Wiman, J., and Almstedt A.E., Hydrodynamics of a pressurized fluidized bed with horizontal tubes: influence of pressure, fluidization velocity and tube bank geometry. *Chemical Engineering Science*, 50, (1995), 581-592.
- Park, A., Bi, H.T. and Grace, J.R., Modeling charge transfer and induction in gas-solid fluidized beds. *Journal of Electrostatics*, 55, (2002a), 135-158.

- Park, A., Bi, T.H. and Grace, J.R., Reduction of electrostatic charges in gas-solid fluidized bed. *Chemical Engineering Science*, 57, (2002b), 153-162.
- Park, S.S., Choi, Y.T., Lee, G.S. and Kim, S.D., Coal combustion characteristics in an internal circulating fluidized bed-combustor. In *Circulating Fluidized bed Technology III*, (1991), 497-503.
- Pemberton, S.T. and Davidson, J.F., Elutriation from fluidized beds-I. Particle ejection from the dense phase into the freeboard. *Chemical Engineering Science*, 41, (1986), 243-251.
- R. Siddique, *Waste Materials and By-Products in Concrete*, Springer, Berlin, 2008.
- Reitz, J.R., Milford, F.J. and Christy, R.W., *Foundations of Electronic Theory*, 4th ed., pp.1-126, Addison-Wesley Publishing Company, Massachusetts, 1993.
- Rokkam, R., Fox, R., Muhule, M., Computational fluid dynamics and electrostatic modeling of polymerization fluidized-bed reactors. *Powder Technology*, 203, (2010a), 109–124.
- Rokkam, R., Fox, R., Muhule, M., CFD modeling of electrostatic forces in gas-solid fluidized beds. *Journal of Computational Multiphase Flows*, 2, (2010b), 189–205.
- Romanova, T.T., Effect of temperature on total entrainment of dust from a polydispersed fluidized bed. *Deposited Doc., Vintiti 5129*, 80, (1980).
- Sanari, T. and Kunii, D., unpublished paper (1962) referred to in Chen, L., *Fluidized bed freeboard phenomena study Ph.D. Dissertation*, University of West Virginia, 1981.
- Senior, R.C., *Circulating fluidized bed fluid and particle mechanics: modeling and experimental studies with application to combustion*, Ph.D. Dissertation, University of British Columbia, 1992.
- Sishtla, C., Chan, I., and Knowlton, T., *Fluidization V*, (Ostergaard, and Sorenson, eds.), Engineering foundation, (1986), p.127.
- Sookai, S., Carsky, M. and Baloyi, S., Results of fluidized bed hydrodynamic and entrainment studies for powders varying in particle size, density and shape. *Industrial Fluidization Journal*, South Africa, (2005), 211-221.
- Sycheva, T. and Donat, E., Fines elutriation. *International Chemical Engineering*, IS, (1975), 346.
- Tannous, K., Donida, M.W. and Obata, L.A., Entrainment of heterogeneous particles from gas-fluidized bed. *Particulate Science and Technology*, 26, (2008), 222-234.

- Tardos, G., and Pfeffer, R., A method to measure electrostatic charge on a granule in a fluidized bed. *Chemical Engineering Communications*, 4, (1980), 665-671.
- Tasirin, S. and Geldart, D., Entrainment of fines from fluidized beds with an expanded freeboard. *Chemical Engineering Communications*, 166, (1998), 217-230.
- Tasirin, S.M. and Geldart, D., The elutriation of fine and cohesive particles from gas fluidized beds. *Chemical Engineering Communication*, 173, (1999), 175-195.
- Wang, C., Yao, J., Matsusaka, S. and Masuda, H., Electrostatics of the granular flow in a pneumatic conveying system. *Industrial Engineering Chem. Res.*, 43, (2004), 7181-7199.
- Wen, C.Y. and Chen, L.H., Fluidized bed freeboard phenomena: Entrainment and elutriation. *AIChE Journal*, 28, (1982), 117-128.
- Wen, C.Y. and Yu, Y.H., A generalized method for predicting the minimum fluidization velocity. *AIChE Journal*, 12, (1966), 610-612.
- Werther, J. and Harge, E., Elutriation and Entrainment. *Handbook of Fluidization and Fluid Particle Systems*, Chapter 4, (2003), 113-128.
- Wittmann, K., Helmrich, H., Schugerl, K., Measurements of bubble properties in continuously operated fluidized bed reactors at elevated temperatures. *Chemical Engineering Science*, 36 (1981), 1673–1677.
- Wolny, A. and Kazmierczak, W., Triboelectrification in fluidized bed of polystyrene. *Chemical Engineering Science*, 44, (1989), 2607-2610.
- Wolny, A. and Opalinski, I., Electric charges neutralization by addition of fines to a fluidized bed composed of coarse dielectric particles. *Journal of Electrostatics*, 14, (1983), 279-289.
- Wouter de vos, The effect of particle shape on solid entrainment in gas-solid fluidization, MS Thesis, University of Pretoria, (2008).
- Yang, W.C., Bubbling fluidized bed. Chapter 3 in *Handbook of Fluidization and Fluid Particle Systems*, (2003), 58-111.
- Yao, L., Bi, H. and Park, A., Characterization of electrostatic charges in freely bubbling fluidized beds with dielectric particles, *Journal of Electrostatics*, 56, (2002), 183-197.
- Yoshida, K., Ueno, T. and Kunii, D., Mechanism of bed to wall heat transfer in a fluidized bed at high temperatures. *Chemical Engineering Science*, 29, (1974), 77-82.
- Zenz, F.A. and Weil, N.A., A theoretical-empirical approach to the mechanism of particle entrainment from fluidized beds. *AIChE Journal*, 4, (1958), 472-479.

Zhao, H., Castle, G.S. and Inculet, I.I., Bipolar charging in polydisperse polymer powder in industrial processes. IEEE Journal, 2, (2000), 53-841.

Zimmer, E., Die elektrostatische Aufladung von Hochpolymeren Isolierstoffen, Kustoffe, 60, (1970), 465-468.

Appendix A – Equipment Photographs

A.1. Experimental Apparatus



Figure A.1 Photograph of experimental apparatus.

A.2. Fluidization Straight Section



Figure A.2 Photograph of fluidization section.

A.3. Fluidization Expanded Section



Figure A.3 Photograph of fluidization expanded section.

A.5. Electrostatics Measurement Techniques

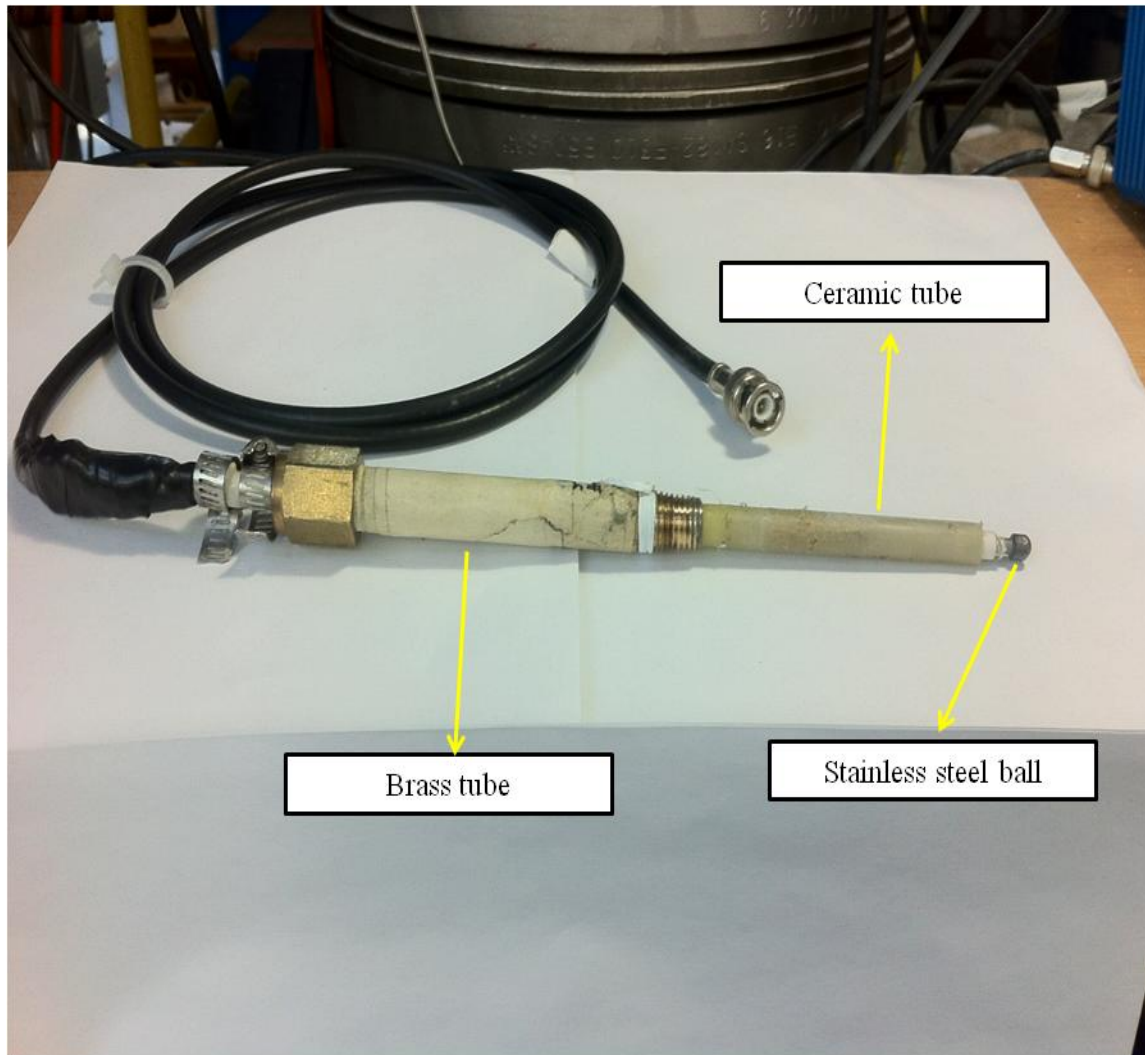


Figure A.5 Photograph of collision ball probe.

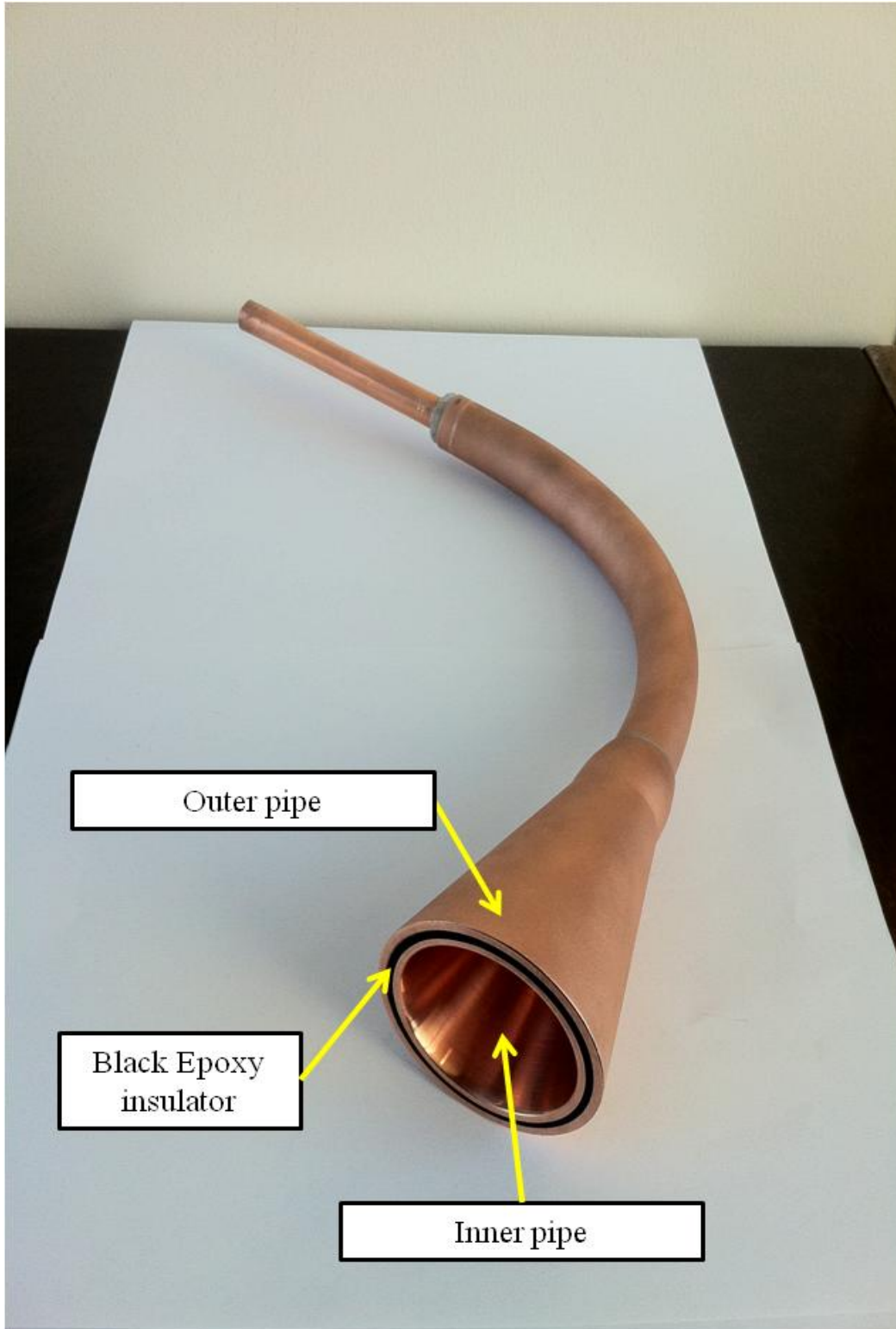


Figure A.6 Photograph of freeboard sampler.



Figure A.7 Photograph of current detection pipe.

Appendix B – Particles Size Distributions Graphs

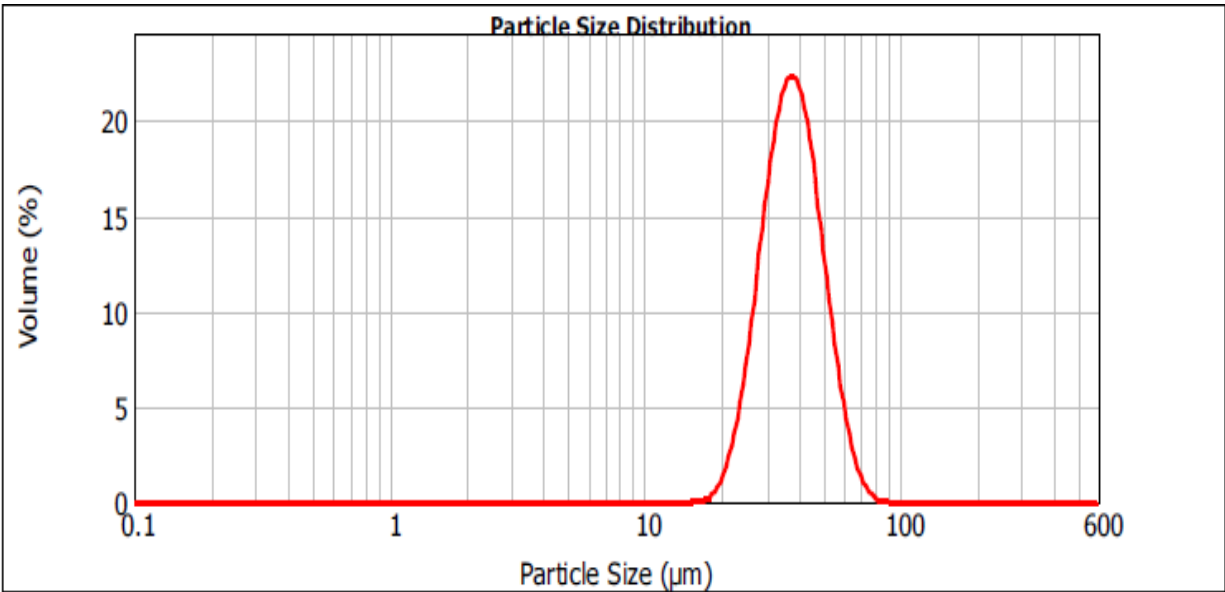


Figure B.1 Particle size distribution of GBF particles

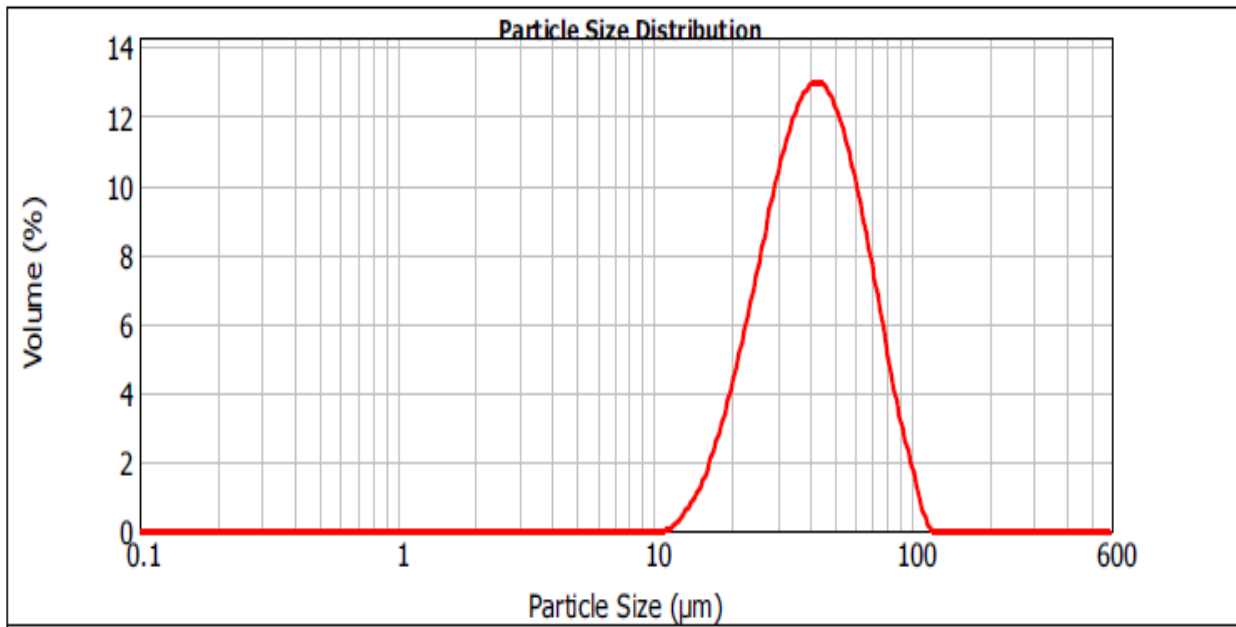


Figure B.2 Particle size distribution of PEF particles

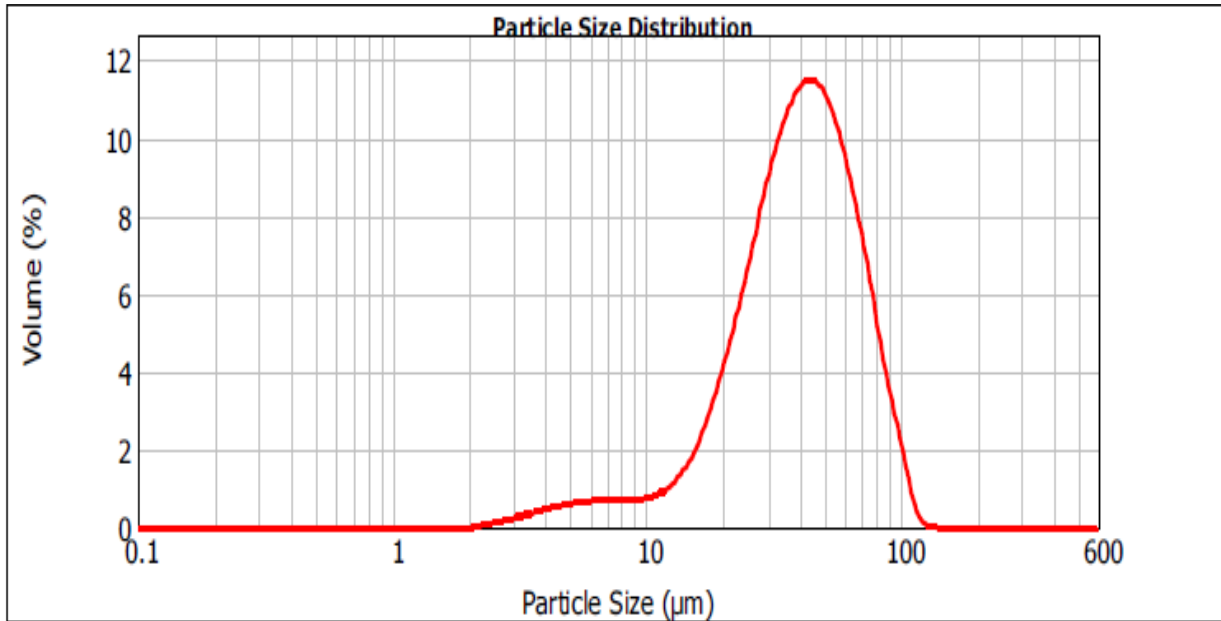


Figure B.3 Particle size distribution of Al₂O₃ particles

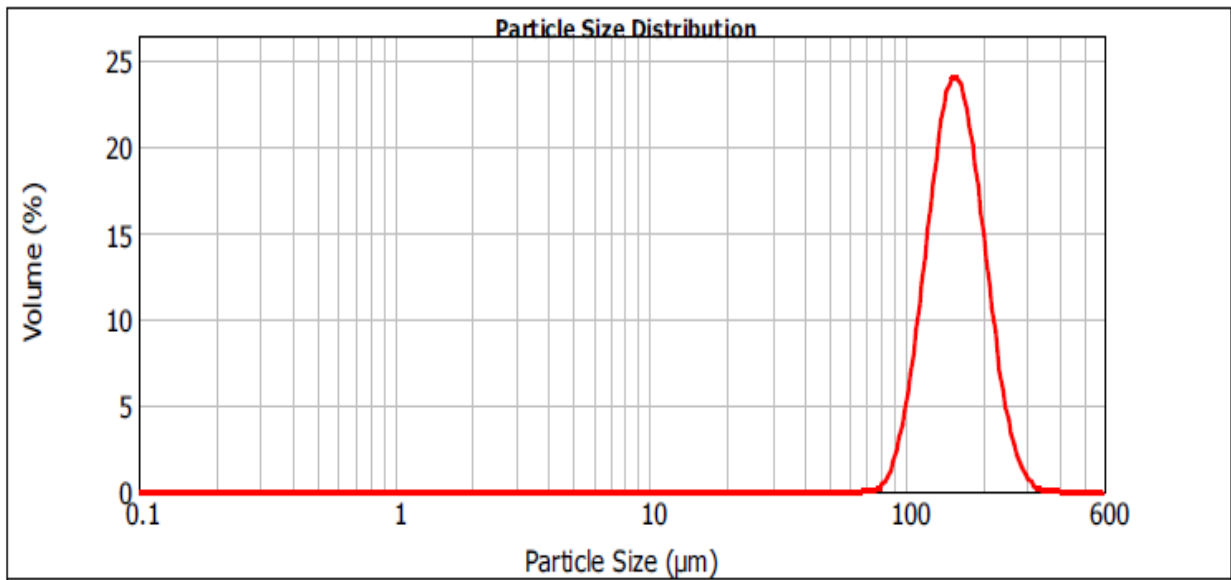


Figure B.4 Particle size distribution of GBS particles

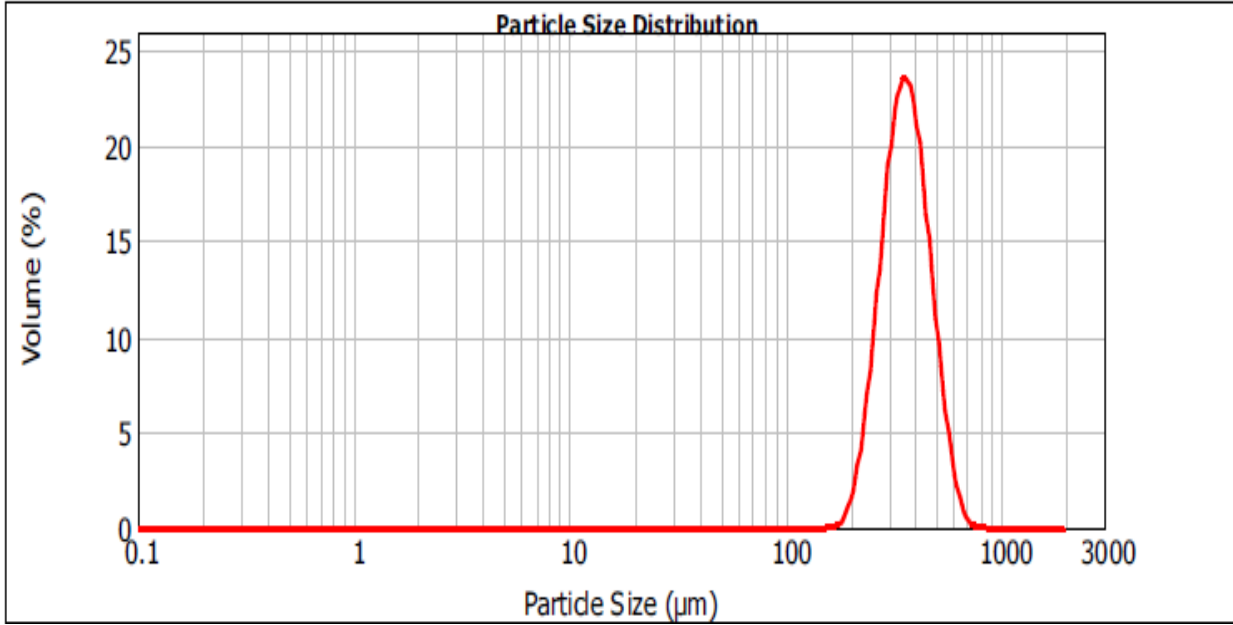


Figure B.5 Particle size distribution of GBM particles

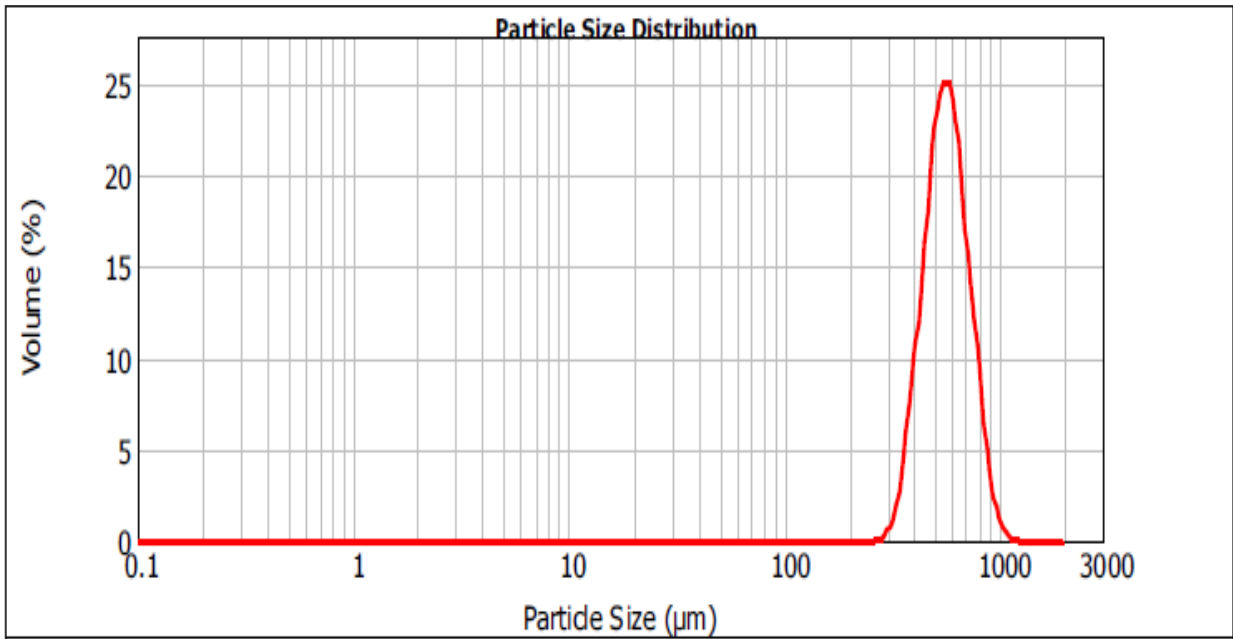


Figure B.6 Particle size distribution of GBL particles

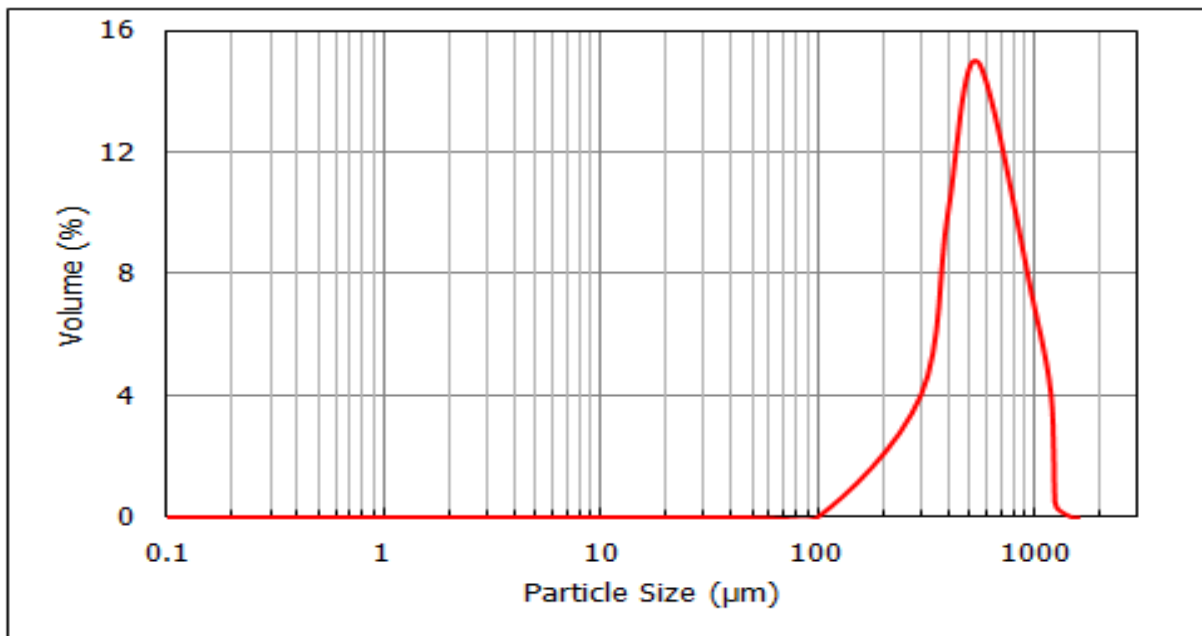


Figure B.7 Particle size distribution of HDPE particles

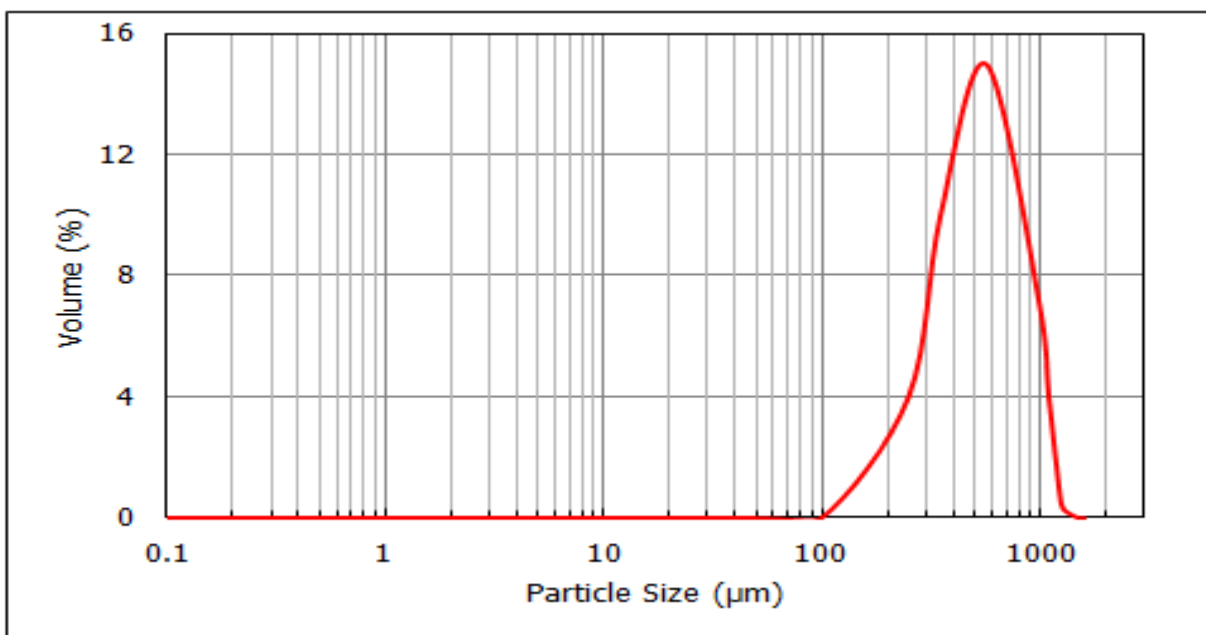


Figure B.8 Particle size distribution of LDPE particles

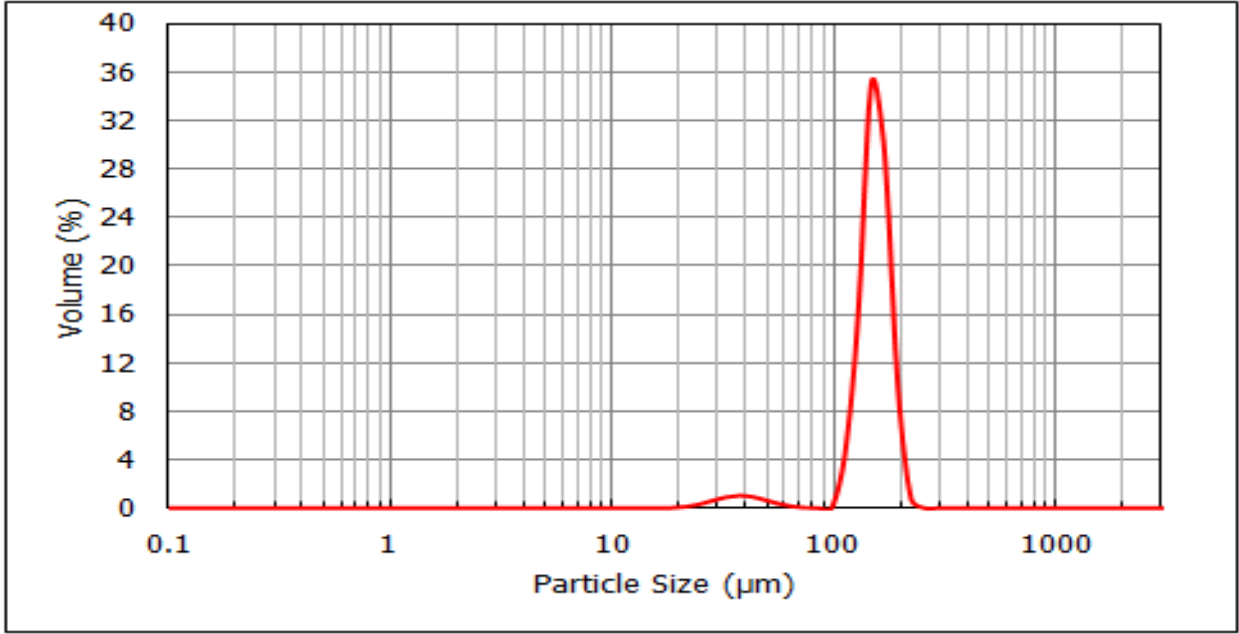


Figure B.9 Particle size distribution of M1 particles

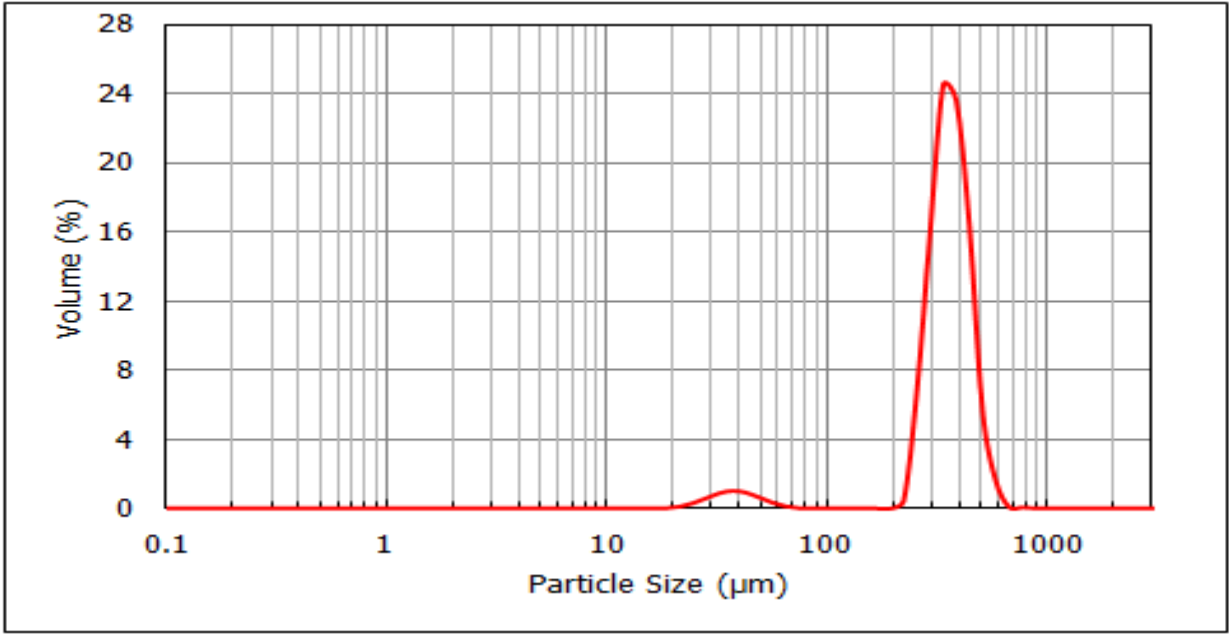


Figure B.10 Particle size distribution of M2 particles

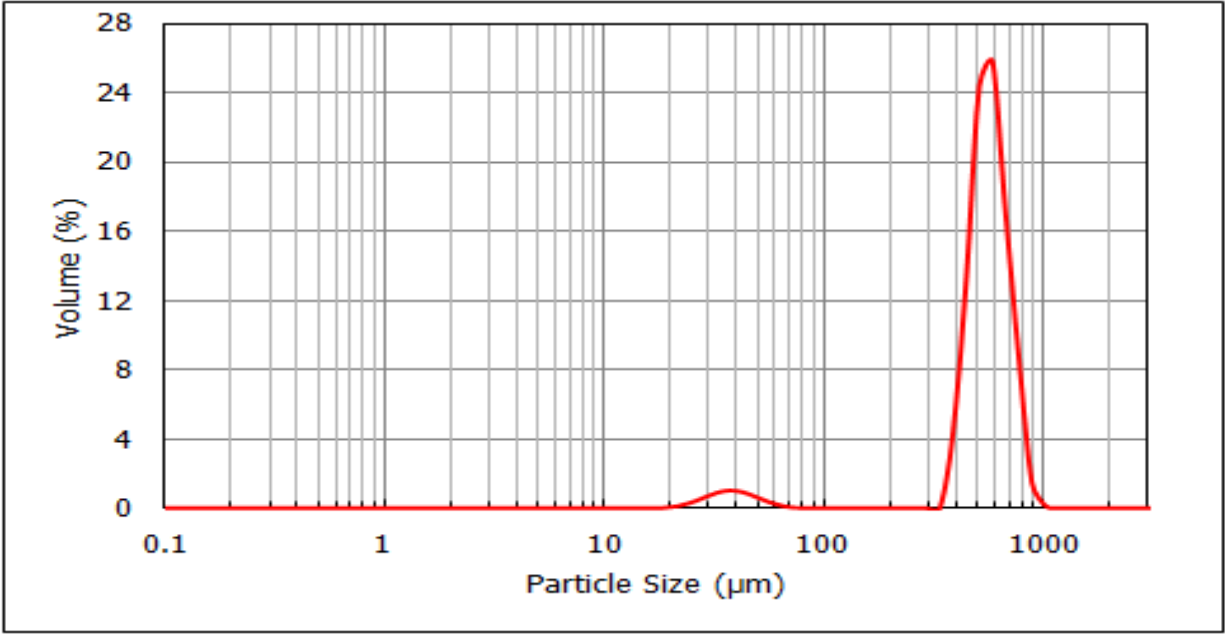


Figure B.11 Particle size distribution of M3 particles

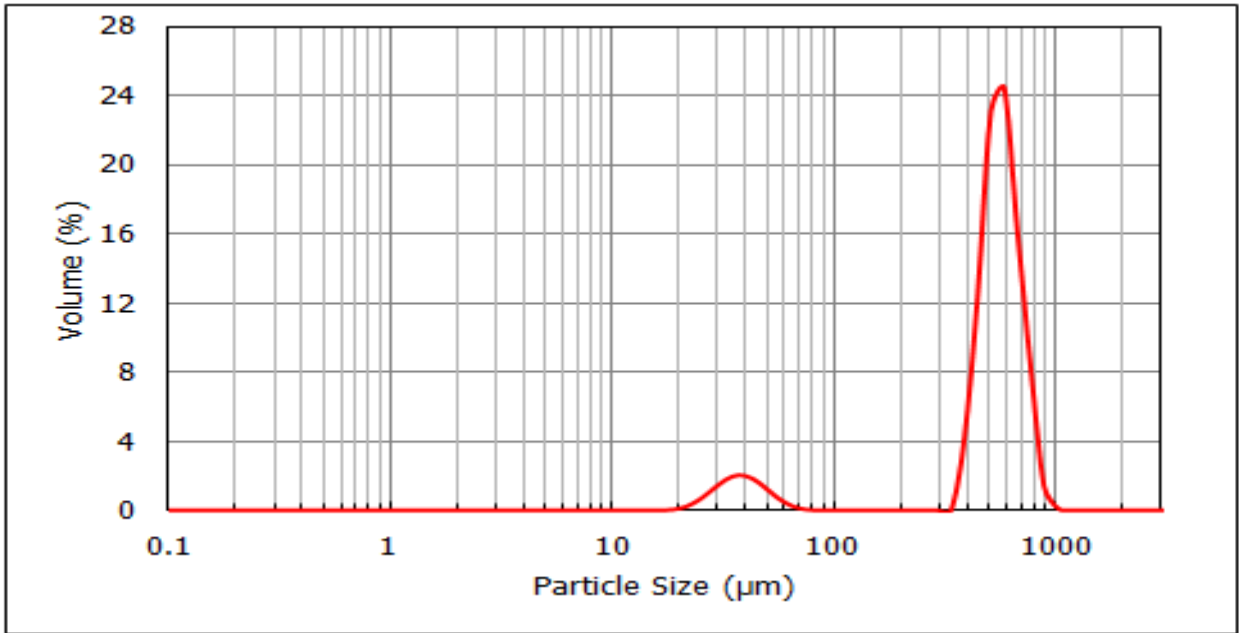


Figure B.12 Particle size distribution of M4 particles

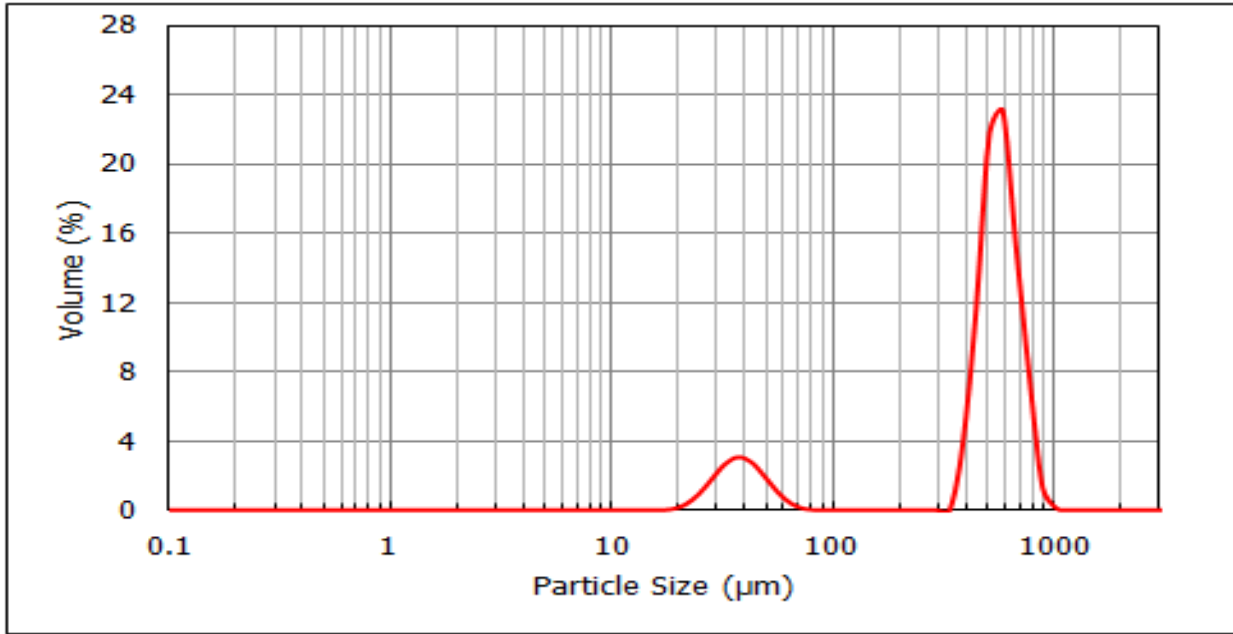


Figure B.13 Particle size distribution of M5 particles

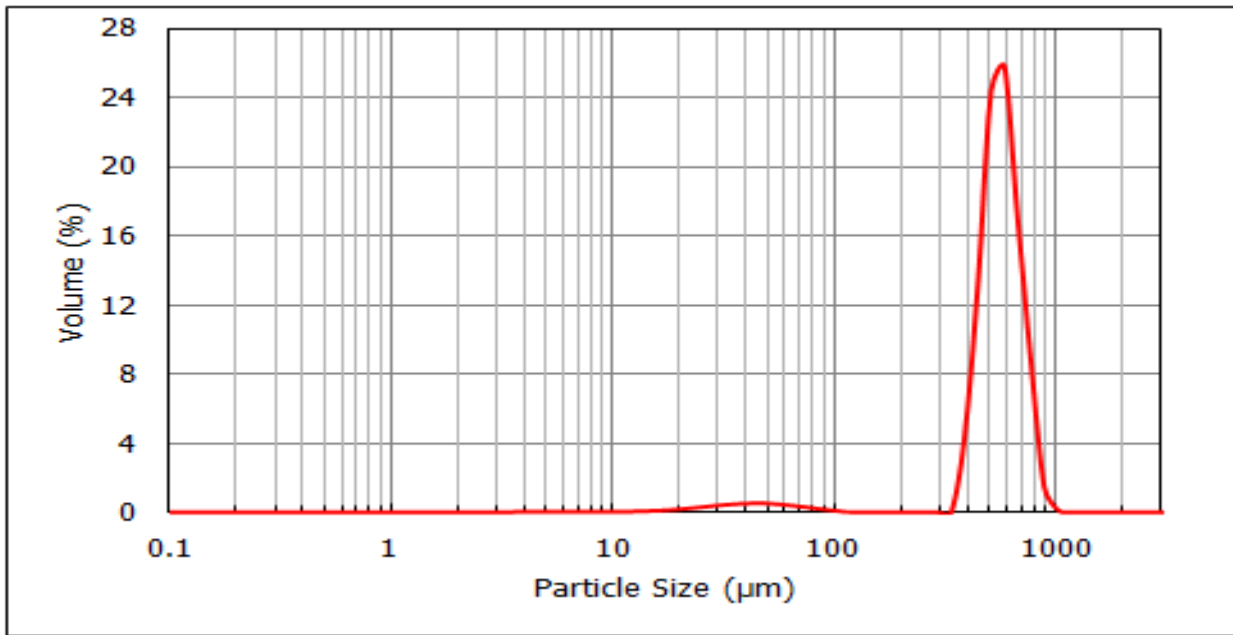


Figure B.14 Particle size distribution of M6 particles

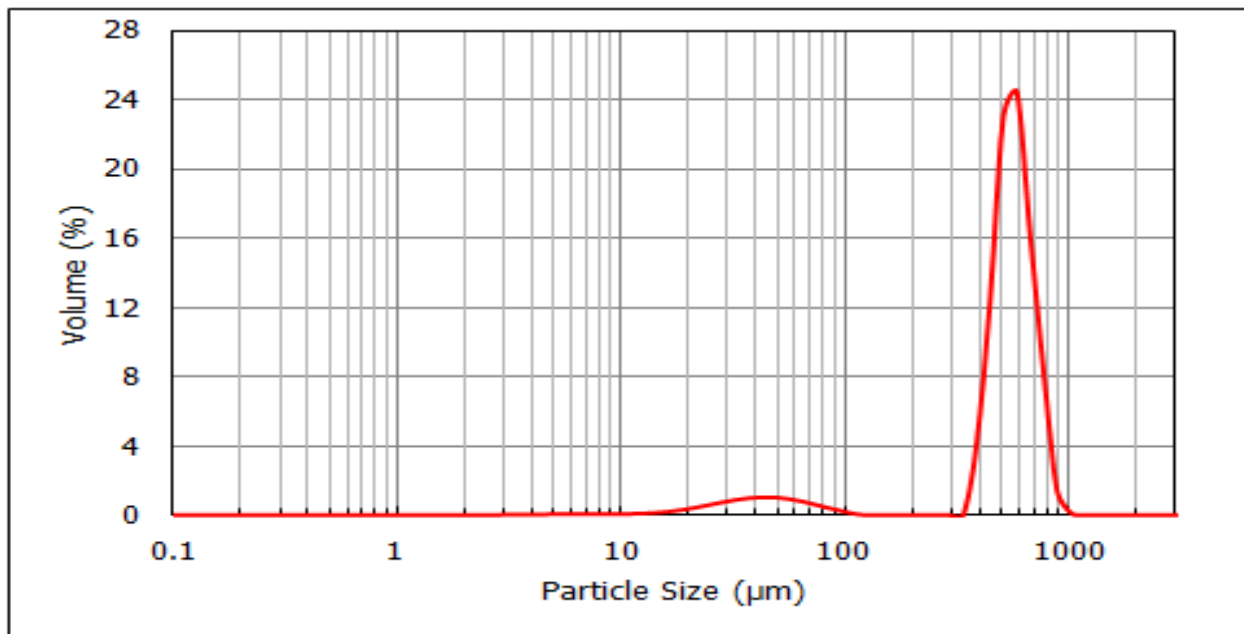


Figure B.15 Particle size distribution of M7 particles

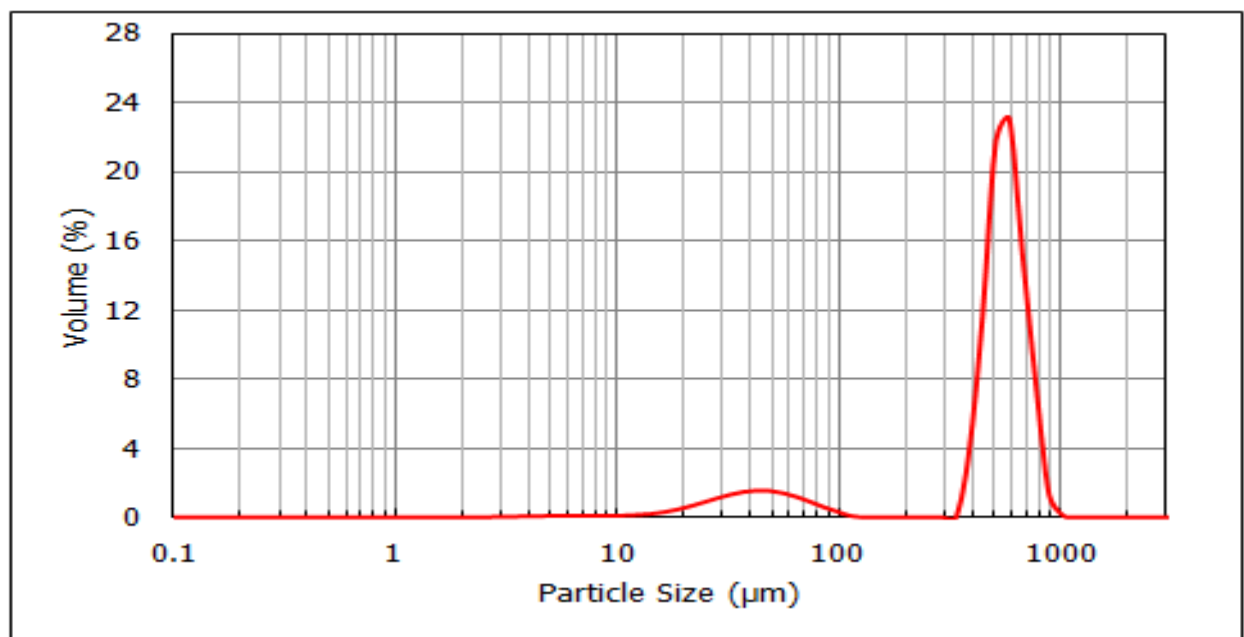


Figure B.16 Particle size distribution of M8 particles

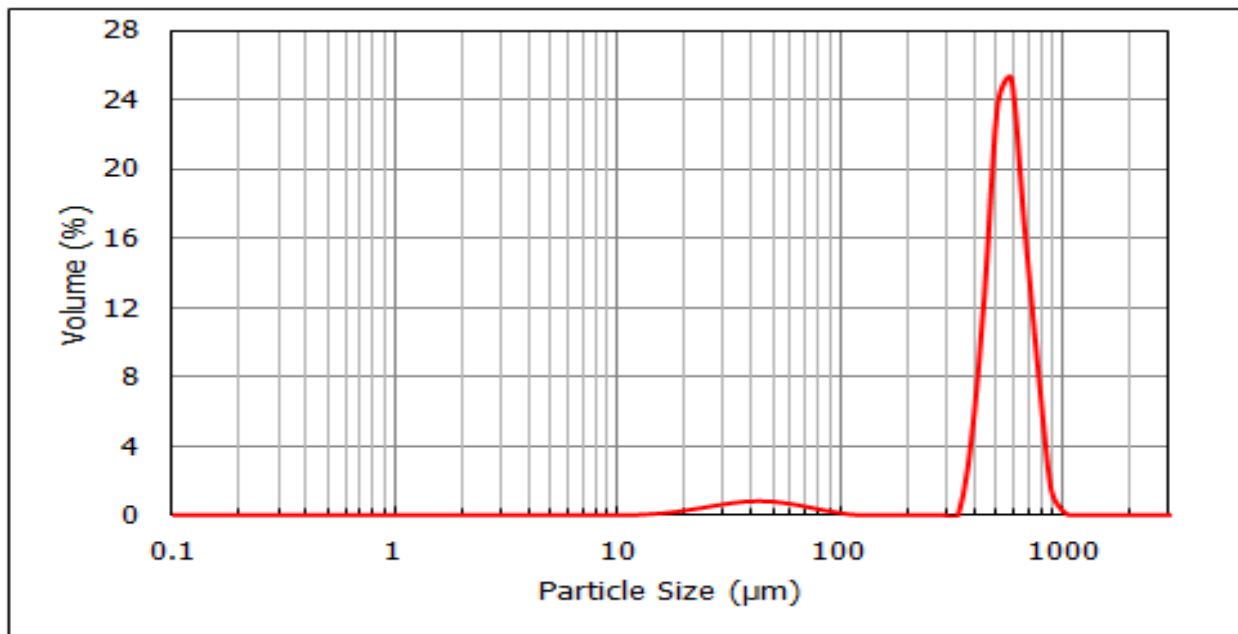


Figure B.17 Particle size distribution of M9 particles

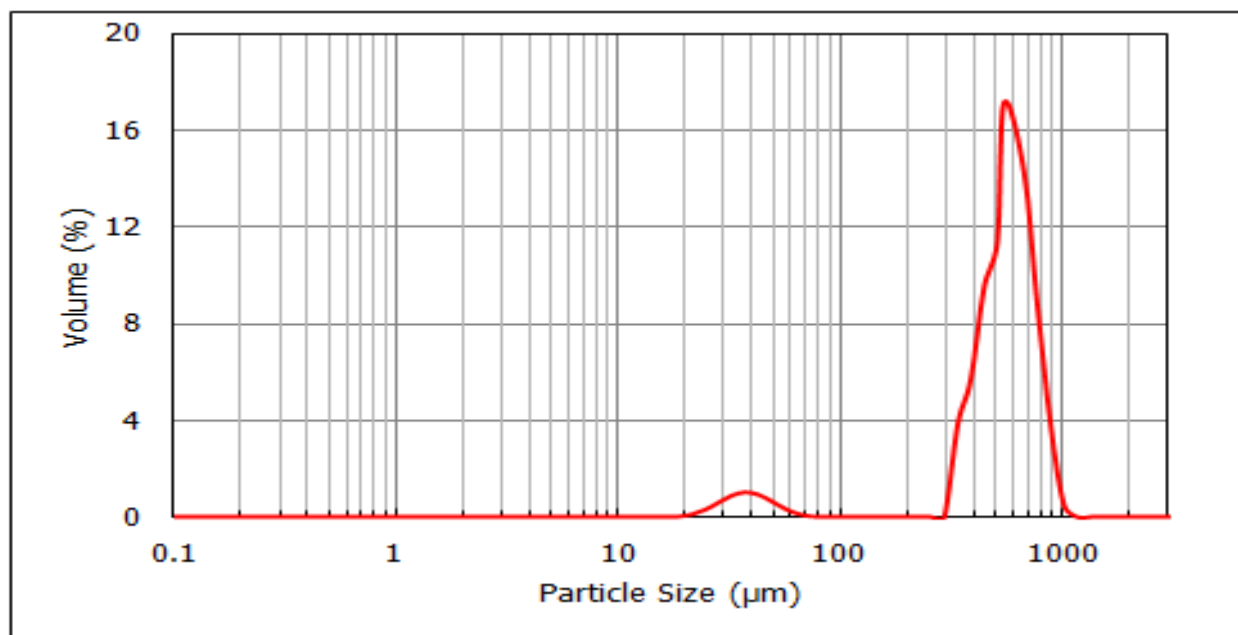


Figure B.18 Particle size distribution of M10 particles

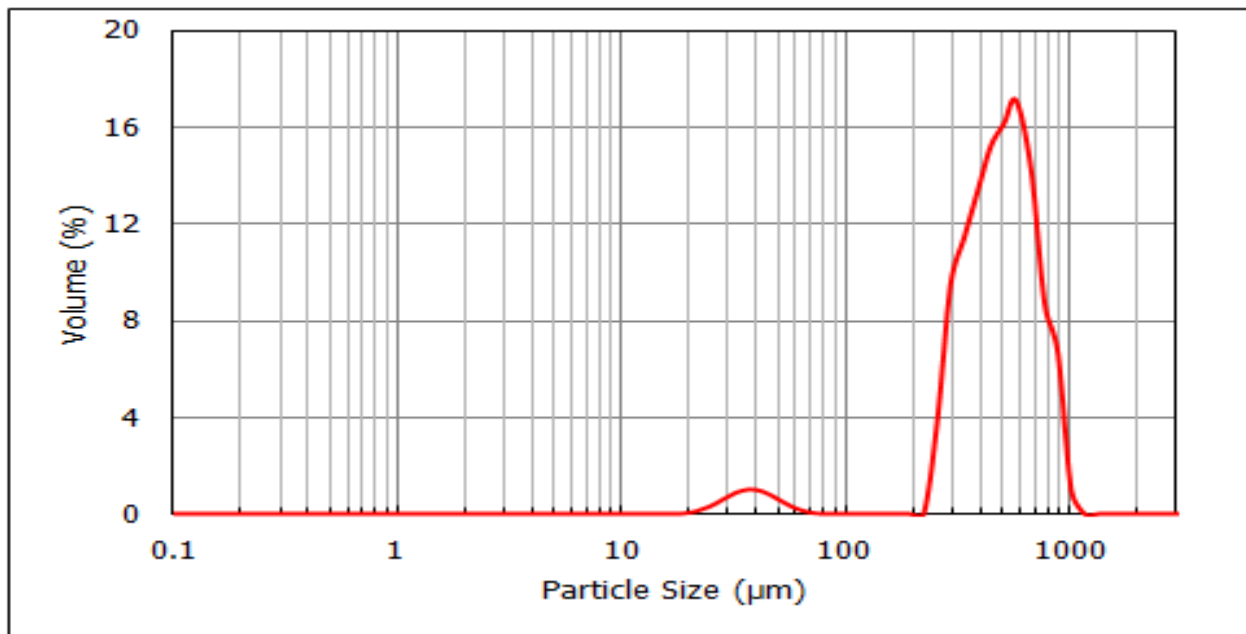


Figure B.19 Particle size distribution of M11 particles

Appendix C – Particle Properties

C.1. Calculation of Minimum Fluidization Velocity of M3 Binary Mixture

The minimum fluidization velocity (U_{mf}) was calculated by the correlation of Goossens et al. (1971) who modified the equation of Wen and Yu (1966) to account for mixture particle density, ρ_M , and the mixture particle size, d_M , as follows:

$$\frac{U_{mf}\rho_g d_M}{\mu} = \left[(33.7)^2 + 0.0408 \frac{d_M^3 \rho_g (\rho_M - \rho_g) g}{\mu^2} \right]^{0.5} - 33.7 \quad (C.1)$$

where

$$\frac{1}{\rho_M} = \frac{X_F}{\rho_F} + \frac{(1 - X_F)}{\rho_C} \quad (C.2)$$

and

$$d_M = \frac{s_0}{S} d_F d_C \quad (C.3)$$

where

$$s_0 = (1 - X_F) \rho_F d_F + X_F \rho_C d_C \quad (C.4)$$

and

$$S = (1 - X_F) \rho_F + X_F \rho_C \quad (C.5)$$

Here ρ_g is the gas density, μ is the gas viscosity, X_F is the weight fraction of fine particles, ρ_F and ρ_C are the densities of the fine and coarse particles, respectively, and d_F and d_C are the mean diameter of fine and coarse particles.

By solving Eq (C.1-C.5) for M3 mixture at $P = 414$ kPa and $T = 22$ °C gives $U_{mf} = 0.0883$ m/s.

C.2. Calculation of Total Surface Area of GBF

For GBF particles:

$d_p = 38 \mu\text{m}$, $\phi = 1$, $\rho_p = 2700 \text{ kg/m}^3$, $m_F = 3.4 \text{ g}$, $P = 414 \text{ kPa}$, $T = 22 \text{ }^\circ\text{C}$, $\text{RH} = 12\%$, $U_g = 0.3 \text{ m/s}$.

Total surface area (A_s) of GBF fine particles was calculated as

$$A_s = n (\pi d_p^2) / \phi \quad (\text{C.6})$$

where n is the number of particles, d_p is the particle diameter and ϕ is the particle sphericity.

The number of particles was calculated from:

$$n = 6 m_F / (\pi d_p^3 \rho_p) \quad (\text{C.7})$$

where m_F is the mass of particles sample and ρ_p is the particle density. Solving Eq (C.7) for GBF particles gives

$n = 4.4 \times 10^7$, then solving Eq (C.6) gives $A_s = 0.474 \text{ m}^2$.

C.3. Calculation of Electrostatic and Gravity Forces

The electrostatic force (F_e) between two charged particles was calculated by Coulomb's law:

$$F_e = \frac{1}{4\pi k \epsilon_0} \frac{q_C q_F}{d^2} \quad (\text{C.8})$$

where q_F is the charge carried by fine particles, q_C is the charge carried by the coarse particle, d is the distance between their centers, k is the dielectric constant of particles and ϵ_0 is the electric constant equal to $8.85 \times 10^{-12} \text{ C}^2/\text{N.m}^2$.

For GBF – GBL binary mixture at the above operating conditions in Appendix C.2,

$q_F = 1.36 \times 10^{-14} \text{ C}$, $q_C = 1.31 \times 10^{-13} \text{ C}$, $d = 294 \mu\text{m}$, $k = 5$

Solving Eq (C.8) for GBF-GBL binary mixture gives $F_e = 3.55 \times 10^{-10} \text{ N}$.

The gravity force (F_g) exerted on GBF particle was calculated as

$$F_g = \pi/6 d_p^3 (\rho_p - \rho_g) g \quad (C.9)$$

where ρ_g is the gas density and g is the gravitational acceleration constant equal to 9.8 m/s^2 .

Solving Eq (C.9) for GBF particle gives $F_g = 7.6 \times 10^{-10} \text{ N}$.